Une approche mathématique de l'imagerie optique par colorant potentiométrique

Hugo Raguet

Université Paris-Dauphine
École Doctorale de Dauphine

UNE APPROCHE MATHÉMATIQUE DE L'IMAGERIE OPTIQUE PAR COLORANT POTENTIOMÉTRIQUE

A Signal Processing Approach to Voltage-Sensitive Dye Optical Imaging

THÈSE

Pour l'obtention du titre de

Docteur en Sciences
Spécialité Mathématiques Appliquées

Présentée par

Hugo RAGUET

Soutenue publiquement le 22 septembre 2014 devant le jury composé de

Dirk	Jancke	Ruhr-Universität Bochum	Rapporteur
Jean-Christophe	Pesquet	Université Paris-Est Marne-la-Vallée	Rapporteur
Frédéric	Chavane	Institut de Neurosciences de la Timone	Examinateur
Laurent	Cohen	Université Paris-Dauphine	Examinateur
Bertrand	Thirion	INRIA	Examinateur
Dimitri	Van De Ville	Université de Genève	Examinateur
Gabriel	Peyré	CNRS, Université Paris-Dauphine	Directeur
Yves	Frégnac	CNRS	Co-directeur
Jalal	Fadili	ENSICAEN	Invité

Résumé

L'imagerie optique par colorant potentiométrique est une méthode d'enregistrement de l'activité corticale prometteuse, mais dont le potentiel réel est limité par la présence d'artefacts et d'interférences dans les acquisitions. À partir de modèles existant dans la littérature, nous proposons un modèle génératif du signal basé sur un mélange additif de composantes, chacune contrainte dans une union d'espaces linéaires déterminés par son origine biophysique. Motivés par le problème de séparation de composantes qui en découle, qui est un problème inverse linéaire sous-déterminé, nous développons : (1) des régularisations convexes structurées spatialement, favorisant en particulier des solutions parcimonieuses ; (2) un nouvel algorithme proximal de premier ordre pour minimiser efficacement la fonctionnelle qui en résulte ; (3) des méthodes statistiques de sélection de paramètre basées sur l'estimateur non biaisé du risque de Stein. Nous étudions ces outils dans un cadre général, et discutons leur utilité pour de nombreux domaines des mathématiques appliqués, en particulier pour les problèmes inverses ou de régression en grande dimension. Nous développons par la suite un logiciel de séparation de composantes en présence de bruit, dans un environnement intégré adapté à l'imagerie optique par colorant potentiométrique. Finalement, nous évaluons ce logiciel sur différentes données, synthétiques et réelles, montrant des résultats encourageants quant à la possibilité d'observer des dynamiques corticales complexes.

Mots-clés : imagerie optique par colorant potentiométrique, problème inverse, séparation de composantes, parcimonie structurée, optimisation convexe, méthode proximale, estimation du risque, sélection de paramètre.

Abstract

Voltage-sensitive dye optical imaging is a promising recording modality for the cortical activity, but its practical potential is limited by many artifacts and interferences in the acquisitions. Inspired by existing models in the literature, we propose a generative model of the signal, based on an additive mixtures of components, each one being constrained within an union of linear spaces, determined by its biophysical origin. Motivated by the resulting component separation problem, which is an underdetermined linear inverse problem, we develop: (1) convex, spatially structured regularizations, enforcing in particular sparsity on the solutions; (2) a new first-order proximal algorithm for minimizing efficiently the resulting functional; (3) statistical methods for automatic parameters selection, based on Stein's unbiased risk estimate. We study those methods in a general framework, and discuss their potential applications in various fields of applied mathematics, in particular for large scale inverse problems or regressions. We develop subsequently a software for noisy component separation, in an integrated environment adapted to voltage-sensitive dye optical imaging. Finally, we evaluate this software on different data set, including synthetic and real data, showing encouraging perspectives for the observation of complex cortical dynamics.

Keywords: voltage-sensitive dye optical imaging, inverse problem, component separation, structured sparsity, convex optimization, proximal method, risk estimation, parameter selection.

Table of Contents

Introduction

A Signal Processing Approach to Voltage-Sensitive Dye Optical Imaging

Voltage-sensitive dye optical imaging (VSDOI) is a recording modality of the cortical neuronal activity which is very promising for understanding the low-level sensory processing, particularly in mammals. In principles, this modality allows to observe *in-vivo* entire neuronal networks operating, with a temporal precision in the order of the millisecond and a spatial precision in the order of tens of microns. To put it differently, it represents for neuroscientists the possibility to eventually link, within the same theoretical framework, microscopic knowledge with macroscopic observations.

Unfortunately, the complexity of the experimental protocols, the presence of artifacts and interferences in the acquisitions, and the current lack of knowledge on the nature of the observed signal are so many limitations to unleash the true potential of this method. However, since its introduction back in the eighties, VSDOI has been under constant improvements, as reported by Davila *et al.* (1973); Grinvald *et al.* (1999); Shoham *et al.* (1999); Grinvald and Hildesheim (2004); Frostig (2009); Chemla and Chavane (2010b); Peterka *et al.* (2011) and many others. Most of those improvements are technological, in the sense that they can be attributed to more accurate recording devices, more controlled experimental conditions, and chemical synthesis of better dyes, *i.e.* more adapted fluorescent molecules enabling optical measurement of neuronal activity.

Naturally, as VSDOI became more reliable, it gained in popularity, and has already been used extensively by neurobiologists for *in-vivo* functional studies of the cortex, in various experimental conditions and subjects, from the anesthetized rodent to the awake monkey. In order to cope with the exceptionally high level of noise in the recordings, many authors developed, independently, their own methods for extracting the signal of interest. As reviewed in this thesis, these are often *ad-hoc* methods, for their particular experimental conditions and the specific phenomenon under investigation. In other words, the denoising process is often merged together with the biological analysis of the data which would shed light on a neuroscientific question raised *a priori*.

It is at the heart of this thesis to step back from the actual goal of VSDOI, that is understanding how information is processed within the cortex, in order to get a better understanding of the signal itself, and confront VSDOI data to the most recent advances in mathematical theories of signal processing.

Outline

This work is a collaboration between the image processing team of Gabriel Peyré from the research center CEREMADE (Université Paris-Dauphine, France), and the neuroscience team of Yves Frégnac from the laboratory UNIC (Gif-sur-Yvette, France). The investigation of VSDOI was primarily possible thanks to Cyril Monier at UNIC, and later thanks to Isabelle Ferezou. We also collaborated with another experimentalist, Esin Yavuz, while she was working on her Ph.D. thesis at UNIC. Let us mention here that she also developed a method of signal processing for VSDOI, but from a different and complementary perspective from ours, since she was investigating specific functional properties within the cat's visual cortex (Yavuz, 2012).

This collaboration leads us to work on disparate domains. Because of this interdisciplinarity, the chapters of this thesis are intended to be as independent as possible; though they are all linked by the main objective: developing a denoising method general enough to apply to most *in-vivo* VSDOI recordings.

First, we gather several issues and methods described in the VSDOI literature, and cast them in the same theoretical framework. As far as we know, this is new and constitutes our first contribution. We report it in Chapter I, setting the context and the general terms of our problematic. In brief, the VSDOI signal is a translation of changes in membrane potential, averaged over hundredth of neurons, into changes in emitted fluorescence. This signal is perturbed by many artifacts presenting characteristic temporal signatures. In addition, quantum light fluctuations induce high frequency variations. Altogether, denoising VSDOI consists in estimating the reference *baseline fluorescence* and the *gain* relating potential changes to fluorescence changes, and to extract the variations due to neuronal activity out of the other components.

We formulate then a linear component separation problem, that we intend to solve within the *sparse regularization* framework, popular in all kind of applications. Inspired in particular by the work of Reynaud *et al.* (2011), where temporal morphology of the artifact components are characterized in detail, we extend it to a nonlinear sparse model specifically adapted to VSDOI signal. This is our second contribution, described in Chapter II.

Our model defines the final component separation as the solution of a large scale, complex minimization problem, involving many parameters. The mathematical challenges raised by this model retain for a large part the focus of the subsequent work. Diverting from our original application, we delve into general mathematical tools for tackling generic *inverse problems*, extending already existing tools. In Chapter III, we develop and analyze a new *first-order proximal optimization algorithm* which seems the most suitable for addressing our minimization problem. We show then in Chapter IV how this can be useful in many applications, notably by formulating the terms of our VSDOI model in more general settings, defining in particular a new *isotrope discrete total variation semi-norm*, and by exposing in a restrained but unified framework the extent of proximal methods for signal processing.

This is however not sufficient yet for our VSDOI denoising purpose, because our model involves numerous parameters influencing drastically the resulting component

separation. In Chapter V we investigate practical use *Stein's unbiased risk estimator* in the context of signal processing, improving over some theoretical formulations existing in the literature and exploring empirically some heuristics overcoming further theoretical and practical concerns.

Finally, we turn back in Chapter VI to our main motivation and describe in details how the above theoretical developments can be adapted in practice to our VSDOI model. The full denoising method is implemented in an integrated environment suitable for visual and numerical explorations of VSDOI data, written in Matlab, interfacing with Mex the optimization algorithms written in C. This allows us to test our approach on various data sets, and the first results that we obtained are presented in Chapter VII. This constitutes the basis for discussing some practical choices in our model and suggesting research directions for improving the final method.

Previous Works and Contributions

As mentioned earlier, the examination of the VSDOI literature in a pure signal processing point of view is in itself a contribution; we refer the reader directly to Chapter I for the biological and technological context of this thesis. In the following, we precise the mathematical context, introducing the particular perspectives that we adopt along the different chapters introduced above.

Spatially Structured Sparse Morphological Component Separation

Sparsity and Structured Sparsity

The vast majority of signal processing models falls into the range of linear generative models, where the signal is encoded within coefficients of linear representations, supposed to reflect adequately its physical origin (Mallat, 2008). The task of retrieving such coefficients from given observations of the phenomenon at hand is coined *linear inverse problem*.

When dealing with underdetermined problems, *i.e.* one has access to less observations values than the number of coefficients in the models, one of the most popular framework in modern signal processing relies on *sparsity*. The main idea is that, in spite of the possible complexity, which translates into a large number of coefficients in the linear representation, each particular instance of signal within the model can be well approximated by only a few nonzero coefficients. This is referred to as the sparsity *prior*, enabling the same model to capture a wide variety of signals, while using low-dimensional representation, ensuring good properties like compressibility, separation capability or robustness to noise. See again Mallat (2008) for a nice overview of the theoretical properties of sparse models and of the extent of their applications.

In order to find a convenient sparse representation of a signal, a classical approach is to solve a minimization problem defined as the sum of two terms: a *data-fidelity* term

which measures the distance between reconstruction and observed data, and a *penalization* term which account for the number of selected regressors used for the reconstruction (see § 2.3). The solution of such a problem is thus a compromise between accuracy of reconstruction and sparsity. Common choices are the sum of square errors (often motivated by a Gaussian noise) for the data-fidelity, and ℓ_0*-pseudo-norm* (which simply counts the number of nonzero coefficients) for the penalization. The latter term being nonconvex, it is often replaced by the ℓ_1-norm (equal to the sum of the modulus of the coefficients) which is convex and allows for more efficient minimizations and more stable results (see Tibshirani (1994) for its use on regression problems, and Chen *et al.* (1998) for denoising and optimization considerations).

Sparsity principles can be adapted to reflect existing structures in the model. A meaningful example is the use of *group sparsity*, where the sparsity pattern (*i.e.* the distribution of the nonzero coefficients) is constrained to take into account relationship between coefficients. The first attempts in that direction can be found in Hall *et al.* (1997) or Cai (1999), and has been extensively used in signal processing and statistical regression applications (Chaux *et al.*, 2005; Yu *et al.*, 2008; Gribonval *et al.*, 2008; Zhao *et al.*, 2009; Obozinski *et al.*, 2010; Jenatton *et al.*, 2011).

This can be done for instance by replacing the aforementioned sum of modulus of isolated coefficients by a sum of norms defined over well-chosen groups of coefficients. More precisely in our case, adjacent pixels of a VSDOI acquisition tend to be influenced by the same biophysical phenomenon; and a sparse model that pools together coefficients of such pixels might benefit from their relationship.

Another popular spatially structured penalization is the *total variation* (TV) initially introduced by Rudin *et al.* (1992) for image denoising. At each pixel, it penalizes the coefficients of the *spatial gradient* (the partial derivative of a signal with respect to spatial coordinates) by pooling them together under an Euclidean norm. This promotes sparse gradients in the resulting signals, *i.e.* piecewise constant signals, see Chambolle *et al.* (2010) for a comprehensive review in the context of image processing.

Sparsity in Source Separation

Sparsity has been used for *blind source separation* at least back to Zibulevsky and Pearlmutter (2001), and has been applied successfully in various fields ever since, as reviewed in Bobin *et al.* (2008). Sparsity is introduced in a source separation problem by mean of *sparsifying dictionaries*, which are (possibly redundant) sets of regressors in which the sources are supposed to have sparse representations. Usually, one different dictionary is introduced for each source. Then, the sparsity prior is relevant when the sources to be separated exhibits *morphological diversity*, that is when each source has its sparsest representation (with the least nonzero coefficients) in its corresponding dictionary rather than in the dictionaries dedicated to the other sources. In this context, one method of particular importance is the *morphological components analysis* (MCA, Starck *et al.* (2004)) and its extensions, that find sparse representations of the sources using iterative algorithms inspired by *matching pursuit* (Mallat and Zhang, 1993) and *basis pursuit* (Chen *et al.*, 1998).

Within such methods, sparsifying dictionaries are often specific *transforms* designed

for the purpose. The most important and broader class of such transforms corresponds to *wavelet* regressors, which are known to provide good sparse approximations of piecewise smooth signals (Mallat, 2008). In particular, sparse wavelet models can retrieve transcient phenomena without prior knowledge on their localization in time.

Sparsity in Neuroimaging

Recently, sparse methods received a lot of attention from the neuroimaging community. This is particularly true for fMRI modality, where the need for *single trial* (*i.e.* without averaging multiple acquisitions), paradigm-free (*i.e.* without knowledge of the signal of interest) *regression* and *deconvolution* methods is increasing. Caballero-Gaudes *et al.* (2013) for instance demonstrates the advantage of using sparse regression as an alternative to the *general linear model* (GLM) (Friston *et al.*, 1995), more classical in fMRI studies.

Among different sparse models developed for fMRI studies, many make use of the spatial and/or temporal structure on the data. Some representative examples deal with *reverse inference* problems (also dubbed as "brain reading"), which aim at predicting the specific task or stimulus experienced by the subject, from the its brain activity. In Michel *et al.* (2011) and in Jenatton *et al.* (2012), spatially structured sparsity priors are used to enhance *classification* and *regression* models, based on 3d volumes of fMRI activation maps. More precisely, the former imposes the activity of interest to be localized within *hierarchical blocks* of voxels, while the latter uses TV regularization (see above). Note however that those approaches does not attempt to retrieve brain activity *per se* (the 3 D activation maps are actually obtained by GLM) and that the sparsity priors are applied to predictive models. An even more significant example of structured sparse model in the context of retrieval of neuronal activity can be found in Karahanoğlu *et al.* (2013), where the authors use the full spatiotemporal structure of fMRI data for an efficient, paradigm-free deconvolution.

Contributions: Application to Voltage-Sensitive Dye Optical Imaging

We develop along Chapter II a method that aims at both capturing complex spatiotemporal dynamics of VSDOI signals while working at the single trial level. We model the VSDOI signal as the sum of three main components: bleaching, periodic artifacts and neuronal activity. They are assumed to be modulated by a space-dependent gain and perturbed by a random, spatially heteroscedastic, white, additive Gaussian noise. Our method can be seen as a nonlinear extension of the GLM of Reynaud *et al.* (2011) described in § I.3.5, where it is assumed that the time course of each component can be well approximated as a linear combination of a few regressors with the right shape, or morphology. However for each component we enlarge the family of possible regressors: sinusoidal regressors of many different frequencies for the periodic artifacts, and an overcomplete set of wavelets for the neuronal activity. Then we look for a reconstruction which is close to the observation and in the same time involves as few regressors as possible. This sparsity prior enables a selection of the active regressors that is adaptive to the observation, thus allowing to separate a broader class of artifacts and neuronal

dynamics. In particular, no assumption is made about the activation time or the overall dynamic of the neuronal activity.

In order to improve further the component separation, on top of the morphology and sparsity priors on the time-course of the components, we take into account their spatial structure. To this purpose, sparsity is promoted by carefully designed *spatially structured penalizations*. Periodic artifacts coefficients are penalized by a mixed ℓ_1-ℓ_2-*norm* defined over spatial blocks of neighbouring coefficients, leading to spatially coherent frequency selections. In addition of a similar ℓ_1-ℓ_2-norm, neuronal activity coefficients are also penalized by a TV *semi-norm*, favouring piecewise homogeneous maps of activity.

In source separation, the "blind" terminology refers to the fact that in some problems, not only the sources but also their linear combination leading to the observation is unknown, and must be learn from the data; whereas in our case, the components are simply supposed to add up to form the signal. We call the resulting method *spatially-structured sparse morphological component separation*, abbreviated as SMCS. It is specifically designed to target VSDOI applications. Of course, it can be adapted to any noisy component separation problem, where the components have distinct temporal morphologies that can be sparsely represented in known dictionaries, and suitable spatial structures. The SMCS shares many similarities with MCA, and qualitative comparisons of those approaches are discussed.

Note finally that in the same framework, we also explore the possibility to enforce other priors than sparsity, such as bounds on amplitudes of certain components. Altogether, recovering the components of our model requires the solution of a convex minimization problem of the form

$$\text{find } \hat{x} \text{ in } \operatorname*{argmin}_x \ \tfrac{1}{2}\|y - Dx\|_2^2 + g^{(\Lambda)}(x) \ ,$$

where y is the observed signal, x are the coefficients of the different components within the linear representation D, and g is a sum of complex penalizations, depending on some parameter Λ.

Proximal Splitting Methods for Convex Optimization

The above minimization problem is convex, but high-dimensional and nondifferentiable, with complex relationships between the coefficients. A striking feature of the functional is, however, that the data fidelity term $\frac{1}{2}\|y - Dx\|_2^2$ is differentiable, while the penalization term $g^{(\Lambda)}$ can be decomposed as a sum of penalizations with simpler structures. Thus, the problem can be naturally recast in a more general form, as

$$\min_x \Big\{ F(x) \stackrel{\text{def}}{=} f(x) + \sum_{i=1}^{n} g_i(x) \Big\} \ , \tag{1}$$

where f is smooth, and each function g_i is said to be *simple*, in the sense that one can compute efficiently its *Moreau's proximity operator* (Moreau, 1965), defined as

$$\text{prox}_{g_i}(x) \stackrel{\text{def}}{=} \operatorname*{argmin}_\xi \ \tfrac{1}{2}\|x - \xi\|^2 + g_i(\xi) \ .$$

This operator can be seen as an implicit version of a gradient descent, defined for possibly nonsmooth convex functions.

Simple functions can be iteratively minimized through repeated applications of their proximity operator (*proximal point algorithm*, Rockafellar (1976)); however, sums of simple functions are not necessarily simple themselves. Nonetheless, a wide class of algorithms enables minimizing such sums, essentially by using proximity operators of each separated simple functions. They are thus called *proximal splitting algorithms*, and we review below their main properties and conditions of applicability.

Taxonomy of Proximal Splitting Algorithms

Certainly the most popular proximal algorithm is the *forward-backward*, which applies for solving (1) on any real Hilbert space $\mathcal{H}$ when f is differentiable with a Lipschitz continuous gradient, and $n \overset{\text{set}}{=} 1$ with $g \overset{\text{set}}{=} g_1$ is simple. This scheme consists in performing alternatively a gradient descent (corresponding to an explicit step on the function f) followed by a proximal step (corresponding to an implicit step on the function g). Such a scheme can be understood as a generalization of the projected gradient method. This algorithm, which finds its roots in numerical analysis for partial differential equations, has been well-studied for solving monotone inclusion and convex optimization problems (Bredies and Lorenz, 2008; Chen and Rockafellar, 1997; Combettes and Wajs, 2005; Gabay, 1983; Mercier, 1979; Passty, 1979; Tseng, 1991, 2000). In addition Beck and Teboulle (2009) and Nesterov (2013) proposed accelerated multi-step versions for convex optimization, enjoying a faster convergence rate of $o(1/k^2)$ on the objective F in the general case, where k is the iteration counter.

Other splitting methods do not require smoothness on any part of the composite functional F. The *Douglas-Rachford* scheme was originally developed to find the zeros of the sum of two linear operators (Douglas and Rachford, 1956), and then two nonlinear operators in Lieutaud (1969) or two maximal monotone operators in Lions and Mercier (1979), see also Combettes (2004); Eckstein and Bertsekas (1992). This scheme applies to minimizing g_1+g_2, provided that g_1 and g_2 are simple. The *backward-backward* algorithm (Acker and Prestel, 1980; Bauschke *et al.*, 2005; Combettes, 2004; Lions, 1978; Passty, 1979) can be used to minimize $F \overset{\text{def}}{=} g_1 + g_2$ when the functions involved are the indicator functions of nonempty closed convex sets, or involve *Moreau envelopes*. Interestingly, if one of the functions g_1 or g_2 is a Moreau envelope and the other is simple, the backward-backward algorithm amounts to a forward-backward scheme.

Now, if L is a bounded injective linear operator, it is possible to minimize $F \overset{\text{def}}{=} g_1 \circ L + g_2$ by applying these splitting schemes on the *Fenchel-Rockafellar dual* problem. It was shown that applying the Douglas-Rachford scheme leads to the *alternating direction method of multipliers* (ADMM) (Gabay and Mercier, 1976; Fortin and Glowinski, 1983; Gabay, 1983; Glowinski and Tallec, 1989; Eckstein and Bertsekas, 1992). For non-necessarily injective L and g_2 strongly convex with a Lipschitz continuous gradient, the forward-backward algorithm can be applied to the Fenchel-Rockafellar dual (Combettes *et al.*, 2010; Fadili and Peyré, 2010; Beck and Teboulle, 2014). Dealing with an arbitrary bounded linear operator L can be achieved using primal-dual methods motivated by the

classical Kuhn-Tucker theory. Starting from methods to solve saddle-point problems such as the *Arrow-Hurwicz* method (Arrow *et al.*, 1958) and its modification (Popov, 1980), or the *extragradient* method (Korpelevich, 1976), this problem received a lot of attention more recently (Chen and Teboulle, 1994; Tseng, 1997; Solodov, 2004; Briceño-Arias and Combettes, 2011; Chambolle and Pock, 2011; Monteiro and Svaiter, 2013).

It is also possible to extend the Douglas-Rachford algorithm to an arbitrary number $n > 2$ of simple functions. Inspired by the method of partial inverses of Spingarn (1983, section 5), most methods rely either explicitly or implicitly on introducing auxiliary variables and bringing back the original problem to the case $n \overset{\text{set}}{=} 2$ in the product space $\mathcal{H}^n$. Doing so yields iterative schemes in which one performs independent parallel proximal steps on each of the simple functions and then computes the next iterate by essentially averaging the results. Variants have been proposed by Combettes and Pesquet (2008), and by Eckstein and Svaiter (2009) who describe a general projective framework that does not reduce the problem to the case $n \overset{\text{set}}{=} 2$. These extensions however do not apply to the forward-backward scheme, which can only handle $n \overset{\text{set}}{=} 1$.

Recently proposed methods extend existing splitting schemes to handle the sum of any number n of composite functions of the form $g_i \circ L_i$, where each g_i is simple and each L_i are bounded linear operators. Let us denote L_i^* the adjoint operator of L_i. If L_i satisfies $L_i L_i^* = \nu \operatorname{Id}$ for any $\nu \in \mathbb{R}_*$ (it is a so-called *tight frame*), $g_i \circ L_i$ is simple as soon as g_i is simple and L_i^* is easy to compute (see Proposition IV.3.7). This case thus reduces to the previously reviewed ones. If L_i is not a tight frame but $(\operatorname{Id} + L_i^* L_i)$ or $(\operatorname{Id} + L_i L_i^*)$ is easily invertible, it is again possible to reduce the problem to the previous cases by augmenting the dimensionality by as many auxiliary variables as the number of linear operator L_i, each belonging to the range of L_i (this is detailed in § IV.3.1.2). Note however that, if solved with the Douglas-Rachford algorithm on the product space, the auxiliary variables are also duplicated, which would increase significantly the dimensionality of the problem. Some dedicated parallel implementations were specifically designed for the case where $(\sum_i L_i^* L_i)$ or $(\sum_i L_i L_i^*)$ is easily invertible, see for instance Eckstein (1994); Pesquet and Pustelnik (2012). If an L_i satisfy none of the above properties, it is still possible to call on primal-dual methods, either by writing $F \overset{\text{def}}{=} \sum_i g_i \circ L_i = g \circ l$ with $l(x) \overset{\text{def}}{=} (L_i(x))_i$ and $g\big((x_i)_i\big) \overset{\text{def}}{=} \sum_i g_i(x_i)$ (see for instance Dupé *et al.* (2011)); or by minimizing on the product space $\tilde{F}\big((x_i)_i\big) \overset{\text{def}}{=} \sum_i g_i(L_i(x_i)) + \iota_{\mathcal{S}}\big((x_i)_i\big)$ (Briceño-Arias and Combettes, 2011), where $\iota_{\mathcal{S}}$ is the *indicator function* of the closed convex set $\mathcal{S}$ defined in § III.1.2.

Contribution: A Generalized Forward-Backward Splitting Algorithm

In spite of the wide range of already existing proximal splitting methods, none seems satisfying to address explicitly the case where $n > 1$ and f is smooth but not necessarily simple. A workaround that has been proposed previously used nested algorithms to compute the proximity operator of $\sum_i g_i$ within subiterations, see for instance Chaux *et al.* (2009); Dupé *et al.* (2009); Huang *et al.* (2011); this leads to theoretical as well as practical difficulties to select the number of subiterations.

In Chapter III, we extend the celebrated forward-backward algorithm to our needs.

Since convex minimization problems can be recast as *monotone inclusion* problems, we use the more general, and somewhat more elegant, monotone operator framework. After recalling the main terminology and properties, we introduce an algorithm for finding a zero of a sum of *maximal monotone operators* $B + \sum_{i=1}^{n} A_i$, where B is *cocoercive*. It involves the computation of B in an explicit (forward) step and the parallel computation of the resolvents of each A_i in a subsequent implicit (backward) step. We prove its convergence in infinite dimension, and robustness to summable errors on the computed operators in the explicit and implicit steps.

In particular, this allows efficient minimization of the sum of convex functions $f + \sum_{i=1}^{n} g_i$, where f has a Lipschitz continuous gradient and each g_i is simple in the sense that its proximity operator is easy to compute. The resulting method makes use of the regularity of f in the forward step, and the proximity operators of the simple functions are applied in parallel in the backward step.

To the best of our knowledge, it is among the first algorithms to tackle the case where $n > 1$. Recently, Monteiro and Svaiter (2013) proposed an algorithm for minimizing $F \stackrel{\text{def}}{=} f + g$ under linear constraints. We show in § III.2.3 how this can be adapted to address the general problem (1), while achieving full proximal splitting and using the gradient of f. In the process of publishing our work, we became aware that other authors (Combettes and Pesquet, 2012; Condat, 2013; Vũ, 2013) have independently and concurrently developed primal-dual algorithms to solve problems that encompass the one we consider here. These approaches and algorithms are however different from ours in many important ways. This will be discussed in detail in § III.2.3. We also report some numerical experiments in § IV.5.3, suggesting that our primal algorithm is more adapted for imaging problems of the form (1).

This work was done in close collaboration with Jalal Fadili from the research center GREYC (Caen, France). A significant part has been published in Raguet *et al.* (2013); a notable difference with the article is a slight improvement on the relaxation constants of the iterates, denoted ρ_k in Algorithm III.1 and Algorithm III.2. On this point, we are grateful to Yuchao Tang, Xi'an Jiaotong university, for pointing out the result of Ogura and Yamada (2002) on the composition of two α-averaged operators, reproduced here in Lemma III.1.1 (iii).

Splitting Structured Penalizations for Signal Processing

Proximal Algorithms for Inverse Problems

As we have seen earlier in the particular context of sparsity, numerical solutions of inverse problems often require the minimization of large scale objective functionals, taking into account both a fidelity term to the observations and regularization terms reflecting the priors one can have on the signal. Clearly, such functionals are composite by construction, hence fitting in the class of problem considered in the previous chapter. Within the present thesis, the most meaningful example is our SMCS variational problem introduced in § II.2.3.

In many situations, this leads to the minimization of a convex functional that can be split into the sum of convex smooth and nonsmooth terms. The smooth part of the objective is often the data fidelity term, reflecting some knowledge about the forward model, *i.e.* the noise and the measurement or degradation operator. This is for instance the case if the operator is linear and the noise is additive and Gaussian, in which case the data fidelity is a quadratic functional. In contrast, the most successful regularizations that have been advocated are nonsmooth, what typically allows to preserve sharp and intricate structures in the recovery. In order to better model the data, composite priors can be constructed by summing several suitable regularizations, as it is the case for our SMCS model. Moreover, while the proximity operator of the ℓ_1-norm penalization is a simple soft-thresholding (see § IV.3.4.3), the use of complex or mixed regularization priors justifies the splitting of nonsmooth terms into several simpler functions. In this thesis, concrete examples are studied (see § IV.3) and applied to our SMCS model.

Nowadays, most popular approaches for facing continuous optimization problems rely on second-order methods, such as the ubiquitous *interior-point method* (Wright, 2004; Boyd and Vandenberghe, 2004). Nondifferentiable terms are taken into account by well-designed constraints; let us mention in particular that all optimization problems considered in this thesis can be cast as *conic programming* (see for instance Ben-Tal and Nemirovski (2001, section 3.3)). It is thus important here to point out the reasons why first-order methods can be preferred for many signal processing applications. Keep in mind that those are *large scale* problems (usually more than 10^6 variables), for which a reasonable solution is not required with high-precision (because of high level of noise and uncertainty over the parameters). While second-order methods are known to give very accurate solutions in a limited number of iterations, each of those iterations requires the solution of linear systems growing prohibitively large with the dimension of the problem; up to the point where most machines simply cannot store the corresponding matrices. On the contrary, first-order methods can quickly give reasonable solutions, manipulating data whose size is of the same order of magnitude as the inputs. A last point of importance for practitioners is that second-order schemes are usually complicated to implement properly and efficiently, in comparison to the relative simplicity of first-order proximal algorithms.

The composite structure of convex optimization problems raised when solving inverse problems explains the popularity of proximal splitting schemes in signal processing. Depending on the structure of the objective functional, one can resort to the appropriate splitting algorithm as reviewed earlier. For instance, the forward-backward algorithm and its modifications are commonly used for sparse regularization of a smooth data fidelity term, see for instance Figueiredo and Nowak (2003); Daubechies *et al.* (2004); Combettes and Wajs (2005); Fadili *et al.* (2009); Chaux *et al.* (2007); Beck and Teboulle (2009); Briceño-Arias and Combettes (2009). The Douglas-Rachford and its parallelized extensions are also used in a variety of inverse problems involving only nonsmooth functions, see for instance Combettes and Pesquet (2007); Combettes and Pesquet (2008); Chaux *et al.* (2009); Dupé *et al.* (2009); Dupé *et al.* (2011); Dupé *et al.* (2012); Pustelnik *et al.* (2011); Briceño-Arias *et al.* (2011). The ADMM is also applied to some linear inverse problems in Afonso *et al.* (2010); Figueiredo and Bioucas-Dias

(2010). Although we make in this work only limited mention of the primal-dual schemes (Chambolle and Pock, 2011; Dupé *et al.*, 2011), they are among the most flexible to handle more complicated priors. The interested reader may refer to Starck *et al.* (2010, chapter 7) and Combettes and Pesquet (2011) for extensive reviews.

***Contribution:* Structured Penalizations and Efficient Proximal Splitting**

In view of the success of both, nondifferentiable priors for signal processing applications, and their minimizations through proximal splitting algorithms, we review and extend a selective list of such priors and show how they can be split into simple functions.

More precisely, we propose in Chapter IV a natural formalisation of structured penalizations over the Euclidean space $\mathbb{R}^P$, which permits to express all penalizations introduced in our SMCS model (and beyond) in a unified and concise way. We emphasize in particular structures depending on an intrinsic spatial organization of the signal, *e.g.* two-dimensional space for images. At this occasion, we introduce a novel discretization of the total variation semi-norm, and discuss its theoretical and computational advantages over other discretization schemes.

Then, we derive the proximal formulae for each of those penalizations. Though most of these results are already known, we detail them in our specific formalization for comprehensiveness; in addition, since they are ubiquitous in signal processing applications, we also address the general case of linear constraints and quadratic functionals. To our knowledge some results are new, such as the extensions of the proximal calculus with the *tight-frame* property in § IV.3.3, and of some proximal *composition* properties in § IV.3.4.4.

The above derivations shed some light on the practical computational needs of proximal splitting algorithms applied to the class of problems that we consider. We identify common situations where subtle implementation considerations can significantly lighten computational needs; in our opinion such matters is too often neglected in the literature, we thus expose those considerations in a setting as general as possible.

Finally, we design synthetic experiments inspired by classical inverse problems in image processing, illustrating the use of most penalizations that we defined, and enabling comparison of various proximal splitting approaches, including our generalized forward-backward.

Risk Estimation for Parameter Selection

So far, we have seen that increasingly complex signals can be retrieved in ill-posed and noisy settings with the help of equally complex penalizations enforcing various priors. The underlying rationale is that one can replace the knowledge of the signal by the knowledge of an adapted model for it. The success of this approach is thus closely related to the quality of the model, and in particular to the accuracy of the parameters defining it. In the SMCS model described in § II, we intend to overcome the difficult noisy component separation task with a variety of different penalizations, and the problem of parameter selection becomes overwhelming.

Model Selection for Regression and Signal Reconstruction

The idea behind model selection is to view the problem as a statistical estimation, where predictions are inferred through a model fitted over a set of observations. One can then design a convenient *prediction error* function which evaluates the quality of an estimation given the actual observation. Typically, think at mean square errors or correlation coefficients in signal processing, or at success rate or explained variance in the context of regression and classification.

Then, following in particular Efron (2004), two main approaches for assessing the quality of a model are *cross-validation* and *covariance-penalties*. In the cross-validation approach, the model is solved for a reduced set of observations, and one computes the prediction errors between the output of the model and the observations that has not been used. In theory, this should be computed for many different particularizations of the observations to achieve statistical significance, but the generalized cross-validation introduced by Golub *et al.* (1979) does not require so many computations of the model. The advantage of the cross-validation approach is that it usually does not assume any generative model on the data, and is in that sense nonparametric. In contrast, the covariance-penalties approach involves in some way an estimation of the covariance between the estimations and the data, which requires assumptions about their statistical distribution. In the context of signal processing, this often reduces to the knowledge of the noise statistics, and can be estimated in many cases (see in particular § V.1.3).

For that reason, covariance-penalties approaches are preferred for the targeted applications (see Li (1985); Efron (2004)); one of the most popular being *Stein's unbiased risk estimate* (SURE), because it applies to a wide range of nonlinear models, and is especially well-designed for Gaussian noise. In brief, Stein's lemma states that, provided *weak differentiability* conditions of the estimation function (coined *estimator*), the above covariance can be estimated on the derivatives of that function. Hence, the *risk* of the estimation, which is the expectation of the squared error between the estimate and the original signal, taken according to the noise statistics, can be unbiasedly estimated. By computing it for different values of a parameter tuning the model, one can select the parameter minimizing the SURE.

Parameter selection with the SURE specifically for signal processing goes back at least to Donoho and Johnstone (1995), where its expression is derived for the ℓ_1-norm denoising estimator and used for scaling the penalization. Extensions have been subsequently developed to other penalizations such as the ones we consider in this work, (Chaux *et al.*, 2005; Zou *et al.*, 2007; Chaux *et al.*, 2008; Yu *et al.*, 2008; Chesneau *et al.*, 2010; Solo and Ulfarsson, 2010; Dossal *et al.*, 2013) and beyond (Vaiter *et al.*, 2014). Successful applications have been reported for numerous signal denoising tasks (see for instance Blu and Luisier (2007); Van De Ville and Kocher (2009); Luisier *et al.* (2010a); Deledalle *et al.* (2012a); Duval *et al.* (2011); Van De Ville and Kocher (2011); Ramani *et al.* (2012a)). In the same time, theoretical developments of Eldar (2009) enabled the adaption of the SURE to non-Gaussian noise (Luisier *et al.*, 2010b), and to inverse problems beyond denoising (Pesquet *et al.*, 2009). Let us finally mention some numerical methods which do not require the computation of the derivatives of the estimator explicitly, approximating them either by finite differences (Ramani *et al.*, 2008; Deledalle *et al.*,

2014), or, in the case of estimators defined by iterative algorithms, by recursive derivations (Vonesh *et al.*, 2008; Giryes *et al.*, 2011; Ramani *et al.*, 2012b).

***Contribution:* Risk Estimation for Proximal Denoising**

In Chapter V, we first redefine rigorously the terms and conditions of the SURE for denoising problems with arbitrary Gaussian noise. Then, in the continuity of the previous chapters, we emphasize the fact that any proximity operator can be seen as a denoising estimator, and satisfies the regularity conditions for estimating its risk with the SURE. We give the SURE expressions of the proximity operators of the penalizations defined previously, and study the more involved case of a denoising estimator penalized by *reweighted* $\ell_{1,2}$-norm, inspired by the reweighted ℓ_1-norm of Candès *et al.* (2008).

We then turn to denoising estimators that cannot be reduced to proximity operators of simple functionals, establishing in particular a proper *chain rule* for Lipschitzian functions in arbitrary dimension, which is actually a theoretical prerequisite of the recursive derivation method mentioned above. After describing the practical computational limitations of their use for our purpose, we propose a series of heuristics allowing fast and efficient approximations.

Finally, we exemplify the use of the SURE for parameter estimation in an image denoising setting, and test empirically our heuristics.

A Full Component Separation Method for Voltage-Sensitive Dye Optical Imaging

With all the mathematical and computational tools developed in this thesis, it is possible to apply our spatially structured sparse morphological model to voltage-sensitive dye optical imaging data. In Chapter VI, we expose briefly the rationale that allows us to adapt to component separation problems parameter selection methods originally designed for simple denoising problems. This adaptation requires notably successive approximations of the different components involved in the problem and estimations of the noise statistics. We show that under convenient assumptions, this is actually possible for VSDOI data; in particular, some first approximations involve processing of *blank acquisitions*, *i.e.* acquisitions recorded without specific stimulus presented to the animal, where we assume that only few neuronal activity is present.

Note that the full method, from parameter selection to the resolution of the variational problems, is now decomposed into several interrelated steps. Moreover, at each of those steps, some practical choices remain to be taken. Everything is explained in details within Chapter VI, and summarized on Table VI.1.

Altogether, we implement the full methods and perform the first experiments for evaluating it. In Chapter VII, we first investigate the contributions within the highest frequencies of VSDOI recording, validating in particular the model of the noise proposed in § II.2.1. Then, we run numerical experiments over synthetic data, mimicking real VSDOI data, which allows us to work in a controlled environment and to know the actual targeted components. On such an "oracle" setting, we attest relatively good per-

formances of our method, and we evaluate its pros and cons in comparison to a GLM method. Third, we test the possibility of retrieving actual functional signals, on the well-studied *orientation selectivity* of the cat's primary visual cortex, thanks to data provided by Cyril Monier. Without delving into further functional details, we make use at this occasion of preliminary results of the extensive study in Yavuz (2012). At last, we explore visually the output of our method on data presenting propagating neuronal activity in the mouse's somatosensory cortex, provided by Isabelle Ferezou. Since such propagations can be *evoked* by specific stimuli but also *spontaneous*, we show in particular the ability of our method to retrieve neuronal activity in paradigm-free conditions.

Thanks to those preliminary sets of experiments, it is already possible to discuss the validity of the method, especially concerning the assumptions that we made over the VSDOI signal in Chapters I and II. In addition, we discuss the practical conditions which render difficult the use of the current version of the full method by practitioners.

*

* *

I

Voltage-Sensitive Dye Optical Imaging Ways and Customs

In this chapter, we describe the optical imaging technique based on voltage-sensitive dye for monitoring the cortical neuronal activity at population level. First, we briefly describe its principles and capabilities, pointing out the interest of improving this acquisition modality for the neuroscientific community. Doing so, we introduce the motivation and problematic that are behind the whole work of signal processing presented in this thesis.

We describe also the main causes of limitations encountered by experimentalists and analysts, and the inevitable need for signal processing when dealing with voltage-sensitive dye optical imaging. Finally, a critical review of approaches found in the literature is given and discussed as the starting point of our own reflection.

Contents

1 Monitoring Cortical Activity with VSDOI

1.1 Electrophysiological Background

It is common to consider that modern neuroscience starts with the work of Santiago Ramón y Cajal and Camillo Golgi at the end of the nineteenth century, leading to the *neuron theory*, mostly formulated by Heinrich Wilhelm Gottfried von Waldeyer-Hartz. To date, it is still assumed that most if not all information in the brain is encoded within electrical activity of the nerve cells, the neurons. In brief, the neurons are cells covered by *ion gates* which control the relative concentrations of certain ions between the intracellular and extracellular media, governing in turns the electrical potential between each side of the cellular membrane. Neurons are interconnected by their *neurites*, which are projections of their cell body. Among them, the *axon* sends information to other neurons, and the *dendrites* collect information from other neurons. The neurons are

considered as the elementary processing units, but even the simplest brain functions emerge from the activity of millions of such neurons, interconnected into hierarchical spatial structures, and following specific temporal dynamics.

In order to understand the brain from a computational point of view, it seems necessary to have access to the operating modes of single neurons, as well as their relationship one to the other within each organization level. To this end, the most direct way of recording electrical activity is to put electrodes inside the brain tissue. This can be done either *in vitro* (in specific preparations, usually slices of animal brain), or *in vivo* in living animals. *Intracellular* recordings have the highest accuracy and informs the best on how single neurons work. This allowed Alan Lloyd Hodgkin and Andrew Fielding Huxley to explain the spiking nature of the neuronal activity. The electrical potential of a neuron fluctuates along time because of the activity of other neurons; whenever this potential reaches a critical value, cellular mechanisms within the neuron trigger a fast additional increase of potential of huge amplitude that lasts only for a very short period of time, and propagates along its axon. Those events are called *action potentials*, and take place within the temporal order of the millisecond. In the same context, *extracellular* recordings are often easier to perform, and depending on the electrode size can probe the activity of one or several neurons. In the last case, it is in general difficult to isolate the contribution of each neuron, but it already enables to study the relationships between them.

The biggest advantage of using electrodes is that they have high spatial and temporal resolutions, *i.e.* they can capture every events that take place along time, at microscopic scales. Moreover, it enables recordings wherever it is physically possible to introduce electrodes without damaging the surrounding tissues. Now, though it is possible to record simultaneously from several electrodes, this raises technical difficulties (Lampl *et al.*, 1999) and it is obvious that networks of thousands of neurons cannot be observed by those techniques. In an other approach, *electroencephalography* consists in many electrodes put all over the surface of the head. Those can be recorded for days, and even on human brain since it is noninvasive. However, the resulting spatial resolution is very crude, and only the synchronous activity of thousands of neurons situated at the surface of the brain can be detected that way.

Currently, no other technique gives such direct access to the electrical activity of the neurons. Nevertheless, the brain functions can be investigated indirectly through physiological phenomena that relate to them. For instance, intrinsic physiological changes occur locally whenever significant neuronal activity is triggered, such as increase in blood volume and changes in hemoglobin oxymetry. Then, *labelling techniques* can be used to identify which brain regions are recruited during specific tasks. They usually involve the injection of specific *tracers* in the blood of the animal under investigation. Those tracers are usually molecules that can be later on easily detected, either *post mortem* for simple dyes, or *in vivo* thanks to radioactive or magnetic properties. High concentration of tracers indicates regions of high activity. The most notable example is the *positron emission tomography* which uses radioactive tracers and can be used in human subjects. Labelling methods can screen the whole brain, but like electroencephalography provides only coarse, macroscopic functional information. Worst, each image usually takes

minutes to acquire, so that dynamical aspects cannot be captured. The development of *functional magnetic resonance imaging* (fMRI) enhances drastically macroscopic observations of the brain functions. The most common method is to detect the intrinsic signal by exploiting the difference of magnetization of the blood according to its oxygen concentration. Currently, the spatial resolution goes up to the order of the millimeter, and the temporal resolution reaches the order of the second.

Intrinsic signal can also be observed with *intrinsic optical imaging*, by shedding near infrared light on the surface of the cortex, and recording over time the changes in reflectance induced by the intrinsic changes. Since the acquisition principle is simpler than for fMRI, the spatial resolution reaches nowadays the tenth of a millimeter (Zepeda *et al.*, 2004). Only a limited part on the surface of the cortex can be studied this way, but at this level of precision it becomes possible to distinguish specialized group of neurons that acts as functional units, like *orientation columns* in mammalian primary visual cortices (Rao *et al.*, 1997). Still, temporal resolution cannot be improved because of the time scale of the intrinsic changes, which happens seconds after an actual, significant neuronal activity.

The great interest of the *voltage-sensitive dye optical imaging* (VSDOI), which is the measurement modality at the heart of this thesis and is described in more details in the next section, is that it can, in theory, combine the mesoscopic spatial scale of optical imaging with the real-time temporal resolution of direct electrophysiological measurements.

1.2 The VSDOI Modality

1.2.1 Principles.

Sensitivity to membrane potential of some fluorescent dyes is known for long (at least back to Cohen *et al.* (1974)), and its use for monitoring neuronal activity has been considered ever since. Starting with recordings of action potentials in individual neurons (Davila *et al.*, 1973; Salzberg *et al.*, 1973), the technique got continuously improved along time, and is now a privileged modality for monitoring cortical activity simultaneously at several locations with both high spatial and temporal resolution (Grinvald and Hildesheim, 2004).

To perform VSDOI one stains the neuronal tissue with voltage-sensitive dye, which are fluorescent molecules, also called *fluorophores*. Some of those bind to neurone membranes. Each fluorophore, when illuminated with the correct exciting wavelength, emits light in a different wavelength in return. The fluorophores that are bound to a neurone membrane happen to emit differently according to the electrical potential at the membrane. Thus, filming the emitted fluorescence provides access to the variations of the potential of those membranes along time. The whole process is schematized in Figure 1, see for instance Grinvald *et al.* (1999) or Frostig (2009) for detailed practical methodologies of *in vivo* recordings.

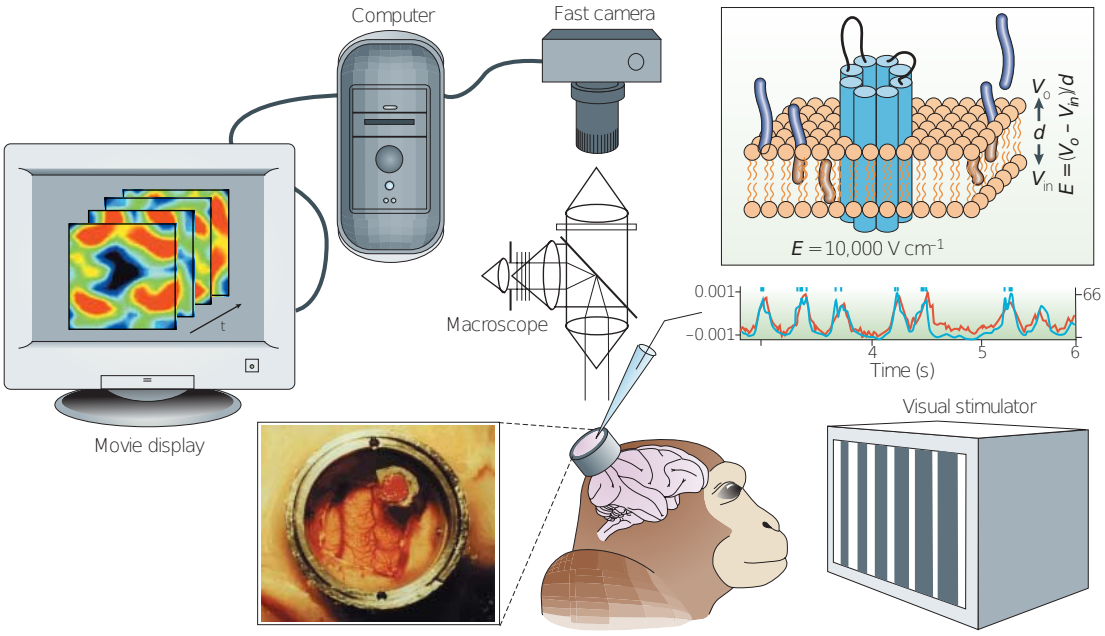

Figure 1: Schematic view of a VSDOI set-up. Reproduced from Grinvald and Hildesheim (2004).

1.2.2 Limitations.

Because the changes in fluorescence follow closely a change in membrane potential, both in time (order of the microsecond) and in space (at molecular scale), the resolution of VSDOI is in theory only limited by two main factors: the quantum nature of photon emissions, and the precision of the optical recording device.

Recorded fluorescence intensity corresponds to the count of the number of photons reaching the detector during a certain time laps. At a given intensity, the number of emitted photons during a given duration is best modeled by a Poisson distribution (Foschini *et al.*, 1975), for which the *variance* increases proportionally to the mean level. Hence, the expected quality of a fluorescence measurement, quantified by the ratio between the mean number of emitted photons and its standard deviation, is proportional to the *square root* of the mean number of photons. As a consequence, it is important to maximize the mean number of photons recorded at each measurement. This is in turn proportional to three main factors: the number of fluorophores within the focus of the detector, the duration of each measurement, and the intensity of the exciting light. In any experimental set-up, a compromise must be found between those three factors, in accordance with the instrumental and material conditions.

On the one hand, the quantity of fluorophores reporting potential changes is limited by the total area of neuronal membrane under investigation, and by the physical access to those membranes. Moreover, the quantity of fluorophore introduced in the medium must also be limited in order to avoid *pharmacological* effects, *i.e.* perturbations of the functioning of the neurons due to the presence of the fluorophores. Similarly, the intensity and the duration of the exposure of the exciting light is limited by *photodynamic*

damage that can occur to the medium. See for instance Grinvald *et al.* (1999) and Peterka *et al.* (2011) for more details on those practical limitations.

On the other hand, optical precision is limited by *light scattering* and focal precision, while the quantity of data recorded during a certain amount of time is limited by acquisition and data-storage speed. Horizontal spatial resolution (parallel to the cortical surface and orthogonal to the optical axis) goes below a tenth of a micron when using confocal (Holthoff *et al.*, 2010) or two-photon (Acker *et al.*, 2011) microscopy. This actually allows to discriminate between neuron compartments. Unfortunately, only two-photon techniques allows such precision in the vertical axis. For all other recording techniques, the focal plan is much thicker. This can be limited *in vitro* by reducing the thickness of the sample itself (thin brain slices), but *in vivo*, contributions of several cortical layers might be mixed in the signal, depending on the dye distribution along the depth of the cortex. Concerning the spatial extent of the field of view, most commercial devices available nowadays exceed 1000×1000 pixels, and temporal resolution goes up to 10 kHz, allowing to capture every events of an action potential (Tominaga and Tominaga, 2013).

The final compromise between spatial and temporal resolution, data quantity, and recording quality depends on the phenomena under investigation and on the experimental conditions. In particular, *in vitro* experiments allows more flexibility than *in vivo*, but does not give access to the same information. In all the present work we are mostly interested in *in vivo* recordings, at population level, with spatial resolution between 10 and 100 µm, sampling frequency between 100 Hz and 1 kHz, and spatial extent no more than 100×100 pixels.

1.3 The Targeted Signal

Before diving into the technical aspects of VSDOI signal processing, let us describe the phenomena one would like to investigate thanks to the VSDOI modality. Those considerations are useful in order to understand the motivation and ambition that lies behind the work developed in this manuscript.

1.3.1 The Cortical Phenomena Under Investigation

The use of VSDOI at single cells level is justified when direct intracellular recording is rendered impossible, often because it is too invasive or because the targeted site is too small for the insertion of an electrode. However, the advantage of the VSDOI modality which is the most interesting to us is its ability to record in real-time the activity of entire networks comprising thousands of neurons. At the population level, VSDOI is more sensitive to subthreshold potential variations of many synchronous neurons than to individual spiking activity (Chemla and Chavane, 2010a). Although it does not reveal the action potentials, such mesoscopic information is useful to understand the mechanisms of integration of individual neurons activity within local networks. In particular, spatiotemporal dynamics of functional structures, population encoding of sensory stimuli, long-range connectivity, and propagating phenomenon can be studied; see Grinvald

and Hildesheim (2004) and Chemla and Chavane (2010a) for more details on the cortical mechanisms best revealed by VSDOI.

1.3.2 The Question of the Ongoing Activity

When studying functional organization of the cortex, the usual approach is to analyze the activity evoked *in vivo* by certain stimuli. However, it has been observed that the variability of the neuronal response to several repetitions of the same stimulus is sometimes as significant as the response itself; see Arieli *et al.* (1995) and references therein. Moreover, even in the absence of specific stimulus, neurons exhibit spontaneous activity that is often highly structured in space and time, at both at the single cell level and at the population level. This spontaneous or *ongoing* activity can be observed with any recording modality, and presents a wide variety of dynamics, usually highly dependent to the conscious state of the subject (anesthetized or awake).

Many important questions arise about the ongoing activity. Neither its origin and mechanisms, nor its relationship to the activity evoked by a specific stimulus and its role in perceptual attention are yet well understood. Experiments with VSDOI could provide precious information, but let us emphasize here that ongoing activity is also an obstacle for VSDOI recordings at population level. As described in the next section, VSDOI acquisitions are corrupted by many nonneuronal artifacts, so that up to now information is extracted by averaging over repetitions, or using ad-hoc processing methods retrieving the evoked, reproducible signal and discarding the variability. Although VSDOI has already been used in studies of ongoing dynamics (see again Arieli *et al.* (1995), or Arieli *et al.* (1996)), precaution must be taken for their interpretation. This underlines the need for new processing methods that would capture all the variability at the single acquisition (also dubbed *trial*) level.

On a VSDOI signal processing point of view, it is important to distinguish several temporal and spatial scales of ongoing dynamics. At the lowest frequency scale, spontaneous organization of cortical assemblies presents *up* and *down* states, that are respectively *depolarized* and *hyperpolarized* temporary states, resulting respectively in higher and lower activity levels for durations in the order of the second. Such slow fluctuations are usually associated with high level of synchrony, involving entire networks at the spatial scale of the millimeter, see for instance Lampl *et al.* (1999); Petersen *et al.* (2003). Then, faster spontaneous events that are often reported concern propagating waves of activity running across neuronal networks, especially in the cortex. Such events are highly structured, and usually closely resemble events that can be evoked by specific stimuli. They are however very diverse, with many different propagation velocities and spatial extents, with frequency scales in order of magnitude from 1 up to 100 Hz, see for instance the review of Muller and Destexhe (2012). Finally, individual neurons within networks always exhibit fluctuations of activity, both in term of spiking activity and of subthreshold potential variations, due to a wide variety of sources and often considered as random noise (Destexhe and Rudolph-Lilith, 2012). Notably, these fluctuations might have characteristic frequency above 100 Hz and show little correlation from one neuron to another.

This division according to three different spatiotemporal frequency scales might,

or might not, have actual biological relevance. However, they seem to relate to distinct phenomena and, more importantly, their respective influences on VSDOI acquisitions are as significant as they are different.

2 The Challenge of VSDOI *in vivo*

In spite of the constant enhancement of the VSDOI technique along several decades, *in vivo* recording remains a technical challenge, due to a wide variety of artifacts and noise that corrupt the signal, and that can also differ greatly according to the experimental conditions.

2.1 From Fluorescence to Neuronal Activity: What Are We Recording?

As introduced in § 1.2.1, the fluorophores bound to a neuronal membrane fluoresce differently according to the electrical potential at the membrane. This knowledge, however, is not sufficient to deduce changes in neurons membrane potential. First of all, hundreds to thousands of neurons contribute to each single pixel of the recorded acquisition and it is impossible to differentiate between contributions of axonal or dendritic activity, of inhibitory or excitatory neurons, or even of some nonneuronal cells (glia, etc.). The different contributions have been studied in particular by Chemla and Chavane (2010b). In general, the best information available is the *variation of membrane potential averaged over multiple compartments of multiple cells, integrated over several cortical layers*. Moreover the interpretation of this variation of membrane potential is delicate because one does not know the *baseline activity*, the reference value to which the variation should be computed.

Now, how does one link the VSDOI acquisition to this average potential variation? The mechanism linking variations in membrane potential to variations in fluorescence has already been investigated (Peterka *et al.*, 2011) and the relationship between those variations is supposed to be linear. But what is the *gain* of this linear relationship? For a given spatial position and at a given instant (a pixel of a frame in the acquisition), it should depend on the *quantity of fluorophores bound to the membrane* and to the illumination intensity. Here again one often assumes linear relationship between intensity of fluorescence and fluorophore concentration, see for instance Tanke *et al.* (1982) in the context of microscopy. Also, keep in mind that only fluorophores bound to a neuronal membrane contribute to the desired signal, so that the area of stained membrane should be taken into account as well. Unfortunately one does not have access to this information.

Moreover, VSDOI records the *absolute* fluorescence intensity (*i.e.* the number of photons detected during the frame duration at each pixel). In order to get variations of fluorescence, one needs another baseline value, the *baseline fluorescence*, that is to say the fluorescence intensity that would be recorded independently from any neuronal activity (and from other existing biophysical sources of variations). Baseline activity and

baseline fluorescence are hard to distinguish from the sole information of the recorded fluorescence. This is an important issue in VSDOI, because many studies could be influenced by the way baseline activity is defined and estimated. Indeed, recall from § 1.3.2 that ongoing activity can reach the order of magnitude of an evoked activity, so that it is impossible to define the baseline activity as the level of activity when no stimulus is presented. It is common to estimate the baseline activity mixed with the baseline fluorescence, as the recorded values in the first frames of the acquisition where no evoked activity is expected. It is then subtracted from all the frames (see § 3). Using such approach, influence of spontaneous activity over those first frames is passed on to the entire acquisition, and should be taken into account. Unfortunately, this is difficult: variations of fluorescence in VSDOI that is actually due to neuronal activity is known to be in the order of a *thousandth* of the baseline fluorescence (Grinvald *et al.*, 1999). Even worse: many nonneuronal sources of variations actually *exceed* this ratio.

2.2 Sources of Noise and Artifacts

Many phenomena cause measurement errors. Like every fluorescence based modality, VSDOI is affected by *dye photobleaching*. When illuminated by exciting light, the fluorophores have the tendency to degrade or to react with other molecules so that they do not emit light anymore (Song *et al.*, 1995). This results in an overall decrease of the recorded fluorescence over time, independently from any neuronal activity. It is important to note that several mechanisms are involved and bring forth different bleaching dynamics. For instance, when fluorophores form nonfluorescent complexes with other molecules in a reversible fashion, they will fluoresce again when they retrieve their initial conformation. This results in a *fast* fluorescence decrease affecting the signal (as observed for instance in Chen *et al.* (2008); Reynaud *et al.* (2011)) as soon as the observation field is illuminated for recording, until a steady-state equilibrium is reached. Switching off the illumination modifies the equilibrium back to the previous state and the concentration of fluorescing molecules progressively goes back close to its initial value. Now, if a fluorophore degrades, it stops to fluoresce permanently. This process causes a *slow* fluorescence decrease (as reported for instance in Lippert *et al.* (2007); Takagaki *et al.* (2008)), hardly detectable at the time scale of a single acquisition. However, it can be seen by comparing successive acquisitions recorded during several hours of experimental protocol, until the fluorescence is too low for recording. The term bleaching or photobleaching is used independently in the literature to refer to both phenomena; and even sometimes to other phenomena that are strictly speaking unrelated to photobleaching but lead to similar fluorescence dynamic, *e.g.* wash-out of the dye along experimentation (see again Lippert *et al.* (2007); Takagaki *et al.* (2008)).

For *in vivo* experiments, emitted fluorescence due to neuronal activity suffers from other important interferences. This is mainly due to absorption properties of the biological tissues and of the hemoglobin in the blood of the living animal, as described extensively in Shoham *et al.* (1999). In particular most *in vivo* VSDOI acquisitions are contaminated by periodic components corresponding to the heartbeats of the animal; similarly, respiration artifacts are present. Also, the intrinsic signal described in § 1.1,

which is actually the signal of interest when performing intrinsic imaging, causes in VSDOI an intrinsic artifact. On acquisitions longer than one second, it leads to a slow decrease followed by an increase of the fluorescence subsequently to high neuronal activity.

Finally, we call *shot noise* the quantum fluctuations of the exciting light and of the emitted fluorescence described in § 1.2.2. Let us also mention mechanical vibrations of the experimental table, oscillations of the alternative current that supplies the experimental device, and thermal noise of the camera as other possible nonneuronal sources of fluorescence variations (Grinvald *et al.*, 1999). Those phenomena create high frequency fluctuations of the VSDOI signal, which are difficult to separate from high frequency ongoing activity.

2.3 From Neuronal Activity to Fluorescence: Modeling the Signal

Even though artifacts present distinctive dynamics, the way they act on the signal is nontrivial. Supposing for instance that the bleaching affects uniformly all fluorophores in the medium, its action on the signal should be strictly multiplicative, that is to say bleaching is a modulation of the gain over time. Alternatively if bleaching affects mostly fluorophores that are *not* bound to a neuronal membrane, its influence with respect to the neuronal signal should be considered additive. Interestingly, those two opposed alternatives are considered in the literature without further motivation, for instance when performing blank subtraction and blank division methods (see § 3.1). Note however that since the baseline fluorescence dominates all other components in the signal, both assumptions often lead to similar results (see Annex A), so that to our knowledge, the question has never truly been discussed. Note also that in most processing techniques, all contributions in the signal are considered additive (see § 3).

A similar question arises about the nature and statistics of random noise. On the one hand, noise that results from a multitude of small contributions, like random fluctuations of membrane potential, are usually modeled as Gaussian noise (Reynaud *et al.*, 2011), with neglected spatiotemporal correlations. On the other hand, recall from § 1.2.2 that shot noise is best modeled with a Poisson distribution, for which the variance increases proportionally to the mean signal level. Note once again that since the constant baseline fluorescence dominates all other components in the signal, this can be neglected when analysing the time course of a single pixel. However important variations of the baseline fluorescence from one pixel to another can lead to significant bias when performing spatial analysis without taking it into account.

3 VSDOI Denoising: Previous Approaches

Depending on the acquisition material (type of dye, camera and other device-specific conditions), on the observed cortical network (which animal, anesthetized or awake, which cortical area), on the observed phenomenon (spontaneous or evoked activity),

on the length of the acquisitions (from less than one second to several seconds), and on the duration of the protocol (up to several hours of recording), the possible artifacts and noise do not have the same influence on the observed signal. This is why it exists in the literature many different approaches to extract the neuronal activity of interest from the raw signal.

We make here a (nonexhaustive) list of those approaches, in order to illustrate their variety and to infer some common *priors* that are made on the nature of the components in the VSDOI signal.

3.1 Blank Subtraction

The most common processing is the *blank subtraction* (BkS). A blank is an acquisition recorded while no stimulus is presented to the animal. With an acquisition in stimulus condition (called stimulus acquisition in the following) and a corresponding blank, one retrieves the stimulus evoked neuronal response by essentially subtracting the latter from the former. Usually both acquisitions are first separately normalized by dividing each frame (pixel-to-pixel) by a so-called *zero-frame* which is the mean of several frames taken at the beginning of the acquisition. The blank subtraction method relies on the assumption that the artifacts and noise act additively on the signal, and that their time courses are the same in the blank and in the stimulus acquisitions. It is thus better to record a corresponding blank just before or right after any stimulus acquisition, so that the conditions are as similar as possible. This is significantly improved by synchronizing the acquisitions with the heartbeat of the animal, and even with its respiration in the case of anesthetized animals under intubation. The division by the zero-frame assumes that all the components are proportional to the same resting fluorescence value which can be estimated on the first frames. The division pixel-to-pixel accounts for the differences of fluorophore concentration and of illumination from one spatial position to another. Let us finally note that simple subtraction assumes that the baseline fluorescence of both the blank and the stimulus are the same (after zero-frame division).

Variations on this method can be found. The blank is sometimes smoothed by low-pass filtering or by averaging all blank acquisitions (Markounikau *et al.*, 2010). It can also be replaced by the so-called "cocktail blank", which is the mean over a set of acquisitions supposed to active successively all regions of the observed cortical area, in an uniform fashion (Grinvald *et al.*, 1999). Also if a notion of orthogonality can be defined over the space of stimuli (*e.g.* when studying ocular dominance or orientation selectivity in the visual cortex) it is possible to subtract an orthogonal stimulus acquisition instead of subtracting a blank (Shoham *et al.*, 1999). This does not give access to the evoked neuronal dynamic but it is useful for revealing functional cortical maps. Sometimes a division is considered in place of a subtraction (Grinvald *et al.*, 1999; Jancke *et al.*, 2004). As discussed in § 2.3, there is no consensus about which approach is best.

The blank subtraction method is illustrated in Figure 2, over a data set where acquisitions are synchronized with the heartbeat of the animal. Without delving into details about the observed signal (see § VII.3), the raw traces in (a) show the level of the noise

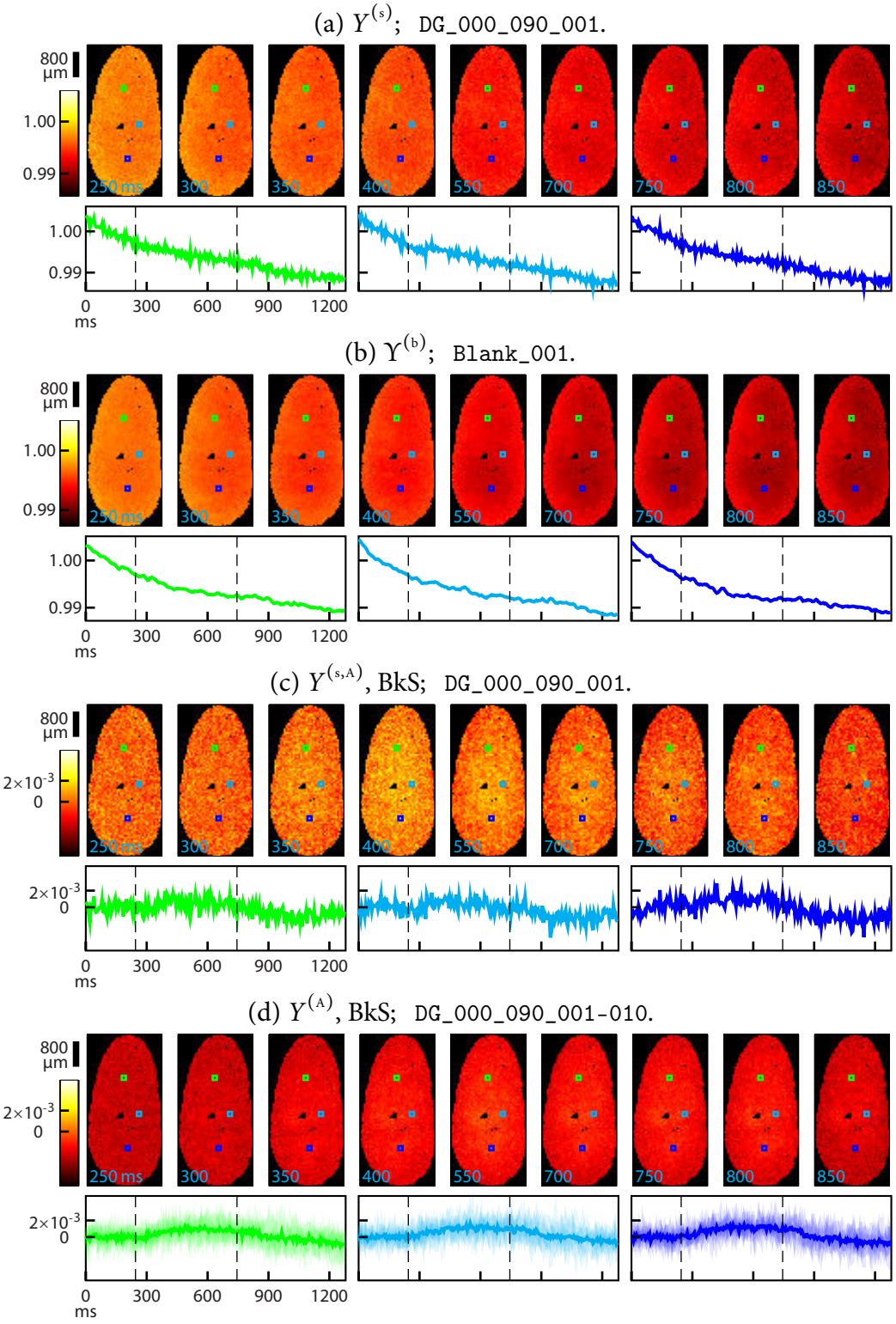

Figure 2: Blank subtraction on the protocol `Cat_Gratings`. See *opposite*.

Figure 2, *opposite*: Blank subtraction on the protocol `Cat_Gratings` used in § VII.3. The time courses correspond to spatial positions indicated on the frames by a square of the same color. Vertical dashed line indicates stimulus onset and offset. The exact blank subtraction method used is detailed in § VII.3.1.1.
(a) Stimulus condition acquisition normalized by the zero-frame, single trial.
(b) Blank acquisition normalized by the zero-frame and low-pass filtered, single trial.
(c) Retrieved neuronal activity by subtraction, single trial.
(d) Retrieved neuronal activity, average across ten trials, with single trials time courses plotted in transparency.

and artifacts in comparison to the reproducible evoked signal (d). One sees from (c) that with the blank subtraction method, single trials are still too contaminated for analysis without averaging.

3.2 Baseline Fluorescence, Gain and Bleaching

Chakraborty *et al.* (2007) perform VSDOI *in vitro* (on brain slices) so that the signal is not affected by physiological artifacts. They evaluate both baseline fluorescence and gain by averaging the first 100 ms of each acquisitions for each pixel. The (fast) bleaching is then handled by subtracting to the time course of all pixels a single linear function fitted on the mean over the entire image. To avoid frames where evoked neuronal activity is the most likely to appear, the fit is performed only on the second temporal half of the acquisition. A similar method is used in Chen *et al.* (2008) but on spatial bins of pixels. The authors do not precise how they select the bins. They evaluate both a baseline fluorescence and a gain for each bin by averaging the signals over all time frames of all trials, even though slow bleaching can affect baseline fluorescence and gain from one trial to the other. Then a linear function is fitted and subtracted for each bin. The fit is performed on the time frames before and after the expected neuronal response period.

As already mentioned, some authors reporting on VSDOI observe slow bleaching (*i.e.* with a time constant between minutes and hours, see § 2.2) but no fast bleaching (*i.e.* with time constant less than a second). Our guess is that they focus on long recordings (10 s or more) for which the first seconds of illumination are not recorded. Concerning the slow bleaching affecting the gain and the baseline fluorescence of the acquisitions between trials, Takagaki *et al.* (2008) show that setting the gain as equal to the baseline fluorescence (typically estimated by averaging the first frames) induces a strong bias due to different bleaching kinetics between gain and baseline fluorescence. They propose to estimate the gain as the peak-to-peak amplitude of epileptiform spikes elicited by injection of bicuculline methiodide. Unfortunately this is not practicable in most physiological experiments. Moreover, in their setting, the way they measure the baseline fluorescence is unclear and could also induce bias.

3.3 Heartbeat Triggered Averaged

The heartbeat triggered average method takes advantage of the fact that an electrocardiogram is recorded simultaneously to the acquisitions and that all acquisitions are triggered at the same phase of the electrocardiogram. Chen *et al.* (2008) model the heartbeat artifact as the repetition of a pattern approximated by the concatenation of two "half-Gaussian": one for a rising edge and one for a falling edge. Width and amplitude of those Gaussians are fitted on all available blanks. The resulting heartbeat artifact of a given acquisition is reconstructed by concatenation of several copies of this pattern, shifted in time such that their centers correspond to the peaks of the simultaneously recorded ECG, accounting for possible variations of heartbeat durations with time. The amplitude of each pattern is fixed constant along heartbeats to avoid overfitting. In the subsequent analysis, the authors average the time courses within a spatial region of interest in order to obtain a single time course for each acquisition; so it seems that only one heartbeat time course by acquisition (*i.e.* as opposed to a heartbeat time course for each pixel) is reconstructed and then subtracted to the acquisition. Other heartbeat triggered average procedures for estimating and subtracting the heartbeat artifact can be found in the literature for ECG-locked VSDOI acquisitions, see for instance Arieli *et al.* (1995); Ma *et al.* (2004); Lippert *et al.* (2007).

3.4 Automatic Component Separation Methods

Methods like heart triggered average or bleaching fit are based on *a priori* knowledge about the biophysical origin of those components. The approach is to reconstruct them according to this knowledge (*e.g.* heartbeat is synchronous with ECG), and subtract the result from the observation. Other attempts have been made to identify and retrieve all or parts of the components, directly from the acquisition with help of statistical estimation methods. In particular, principal component analysis (PCA, Jolliffe (2002)) and independent component analysis (ICA, Hyvärinen and Oja (2000)) are reported to be quite efficient. Both methods rely on the hypothesis that the signal is decomposed as a sum of components (called *modes*) that are uncorrelated (PCA) or independent (ICA) across observations.

Maeda *et al.* (2001) and Inagaki *et al.* (2003) consider ICA on the temporal domain, within each single trial, to separate neuronal activity from heartbeat and respiration (no bleaching is described). Later, Reidl *et al.* (2007) propose an ICA on the spatial domain within each single trial. The authors normalize their data by zero-frame (see § 3.1) and then subtract a bleaching time course estimated as a low-pass filtered average of blanks. After ICA they obtain spatial modes which enable to identify functional maps over the studied cortical surface. As a refined denoising process after blank subtraction, Onat *et al.* (2011a); Onat *et al.* (2011b) use, on each single trial, *singular value decomposition* (SVD) of the space-time data matrix (*i.e.* the matrix obtained after concatenation of each frame reorganized as a column vector). They obtain several spatiotemporal modes defined as the separable outer product between the left singular vectors (which are nothing but the principal components of an uncentered spatial PCA) and the corresponding right singular vectors (which are the principal components of an uncentered tempo-

ral PCA). Then they classify the spatiotemporal modes according to the corresponding singular values, and to some other information such that the oscillatory behavior of the time course of the modes. Some are attributed to neuronal activity, some to artifacts, and the remaining ones (corresponding to small singular values) to residual noise.

In general, though ICA and PCA provide convenient ways for decomposing VSDOI signals, it is difficult to evaluate the nature (noise, artifact, or signal) of the resulting modes; if even possible. Indeed, the statistical hypotheses are strong (for instance PCA leads to orthogonal modes) and learning the modes on the data raises theoretical and practical difficulties. Usually the underlying statistical model is either on the spatial modes (in that case, each frame is an observation) or on the temporal modes (each pixel is an observation). A full spatiotemporal model would require an enormous amount of trials to be statistically accurate.

3.5 General Linear Model

A last method relying on the decomposition into several modes has been developed in (Reynaud *et al.*, 2011). The authors use the general linear model (GLM[1]) framework, widely used in fMRI (Friston *et al.*, 1995). It is fundamentally different from PCA or ICA. Indeed in this framework the modes (called regressors) must be known *prior* to the decomposition. The idea is to introduce a set of regressors for each component contributing to the signal, and to find a linear combination of those regressors which best approximates the actual contribution of each component in the observed signal. The coefficients of the linear combination are taken so as to minimize the distance between the reconstructed and the observed signal. As long as the introduced regressors are all together linearly independent, the set of minimizing coefficients is unique and is the solution of a small size linear system. If the regressors representing the artifacts and those representing the neuronal activity are decorrelated enough, then the resulting linear reconstruction should separate well the artifacts from the neuronal activity. Meanwhile if the regressors are well chosen the reconstruction should be accurate.

The crucial task in this approach is the design of the regressors. Each set of regressors constitutes a linear approximation basis, reducing the dimensionality of the component to the number of corresponding regressors. If this dimension is too high, the linear approximation of the component may overfit and capture noise and other components. If it is too low, the component cannot be recovered properly. In Reynaud *et al.* (2011) the authors take advantage of the strong temporal morphology of the components, refining their estimation through experiments designed to isolate as much as possible each component from the others. In brief, they identify three components on top of the neuronal response: bleaching, heartbeat and illumination fluctuation. Bleaching is modeled as a decaying exponential (*i.e.* with a regressor decaying exponentially at a given rate) and the two others are modeled as oscillating components (*i.e.* with sinusoidal regressors at a given set of frequencies). Fluctuation of the light source is first characterized on recordings of an illuminated paper surface, *i.e.* no dye is present. After a power spectrum analysis, five harmonics of a dominant fundamental frequency are selected. Then

[1] not to be confused with Generalized Linear Model, a broader class of models in statistics.

the bleaching time constant and the fundamental frequency of the heart are estimated simultaneously by fitting blank recordings. Two harmonics are introduced for the heart. Finally, a constant regressor is added to account for the baseline fluorescence.

In the GLM framework, reducing the dimensionality of the response space is the most delicate part. It strongly depends on the expected complexity of the response and on the information one wishes to extract from the VSDOI acquisition. Consider for instance the problem of establishing a map of orientation selectivity on the primary visual cortex of a mammal (as we do in § VII.3). A classical approach is to present full field, drifting contrast gratings of well-chosen spatiotemporal frequency. In response to such visual stimuli one expects VSDOI to record an overall synchronous raise of neuronal activity. The level of activity reached at a given pixel depends on the orientation selectivity of the underlying neurons, and the space resolution of VSDOI allows to discriminate between several preferred orientations. In such a setting, the information one wishes to recover is only a scalar per pixel, namely the reached level of activity. Thus the response component's dimensionality can be reduced to only one, by introducing a single "gate-shaped" response regressor that mimics roughly the temporal morphology of the response: zero-valued up to some plausible delay after stimulus onset, then nonzero constant up to the stimulus offset, then back again to zero. In Reynaud *et al.* (2011) the stimuli used are also simple but more localized in space. Similar response morphology is expected but with delays varying from pixel to pixel. Hence the response space is also constituted by "gate-shaped" vectors, but with varying rising and decreasing times, as illustrated on Figure II.1(d). SVD is further applied to the set of such vectors with all plausible delays to finally retain a ten-dimensional response space able to capture most of the considered spatiotemporal dynamic.

3.6 Towards Better Denoising Methods

In general, it is clear to us that VSDOI has not yet released all its potential for *in vivo* studies of the cerebral cortex. Up to now, only this modality provides real-time monitoring of neuronal activity at mesoscopic, population level; and understanding this scale of organization is a mandatory step for understanding brain function. During the last decades outstanding improvements have been made regarding the experimental technique, whether it is on the quality of the dyes, the building of the experimental set-up, or the optical device. Even though developments of the hardware aspects of VSDOI, *i.e.* attempts to overcome the biological and physical limitations presented above, can still be expected, we believe that some efforts remain to be made on its software counterparts, *i.e.* better signal modeling and application of state-of-the-art signal processing techniques. We sum up here the general principles that, besides the previous approaches presented above, has driven the work developed in this thesis.

3.6.1 Using the Spatiotemporal Structure.

On top of their strong temporal morphologies, many components in the VSDOI signal have spatially structured origin, *e.g.* heartbeat artifact is stronger on veins, vibrations and illumination fluctuations affects the whole field, and neuronal activity is

organized in functional units or can exhibit wave-like patterns. In spite of the variety of VSDOI processing methods, none seems to take advantage of the entire spatiotemporal structure of the observations. Consider for instance PCA or ICA on the spatial domain (§ 3.4). The time frames are modeled as independent observations, and permuting them randomly results in exactly the same spatial modes. Hence, temporal structure is not taken into account while learning the different components. Similarly but the other way around, the GLM proposed in Reynaud *et al.* (2011) (see § 3.5) processes each pixel independently, without taking into account any spatial structure. As for the SVD used in Onat *et al.* (2011a); Onat *et al.* (2011b), the signal is decomposed into modes that are spatiotemporal but separable along space and time, limiting drastically the dynamic that can be retrieved from a few modes.

Recently, Yavuz (2012) proposed a procedure for assessing and refining the source separation provided by the GLM of Reynaud *et al.* (2011), mixing both spatial and temporal information. First, a components separation in the temporal domain is obtained using GLM, and the result is divided into two groups of components: one comprising the sum of all artifacts (but the bleaching), and the other containing the neuronal response and the residuals. Then, spatial PCA is performed on each of those groups, and on the group of artifacts found within the blank acquisitions. Finally, the resulting components are compared with the blank components, based on the correlation between their corresponding (temporal) coefficients. Artifacts components presenting low correlation with the blank are re-labeled as neuronal activity components, and neuronal activity components presenting high correlation with the blank are re-labeled as artifacts. This approach has the double advantage of combining both model-based and statistical methods, and of using both temporal and spatial information. However, each step suffers from the aforementioned limitations of GLM and PCA, and combining temporal *then* spatial information in two separated steps might not be optimal.

3.6.2 Using Nonlinear Representations.

In general, separating the sources using spatiotemporal components is a difficult task. Even when the temporal dynamic of each pixel is simple, the relative delays and amplitudes from one pixel to another result in a wide variety of possible spatiotemporal patterns, and the dimensionality of the problem becomes prohibitively large. The last decades of research in signal processing, both theory and practice, demonstrated the advantages of nonlinear models of signals. Of particular interest to us is the *sparsity* framework, whose principles are presented in the introuction of this thesis. Such framework is perfectly suitable to enforce all kind of priors on the signal, without limiting its potential diversity. In particular, we focus on representations that do not assume the knowledge of activation time and shape of the signal.

Appendix

A Subtraction Approximates Division

Assuming that bleaching is modulating the gain (*i.e.* has a multiplicative effect), we write the observed signal as $Y(t) = gB(t) \cdot S(t)$ where g is an arbitrary gain scaling the signal, B accounts for variations of fluorophore concentration due to bleaching, and S is the signal of interest (possibly mixed with artifacts other than bleaching).

Now, if the baseline fluorescence is much higher than any other components of the signal we can write (we drop the dependence in t for brevity) $B = 1 + b$ and $S = 1 + s$, with $b \ll 1$ and $s \ll 1$. Developing Y gives $Y/g = 1 + s + b + sb$ so that $Y/g - B = s + sb$. We see that, after normalization by the overall gain g, performing bleaching subtraction retrieves s up to a relative error b.

In practice, the order of magnitude of b never exceeds 10^{-2}; in consequence, the relative difference between both approaches can usually be neglected. The same argument can of course be applied to components in the signal other than bleaching; in particular, this phenomenon explains why some authors perform blank subtraction and others use blank division (see § 3.1).

References

C. D. Acker, P. Yan, and L. M. Loew. Single-voxel recording of voltage transients in dendritic spines. *Biophysical Journal*, 101(2):L11–L13, 2011.

A. Arieli, D. Shoham, R. Hildesheim, and A. Grinvald. Coherent spatiotemporal patterns of ongoing activity revealed by real-time optical imaging coupled with single-unit recording in the cat visual cortex. *Journal of Neurophysiology*, 73(5):2072–2093, 1995.

A. Arieli, A. Sterkin, A. Grinvald, and A. Aertsen. Dynamics of ongoing activity: Explanation of the large variability in evoked cortical responses. *Science*, 273(5283): 1868–1871, 1996.

S. Chakraborty, A. Sandberg, and S. A. Greenfield. Differential dynamics of transient neuronal assemblies in visual compared to auditory cortex. *Experimental Brain Research*, 182(4):491–498, 2007.

S. Chemla and F. Chavane. A biophysical cortical column model to study the multi-component origin of the VSDI signal. *NeuroImage*, 53(2):420–438, 2010a.

S. Chemla and F. Chavane. Voltage-sensitive dye imaging: Technique review and models. *Journal of Physiology Paris*, 104(1-2):40–50, 2010b.

Y. Chen, W. S. Geisler, and E. Seidemann. Optimal temporal decoding of neural population responses in a reaction-time visual detection task. *Journal of Neurophysiology*, 99(3):1366–1379, 2008.

L. B. Cohen, B. M. Salzberg, H. V. Davila, W. N. Ross, D. Landowne, A. S. Waggoner, and C. H. Wang. Changes in axon fluorescence during activity: molecular probes of membrane potential. *Journal of Membrane Biology*, 19(1):1–36, 1974.

H. V. Davila, B. M. Salzberg, L. B. Cohen, and A. S. Waggoner. A large change in axon fluorescence that provides a promising method for measuring membranepotential. *Nature New Biology*, 241(109):159–160, 1973.

A. Destexhe and M. Rudolph-Lilith. *Neuronal Noise*. Number 8 in Computational Neuroscience. Springer, 2012.

G. J. Foschini, R. D. Gitlin, and J. Salz. Optimum direct detection for digital fiber-optic communication systems. *The Bell System Technical Journal*, 54(8):1389–1430, 1975.

K. J. Friston, A. P. Holmes, K. J. Worsley, J. B. Poline, C. Frith, and R. S. J. Frackowiak. Statistical parametric maps in functional imaging: A general linear approach. *Human Brain Mapping*, 2(4):189–210, 1995.

R. D. Frostig, editor. *In Vivo Optical Imaging of Brain Function*. Frontiers in Neuroscience. CRC Press, 2nd edition, 2009.

A. Grinvald and R. Hildesheim. VSDI: a new era in functional imaging of cortical dynamics. *Nature Reviews Neuroscience*, 5(11):874–885, 2004.

A. Grinvald, D. Shoham, A. Shmuel, D. Glaser, I. Vanzetta, E. Shtoyerman, H. Slovin, C. Wijnbergen, R. Hildesheim, and A. Arieli. In-vivo optical imaging of cortical architecture and dynamics. In *Modern Techniques in Neuroscience Research*, pages 893–969. Springer, 1999.

K. Holthoff, D. Zecevic, and A. Konnerth. Rapid time course of action potentials in spines and remote dendrites of mouse visual cortex neurons. *The Journal of Physiology*, 588(7):1085–1096, 2010.

A. Hyvärinen and E. Oja. Independent component analysis: algorithms and applications. *Neural Networks*, 13(4-5):411–430, 2000.

S. Inagaki, T. Katura, H. Kawaguchi, and W. J. Song. Isolation of neural activities from respiratory and heartbeat noises for in vivo optical recording in guinea pigs using independent component analysis. *Neuroscience Letters*, 352(1):9–12, 2003.

D. Jancke, F. Chavane, S. Naaman, and A. Grinvald. Imaging cortical correlates of illusion in early visual cortex. *Nature*, 428(6981):423–426, 2004.

I. T. Jolliffe. *Principal Component Analysis*. Springer, New York, NY, USA, 2002.

I. Lampl, I. Reichova, and D. Ferster. Synchronous membrane potential fluctuations in neurons of the cat visual cortex. *Neuron*, 22(2):361–374, 1999.

M. T. Lippert, K. Takagaki, W. Xu, X. Huang, and J. Y. Wu. Methods for voltage-sensitive dye imaging of rat cortical activity with high signal-to-noise ratio. *Journal of Neurophysiology*, 98(1):502–512, 2007.

H. T. Ma, C. H. Wu, and J. Y. Wu. Initiation of spontaneous epileptiform events in the rat neocortex in vivo. *Journal of Neurophysiology*, 91(2):934–945, 2004.

S. Maeda, S. Inagaki, H. Kawaguchi, and W. J. Song. Separation of signal and noise from in vivo optical recording in Guinea pigs using independent component analysis. *Neuroscience Letters*, 302(2-3):137–140, 2001.

V. Markounikau, C. Igel, A. Grinvald, and D. Jancke. A dynamic neural field model of mesoscopic cortical activity captured with voltage-sensitive dye imaging. *PLoS Computational Biology*, 6(9):e1000919, 2010.

L. Muller and A. Destexhe. Propagating waves in thalamus, cortex and the thalamocortical system: Experiments and models. *Journal of Physiology Paris*, 106(5-6):222–238, 2012.

S. Onat, P. Konig, and D. Jancke. Natural scene evoked population dynamics across cat primary visual cortex captured with voltage-sensitive dye imaging. *Cerebral Cortex*, 21(11):2542–2554, 2011a.

S. Onat, N. Nortmann, S. Rekauzke, P. Konig, and D. Jancke. Independent encoding of grating motion across stationary feature maps in primary visual cortex visualized with voltage-sensitive dye imaging. *NeuroImage*, 55(4):1763–1770, 2011b.

D. S. Peterka, H. Takahashi, and R. Yuste. Imaging voltage in neurons. *Neuron*, 69(1): 9–21, 2011.

C. C. H. Petersen, T. T. G. Hahn, M. Mehta, A. Grinvald, and B. Sakmann. Interaction of sensory responses with spontaneous depolarization in layer 2/3 barrel cortex. *Proceedings of the National Academy of Sciences*, 100(23):13638–13643, 2003.

S. C. Rao, L. J. Toth, and M. Sur. Optically imaged maps of orientation preference in primary visual cortex of cats and ferrets. *Journal of Comparative Neurology*, 287(3): 358–370, 1997.

J. Reidl, J. Starke, D. B. Omer, A. Grinvald, and H. Spors. Independent component analysis of high-resolution imaging data identifies distinct functional domains. *NeuroImage*, 34(1):94–108, 2007.

A. Reynaud, S. Takerkart, G. S. Masson, and F. Chavane. Linear model decomposition for voltage-sensitive dye imaging signals: application in awake behaving monkey. *NeuroImage*, 54(2):1196–1210, 2011.

B. M. Salzberg, H. V. Davila, and L. B. Cohen. Optical recording of impulses in individual neurones of an invertebrate central nervous system. *Nature*, 246(5434):508–509, 1973.

D. Shoham, D. E. Glaser, A. Arieli, T. Kenet, C. Wijnbergen, Y. Toledo, R. Hildesheim, and A. Grinvald. Imaging cortical dynamics at high spatial and temporal resolution with novel blue voltage-sensitive dyes. *Neuron*, 24(4):791–802, 1999.

L. Song, E. J. Hennink, I. T. Young, and H. J. Tanke. Photobleaching kinetics of fluorescein in quantitative fluorescence microscopy. *Biophysical Journal*, 68(6):2588–2600, 1995.

K. Takagaki, M. T. Lippert, B. Dann, T. Wanger, and F. W. Ohl. Normalization of voltage-sensitive dye signal with functional activity measures. *PLoS ONE*, 3(12):e4041, 2008.

H. J. Tanke, P. van Oostveldt, and P. van Duijn. A parameter for the distribution of fluorophores in cells derived from measurements of inner filter effect and reabsorption phenomenon. *Cytometry*, 2(6):359–369, 1982.

T. Tominaga and Y. Tominaga. A new nonscanning confocal microscopy module for functional voltage-sensitive dye and calcium imaging of neuronal circuit activity. *Journal of Neurophysiology*, 110(2):553–561, 2013.

E. Yavuz. *Source separation analysis of visual cortical dynamics revealed by voltage sensitive dye imaging*. PhD thesis, École doctorale Cerveau, Cognition et Comportement (Paris), 2012.

A. Zepeda, C. Arias, and F. Sengpiel. Optical imaging of intrinsic signals: recent developments in the methodology and its applications. *Journal of Neuroscience Methods*, 136(1):1–21, 2004.

▪ II ▪

Spatially Structured Sparse Morphological Component Separation for Voltage-Sensitive Dye Optical Imaging

Within this chapter, we detail our model of the signal acquired by *in vivo* voltage-sensitive dye optical imaging and our theoretical approach for separating the neuronal activity from the artifacts. In order to fulfill the conclusive requirements of the previous chapter, our method relies on the sparsity framework, presented in the introduction of this thesis.

In the previous chapter, § I.3.5, we explained that in the GLM framework, the possible components that can be retrieved lie within a low-dimensional vector space, conditioned by their corresponding set of regressors. It is difficult to allow for more complex dynamics, since it requires to increase the dimensionality of those vector space. Indeed, the more correlated are the regressors of two different components, the less robust to noise is their separation capability. Increasing the complexity to the point where the set of regressors span the whole space results in a model which captures any artifact or noise. The solution of the source separation problem is not unique as soon as regressors representing different components are not linearly independent; if two components have representation spaces with nonzero intersection, the signal along this intersection can be attributed arbitrarily to one component or to the other.

In the GLM terms, the idea of a *sparse* model is to introduce a large set of regressors, typically richer than within the GLM framework, modeling the signal, and seek for a sparse reconstruction where only a limited number of those regressors can be selected, *i.e.* most regressors must be weighted with coefficient zero.

This chapter contains important notations that will be used all along this thesis, and the definition of the functionals used to enforce our assumptions on the signal. After setting the terms of our approach, we discuss the practical challenges that it raises before being applicable to voltage-sensitive dye optical imaging data.

CONTENTS

1 Preliminary Notations

We represent a VSDOI *acquisition* comprising T frames of P pixels as a matrix

$$\tilde{Y} \overset{\text{def}}{=} \left(\tilde{y}_{t,p}\right)_{\substack{1\le t\le T\\ 1\le p\le P}} \in \mathbb{R}^{T\times P}.$$

The time course of the acquisition at the pixel indexed by $p \in \{1,\dots,P\}$ is the column vector $\tilde{Y}_p \overset{\text{def}}{=} \left(\tilde{y}_{t,p}\right)_{1\le t\le T} \in \mathbb{R}^T$.

The signal is decomposed into different spatiotemporal *components* $Y^{(c)} \overset{\text{def}}{=} \left(y^{(c)}_{t,p}\right)_{t,p} \in \mathbb{R}^{T\times P}$ that have the same size as $\tilde{Y}$. The *residual* component, which is the part of the signal that cannot be explained by the previous components, is denoted $\tilde{R} \overset{\text{def}}{=} \left(\tilde{r}_{t,p}\right)_{t,p} \in \mathbb{R}^{T\times P}$. This residual is modeled as a Gaussian white noise whose standard deviation varies in space and time; the matrix of those standard deviations is denoted $\tilde{\Sigma} \overset{\text{def}}{=} \left(\tilde{\sigma}_{t,p}\right)_{t,p} \in \mathbb{R}^{T\times P}$. In a similar fashion, since the *gain* might vary in space and time, we store its values in a matrix $G \overset{\text{def}}{=} \left(g_{t,p}\right)_{t,p} \in \mathbb{R}^{T\times P}$.

The time course of all pixels of a component (c) is linearly estimated in a certain *dictionary* of K_c *regressors* (also called *atoms*),

$$D^{(c)} \stackrel{\text{def}}{=} \left(d_{t,k}^{(c)}\right)_{\substack{1\le t\le T\\ 1\le k\le K_c}} \in \mathbb{C}^{T\times K_c} .$$

The time course of the regressor indexed by a given $k \in \{1,\dots,K_c\}$ is then the column vector $D_k^{(c)} \stackrel{\text{def}}{=} \left(d_{t,k}^{(c)}\right)_t \in \mathbb{C}^T$.

The *coefficients* of the linear representation constitute the matrix

$$X^{(c)} \stackrel{\text{def}}{=} \left(x_{k,p}^{(c)}\right)_{\substack{1\le k\le K_c\\ 1\le p\le P}} \in \mathbb{C}^{K_c\times P} .$$

More precisely, we have for the pixel p of the frame t, $y_{t,p}^{(c)} = \sum_{k=1}^{Kc} d_{t,k}^{(c)} x_{k,p}^{(c)}$; in matrix notation $Y^{(c)} = D^{(c)}X^{(c)}$.

Note that for notational convenience we allow the regressors and coefficients to be complex valued. Since we deal with real valued signals, it is always implied that we consider the real part of the resulting component $Y^{(c)} = \Re\left(D^{(c)}X^{(c)}\right)$.

It is then possible to shorten further the notations by concatenating horizontally (respectively vertically) the dictionaries $D \stackrel{\text{def}}{=} \left(D^{(c)}\right)_c \in \mathbb{C}^{T\times K}$ (respectively the coefficients matrices $X \stackrel{\text{def}}{=} \left(X^{(c)}\right)_c \in \mathbb{C}^{K\times P}$), where $K \stackrel{\text{def}}{=} \sum_c K_c$. This way, we can write with matrix notation the sum of the components $\sum_c Y^{(c)} = DX$.

Some more matrix notations will be useful in the sequel. Given two matrices of the same size $M \stackrel{\text{def}}{=} \left(m_{i,j}\right)_{i,j}, N \stackrel{\text{def}}{=} \left(n_{i,j}\right)_{i,j} \in \mathbb{C}^{I\times J}$, we define the *termwise matrix multiplication* $M\cdot N \stackrel{\text{def}}{=} P \in \mathbb{C}^{I\times J}$ with $P \stackrel{\text{def}}{=} \left(m_{i,j}n_{i,j}\right)_{i,j}$, and the *termwise matrix division* $M/N \stackrel{\text{def}}{=} Q \in \mathbb{C}^{I\times J}$ with $Q \stackrel{\text{def}}{=} \left(m_{i,j}/n_{i,j}\right)_{i,j}$. Also, we define ℓ_2*-norm* of M as[1]

$$\|M\|_2 \stackrel{\text{def}}{=} \sqrt{\sum_{i=1}^{I}\sum_{j=1}^{J} |m_{i,j}|^2} .$$

Finally, we denote the *transpose* of M by

$${}^{\mathrm{t}}M \stackrel{\text{def}}{=} \left(m_{i,j}\right)_{\substack{1\le j\le J\\ 1\le i\le I}} \in \mathbb{C}^{J\times I} ,$$

and when M is a square matrix (*i.e.* $I = J$), we define the *trace* of M as $\mathrm{tra}\,(M) \stackrel{\text{def}}{=} \sum_{i=1}^{I} m_{i,i} \in \mathbb{R}$.

In general, a variable with a tilde ($\tilde{}$) denotes a variable representing raw data, as it is recorded during the acquisition. Alternatively, a variable with no tilde indicates that it has been normalized by the gain. For instance, we define $Y \stackrel{\text{def}}{=} \tilde{Y}/G$.

[1] note that it is called *Frobenius norm* in other contexts, and should not be confused with the matrix operator norm.

2 The Model

Using above notations, our model for the VSDOI signal is

$$\tilde{Y} = G \cdot \Big(\sum_c Y^{(c)} \Big) + \tilde{R} \,. \tag{1}$$

2.1 Gain and Residual

The spatiotemporal matrix G represents the gain between the amplitude of the components and the intensity of recorded fluorescence. The gain is supposed to vary only from one pixel to an other, and to be constant for the duration of an acquisition. That is, for each pixel p, there exists $g_p \in \mathbb{R}$ such that for all time t, $g_{t,p} = g_p$. The residual $\tilde{R}$ takes into account modeling errors and random noise that corrupts the acquisition. We model mathematically this error as the sum of two independent random terms, one Poissonian term accounting for fluorescence and camera shot noise, and one Gaussian accounting for every other contributions. Now, a Poissonian variable with large mean can be seen as a sum of many smaller, independent Poissonian variables. By the central limit theorem, this is well approximated by a Gaussian variable whose standard deviation is proportional to its mean. As a result, the errors at each pixel of each frame are supposed to be realizations of Gaussians whose variances are determined by an affine function of the mean fluorescence intensity. The intercept of this affine function determines a part of the noise which is constant across the whole acquisition, while its slope scales the influence of the shot noise. Recall that the baseline fluorescence dominates all other components, so that the level of fluorescence is essentially determined by the gain. As a consequence, noise level is also assumed to vary only from pixel to pixel and to remain constant along time, *i.e.* for each pixel p, there exists $\tilde{\sigma}_p \in \mathbb{R}$ such that for all time t, $\tilde{\sigma}_{t,p} = \tilde{\sigma}_p$.

2.2 Components Regressors

Following Reynaud *et al.* (2011), we consider three components, namely bleaching, periodic artifacts and neuronal activity, denoted respectively by (B), (P) and (A).

2.2.1 Bleaching.

The regressors modeling the bleaching component are decaying exponentials,

$$d_{t,k}^{(\mathrm{B})} \overset{\text{set}}{=} \exp\left(-t/\tau_k\right) , \tag{2}$$

for a set of time constants $\mathcal{T} \overset{\text{def}}{=} \{\tau_k\}_{1 \le k \le K_\mathrm{B}}$, as illustrated on Figure 1(a). Since the bleaching is usually the component with lowest frequency and highest amplitude, we model the baseline fluorescence within the bleaching component by introducing one constant regressor, corresponding to $\tau_k = +\infty$. Moreover those regressors are highly correlated with the low-frequency regressors of the other components, making difficult their separation with the sole sparsity framework. Hence for this component the sparsity level

is imposed, that is to say the dictionary $D^{(\mathrm{B})}$ is very restrained. In practice one or two regressors (on top of the constant one) are sufficient to capture most of the bleaching dynamics; introducing more regressors leads to overfitting. In consequence, the choice of the nonlinear parameter $\mathcal{T}$ is crucial; it is described in § VI.2.1.

2.2.2 Periodic Artifacts.

The regressors modeling the periodic artifacts component are sinusoidal complex exponentials,

$$d^{(\mathrm{P})}_{t,k} \overset{\text{set}}{=} \exp\left(\mathrm{i}2\pi f_k t\right), \tag{3}$$

for a set of frequencies $\mathcal{F} \overset{\text{def}}{=} \{f_k\}_{1\leq k\leq K_\mathrm{P}}$, as illustrated on Figure 1(b). Since relevant frequencies are automatically selected thanks to sparsity regularization, this set can be as large as one wants. Nevertheless it is not worth introducing frequencies higher that the Nyquist-Shannon frequency (half the sampling frequency of the acquisition), and frequencies lower than the inverse of the acquisition duration are hardly detected. Moreover introducing too many frequencies increases vainly the computational cost for retrieving the coefficients of the model as proposed in § 2.3.

2.2.3 Neuronal Acticity.

Finally, as briefly motivated in the introduction, we model the neuronal activity with wavelet regressors. Wavelets are functions that are dilated, shifted replica of one given *mother wavelet* ψ, a compactly supported function with a certain level of regularity. Up to discretization, the wavelet regressors are thus defined as

$$d^{(\mathrm{A})}_{t,k} \overset{\text{set}}{=} \psi\left(2^{j_k} t - t_k\right), \tag{4}$$

where t_k and j_k are respectively the *time* and *scale* of the wavelet indexed by k, as illustrated on Figure 1(b). More precisely, t_k ranges from 1 to T, and j_k ranges from 0 to $\log_2(T)-1$, resulting in an order of $T\log_2(T)$ possible regressors. This allows to capture interesting features of a signal, smooth parts as well as transients and singularities, with a few regressors selected at the right temporal localization and scale.

By choosing an *orthogonal* mother wavelet (Daubechies, 1992), one can ensure that ${}^{\mathrm{t}}D^{(\mathrm{A})}_k D^{(\mathrm{A})}_{k'} = 0$, when $k \neq k'$, $j_k \leq j_{k'}$ and $t_k \equiv t_{k'}\left[2^{\log_2(T)-1-j_k}\right]$. In this case, $D^{(\mathrm{A})}$ can be seen as the concatenation of several families of orthogonal regressors, and its *right-inverse* can be computed from its adjoint. More precisely, for any $Y \in \mathbb{R}^T$

$$Y = \sum_{k=1}^{K_\mathrm{A}} 2^{j_k-\log_2(T)-1} D^{(\mathrm{A})}_k \left({}^{\mathrm{t}}D^{(\mathrm{A})}_k Y\right), \tag{5}$$

where $2^{j_k-\log_2(T)-1}$ is a scaling coefficient accounting for the *redundancy* of the scale j_k. This property is of particular interest for computational purpose.

In practice wavelet synthesis and transforms (multiplication by $D^{(\mathrm{A})}$ and its adjoint) are computed through filtering, successively applied along the scales (Mallat and Zhong,

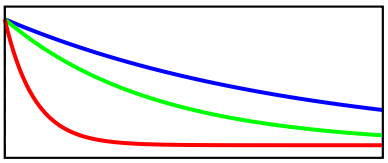

(a) Decaying exponentials with three different time constants.

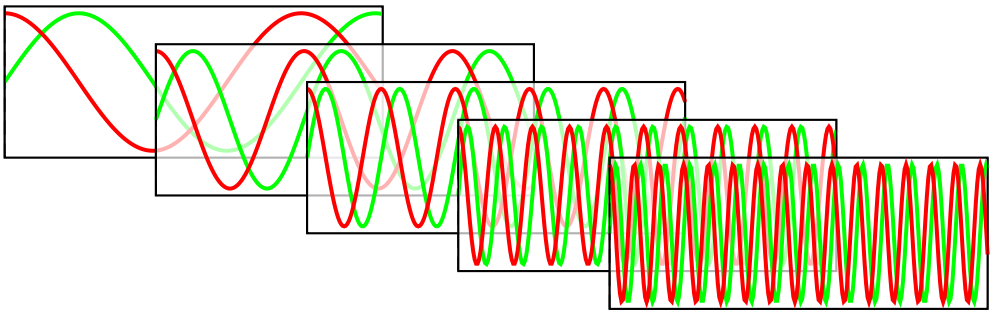

(b) Sinusoids at five different frequencies, weighted by two complex phases in quadrature.

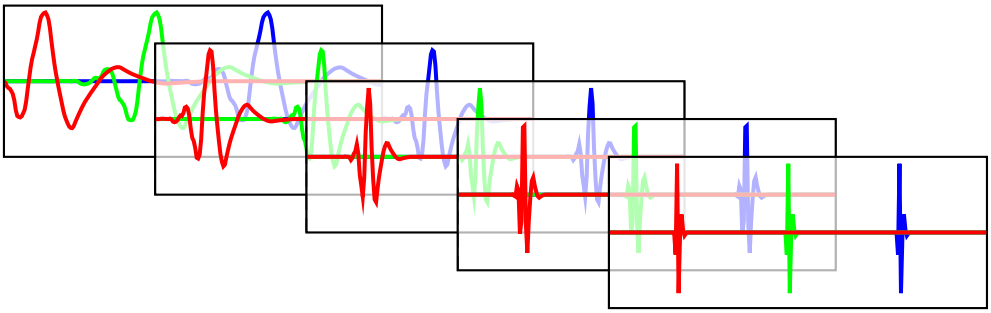

(c) Wavelets at five different scales and three different times.

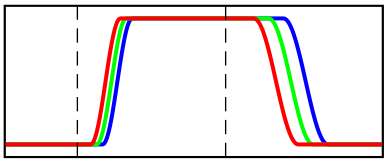

(d) "Gate-shaped" regressors with three different delays with respect to stimulus onset and offset, indicated by dashed lines.

Figure 1: Illustration of the components regressors in SMCS and GLM.
(a) Bleaching regressors (2);
(b) Periodic artifacts regressors (3);
(c) Neuronal activity regressors in SMCS (4);
(d) Neuronal activity regressors as can be designed for the GLM framework; see § I.3.5.

1992). Low scale (*i.e.* low frequency) wavelets are often too correlated with other regressors to be useful in source separation. Hence, we usually compute only the steps for j ranging from a certain $j_{\min}$ up to $\log_2(T) - 1$.

2.3 Retrieving the Components

In order to retrieve the coefficients of the model, our approach consists in two steps. First, the gain G and the noise level $\tilde{\Sigma}$ must be estimated (details given in Chapter VI); we get a noisy estimate of the mixture of components by dividing the observation by the gain. We then retrieve the coefficients by solving an optimization problem,

$$\text{find } \hat{X} \text{ in } \underset{X \in \mathbb{C}^{K \times P}}{\operatorname{argmin}} \ \tfrac{1}{2} \| (Y - DX)/\Sigma \|_2^2 + \Psi^{(\Lambda)}(X) \ . \tag{6}$$

The left-hand term in the summand is the data-fidelity term; the division by Σ accounts for the confidence one has on the observation depending on the noise level. Up to a constant, it is actually equal to the opposite of the log-likelihood of the sum of the components being DX given the noisy observation Y, under our statistical assumptions on the residual R (see § 2.1).

The right-hand term is a *regularization* ensuring that the resulting coefficients are relevant, in spite of the large number of regressors in D. Such approach, in which one defines an optimization problem whose solutions have the properties of the signal one is looking for, is called *variational*. In our model, Ψ is a sum of *penalizations* over the coefficients, notably promoting the sparsity of the solution: only a few coefficients can be nonzero. The next section describes the penalizations that we design for noisy source separation in VSDOI, and precise the dependancy on the parameters Λ. Note also that the use of these penalizations is illustrated on simple problems inspired by image processing applications in § IV.5.3 and in § V.4.

3 Spatially Structured Penalizations

A classical sparsity promoting penalization is the ℓ_1-norm, weighted by a nonnegative scaling parameter $\Lambda \overset{\text{def}}{=} \left(\lambda_{k,p}\right)_{k,p} \in \mathbb{R}^{K \times P}$,

$$\|\Lambda \cdot X\|_1 = \sum_{k=1}^{K} \sum_{p=1}^{P} \lambda_{k,p} |x_{k,p}| \ . \tag{7}$$

However, this penalization considers each coefficients of each pixel individually; this is not robust enough to noise to provide good source separation for VSDOI. In order to benefit from the spatial structure of the components, we design some sparsity enforcing penalizations utilizing spatial information.

3.1 Periodic Artifacts: $\ell_{1,2}$-Norm by Blocks

When performing VSDOI, fluctuations in the illumination supply affect the whole observation field; animal respiration and cortical movements affect entire spatial areas

in unison; heartbeat artifacts are much stronger along the veins. In general, because of the biophysical origins of the periodic artifacts, when a given frequency affects the time course of one given pixel, chances are that the same frequency also affects neighbouring pixels, with similar intensity.

Thus, detection of significant frequencies is improved by replacing, in the ℓ_1-norm, the modulus of a single coefficient by the norm of a group of coefficients of neighboring pixels. We call a *block structure* (over the k-th coefficient map) a family of *spatial blocks* of neighboring pixels. Then, given a family $B^{(\mathrm{P})} \overset{\text{def}}{=} \left(B_k^{(\mathrm{P})}\right)_{1\leq k\leq K_\mathrm{P}}$, where for each frequency k, $B_k^{(\mathrm{P})}$ is a block structure, we define the $\ell_{1,2}$-norm by blocks

$$\left\|X^{(\mathrm{P})}\right\|_{\ell,\Lambda_B^{(\mathrm{P})}} \overset{\text{def}}{=} \sum_{k=1}^{K_\mathrm{P}} \sum_{b\in B_k^{(\mathrm{P})}} \lambda_{k,b}^{(\mathrm{P})} \left\|X_{k,b}^{(\mathrm{P})}\right\|_2 , \tag{8}$$

where for a block b, we denote $\left\|X_{k,b}^{(\mathrm{P})}\right\|_2 \overset{\text{def}}{=} \sqrt{\sum_{p\in b} \left|x_{k,p}^{(\mathrm{P})}\right|^2}$. The scaling parameter $\Lambda_B^{(\mathrm{P})} \overset{\text{def}}{=} \left\{B^{(\mathrm{P})}, \left(\lambda_{k,b}^{(\mathrm{P})}\right)_{(k,b):\, \substack{1\leq k\leq K_\mathrm{P} \\ b\in B_k^{(\mathrm{P})}}}\right\}$ allows to weight differently the penalization on each block.

The choice of the block structures in $B^{(\mathrm{P})}$ is discussed in § 3.5. Note that in the particular case where for all $k \in \{1,\dots,K_\mathrm{P}\}$, $B_k^{(\mathrm{P})}$ comprises all blocks restrained to individual pixels, *i.e.* $\forall\, k \in \{1,\dots,K_\mathrm{P}\}$, $B_k^{(\mathrm{P})} \overset{\text{set}}{=} (\{p\})_{1\leq p\leq P}$, then the $\ell_{1,2}$-norm amounts to the ℓ_1-norm (7).

3.2 Refinement: Reweighted $\ell_{1,2}$-Norm Penalization

Candès *et al.* (2008) introduced a method to improve sparse approximations based on ℓ_1 penalizations. The idea is that smaller weights $\lambda_{k,p}^{(\mathrm{P})}$ should be introduced for frequencies and pixels known to be significant in the model. After solving a problem of the form $\operatorname{argmin}_X \frac{1}{2}\|Y - DX\|_2^2 + \|\Lambda \cdot X\|_1$ for some Λ, the authors propose to modify the weights in Λ according to the solution: lower weights are chosen for high coefficients found in X. Then, the problem can be solved again with these more adapted weights, and this procedure is repeated until the weights and the solution does not evolve anymore.

Following this approach, we propose a reweighted version of the $\ell_{1,2}$ penalizations, which allows to refine adaptively the weights over the blocks for the periodic artifacts penalization (1). Starting from some weights on spatial blocks $\Lambda_B^{(\mathrm{P,rw})}$, we solve successively (6) with weights updated according to

$$\lambda_{k,b}^{(\mathrm{P})} \leftarrow \frac{\lambda_{k,b}^{(\mathrm{P,rw})}}{\left\|X_{k,b}^{(\mathrm{P})}\right\|_2 \lambda_{k,b}^{(\mathrm{P,rw})} + 1} , \tag{9}$$

where $X^{(\mathrm{P})}$ are the periodic artifacts coefficients for the current solution. One can see that the highest is the norm of a block of coefficients, the lowest is its corresponding weight in the next optimization step. It should be noted however that, as opposed to the reweighted ℓ_1 proposed in Candès *et al.* (2008), the weights in $\Lambda_B^{(\mathrm{P})}$ updated by (9) can never exceed the weights in $\Lambda_B^{(\mathrm{P,rw})}$.

3.3 Neuronal Activity: $\ell_{1,2}$-Norm for Sparse Temporal Wavelets Total Variation for Sparse Spatial Gradients

Similarly to the periodic artifacts component, neuronal activity of neighboring pixels in VSDOI are often highly correlated. For instance, many publications on VSDOI report wave-like patterns of activity (Wu *et al.*, 2008), where at each time frame, regions of homogeneous activity are distinguishable. In the same time, sharp differences of activity can be present between these regions.

Thus, we penalize the neuronal activity component by an other $\ell_{1,2}$-norm, parameterized by $\Lambda_B^{(\mathrm{A})} \overset{\text{def}}{=} \left\{B^{(\mathrm{A})}, \left(\lambda_{k,b}^{(\mathrm{A},\ell)}\right)_{(k,b):\substack{1\le k\le K_\mathrm{A}\\ b\in B_k^{(\mathrm{A})}}}\right\}$. Note however that $\ell_{1,2}$-norm is less adapted for neuronal activity than for the periodic artifacts component. Indeed, it tends to select groups of coefficients with similar modulus, but without regards to their signs. A given frequency may influence a spatial area with different phases from pixel to pixel. On the contrary, neuronal activity time course at pixels with similar intensity must have the same sign.

This can be modeled in our sparsity framework as the hypothesis that the spatial gradient of each spatial map of coefficients is sparse. The spatial gradient is defined by approximating the spatial derivatives in each direction by finite differences. More precisely, given a coefficient index $k \in \{1, \dots, K_\mathrm{A}\}$ and a block b of size 2×2 pixels, the spatial gradient of the k-th coefficient map of $X^{(\mathrm{A})}$ at the center of b is defined as the four-dimensional vector[2]

$$\Delta X_{k,b}^{(\mathrm{A})} \overset{\text{def}}{=} \left(x_{k,p}^{(\mathrm{A})} - x_{k,b}^{(\mathrm{A})}\right)_{p\in b} \qquad \text{(10)}$$

where we denote $x_{k,b}^{(\mathrm{A})} \overset{\text{def}}{=} \frac{1}{4}\sum_{p\in b} x_{k,p}^{(\mathrm{A})}$ the average value of the coefficients within the block b.

This approximates the spatial derivatives at the red dot in the diagram in (10), along the directions indicated by the arrows. Note that other choices for the finite differences are possible; to our knowledge, such discrete spatial gradient with four coordinates is new, and presents both theoretical and computational advantages, as detailed in § IV.2.

Then, we enforce sparsity on the spatial gradients of the coefficients $X^{(\mathrm{A})}$ by using the two-dimensional total variation semi-norm penalization over each coefficient map,

$$\begin{aligned}\left\|X^{(\mathrm{A})}\right\|_{\delta,\Lambda_{\mathrm{TV}}^{(\mathrm{A})}} &\overset{\text{def}}{=} \sum_{k=1}^{K_\mathrm{A}} \sum_{b\in B_{\mathrm{TV}}} \lambda_{k,b}^{(\mathrm{A},\delta)} \left\|\Delta X_{k,b}^{(\mathrm{A})}\right\|_2 ,\\ &= \sum_{k=1}^{K_\mathrm{A}} \sum_{b\in B_{\mathrm{TV}}} \lambda_{k,b}^{(\mathrm{A},\delta)} \sqrt{\sum_{p\in b}\left(x_{k,p}^{(\mathrm{A})} - x_{k,b}^{(\mathrm{A})}\right)^2} ,\end{aligned} \qquad \text{(11)}$$

where B_{TV} is the block structure containing all possible blocks of size 2×2, and $\Lambda_{\mathrm{TV}}^{(\mathrm{A})} \overset{\text{def}}{=} \left\{B_{\mathrm{TV}}, \left(\lambda_{t,b}^{(\mathrm{A},\delta)}\right)_{(t,b):\substack{1\le k\le K_\mathrm{A}\\ b\in B_{\mathrm{TV}}}}\right\}$ allows to weight differently the penalization over each block.

[2] the notation Δ for the discrete spatial gradient emphasizes the fact that the spatial derivatives are approximated by finite differences; it should not be confused with the usual notation for the Laplacian operator.

3.4 Some Suitable Hard Constraints

Using the variational framework that we defined in § 2.3 also allows to enforce other properties of the signal we are looking for, not necessarily related to sparsity. Here, we define penalizations which are useful for VSDOI component separations. They are dubbed "hard constraints" because they all have in common that they bear no compromise: they define subsets of the optimization space in which the solution of (6) must lie, whatever might be the observations or other constraints in the problem. They are defined as *convex indicator functions* which are functions that take value 0 within a certain set and $+\infty$ outside.

3.4.1 Bleaching: Nonnegative Orthant.

The bleaching component captures the fluctuations of the baseline fluorescence, which is by nature a positive quantity. Since bleaching regressors are nonnegative, the bleaching coefficients are necessarily nonnegative as well. We ensure this with the convex indicator function of the *nonnegative orthant*

$$\iota_{+}\left(X^{(\mathrm{B})}\right) \overset{\text{def}}{=} \begin{cases} 0 & \text{if } \forall\, k \in \{1,\dots,K_{\mathrm{B}}\},\, \forall\, p \in \{1,\dots,P\},\, x_{k,p}^{(\mathrm{B})} \in \mathbb{R}_{+}\,, \\ +\infty & \text{otherwise}\,. \end{cases} \tag{12}$$

3.4.2 Periodic Artifacts: Bounded Amplitude.

In order to ensure stability of the component separation results and enforce prior knowledge over the components amplitudes, one can bound from above the coefficients of the periodic artifacts. We introduce a hard constraint which is spatially structured similarly to the $\ell_{1,2}$-norm by blocks, as

$$\iota_{\overline{\ell_{M_B^{(\mathrm{P})}}}}\left(X^{(\mathrm{P})}\right) \overset{\text{def}}{=} \begin{cases} 0 & \text{if } \forall\, k \in \{1,\dots,K_{\mathrm{P}}\},\, \forall\, b \in B_k^{(\mathrm{P})},\, \left\|X_{k,b}^{(\mathrm{P})}\right\|_2 \leq \mu_{k,b}^{(\mathrm{P})}\,, \\ +\infty & \text{otherwise}\,, \end{cases} \tag{13}$$

where $M_B^{(\mathrm{P})} \overset{\text{def}}{=} \left\{B^{(\mathrm{P})}, \left(\mu_{k,b}^{(\mathrm{P})}\right)_{(k,b):\, \substack{1\leq k\leq K_{\mathrm{P}} \\ b\in B_k^{(\mathrm{P})}}}\right\}$ sets the maximal amplitude of each spatial block of coefficients.

3.4.3 Neuronal Activity: Bounded Deviation and Known Bounds.

In a similar fashion, one can control the amplitude of the spatial gradients of the neuronal activity coefficients with a penalization which is spatially structured as like the total variation, as

$$\iota_{\overline{\delta_{M_{\mathrm{TV}}^{(\mathrm{A})}}}}\left(X^{(\mathrm{A})}\right) \overset{\text{def}}{=} \begin{cases} 0 & \text{if } \forall\, k \in \{1,\dots,K_{\mathrm{A}}\},\, \forall\, b \in B_{\mathrm{TV}},\, \left\|X_{k,b}^{(\mathrm{A})}\right\|_2 \leq \mu_{k,b}^{(\mathrm{A})}\,, \\ +\infty & \text{otherwise}\,, \end{cases} \tag{14}$$

where $M_{\mathrm{TV}}^{(\mathrm{A})} \overset{\text{def}}{=} \left\{B_{\mathrm{TV}}, \left(\mu_{k,b}^{(\mathrm{A})}\right)_{(k,b):\, \substack{1\leq k\leq K_{\mathrm{A}} \\ b\in B_{\mathrm{TV}}}}\right\}$ sets the maximal amplitude of each spatial gradients.

Moreover, it might happen that in some VSDOI experiments, the experimentalist knows in advance that at some points in time, no neuronal activity should be expected; or on the contrary, that the neuronal activity should be above a certain value. This can be easily transposed in our variational framework, again with a convex indicator function:

$$\iota_{\left[\underline{Y}^{(\mathrm{A})},\overline{Y}^{(\mathrm{A})}\right]}\left(Y^{(\mathrm{A})}\right) \overset{\text{def}}{=} \begin{cases} 0 & \text{if } \forall\, t \in \{1,\dots,T\},\, \forall\, p \in \{1,\dots,P\}, \\ & \qquad y_{t,p}^{(\mathrm{A})} \in \left[\underline{y}_{t,p}^{(\mathrm{A})}, \overline{y}_{t,p}^{(\mathrm{A})}\right], \\ +\infty & \text{otherwise}, \end{cases} \tag{15}$$

where the spatiotemporal bounds $\underline{Y}^{(\mathrm{A})}$ and $\overline{Y}^{(\mathrm{A})}$ define respectively the minimum and maximum values of the neuronal activity. Some or all of those values can be $\pm\infty$ when no bound is known.

3.5 Structure of the Parameters

Altogether, the penalization $\Psi^{(\Lambda)}$ in (6), where Λ stands for the set of all parameters involved, expands for all $X \in \mathbb{C}^{K\times P}$, as

$$\begin{aligned}\Psi^{(\Lambda)}(X) \overset{\text{set}}{=} \left\|X^{(\mathrm{A})}\right\|_{\ell,\Lambda_B^{(\mathrm{A})}} + \left\|X^{(\mathrm{A})}\right\|_{\delta,\Lambda_{\mathrm{TV}}^{(\mathrm{A})}} + \iota_{\overline{\delta}_{M_{\mathrm{TV}}^{(\mathrm{A})}}}\left(X^{(\mathrm{A})}\right) + \iota_{\left[\underline{Y}^{(\mathrm{A})},\overline{Y}^{(\mathrm{A})}\right]}\left(D^{(\mathrm{A})}X^{(\mathrm{A})}\right) \\ + \iota_{+}\left(X^{(\mathrm{B})}\right) + \left\|X^{(\mathrm{P})}\right\|_{\ell,\Lambda_B^{(\mathrm{P})}} + \iota_{\overline{\ell}_{M_B^{(\mathrm{P})}}}\left(X^{(\mathrm{P})}\right).\end{aligned} \tag{16}$$

In all generality, there can be one different weight for each spatial block of each coefficient map involved in (16). In practice, one should reduce as much as possible the number of degrees of freedom of the model to avoid overfitting and to be able to set relevant parameters automatically (see the discussion § 4.2). Our approach is to set, for each component (c) and each regressor $k \in \{1,\dots,K_c\}$, a unique parameter. Such parameter can be denoted $\lambda_k^{(c)}$, it is characteristic of the significance of regressor k of component (c) over the entire spatiotemporal dynamic. The final map of weights is set as a function of the spatially varying residual level σ_p, proportionnaly to $\lambda_k^{(c)}$; such function is explicited in § VI.1.1.

Since we are working with blocks instead of isolated coefficients, we extend the previous principle to block structures. For each component (c) and each regressor $k \in \{1,\dots,K_c\}$, we chose first a *block side length* $\mathsf{s}_k^{(c)}$. Then, the family of blocks $B_k^{(c)}$ contains all possible square blocks of $\mathsf{s}_k^{(c)} \times \mathsf{s}_k^{(c)}$ pixels. Note that this comprises incomplete blocks at the boundary of the spatial domain, where we apply null boundary conditions, as explained in § IV.1. Finally, for each of those blocks, the corresponding penalization weight is set now as a function of $\|\Sigma_b\|_2$, where $\|\Sigma_b\|_2 = \sqrt{\sum_{p\in b}\sigma_p{}^2}$, proportionaly to $\lambda_k^{(c)}$.

The setting of maximum amplitude values $M_B^{(c)}$ is slightly different, because they should only depend on the underlying signal amplitude and not on the noise level. Proportionaly to an overall scaling, $\mu_k^{(c)}$, the maximum amplitude over each block is then only a function of the block size.

Those scalings are discussed in more details in § VI.1.1.

4 Discussion

The entire SMCS approach has been described, but many theoretical and technical questions remain. Before going further on our way to VSDOI signal separation, it is judicious to introduce those questions here.

4.1 Comparison with MCA

As already highlighted, the motivation behind SMCS is the possibility to take advantage of the distinct morphologies of the components in the temporal domain, together with their spatial structure. The former is done by representing each component in an adapted dictionary, and the latter by imposing over the corresponding coefficients a structured sparsity.

Alternatively, one could think of using the spatial information by applying sparsifying spatial transforms over the coefficients X of our model. This would correspond to representing the data within huge dictionaries of separable spatiotemporal regressors, as advocated by the *multichannel* MCA approach, evoked in the introduction. Doing so, one could get rid of the complex penalizations designed along this chapter. However, the kind of spatial transforms that should be used for the different components within VSDOI data is not obvious to us. Moreover, using for instance the spatial equivalent of our redundant wavelet transform presented in § 2.2.3 would multiply the number of coefficients in the problem by a factor of order $\log_2(P)$. Finally, the study of multichannel MCA performances for component separation in the presence of noise are rather limited. The approach advised in Bobin *et al.* (2008, §IV.E. or §V.A.3.b.), that tends to select only coefficients with amplitude three or four times higher than the noise standard deviation, is impracticable for VSDOI signals where noise and components have similar orders of magnitude.

In spite of those limitations, adapting MCA to the context of VSDOI component separation would be an interesting and instructive work; however, the SMCS model led us to focus on other challenges, introduced below.

4.2 Many Parameters for Many Penalizations

In the GLM model, precise knowledge of the neuronal dynamic is needed for the design of the regressors; in the case of Reynaud *et al.* (2011) this boils down to setting parameters controlling the possible neuronal response delays, rising and decreasing times, as well as the dimensionality of the response component space. Other parameters are the different frequencies of oscillating artifacts and the bleaching time constant. In their case, those parameters are estimated on specifically designed experiments, as outlined in § I.3.5.

In our sparsity framework, precision on those settings can be drastically relaxed, at the cost of new parameters. They typically are scaling parameters, tuning the relative influence between the data-fidelity and the penalization. In variational signal processing approaches, the values of these parameters are sometimes chosen arbitrarily by trial-and-error, or according to some heuristics. When a quality criterion can be defined,

for instance in regression of classification problems, parameters can be set by *cross-validation*. More involved methods estimate those parameters directly from the data, often based on statistical assumptions on the observed signal. A common drawback of all those methods, however, is that they require, for each set of parameters that one wants to test, a full solution of the model.

In the SMCS model, that means to find, for each set of parameters, a solution of (6), where the penalization Ψ is the complex functional defined in (16). In contrast to the GLM model described in § I.3.5, it is not the solution of a linear system, and it cannot be solved for each pixel independently, because of the spatially structured penalizations. The resulting optimization problem is then high dimensional ($X \in \mathbb{C}^{K \times P}$ has an order of $PT \log_2(T)$ coefficients). Moreover, it is convex but nondifferentiable.

4.3 Splitting the Problem

The above review is not encouraging; most of the obstacles are due to the complex spatial penalizations in Ψ, especially the $\ell_{1,2}$-norm on overlapping blocks of coefficients, or the TV semi-norm, which both introduce dependencies between all pixels.

Along the three following chapters of this thesis, we propose and develop solutions that relies on the same general principles: splitting the problem into several, simpler subproblems. To give an illustration, consider for instance that a simple ℓ_2-norm penalization is much easier to handle on an isolated block of coefficients than within a full $\ell_{1,2}$-norm with overlapping blocks. In the two next chapters, we define rigorously this kind of property, and develop an optimization algorithm that uses them in order to minimize more complicated functions. Further on, we show how the same property enables the use of statistical estimation of parameters for some subproblems. Finally, a subsequent chapter details how those methods can be applied in the case of noisy components source separation for VSDOI, thanks to successive approximations of the whole SMCS model.

References

J. Bobin, J.-L. Starck, Y. Moudden, and J. M. Fadili. Blind source separation: The sparsity revolution. volume 152 of *Advances in Imaging and Electron Physics*, chapter 5, pages 221–302. Elsevier, 2008.

E. J. Candès, M. B. Wakin, and S. P. Boyd. Enhancing sparsity by reweighted ℓ_1 minimization. *Journal of Fourier Analysis and Applications*, 14(5):877–905, 2008.

I. Daubechies. *Ten Lectures on Wavelets*. Society for Industrial and Applied Mathematics, 1992.

S. Mallat and S. Zhong. Characterization of signals from multiscale edges. *Pattern Analysis and Machine Intelligence, IEEE Transactions on*, 14(7):710–732, 1992.

A. Reynaud, S. Takerkart, G. S. Masson, and F. Chavane. Linear model decomposition for voltage-sensitive dye imaging signals: application in awake behaving monkey. *NeuroImage*, 54(2):1196–1210, 2011.

J. Y. Wu, X. Huang, and C. Zhang. Propagating waves of activity in the neocortex: What they are, what they do. *The Neuroscientist*, 14(5):487–502, 2008.

▪ III ▪

A Generalized Forward-Backward Splitting Algorithm

The previous chapter defines a variational problem that must be solved efficiently for retrieving the coefficients of our voltage-sensitive dye optical imaging model. As underlined in § II.4.2, this is a minimization problem which is convex, but nondifferentiable and high-dimensional, with complex relationships between the coefficients. In the same time, we observed that it can be decomposed as a sum of functionals which are, individually, much simpler to handle.

In fact, in that particular context, simplicity is a well defined property: a functional is called *simple* if one can compute efficiently its Moreau's proximity operator, defined in the introduction of this thesis. As explained at this occasion, functionals that are sums of simple functions can be efficiently minimized with help of the proximity operators of each of their terms.

The particular case of the forward-backward algorithm makes use of both the simplicity of a term (through its proximity operator) and the smoothness of an other term (through a gradient descent steps). This is interesting to us because the data-fidelity term of our functional is smooth, but not simple. Unfortunately, only one simple function can be involved in the splitting.

In this chapter, we present a generalized forward-backward splitting algorithm, allowing efficient minimization of the sum of convex functions $f + \sum_{i=1}^{n} g_i$, where f has a Lipschitz continuous gradient and each g_i is simple in the sense that its proximity operator is easy to compute. The resulting method makes use of the regularity of f in the forward step, and the proximity operators of the simple functions are applied in parallel in the backward step.

While the forward-backward algorithm cannot deal with more than $n \overset{\text{set}}{=} 1$ nonsmooth function, we generalize it to the case of arbitrary n, without resorting to partial resolutions of subproblems.

Contents

This chapter is the most technical part of this thesis, and many notations are specific to it and to the next one. Throughout this chapter, $\mathcal{H}$ denotes a real Hilbert space endowed with scalar product $\langle \cdot \,|\, \cdot \rangle$ and associated norm $\|\cdot\|$, Id is the identity operator on $\mathcal{H}$, and n is a strictly positive integer, $n \geq 2$. Then, $\Gamma_0(\mathcal{H})$ is the class of *lower semicontinuous*, *proper*, *convex* functions from $\mathcal{H}$ to $]-\infty, +\infty]$.

1 Monotone Inclusion and Minimization Problems

We consider the following monotone inclusion problem

$$\text{Find } x \in \left\{ \operatorname{zer}\left(B + \sum_{i=1}^{n} A_i\right) \stackrel{\text{def}}{=} \left\{ x \in \mathcal{H} \;\middle|\; 0 \in Bx + \sum_{i=1}^{n} A_i x \right\} \right\}, \tag{1}$$

where $B\colon \mathcal{H} \mapsto \mathcal{H}$ is cocoercive, and for all i, $A_i\colon \mathcal{H} \mapsto 2^{\mathcal{H}}$ is a maximal monotone set-valued map.

The structured monotone inclusion problem (1) is fairly general, and a wide range of iterative algorithms to solve it takes advantage of the specific properties of the operators involved in the summand. As we will see, one crucial property is the possibility to compute the *resolvent* of a maximal monotone operator A, denoted J_A. It is defined as (see § 1.1 for details)

$$J_A x = \xi \quad \stackrel{\text{def}}{\Leftrightarrow} \quad x \in \xi + A\xi \,.$$

For a given $x \in \mathcal{H}$, computing $J_A x$ is in itself a monotone inclusion problem, but it turns out that it can be solved efficiently for many operators, *e.g.* the action of the resolvent can be easily computed in closed form. Our interest is in *splitting* methods for solving problem (1): iterative algorithms which evaluate individually the operator B (cocoercive) and the resolvents J_{A_i}, at various points of $\mathcal{H}$, but not the resolvents of sums.

While such inclusion problems arise in various fields, our main motivation is to solve convex minimization problems. Indeed, it is well-known that the subdifferential ∂g_i of a function $g_i \in \Gamma_0(\mathcal{H})$ is a maximal monotone map. Its resolvent $J_{\partial g_i}$ can be shown (see § 1.1) to be equal to the *Moreau's proximity operator* of g (Moreau, 1965), defined for all $x \in \mathcal{H}$ as

$$\operatorname{prox}_g(x) \stackrel{\text{def}}{=} \operatorname*{argmin}_{\xi \in \mathcal{H}} \tfrac{1}{2}\|x - \xi\|^2 + g(\xi) \,. \tag{2}$$

Note that, using *strong convexity* of the squared norm, one can show that the minimizer exists and is unique, so that the proximity operator is well defined. Again, this can be solved explicitly for many functions; such functions are dubbed *simple*.

If moreover $f \in \Gamma_0(\mathcal{H})$ is differentiable with a Lipschitz continuous gradient, then Baillon-Haddad Theorem (Baillon and Haddad, 1977) asserts that ∇f is cocoercive. Defining $F \stackrel{\text{def}}{=} f + \sum_{i=1}^n g_i$, *Fermat's rule* on convex optimization states that the set of minimizers[1] of F verifies

$$\operatorname{argmin} F \stackrel{\text{def}}{=} \left\{ x \in \mathcal{H} \,|F(x) = \inf_{\xi \in \mathcal{H}} F(\xi) \right\} = \operatorname{zer}\left(\partial F\right) . \tag{3}$$

Now, under domain qualification conditions, $\partial F = \nabla f + \sum_{i=1}^n \partial g_i$. Therefore, identifying B with ∇f and each A_i with ∂g_i, solving (1) allows to solve

$$\min_{x \in \mathcal{H}} \left\{ F(x) \stackrel{\text{def}}{=} f(x) + \sum_{i=1}^n g_i(x) \right\} . \tag{4}$$

This chapter introduces a novel generalized forward-backward (GFB) algorithm for solving the monotone inclusion (1). The algorithm achieves full splitting where all operators are used separately: an explicit step for B and a parallelized, implicit step through the resolvent of each A_i. We prove convergence of the algorithm even when summable errors contaminates the iterations.

We first recall some essential definitions and properties of monotone operator theory that are necessary to our exposition. Note that the next chapter also makes use of some of these results. The interested reader may refer to Phelps (1993); Bauschke and Combettes (2011) for a comprehensive treatment. As we will deal with maximal monotone operator splitting, we also introduce specific notations on the product space $\mathcal{H}^n$.

Then, we present in § 2 the algorithm, and state our main theoretical results before commenting on some relevant aspects and on alternatives in the literature. Finally, § 3 details the convergence analysis.

[1] throughout this thesis, if $C \subseteq \mathcal{H}$ is a subset of $\mathcal{H}$, we also use the notation $\operatorname{argmin}_{x \in C} F(x)$ or simply $\operatorname{argmin}_C F$ for the set $\left\{ x \in C \,\middle|\, F(x) = \inf_{\xi \in C} F(\xi) \right\}$. Moreover, in the case where $\operatorname{argmin}_C F = \{x\}$ is a singleton, *i.e.* the minimizer exists and is unique, we abusively use the notation $\operatorname{argmin} F$ for denoting the element x.

1.1 Definitions and Properties

In the following, $A\colon \mathcal{H} \to 2^{\mathcal{H}}$ is a set-valued operator and $T\colon \operatorname{dom} T \to \mathcal{H}$ is a single-valued operator. Recall that Id denotes the identity operator on $\mathcal{H}$.

Definition 1.1 (graph, inverse, domain, range and zeros)**.** The *graph* of A is the set $\operatorname{gra} A \stackrel{\text{def}}{=} \{(x, y) \in \mathcal{H}^2 \mid y \in Ax\}$. The *inverse* of A, noted A^{-1}, is the operator whose graph is $\operatorname{gra} A^{-1} \stackrel{\text{def}}{=} \{(x, y) \in \mathcal{H}^2 \mid (y, x) \in \operatorname{gra} A\}$. The *domain* of A is $\operatorname{dom} A \stackrel{\text{def}}{=} \{x \in \mathcal{H} \mid Ax \neq \emptyset\}$. The *range* of A is $\operatorname{ran} A \stackrel{\text{def}}{=} \{y \in \mathcal{H} \mid \exists\, x \in \mathcal{H},\ y \in Ax\}$, and its set of *zeros* is $\operatorname{zer} A \stackrel{\text{def}}{=} \{x \in \mathcal{H} \mid 0 \in Ax\} = A^{-1}(0)$.

Definition 1.2 (resolvent and reflection operators)**.** The *resolvent* of A is the operator $J_A \stackrel{\text{def}}{=} \big(\operatorname{Id} + A\big)^{-1}$. The *reflection operator* associated to J_A is the operator $R_A \stackrel{\text{def}}{=} 2J_A - \operatorname{Id}$.

Definition 1.3 (maximal monotone operator)**.** A is *monotone* if

$$\forall\, x, y \in \mathcal{H}, \quad (u \in Ax \text{ and } v \in Ay) \Rightarrow \langle u - v \,|\, x - y\rangle \geq 0\,.$$

It is moreover *maximal monotone* if its graph is not strictly contained in the graph of any other monotone operator.

Definition 1.4 (uniformly monotone operator)**.** A is *uniformly monotone* of modulus $\phi\colon [0, +\infty[\to [0, +\infty]$ if ϕ is a nondecreasing function that vanishes only at zero, such that

$$\forall\, x, y \in \mathcal{H}, \quad (u \in Ax \text{ and } v \in Ay) \Rightarrow \langle u - v \,|\, x - y\rangle \geq \phi(\|x - y\|)\,.$$

Definition 1.5 (nonexpansive and α-averaged operators)**.** T is *nonexpansive* if

$$\forall\, x, y \in \operatorname{dom} T, \qquad \|Tx - Ty\| \leq \|x - y\|\,.$$

For $\alpha \in]0, 1[$, T is *α-averaged* if there exists R nonexpansive such that $T = (1-\alpha)\operatorname{Id} + \alpha R$. We denote $\mathcal{A}(\alpha)$ the class of α-averaged operators on $\mathcal{H}$. In particular, $\mathcal{A}\big(\frac{1}{2}\big)$ is the class of *firmly nonexpansive* operators.

Definition 1.6 (cocoercive operator)**.** For $\beta \in]0, +\infty[$, T is *β-cocoercive* if $\beta T \in \mathcal{A}\big(\frac{1}{2}\big)$.

The following lemma is useful for manipulating averaged and cocoercive operators.

Lemma 1.1. *Let $\alpha_1, \alpha_2 \in]0, 1[$, $\beta \in]0, +\infty[$, T_1 and T_2 be respectively α_1- and α_2-averaged operators, and T be β-cocoercive. Then,*

(i) $\forall\, \gamma \in]0, 2\beta[, \quad \operatorname{Id} - \gamma T \in \mathcal{A}\big(\frac{\gamma}{2\beta}\big)$;

(ii) $\forall\, \rho \in \big]0, \frac{1}{\alpha_1}\big[, \quad \operatorname{Id} + \rho(T_1 - \operatorname{Id}) \in \mathcal{A}(\rho\alpha_1)$.

(iii) $\alpha \stackrel{\text{def}}{=} \frac{\alpha_1 + \alpha_2 - 2\alpha_1\alpha_2}{1 - \alpha_1\alpha_2} \in]0, 1[$, *and* $T_1 T_2 \in \mathcal{A}(\alpha)$.

Proof. (i). By definition, $\beta T = \frac{1}{2}(\mathrm{Id} + R)$ for some nonexpansive operator R, so that $\mathrm{Id} - \gamma T = \left(1 - \frac{\gamma}{2\beta}\right)\mathrm{Id} + \frac{\gamma}{2\beta}(-R)$. Since R is nonexpansive, $-R$ is nonexpansive as well, which terminates the proof.
(ii). By definition, $T_1 = (1-\alpha_1)\,\mathrm{Id} + \alpha_1 R_1$ for some nonexpansive operator R, so that $\mathrm{Id} + \rho(T_1 - \mathrm{Id}) = \mathrm{Id} + \rho\alpha_1(R_1 - \mathrm{Id}) = (1 - \rho\alpha_1)\,\mathrm{Id} + \rho\alpha_1 R_1$.
(iii). See Ogura and Yamada (2002, Theorem 3). Note that these authors actually define α-averaged operators with $\alpha \in [0,1[$, but the above result is easily derived from theirs, noticing that $\alpha_1 + \alpha_2 \geq 2\min(\alpha_1, \alpha_2) > 2\alpha_1\alpha_2$, ensuring $\alpha \in \mathbb{R}_{+*}$. ∎

Let us establish some useful characterizations of firmly nonexpansive operators.

Lemma 1.2. *The following statements are equivalent:*

(i) *T is firmly nonexpansive with full domain (i.e.* $\operatorname{dom} T = \mathcal{H}$*);*

(ii) *$2T - \mathrm{Id}$ is nonexpansive and T has full domain;*

(iii) $\forall\, x, y \in \mathcal{H},\ \|Tx - Ty\|^2 \leq \langle Tx - Ty \,|\, x - y\rangle$*;*

(iv) *T is the resolvent of a maximal monotone operator A, i.e. $T = J_A$.*

Proof. (i) ⇔ (ii): $T \in \mathcal{A}\left(\frac{1}{2}\right) \Leftrightarrow T = \frac{\mathrm{Id}+R}{2}$ for some R nonexpansive.
(i) ⇔ (iii): see Zarantonello (1971). (i) ⇔ (iv): see Minty (1962). ∎

Note that with (iii), one retrieves the characterization of the cocoercivity given in § 2.1. By the Cauchy-Schwarz inequality, β-cocoercivity implies β^{-1}-Lipschitz continuity, but the converse is not true in general. However, it turns out to be the case for gradients of convex functionals. We summarize here some properties of the subdifferential.

Definition 1.7 (subdifferential)**.** For $g : \mathcal{H} \to]-\infty, +\infty]$, its *subdifferential* is the set valued operator

$$\partial g : \begin{array}{ccc} \mathcal{H} & \longrightarrow & 2^{\mathcal{H}} \\ x & \longmapsto & \{u \in \mathcal{H} \,|\, \forall\, h \in \mathcal{H},\ g(x) + \langle u \,|\, h\rangle \leq g(x+h)\} \end{array}. \tag{5}$$

In the following lemma, $\operatorname{dom} g_i \overset{\text{def}}{=} \{x \in \mathcal{H} \,|\, g_i(x) < +\infty\}$ is the *domain* of a function $g \in \Gamma_0(\mathcal{H})$, and $\operatorname{ri}(C)$ (respectively $\operatorname{sri}(C)$) denotes the *relative interior* (respectively the *strong relative interior*), of a convex set $C \subseteq \mathcal{H}$ (see for instance Bauschke and Combettes (2011)).

Lemma 1.3. *Let $F \in \Gamma_0(\mathcal{H})$, $f : \mathcal{H} \to]0, +\infty]$ be proper and convex, $x \in \operatorname{dom} f$ such that f is (Gâteaux) differentiable in x, and for all $i \in \{1, \dots, n\}$, $g_i \in \Gamma_0(\mathcal{H})$. Moreover, suppose that*

$$\forall\, i \in \{2, \dots, n\}, \quad 0 \in \operatorname{sri}\left(\operatorname{dom} g_i - \cap_{j=1}^{i-1} \operatorname{dom} g_j\right). \tag{D}$$

Then,

(i) $\forall\, \xi \in \mathcal{H},\ \xi \in \operatorname{argmin} F \Leftrightarrow 0 \in \partial F(\xi)$*;* (Fermat's rule)

(ii) $\partial f(x) = \{\nabla f(x)\}$;

(iii) $\partial(\sum_{i=1}^n g_i) = \sum_{i=1}^n \partial g_i$.

Proof. (i). $\xi \in \operatorname{argmin} F \Leftrightarrow \forall\, h \in \mathcal{H}, F(\xi) \leq F(\xi + h)$.
(ii). See Bauschke and Combettes (2011, proposition 17.26).
(iii). See Bauschke and Combettes (2011, corollary 16.39); note that in the particular case where $\mathcal{H}$ is finite-dimensional, $\cap_{i=1}^n \operatorname{ri}(\operatorname{dom} g_i) \neq \emptyset$ is a sufficient condition for (D). ■

Lemma 1.4. *Let $\beta \in]0, +\infty[$, $f: \mathcal{H} \to \mathbb{R}$ be a convex differentiable function whose gradient is β^{-1}-Lipschitz continuous, and $g \in \Gamma_0(\mathcal{H})$. Then,*

(i) *$\beta\nabla f \in \mathcal{A}\left(\frac{1}{2}\right)$, i.e. is firmly nonexpansive;*

(ii) *∂g is maximal monotone;*

(iii) *The resolvent of ∂g is the proximity operator of g, i.e. $\operatorname{prox}_g = J_{\partial g}$.*

Proof. (i) This is Baillon-Haddad Theorem (Baillon and Haddad, 1977).
(ii) See Rockafellar (1970). (iii) See Moreau (1965). ■

Finally, a specific case of a proximity operator is the orthognal projector onto a convex subset, whose definitions and properties are recalled here.

Definition 1.8 (indicator, orthogonal projector)**.** Let C be a nonempty, convex, closed subset of $\mathcal{H}$. The *indicator function* of C is the function $\iota_C: \mathcal{H} \to]-\infty, +\infty]$ defined for $x \in \mathcal{H}$ by

$$\iota_C(x) \stackrel{\text{def}}{=} \begin{cases} 0 & \text{if } x \in C\,, \\ +\infty & \text{otherwise}\,, \end{cases}$$

C being nonempty and convex, ι_C is proper and convex. Moreover, C being closed, every convergent sequence in C converges in C so that ι_C is lower semicontinuous. By Lemma 1.4, $\partial\iota_C$ is maximal monotone and the proximity operator of ι_C is well defined. We denote $P_C \stackrel{\text{def}}{=} \operatorname{prox}_{\iota_C}$ and $R_C \stackrel{\text{def}}{=} \operatorname{rprox}_{\iota_C}$. In some context (see next chapter), we also use the notation $\operatorname{proj}_C \stackrel{\text{def}}{=} \operatorname{prox}_{\iota_C}$.

Proposition 1.1 (orthogonal projector on a subspace)**.** *Let S be a closed convex* subspace *of $\mathcal{H}$. Then,*

(i) *P_S is linear;*

(ii) *P_S is* idempotent*, i.e. $P_S \circ P_S = P_S$.*

(iii) *P_S is* self-adjoint*, i.e. $\forall\, x, y \in \mathcal{H}, \langle P_S x \,|\, y\rangle = \langle x \,|\, P_S y\rangle$.*

Proof. See for instance Deutsch (2001, Proposition 5.13). ■

1.2 Product Space

Let $(w_i)_{1\leq i\leq n} \in]0,1]^n$ such that $\sum_{i=1}^n w_i = 1$. We consider $\mathcal{H} \overset{\text{def}}{=} \mathcal{H}^n$ endowed with the scalar product $\langle\!\langle \cdot \,|\, \cdot \rangle\!\rangle$, defined as

$$\forall\, \boldsymbol{x} \overset{\text{def}}{=} (x_i)_i, \boldsymbol{y} \overset{\text{def}}{=} (y_i)_i \in \mathcal{H}, \quad \langle\!\langle \boldsymbol{x} \,|\, \boldsymbol{y} \rangle\!\rangle = \sum_{i=1}^n w_i \langle x_i \,|\, y_i \rangle,$$

and with the corresponding norm $|\!|\!| \boldsymbol{x} |\!|\!| \overset{\text{def}}{=} \sqrt{\sum_{i=1}^n \|x_i\|^2}$. Then, $\mathcal{S} \subseteq \mathcal{H}$ denotes the closed subspace $\mathcal{S} \overset{\text{def}}{=} \left\{ \boldsymbol{x} \overset{\text{def}}{=} (x_i)_i \in \mathcal{H} \;\middle|\; \forall\, i,j,\, x_i = x_j \right\}$, whose orthogonal complement is the closed subspace $\mathcal{S}^\perp \overset{\text{def}}{=} \left\{ \boldsymbol{x} \overset{\text{def}}{=} (x_i)_i \in \mathcal{H} \;\middle|\; \sum_{i=1}^n w_i x_i = 0 \right\}$. We denote by $\mathbf{Id}$ the identity operator on $\mathcal{H}$, and we define the canonical isometry

$$\boldsymbol{C}\colon \begin{array}{ccc} \mathcal{H} & \longrightarrow & \mathcal{S}\,, \\ x & \longmapsto & (x,\dots,x)\,. \end{array}$$

We also introduce the following concatenated operators. Set B and each A_i in problem (1). Given $\boldsymbol{\gamma} = (\gamma_i)_{1\leq i\leq n} \in]0,+\infty[^n$, we define

$$\boldsymbol{\gamma}\cdot\boldsymbol{A}\colon \begin{array}{ccc} \mathcal{H} & \longrightarrow & 2^{\mathcal{H}}\,, \\ \boldsymbol{x} \overset{\text{def}}{=} (x_i)_i & \longmapsto & \times_{i=1}^n \gamma_i A_i(x_i)\,, \end{array}$$

i.e. its graph is

$$\operatorname{gra} \boldsymbol{\gamma}\cdot\boldsymbol{A} \overset{\text{def}}{=} \bigtimes_{i=1}^n \operatorname{gra} \gamma_i A_i = \left\{ (\boldsymbol{x},\boldsymbol{y}) \in \mathcal{H}^2 \;\middle|\; \forall\, i \in \{1,\dots,n\},\; y_i \in \gamma_i A_i x_i \right\}.$$

Finally, we define $\boldsymbol{B}\colon \mathcal{H} \to \mathcal{H}, \boldsymbol{x} \overset{\text{def}}{=} (x_i)_i \mapsto (Bx_i)_i$. Using the maximal monotonicity of each A_i (respectively the β-cocoercivity of B), it is an easy exercise to establish that $\boldsymbol{\gamma}\cdot\boldsymbol{A}$ is maximal monotone (respectively that $\boldsymbol{B}$ is β-cocoercive) on $\mathcal{H}$.

2 Generalized Forward-Backward Splitting

2.1 The Algorithmic Scheme

We consider problem (1) where all operators are maximal monotone, B is β-cocoercive with $\beta \in]0,+\infty[$, *i.e.*

$$\forall\, x,y \in \mathcal{H}, \quad \beta\|Bx - By\|^2 \leq \langle Bx - By \,|\, x - y \rangle\,,$$

and for all $i \in \{1,\dots,n\}$ and any $\gamma \in \mathbb{R}_{+*}$, the resolvent of γA_i, denoted $J_{\gamma A_i}$, is easy to compute. Our generalized forward-backward algorithm is detailed in Algorithm 1.

To state our main theorem that ensures the convergence of the algorithm and its robustness to summable errors, for each $i \in \{1,\dots,n\}$, let $\varepsilon_{1,k,i}$ be the error at iteration k when computing $J_{\frac{\gamma}{w_i}A_i}$, and let $\varepsilon_{2,k}$ be the error at iteration k when computing B. An

Algorithm 1 Generalized forward-backward for solving (1).

REQUIRE $(z_i)_{1\leq i\leq n} \in \mathcal{H}^n$; $(w_i)_{1\leq i\leq n} \in]0,1]^n$ s.t. $\sum_{i=1}^n w_i = 1$;
$\gamma \in]0, 2\beta[$; $\forall\, k \in \mathbb{N},\ \rho_k \in \left]0, \frac{4\beta-\gamma}{2\beta}\right[$.
INITIALIZATION $x \leftarrow \sum_{i=1}^n w_i z_i$; $k \leftarrow 0$.
repeat
  MAIN ITERATION
  for $i \in \{1, \dots, n\}$ **do**

$$z_i \leftarrow z_i + \rho_k\left(J_{\frac{\gamma}{w_i}A_i}\left(2x - z_i - \gamma Bx\right) - x\right); \tag{6}$$

  $x \leftarrow \sum_{i=1}^n w_i z_i$;
  $k \leftarrow k+1$.
until *convergence*;
RETURN x.

inexact GFB algorithm generates sequences $(z_{i,k})_{\substack{1\leq i\leq n\\ k\in\mathbb{N}}}$, and $(x_k)_{k\in\mathbb{N}}$, such that for all $i \in \{1, \dots, n\}$ and $k \in \mathbb{N}$,

$$z_{i,k+1} = z_{i,k} + \rho_k\left(J_{\frac{\gamma}{w_i}A_i}\left(2x_k - z_{i,k} - \gamma_k(Bx_k + \varepsilon_{2,k})\right) + \varepsilon_{1,k,i} - x_k\right), \tag{7}$$

where for all $k \in \mathbb{N}$, $x_k = \sum_{i=1}^n w_i z_i$.

Theorem 2.1. *Suppose that the following assumptions are satisfied:*

(i) $\operatorname{zer}\left(B + \sum_{i=1}^n A_i\right) \neq \emptyset$,

(ii) $\sum_{k\in\mathbb{N}} \rho_k\left(\frac{4\beta-\gamma}{2\beta} - \rho_k\right) = +\infty$,

(iii) $\sum_{k=0}^{+\infty} \rho_k\|\varepsilon_{2,k}\| < +\infty$, *and* $\forall\, i \in \{1, \dots, n\}$, $\sum_{k=0}^{+\infty} \rho_k\|\varepsilon_{1,k,i}\| < +\infty$.

Then the sequence $(x_k)_{k\in\mathbb{N}}$ *defined in (7) converges weakly towards a solution of (1).*
If moreover

(iv) $0 < \inf_{k\in\mathbb{N}} \rho_k \leq \sup_{k\in\mathbb{N}} \rho_k \leq 1$,

(v) *one of the following holds:*

  (1) *B is uniformly monotone,*

  (2) $\times_{i=1}^n \frac{\gamma}{w_i} A_i$ *is uniformly monotone,*

then the convergence is strong.
In addition, a sufficient condition for (2) is that for all $i \in \{1, \dots, n\}$, A_i is uniformly monotone, all with the same modulus ϕ being either subadditive or convex.

Remark 2.1. The definition of uniform monotonicity with modulus ϕ is provided in Section 1.1.

The following corollary specializes Theorem 2.1 to the case of convex optimization problems of the form (4), where all functions belong to $\Gamma_0(\mathcal{H})$, f is differentiable with ∇f being Lipschitz continuous with constant β^{-1}, $\beta \in]0, +\infty[$, and for all $i \in \{1, \dots, n\}$ and any $\gamma \in \mathbb{R}_{+*}$, the proximity operator of γg_i is easy to compute. The resulting scheme is written explicitly in Algorithm 2.

Corollary 2.1. *Let the sequence $(x_k)_{k\in\mathbb{N}}$ be defined by substituting, in (7), B with ∇f and $J_{\frac{\gamma}{w_i}A_i}$ with $\operatorname{prox}_{\frac{\gamma}{w_i}g_i}$. Suppose that*

(i) $\operatorname{argmin} F \neq \emptyset$,

that the domain condition (D), and assumptions (ii)-(iii) of Theorem 2.1 are satisfied. Then, the sequence $(x_k)_{k\in\mathbb{N}}$ converges weakly towards a minimizer of (4).
If moreover assumption (iv) of Theorem 2.1 is satisfied, and

(iv) *one of the following holds:*

(1) *f is uniformly convex,*

(2) *$\bigtimes_{i=1}^{n} \frac{\gamma}{w_i}\partial g_i$ is uniformly monotone,*

then $(x_k)_{k\in\mathbb{N}}$ converges strongly to the unique minimizer of (4).
In addition, a sufficient condition for (2) is that for all $i \in \{1, \dots, n\}$, g_i is uniformly convex, all with the same modulus ϕ being either subadditive or convex.

Remark 2.2. Recall that a function $f \in \Gamma_0(\mathcal{H})$ is uniformly convex of modulus ϕ, if $\phi\colon [0, +\infty[\to [0, +\infty]$ is a nondecreasing function that vanishes only at zero, such that for all x and y in $\operatorname{dom} f$, the following holds:

$$\forall\, t \in]0,1[,\ f(tx + (1-t)y) + t(1-t)\phi(\|x-y\|) \leq tf(x) + (1-t)f(y)\ .$$

The proofs are detailed in § 3. The formulations of Algorithms 1 and 2 are general, but they can be simplified for practical purposes. In particular, the auxiliary variables z_i can all be initialized to 0, the weights w_i set equally to $1/n$, and the relaxation parameters ρ_k can be set to 1, constant along iterations. See also next chapter, § IV.4, for important implementation considerations.

2.2 Special Instances

Our GFB algorithm can be viewed as a hybrid splitting algorithm whose special instances turn out to be classical splitting methods; namely the forward-backward and Douglas-Rachford algorithms.

Relaxed forward-backward. For $n \overset{\text{set}}{=} 1$, the core update operator (6) of Algorithm 1 specializes to

$$x \leftarrow x + \rho_k\big(J_{\gamma A}(x - \gamma Bx) - x\big)\ ,$$

so that x_k given by (7) follows the iterations of the relaxed forward-backward algorithm (Combettes, 2004, Section 6). In this case, convergence can be ensured with step size γ

varying along iterations. For convex minimization problems, known results on convergence rate analysis (on the objective in general) and accelerated versions of the forward-backward algorithm (Beck and Teboulle, 2009; Bredies and Lorenz, 2008; Nesterov, 2013) might be inspiring to study those of our GFB.

Relaxed Douglas-Rachford. If we set $B \overset{\text{set}}{=} 0$, the update of the auxiliary variables in (6) becomes

$$z_i \leftarrow z_i + \rho_k \left(J_{\frac{\gamma}{w_i} A_i} \left(2x - z_i \right) - x \right) ,$$

so that $(z_{i,k})_{i,k}$ given by (7) follows the iterations of the relaxed Douglas-Rachford algorithm on the product space $\mathcal{H}^n$ for solving $0 \in \sum_{i=1}^n A_i x$ (Spingarn, 1983; Combettes and Pesquet, 2008). Interestingly, $B \overset{\text{def}}{=} 0$ is β-cocoercive for any $\beta \in \mathbb{R}_{+*}$. Setting $\gamma \in \mathbb{R}_{+*}$, observe that $\lim_{\beta \to \infty} \frac{4\beta - \gamma}{2\beta} = 2$. One retrieves at the limit the known conditions on the relaxation parameters ρ_k for the relaxed Douglas-Rachford algorithm, namely $\forall\, k \in \mathbb{N},\ \rho_k \in]0, 2[$ and $\sum_{k \in \mathbb{N}} \rho_k (2 - \rho_k) = +\infty$.

Resolvent of the sum of monotone operators. Our GFB scheme provides yet another way for computing the resolvent of the sum of maximal monotone operators $(A_i)_i$. Given a point $y \in \operatorname{ran} (\operatorname{Id} + \sum_{i=1}^n A_i)$, simply consider (1) with $B : x \mapsto x - y$ and $\beta \overset{\text{set}}{=} 1$. It would be interesting to compare this algorithm with the Douglas-Rachford and Dykstra-based variants (Combettes, 2009); this is left to a future work.

2.3 Comparison to Other Works

We make here a comparison of our GFB algorithm to the other proximal splitting algorithms in the literature allowing to solve (4), by computing only proximity operators of each individual g_i and the gradient of f. Each of those algorithms are summed up in Figure 1. Recall that ∇f is supposed to be β^{-1}-Lipschitz continuous. In addition, for Algorithms 3 and 4, each $g_i \in \Gamma_0(\mathcal{H}_i)$ is composed with a linear operator $L_i : \mathcal{H} \to \mathcal{H}_i$, and we define $\mathcal{G} \overset{\text{def}}{=} \bigtimes_{i=1}^n \mathcal{H}_i$ and $n_L \overset{\text{def}}{=} \| \sum_{i=1}^n L_i^* L_i \|$. Also, g_i^* denotes the *Legendre-Fenchel conjugate* of g_i; recall that the proximity operator of g_i^* can be easily deduced from the one of g_i, using Moreau's identity (Moreau, 1965). Finally, for Algorithms 2 and 5, the weights $(w_i)_{1 \le i \le n} \in]0, 1]^n$ are such that $\sum_{i=1}^n w_i = 1$.

Each algorithm has been simplified and rewritten according to our setting, and we identified the parameters that played analogous roles. This enables the comparison of their allowed range, which are further illustrated in the numerical experiments presented within the next chapter.

Relation to Combettes and Pesquet (2012). These authors developed an algorithm to solve a general class of problems that covers (1). They rely on the classical Kuhn-Tucker theory and propose a primal-dual splitting algorithm for solving monotone inclusions involving a mixture of sums, linear compositions, and parallel sums (inf-convolution in convex optimization) of set-valued and Lipschitzian operators. More precisely, the authors exploit the fact that the primal and dual problems have a similar structure, cast

Algorithm 2 Generalized forward-backward for solving (4).

Require $(z_i)_{1\leq i\leq n} \in \mathcal{H}^n$; $\gamma \in]0, 2\beta[$; $\forall\, k \in \mathbb{N}$, $\rho_k \in \left]0, \frac{4\beta-\gamma}{2\beta}\right[$.

Main Iteration

for $i \in \{1, \dots, n\}$ **do**

$z_i \leftarrow z_i + \rho_k\Big(\operatorname{prox}_{\frac{\gamma}{w_i} g_i}\big(2x - z_i - \gamma\nabla f(x)\big) - x\Big)$;

$x \leftarrow \sum_{i=1}^n w_i z_i$.

Algorithm 3 Primal-dual of Combettes and Pesquet (2012).

Require $x \in \mathcal{H}$; $(v_i)_{1\leq i\leq n} \in \mathcal{G}$; $0 < \inf_{k\in\mathbb{N}} \gamma_k \leq \sup_{k\in\mathbb{N}} \gamma_k < \frac{\beta}{1+\beta\sqrt{\sum_{i=1}^n \|L_i\|^2}}$.

Main Iteration

$\xi \leftarrow x - \gamma_k(\nabla f(x) + \sum_{i=1}^n L_i^* v_i)$;

for $i \in \{1, \dots, n\}$ **do**

$u_i \leftarrow \operatorname{prox}_{\gamma_k g_i^*}(v_i + \gamma_k L_i x)$;

$v_i \leftarrow u_i + \gamma_k L_i(\xi - x)$;

$x \leftarrow x - \gamma_k(\nabla f(\xi) + \sum_{i=1}^n L_i^* u_i)$.

Algorithm 4 Primal-dual of Condat (2013) and Vũ (2013).

Require $x \in \mathcal{H}$; $(v_i)_{1\leq i\leq n} \in \mathcal{G}$; $0 < \frac{\gamma}{1-n_L\gamma\varsigma} \leq 2\beta$; $\rho_k \in \left]0, 2 - \frac{1}{2\beta}\frac{\gamma}{1-n_L\gamma\varsigma}\right[$.

Main Iteration

$\xi \leftarrow x - \gamma_k(\nabla f(x) + \sum_{i=1}^n L_i^* v_i)$;

for $i \in \{1, \dots, n\}$ **do**

$v_i \leftarrow v_i + \rho_k\Big(\operatorname{prox}_{\varsigma g_i^*}\big(v_i + \varsigma L_i(2\xi - x)\big) - v_i\Big)$;

$x \leftarrow x + \rho_k(\xi - x)$.

Algorithm 5 Block-decomposition HPE of Monteiro and Svaiter (2013).

Require $(z_i)_{1\leq i\leq n} \in \mathcal{H}^n$; $(v_i)_{1\leq i\leq n} \in \mathcal{H}^n$; $\varsigma \in]0, 1]$; $\gamma = \varsigma\frac{2\varsigma\beta}{1+\sqrt{1+4\varsigma^2\beta^2}}$.

Main Iteration

for $i \in \{1, \dots, n\}$ **do**

$z_i \leftarrow \operatorname{prox}_{\frac{\gamma}{w_i} g_i}\big(\gamma^2 x + (1-\gamma^2)z_i - \gamma\nabla f(x) + \gamma(v_i - u)\big)$;

$v_i \leftarrow v_i + \gamma(x - z_i)$;

$x \leftarrow \sum_{i=1}^n w_i z_i$;

$u \leftarrow \sum_{i=1}^n w_i v_i$.

Figure 1: Proximal splitting algorithms for solving (4). See § 2.3 for details.

the problem as finding a zero of the sum of a Lipschitz continuous monotone map with a maximal monotone operator whose resolvent is easy to compute. They solve the corresponding monotone inclusion using an inexact version of Tseng's forward-backward-forward splitting algorithm (Tseng, 2000).

Removing the parallel sum and setting each involved linear operators as the identity, Combettes and Pesquet (2012, (1.1)) reduces to problem (1). For the sake of simplicity and space saving we do not reproduce here in full their algorithm. However, we present their scheme adapted to the optimization problem $\min_{x\in\mathcal{H}} \left\{ f(x) + \sum_{i=1}^{n} g_i(L_i x) \right\}$, where for each i, $L_i \colon \mathcal{H} \to \mathcal{H}_i$ is a bounded linear operator and g_i belongs to $\Gamma_0(\mathcal{H}_i)$, for some real Hilbert space $\mathcal{H}_i$. Taking $L_i \overset{\text{set}}{=} \mathrm{Id}$ in Algorithm 3 solves (4).

Note that in their scheme, our cocoercivity assumption is relaxed to a Lipschitzianity assumption, but for the application to convex optimization those assumptions are equivalent, by Baillon-Haddad Theorem. While we solve the primal problem, their algorithm solves both the primal and dual ones. Moreover, it allows the step size γ to vary along iterations. However, this step size is bounded by a smaller constant than ours, which scales as $\frac{1}{\sqrt{n}}$, *i.e.* the inverse of the square root of the number of simple functions in the splitting. Note also that it requires two calls to ∇f (and to L_i^*) per iteration; this may significantly increase the computational load of the algorithm.

Relation to Condat (2013) and Vũ (2013). These authors independently developed primal-dual algorithms that solves a similar problem to the one of Combettes and Pesquet (2012). They also use a similar approach, but requires cocoercivity of the Lipschitzian operator and solve the resulting monotone inclusion with an inexact forward-backward algorithm on an appropriate augmented space with a nondiagonal metric. Such a renorming technique was first introduced in He and Yuan (2012) for convergence analysis of relaxations of the Arrow-Hurwicz method (Arrow *et al.*, 1958). The extension of Condat (2013) takes into account a cocoercive operator; on top of that, Vũ (2013) deals with parallel sums. Note that, though very close, the two algorithms are not exactly equivalent, and does not have the same assumptions on the parameters. We show here the version of Condat (2013), which seems to allow slightly better bounds on the explicit step size γ and implicit step size ς. Note that setting $\varsigma \overset{\text{set}}{=} \gamma$, the condition becomes $\gamma \leq \frac{\sqrt{1+16\beta^2 n_L}-1}{4\beta n_L}$, which scales again as $\frac{1}{\sqrt{n}}$.

Relation to Monteiro and Svaiter (2013). Monteiro and Svaiter (2013, Section 5.3, (51)) describe an instance of the *block-decomposition hybrid proximal extragradient* (BD-HPE) for minimizing $F \overset{\text{set}}{=} f + g$ under linear constraints. Our problem (4) can be cast in an equivalent linearly constrained convex programming over $\boldsymbol{\mathcal{H}} \overset{\text{def}}{=} \mathcal{H}^n$, as

$$\min_{\boldsymbol{z}\in\boldsymbol{\mathcal{H}}} f\left(\textstyle\sum_i w_i \boldsymbol{z}_i\right) + \displaystyle\sum_{i=1}^{n} g_i(\boldsymbol{z}_i) \quad \text{such that} \quad P_{\mathcal{S}^\perp}(\boldsymbol{z}) = \boldsymbol{0}\,,$$

where $P_{\mathcal{S}^\perp}$ is the orthogonal projector on the subspace $\mathcal{S}^\perp$ defined in 1.2. As $P_{\mathcal{S}^\perp}$ is self-adjoint, $\boldsymbol{z}$ is an optimal solution if, and only if, there exists $\boldsymbol{v} \in \boldsymbol{\mathcal{H}}$ such that

$$\boldsymbol{0} \in \left(\nabla f\left(\textstyle\sum_j w_j \boldsymbol{z}_j\right)\right)_i + \left(\partial g_i(\boldsymbol{z}_i)/w_i\right)_i + P_{\mathcal{S}^\perp}(\boldsymbol{v}) \quad \text{and} \quad P_{\mathcal{S}^\perp}(\boldsymbol{z}) = \boldsymbol{0}\,,$$

and a minimizer of F is given by $x = \sum_{i=1}^{n} w_i z_i$.

In the resulting iterations the gradient step size γ is bounded by 1, which is penalizing for large values of β. Moreover, it seems necessary to keep track of two sets of auxiliary variables; this may significantly increase the memory load of the algorithm.

When publishing our work, it was claimed by an anonymous reviewer that another application of the BD-HPE, more adapted to our specific problem, leads to the iterations (7) with no under- nor over-relaxation, *i.e.* $\forall\, k \in \mathbb{N},\ \rho_k = 1$. We would like to mention here that the provided proof was incorrect, and deriving the GFB algorithm from the HPE framework seems nontrivial to us.

3 Convergence Proofs

This section is devoted to the convergence proof of the GFB, detailed in two steps. First, we derive an equivalent *fixed point equation* satisfied by any solution of (1). From this, we draw an algorithmic scheme equivalent to GFB and establish its convergence properties and its robustness to summable errors.

3.1 Fixed Point Equation

Now that we have all necessary material, let us characterize the solutions of (1).

Proposition 3.1. *For any $\gamma \in \mathbb{R}_{+*}$, $x \in \mathcal{H}$ is a solution of (1) if and only if there exists $(z_i)_{1\leq i\leq n} \in \mathcal{H}^n$ such that*

$$\begin{cases} \forall\, i \in \{1,\dots,n\},\ z_i = R_{\frac{\gamma}{w_i}A_i}(2x - z_i - \gamma Bx) - \gamma Bx\ , \\ x = \displaystyle\sum_i w_i z_i\ . \end{cases} \tag{8}$$

Proof. Set $\gamma \in \mathbb{R}_{+*}$, we have the equivalence

$$0 \in Bx + \sum_{i=1}^{n} A_i x \quad \Leftrightarrow \quad \exists\, (z_i)_i \in \mathcal{H}^n,\ \begin{cases} \forall\, i,\ w_i(x - z_i - \gamma Bx) \in \gamma A_i x\ , \\ x = \sum_{i=1}^{n} w_i z_i\ . \end{cases}$$

Now,

$$\begin{aligned} w_i(x - z_i - \gamma Bx) \in \gamma A_i x \quad &\Leftrightarrow \quad (2x - z_i - \gamma Bx) - x \in \frac{\gamma}{w_i} A_i x\ , \\ \text{(by Lemma 1.2 (i) } \Leftrightarrow \text{ (iv))} \quad &\Leftrightarrow \quad x = J_{\frac{\gamma}{w_i}A_i}(2x - z_i - \gamma Bx)\ , \\ &\Leftrightarrow \quad 2x - (2x - z_i) = 2J_{\frac{\gamma}{w_i}A_i}(2x - z_i - \gamma Bx) \\ &\qquad\qquad - (2x - z_i - \gamma Bx) - \gamma Bx\ , \\ &\Leftrightarrow \quad z_i = R_{\frac{\gamma}{w_i}A_i}(2x - z_i - \gamma Bx) - \gamma Bx\ . \quad \blacksquare \end{aligned}$$

Before formulating our fixed point equation, we need the following preparatory lemma.

Lemma 3.1. *Let* $\boldsymbol{z} \overset{\text{def}}{=} (z_i)_i \in \mathcal{H}$, $\boldsymbol{b} \in \mathcal{S}$, *and* $\boldsymbol{\gamma} = (\gamma_i)_i \in]0, +\infty[^n$. *Then,*

(i) $P_{\mathcal{S}}(\boldsymbol{z}) = \boldsymbol{C}\big(\sum_{i=1}^n w_i z_i\big)$;

(ii) $R_{\mathcal{S}}(\boldsymbol{z} - \boldsymbol{b}) = R_{\mathcal{S}}\boldsymbol{z} - \boldsymbol{b}$;

(iii) $R_{\boldsymbol{\gamma}\cdot\boldsymbol{A}}\boldsymbol{z} = \big(R_{\gamma_i A_i}(z_i)\big)_i$.

Proof. (i). $P_{\mathcal{S}}(\boldsymbol{z}) = \operatorname{argmin}_{\boldsymbol{y}\in\mathcal{S}} \|\boldsymbol{z} - \boldsymbol{y}\|^2 = \boldsymbol{C}\big(\operatorname{argmin}_{y\in\mathcal{H}} \sum_i w_i \|z_i - y\|^2\big)$. Now, the functional $y \mapsto \sum_i w_i \|z_i - y\|^2$ has gradient $y \mapsto 2\sum_i w_i(y - z_i) = 2(y - \sum_i w_i z_i)$. The result follows from Lemma 1.3 (i)-(ii). (ii). $P_{\mathcal{S}}$ is obviously linear and so is $R_{\mathcal{S}}$. Since $\boldsymbol{b} \in \mathcal{S}$, $R_{\mathcal{S}}\boldsymbol{b} = \boldsymbol{b}$ and the result follows. (iii). By separability of $\boldsymbol{\gamma}\cdot\boldsymbol{A}$ in terms of the components of $\boldsymbol{z}$, we have $J_{\boldsymbol{\gamma}\cdot\boldsymbol{A}}\boldsymbol{z} = \big(J_{\gamma_i A_i} z_i\big)_i$, and then $R_{\boldsymbol{\gamma}\cdot\boldsymbol{A}}\boldsymbol{z} = \big(R_{\gamma_i A_i}(z_i)\big)_i$. ∎

In the sequel, we denote the set of *fixed points* of an operator $\boldsymbol{T}\colon \mathcal{H} \to \mathcal{H}$ by $\operatorname{fix} \boldsymbol{T} \overset{\text{def}}{=} \{\boldsymbol{z} \in \mathcal{H} \mid \boldsymbol{T}\boldsymbol{z} = \boldsymbol{z}\}$.

Proposition 3.2. $(z_i)_{1\le i\le n} \in \mathcal{H}^n$ *satisfies (8) if and only if* $\boldsymbol{z} \overset{\text{def}}{=} (z_i)_i$ *is a fixed point of the following operator*

$$\begin{array}{rcl} \mathcal{H} & \longrightarrow & \mathcal{H} \\ \boldsymbol{z} & \longmapsto & \frac{1}{2}\big[R_{\boldsymbol{\gamma}\cdot\boldsymbol{A}} R_{\mathcal{S}} + \mathbf{Id}\big]\big[\mathbf{Id} - \gamma \boldsymbol{B} P_{\mathcal{S}}\big](\boldsymbol{z})\,, \end{array} \tag{9}$$

with $\boldsymbol{\gamma} = \big(\frac{\gamma}{w_i}\big)_i$.

Proof. Using Lemma 3.1 in (8), we have $P_{\mathcal{S}}\boldsymbol{z} = \boldsymbol{C}(x)$, $\boldsymbol{B}P_{\mathcal{S}}(\boldsymbol{z}) = \boldsymbol{C}(B\boldsymbol{x})$ and $R_{\mathcal{S}} - \gamma\boldsymbol{B}P_{\mathcal{S}} = R_{\mathcal{S}}[\mathbf{Id} - \gamma\boldsymbol{B}P_{\mathcal{S}}]$. Altogether, this yields,

$$\begin{aligned} \boldsymbol{z} \text{ satisfies (8)} \quad &\Leftrightarrow \quad \boldsymbol{z} = R_{\boldsymbol{\gamma}\cdot\boldsymbol{A}} R_{\mathcal{S}}\big[\mathbf{Id} - \gamma\boldsymbol{B}P_{\mathcal{S}}\big]\boldsymbol{z} - \gamma\boldsymbol{B}P_{\mathcal{S}}\boldsymbol{z} \\ &\Leftrightarrow \quad 2\boldsymbol{z} = R_{\boldsymbol{\gamma}\cdot\boldsymbol{A}} R_{\mathcal{S}}\big[\mathbf{Id} - \gamma\boldsymbol{B}P_{\mathcal{S}}\big]\boldsymbol{z} + \big[\mathbf{Id} - \gamma\boldsymbol{B}P_{\mathcal{S}}\big]\boldsymbol{z} \\ &\Leftrightarrow \quad \boldsymbol{z} = \tfrac{1}{2}\big[R_{\boldsymbol{\gamma}\cdot\boldsymbol{A}} R_{\mathcal{S}} + \mathbf{Id}\big]\big[\mathbf{Id} - \gamma\boldsymbol{B}P_{\mathcal{S}}\big]\boldsymbol{z}\,. \quad ∎ \end{aligned}$$

3.2 Properties of the Fixed Point Operator

Expression (9) gives us the operator on which is based our GFB scheme. We first study the properties of this operator that will play a crucial role in the convergence proof.

Proposition 3.3. *For any* $\boldsymbol{\gamma} \in]0, +\infty[^n$, *define*

$$\boldsymbol{T}_{1,\boldsymbol{\gamma}}\colon \begin{array}{rcl} \mathcal{H} & \longrightarrow & \mathcal{H} \\ \boldsymbol{z} & \longmapsto & \frac{1}{2}\big[R_{\boldsymbol{\gamma}\cdot\boldsymbol{A}} R_{\mathcal{S}} + \mathbf{Id}\big]\boldsymbol{z}\,. \end{array} \tag{10}$$

Then, $\boldsymbol{T}_{1,\boldsymbol{\gamma}}$ *is firmly nonexpansive, i.e.* $\boldsymbol{T}_{1,\boldsymbol{\gamma}} \in \mathcal{A}\big(\frac{1}{2}\big)$.

Proof. From Lemma 1.2 (i) ⇔ (ii), $R_{\gamma_i A_i}$ and $R_{\mathcal{S}}$ are nonexpansive, and so is $R_{\boldsymbol{\gamma}\cdot\boldsymbol{A}}$ in view of Lemma 3.1 (iii). Finally, as a composition of nonexpansive operators, $R_{\boldsymbol{\gamma}\cdot\boldsymbol{A}}R_{\mathcal{S}}$ is also nonexpansive, and the proof is complete by definition of $\mathcal{A}\left(\frac{1}{2}\right)$. ∎

Proposition 3.4. *For any $\gamma \in]0, 2\beta[$, define*

$$\boldsymbol{T}_{2,\gamma}\colon \begin{array}{ccc} \mathcal{H} & \longrightarrow & \mathcal{H} \\ \boldsymbol{z} & \longmapsto & [\mathbf{Id} - \gamma \boldsymbol{B} P_{\mathcal{S}}]\,\boldsymbol{z}\,. \end{array} \tag{11}$$

Then, $\boldsymbol{T}_{2,\gamma} \in \mathcal{A}\left(\frac{\gamma}{2\beta}\right)$.

Proof. By hypothesis $\beta B \in \mathcal{A}\left(\frac{1}{2}\right)$, hence $\beta\boldsymbol{B} \in \mathcal{A}\left(\frac{1}{2}\right)$. Then for $\boldsymbol{x}, \boldsymbol{y} \in \mathcal{H}$,

$$\begin{aligned} \left\langle \beta\boldsymbol{B}P_{\mathcal{S}}\boldsymbol{x} - \beta\boldsymbol{B}P_{\mathcal{S}}\boldsymbol{y} \,\middle|\, \boldsymbol{x} - \boldsymbol{y} \right\rangle &= \left\langle \beta P_{\mathcal{S}}\boldsymbol{B}P_{\mathcal{S}}\boldsymbol{x} - \beta P_{\mathcal{S}}\boldsymbol{B}P_{\mathcal{S}}\boldsymbol{y} \,\middle|\, \boldsymbol{x} - \boldsymbol{y} \right\rangle, \\ &= \left\langle \beta\boldsymbol{B}P_{\mathcal{S}}\boldsymbol{x} - \beta\boldsymbol{B}P_{\mathcal{S}}\boldsymbol{y} \,\middle|\, P_{\mathcal{S}}\boldsymbol{x} - P_{\mathcal{S}}\boldsymbol{y} \right\rangle, \\ &\geq \left\| \beta\boldsymbol{B}P_{\mathcal{S}}\boldsymbol{x} - \beta\boldsymbol{B}P_{\mathcal{S}}\boldsymbol{y} \right\|^2, \end{aligned}$$

where we derive the first equality using the fact that $\boldsymbol{B}P_{\mathcal{S}}\boldsymbol{x} \in \mathcal{S}$, the second equality from Proposition 1.1, and the inequality from Lemma 1.2 (i) ⇔ (iii). The same lemma proves that $\beta\boldsymbol{B}P_{\mathcal{S}} \in \mathcal{A}\left(\frac{1}{2}\right)$, and Lemma 1.1 (i) terminates the proof. ∎

Proposition 3.5. *For all $\boldsymbol{\gamma} \in]0, +\infty[^n$ and $\gamma \in]0, 2\beta[$, $\boldsymbol{T}_{1,\boldsymbol{\gamma}}\boldsymbol{T}_{2,\gamma} \in \mathcal{A}(\alpha)$, with $\alpha = \frac{2\beta}{4\beta-\gamma}$.*

Proof. Combine Propositions 3.3 and 3.4 in Lemma 1.1 (iii). ∎

The following proposition defines a maximal monotone operator $\boldsymbol{A}'_{\boldsymbol{\gamma}}$ which will be useful for characterizing the operator $\boldsymbol{T}_{1,\boldsymbol{\gamma}}$.

Proposition 3.6. *For all $\boldsymbol{\gamma} \in]0, +\infty[^n$ there exists a maximal monotone operator $\boldsymbol{A}'_{\boldsymbol{\gamma}}$ such that $\boldsymbol{T}_{1,\boldsymbol{\gamma}} = J_{\boldsymbol{A}'_{\boldsymbol{\gamma}}}$. Moreover for all $\gamma \in \mathbb{R}_{+*}$,*

$$\boldsymbol{y} = \boldsymbol{T}_{1,\boldsymbol{\gamma}}\boldsymbol{T}_{2,\gamma}\boldsymbol{z} \Leftrightarrow \boldsymbol{z} - \boldsymbol{y} - \gamma\boldsymbol{B}P_{\mathcal{S}}\boldsymbol{z} \in \boldsymbol{A}'_{\boldsymbol{\gamma}}\boldsymbol{y}\,.$$

In particular,

$$\operatorname{fix} \boldsymbol{T}_{1,\boldsymbol{\gamma}}\boldsymbol{T}_{2,\gamma} = \operatorname{zer}\left(\boldsymbol{A}'_{\boldsymbol{\gamma}} + \gamma\boldsymbol{B}P_{\mathcal{S}}\right).$$

Proof. The existence of $\boldsymbol{A}'_{\boldsymbol{\gamma}}$ is provided by Proposition 3.3 and Lemma 1.2 (i) ⇔ (iv). Then for any $\boldsymbol{y}, \boldsymbol{z} \in \mathcal{H}$,

$$\begin{aligned} \boldsymbol{y} = \boldsymbol{T}_{1,\boldsymbol{\gamma}}\boldsymbol{T}_{2,\gamma}\boldsymbol{z} &\Leftrightarrow \boldsymbol{y} = \left(\mathbf{Id} + \boldsymbol{A}'_{\boldsymbol{\gamma}}\right)^{-1}\left(\mathbf{Id} - \gamma\boldsymbol{B}P_{\mathcal{S}}\right)\boldsymbol{z} \\ &\Leftrightarrow \boldsymbol{z} - \gamma\boldsymbol{B}P_{\mathcal{S}}\boldsymbol{z} - \boldsymbol{y} \in \boldsymbol{A}'_{\boldsymbol{\gamma}}\boldsymbol{y}\,. \end{aligned}$$

Taking $\boldsymbol{y} \overset{\text{set}}{=} \boldsymbol{z}$ proves the second statement. ∎

Now, let us examine the properties of $\boldsymbol{A}'_{\boldsymbol{\gamma}}$. For brevity, we denote for any $\boldsymbol{z} \in \mathcal{H}$, $\boldsymbol{z}^{\mathcal{S}} \overset{\text{def}}{=} P_{\mathcal{S}}(\boldsymbol{z})$ and $\boldsymbol{z}^{\perp} \overset{\text{def}}{=} P_{\mathcal{S}^{\perp}}(\boldsymbol{z})$.

Proposition 3.7. *For all* $\boldsymbol{\gamma} \in \left]0,+\infty\right[^n$ *and* $(\boldsymbol{y},\boldsymbol{z}) \in \mathcal{H}^2$

$$\boldsymbol{y} \in A'_{\boldsymbol{\gamma}}\boldsymbol{z} \Leftrightarrow \boldsymbol{y}^{\mathcal{S}} - \boldsymbol{z}^{\perp} \in \boldsymbol{\gamma}\cdot A\big(\boldsymbol{z}^{\mathcal{S}} - \boldsymbol{y}^{\perp}\big)\,.$$

Proof. First of all, by definition of $\boldsymbol{T}_{1,\boldsymbol{\gamma}}$ we have

$$\begin{aligned}
\boldsymbol{T}_{1,\boldsymbol{\gamma}} &= \tfrac{1}{2}\Big[\big(2J_{\boldsymbol{\gamma}\cdot A} - \mathbf{Id}\big)(2P_{\mathcal{S}} - \mathbf{Id}) + \mathbf{Id}\Big]\,,\\
&= \tfrac{1}{2}\Big[2J_{\boldsymbol{\gamma}\cdot A}(P_{\mathcal{S}} - P_{\mathcal{S}^\perp}) - (P_{\mathcal{S}} - P_{\mathcal{S}^\perp}) + P_{\mathcal{S}} + P_{\mathcal{S}^\perp}\Big]\,,\\
&= J_{\boldsymbol{\gamma}\cdot A}(P_{\mathcal{S}} - P_{\mathcal{S}^\perp}) + P_{\mathcal{S}^\perp}\,. \qquad (12)
\end{aligned}$$

Therefore,

$$\begin{aligned}
\boldsymbol{y} \in A'_{\boldsymbol{\gamma}}\boldsymbol{z} &\Leftrightarrow \boldsymbol{T}_{1,\boldsymbol{\gamma}}(\boldsymbol{y}+\boldsymbol{z}) = \boldsymbol{z}\,,\\
\text{(by (12))} &\Leftrightarrow J_{\boldsymbol{\gamma}\cdot A}\big((\boldsymbol{y}+\boldsymbol{z})^{\mathcal{S}} - (\boldsymbol{y}+\boldsymbol{z})^{\perp}\big) = \boldsymbol{z} - (\boldsymbol{y}+\boldsymbol{z})^{\perp} = \boldsymbol{z}^{\mathcal{S}} - \boldsymbol{y}^{\perp}\,,\\
&\Leftrightarrow (\boldsymbol{y}+\boldsymbol{z})^{\mathcal{S}} - (\boldsymbol{y}+\boldsymbol{z})^{\perp} - \boldsymbol{z}^{\mathcal{S}} + \boldsymbol{y}^{\perp} \in \boldsymbol{\gamma}\cdot A\big(\boldsymbol{z}^{\mathcal{S}} - \boldsymbol{y}^{\perp}\big)\,,\\
&\Leftrightarrow \boldsymbol{y}^{\mathcal{S}} - \boldsymbol{z}^{\perp} \in \boldsymbol{\gamma}\cdot A\big(\boldsymbol{z}^{\mathcal{S}} - \boldsymbol{y}^{\perp}\big)\,. \quad \blacksquare
\end{aligned}$$

3.3 Convergence

We are now ready to state the main convergence result of our relaxed and inexact GFB splitting algorithm (7) for solving (1).

Theorem 3.1. *Let* $\gamma \in \left]0, 2\beta\right[$, *and set* $\boldsymbol{\gamma} = \left(\frac{\gamma}{w_i}\right)_i \in \left]0,+\infty\right[^n$,
let $(\rho_k)_{k\in\mathbb{N}}$ *be a sequence in* $\left]0, \frac{4\beta-\gamma}{2\beta}\right[$,
let $(\boldsymbol{\varepsilon}_{1,k})_{k\in\mathbb{N}}$ *and* $(\boldsymbol{\varepsilon}_{2,k})_{k\in\mathbb{N}}$ *be sequences in* $\mathcal{H}$,
set $\boldsymbol{z}_0 \in \mathcal{H}$, *and for every* $k \in \mathbb{N}$, *set*

$$\boldsymbol{z}_{k+1} = \boldsymbol{z}_k + \rho_k\Big(\boldsymbol{T}_{1,\boldsymbol{\gamma}}\Big(\boldsymbol{T}_{2,\gamma}\boldsymbol{z}_k + \boldsymbol{\varepsilon}_{2,k}\Big) + \boldsymbol{\varepsilon}_{1,k} - \boldsymbol{z}_k\Big)\,, \qquad (13)$$

where $\boldsymbol{T}_{1,\boldsymbol{\gamma}}$ *and* $\boldsymbol{T}_{2,\gamma}$ *are respectively defined in (10) and (11). If the following conditions are satisfied*

(i) $\operatorname{zer}\Big(B + \sum_{i=1}^n A_i\Big) \neq \emptyset$,

(ii) $\sum_{k\in\mathbb{N}} \rho_k\Big(\frac{4\beta-\gamma}{2\beta} - \rho_k\Big) = +\infty$,

(iii) $\sum_{k=0}^{+\infty} \rho_k\|\boldsymbol{\varepsilon}_{1,k}\| < +\infty$ *and* $\sum_{k=0}^{+\infty} \rho_k\|\boldsymbol{\varepsilon}_{2,k}\| < +\infty$,

then

(a) $\big(\boldsymbol{T}_{1,\boldsymbol{\gamma}}\boldsymbol{T}_{2,\gamma}\boldsymbol{z}_k - \boldsymbol{z}_k\big)_{k\in\mathbb{N}}$ *converges strongly to* 0,

(b) $(\boldsymbol{z}_k)_{k\in\mathbb{N}}$ *converges weakly to a point* $\boldsymbol{z} \in \operatorname{fix}\boldsymbol{T}_{1,\boldsymbol{\gamma}}\boldsymbol{T}_{2,\gamma}$,

(c) $\left(x_k \overset{\text{def}}{=} \sum_{i=1}^n w_i z_{i,k}\right)_{k\in\mathbb{N}}$ *converges weakly to* $x \overset{\text{def}}{=} \sum_{i=1}^n w_i z_i$, *with* $x \in \operatorname{zer}\left(B + \sum_{i=1}^n A_i\right)$.

If moreover

(iv) $0 < \inf_{k\in\mathbb{N}} \rho_k \leq \sup_{k\in\mathbb{N}} \rho_k \leq 1$,

(v) *one of the following holds:*

(1) B *is uniformly monotone,*

(2) $\boldsymbol{\gamma\cdot A}$ *is uniformly monotone,*

then

(d) $(x_k)_{k\in\mathbb{N}}$ *converges strongly to* x.

In addition, a sufficient condition for (2) *is that for all* $i \in \{1,\dots,n\}$, A_i *is uniformly monotone, all with the same modulus* ϕ *being either subadditive or convex.*

Proof. (a)-(b). Denoting $\boldsymbol{T} \overset{\text{def}}{=} \boldsymbol{T}_{1,\gamma}\boldsymbol{T}_{2,\gamma}$ and $\alpha \overset{\text{def}}{=} \frac{2\beta}{4\beta-\gamma}$, Proposition 3.5 shows that there exists $\boldsymbol{R}$ nonexpansive such that $\boldsymbol{T} = (1-\alpha)\mathbf{Id} + \alpha\boldsymbol{R}$. Then, we have for all $k \in \mathbb{N}$,

$$\begin{aligned}\boldsymbol{z}_{k+1} &= \boldsymbol{z}_k + \rho_k\left(\alpha\boldsymbol{R}\boldsymbol{z}_k + \boldsymbol{T}_{1,\gamma}\left(\boldsymbol{T}_{2,\gamma}\boldsymbol{z}_k + \boldsymbol{\varepsilon}_{2,k}\right) + \boldsymbol{\varepsilon}_{1,k} - \boldsymbol{z}_k - \alpha\boldsymbol{R}\boldsymbol{z}_k\right),\\ &= \boldsymbol{z}_k + \mu_k\left(\boldsymbol{R}\boldsymbol{z}_k + \boldsymbol{\varepsilon}_k - \boldsymbol{z}_k\right),\end{aligned}$$

where $\mu_k \overset{\text{def}}{=} \rho_k\alpha$ and $\boldsymbol{\varepsilon}_k \overset{\text{def}}{=} \frac{1}{\alpha}\left(\boldsymbol{T}_{1,\gamma}\left(\boldsymbol{T}_{2,\gamma}\boldsymbol{z}_k + \boldsymbol{\varepsilon}_{2,k}\right) + \boldsymbol{\varepsilon}_{1,k} - (1-\alpha)\boldsymbol{z}_k - \alpha\boldsymbol{R}\boldsymbol{z}_k\right)$. Injecting $\alpha\boldsymbol{R} = \boldsymbol{T} - (1-\alpha)\mathbf{Id}$ gives $\boldsymbol{\varepsilon}_k = \frac{1}{\alpha}\left(\boldsymbol{T}_{1,\gamma}\left(\boldsymbol{T}_{2,\gamma}\boldsymbol{z}_k + \boldsymbol{\varepsilon}_{2,k}\right) + \boldsymbol{\varepsilon}_{1,k} - \boldsymbol{T}_{1,\gamma}\boldsymbol{T}_{2,\gamma}\boldsymbol{z}_k\right)$. By hypothesis, for all $k \in \mathbb{N}$, $\rho_k \in \left]0, \frac{1}{\alpha}\right[$ so that $\mu_k \in]0,1[$. Moreover, condition (ii) provides $\sum_{k\in\mathbb{N}} \rho_k\left(\frac{1}{\alpha} - \rho_k\right) = \sum_{k\in\mathbb{N}} \mu_k(1-\mu_k) = +\infty$. Then, 3.3 shows that $\boldsymbol{T}_{1,\gamma}$ is firmly nonexpansive and in particular nonexpansive, so that for all $k \in \mathbb{N}$, $\|\boldsymbol{\varepsilon}_k\| \leq \frac{1}{\alpha}(\|\boldsymbol{\varepsilon}_{1,k}\| + \|\boldsymbol{\varepsilon}_{2,k}\|)$. Hence, condition (iii) provides $\sum_{k\in\mathbb{N}} \mu_k\|\boldsymbol{\varepsilon}_k\| < +\infty$. Finally, in view of the definition of $\boldsymbol{R}$, we have $\operatorname{fix}\boldsymbol{R} = \operatorname{fix}\boldsymbol{T}$, so that condition (i) with Propositions 3.1 and 3.2 ensure $\operatorname{fix}\boldsymbol{R} \neq \emptyset$. Altogether, all the hypotheses are satisfied in order to apply Combettes (2004, Lemma 5.1), where both (a) and (b) are proven.

(c). For any $y \in \mathcal{H}$ and $k \in \mathbb{N}$, $\langle y \,|\, x_k - x\rangle = \langle y \,|\, \sum_i w_i(\boldsymbol{z}_{i,k} - \boldsymbol{z}_i)\rangle = \sum_i w_i\langle y \,|\, \boldsymbol{z}_{i,k} - \boldsymbol{z}_i\rangle = \langle \boldsymbol{C}(y) \,|\, \boldsymbol{z}_k - \boldsymbol{z}\rangle$. So, (b) provides weak convergence of $(x_k)_{k\in\mathbb{N}}$ towards x, which is a zero of $B + \sum_i A_i$ by Proposition 3.1.

(d). If moreover (iv) is satisfied, in view of Propositions 3.3 and 3.4, the sequence defined in (13) is immediately a particular instance of Combettes (2004, Algorithm 4.1). Then, Combettes (2004, Theorem 3.1 and Remark 3.4) provides

$$\sum_{k\in\mathbb{N}} \left\|(\mathbf{Id} - \boldsymbol{T}_{2,\gamma})\boldsymbol{z}_k - (\mathbf{Id} - \boldsymbol{T}_{2,\gamma})\boldsymbol{z}\right\|^2 = \sum_{k\in\mathbb{N}} \gamma^2\left\|\boldsymbol{B}P_{\mathcal{S}}\boldsymbol{z}_k - \boldsymbol{B}P_{\mathcal{S}}\boldsymbol{z}\right\|^2 < +\infty\,. \tag{14}$$

(1). Now, if B is uniformly monotone, then we have for all $k \in \mathbb{N}$,

$$\begin{aligned}\left\langle \boldsymbol{B}P_{\mathcal{S}}\boldsymbol{z}_k - \boldsymbol{B}P_{\mathcal{S}}\boldsymbol{z} \,\middle|\, \boldsymbol{z}_k - \boldsymbol{z}\right\rangle &= \sum_i w_i\left\langle B\Big(\sum_i w_i z_{i,k}\Big) - B\Big(\sum_i w_i z_i\Big) \,\middle|\, z_{i,k} - z_i\right\rangle\\ &= \left\langle B(x_k) - B(x) \,\middle|\, \sum_i w_i(z_{i,k} - z_i)\right\rangle\\ &\geq \phi\left(\|x_k - x\|\right).\end{aligned}$$

From (b) and (14), we deduce that the right-hand side of the last inequality converges to 0. In view of the properties of ϕ, we obtain strong convergence of $(x_k)_{k\in\mathbb{N}}$ towards x.

(2). Let $\boldsymbol{u} = -\gamma \boldsymbol{B} P_{\mathcal{S}} \boldsymbol{z}$ and define for all $k \in \mathbb{N}$,

$$\boldsymbol{y}_k = \boldsymbol{T}_{1,\gamma} \boldsymbol{T}_{2,\gamma} \boldsymbol{z}_k \quad \text{and} \quad \boldsymbol{u}_k = (\boldsymbol{z}_k - \boldsymbol{y}_k) - \gamma \boldsymbol{B} P_{\mathcal{S}} \boldsymbol{z}_k \,.$$

We then have

$$\|\boldsymbol{u}_k - \boldsymbol{u}\| \leq \|\boldsymbol{y}_k - \boldsymbol{z}_k\| + \gamma \|\boldsymbol{B} P_{\mathcal{S}} \boldsymbol{z}_k - \boldsymbol{B} P_{\mathcal{S}} \boldsymbol{z}\| \,.$$

It follows from (a) and (14) that $\boldsymbol{u}_k$ converges strongly to $\boldsymbol{u}$. On the other hand, by Proposition 3.6, we have

$$\boldsymbol{u} \in \boldsymbol{A}'_\gamma \boldsymbol{z} \quad \text{and} \quad \boldsymbol{u}_k \in \boldsymbol{A}'_\gamma \boldsymbol{y}_k \,.$$

Therefore, applying Proposition 3.7 to the pairs $(\boldsymbol{z}, \boldsymbol{u})$ and $(\boldsymbol{y}_k, \boldsymbol{u}_k)$, and using the fact that $\boldsymbol{\gamma \cdot A}$ is uniformly monotone, we obtain

$$\left\langle (\boldsymbol{u}^{\mathcal{S}} - \boldsymbol{z}^{\perp}) - (\boldsymbol{u}_k^{\mathcal{S}} - \boldsymbol{y}_k^{\perp}) \,\middle|\, (\boldsymbol{z}^{\mathcal{S}} - \boldsymbol{u}^{\perp}) - (\boldsymbol{y}_k^{\mathcal{S}} - \boldsymbol{u}_k^{\perp}) \right\rangle \geq \phi\big(\|(\boldsymbol{z}^{\mathcal{S}} - \boldsymbol{u}^{\perp}) - (\boldsymbol{y}_k^{\mathcal{S}} - \boldsymbol{u}_k^{\perp})\|\big).$$

Now,

$$\begin{aligned}
&\left\langle (\boldsymbol{u}^{\mathcal{S}} - \boldsymbol{z}^{\perp}) - (\boldsymbol{u}_k^{\mathcal{S}} - \boldsymbol{y}_k^{\perp}) \,\middle|\, (\boldsymbol{z}^{\mathcal{S}} - \boldsymbol{u}^{\perp}) - (\boldsymbol{y}_k^{\mathcal{S}} - \boldsymbol{u}_k^{\perp}) \right\rangle \\
&\qquad = \left\langle (\boldsymbol{u}^{\mathcal{S}} - \boldsymbol{u}_k^{\mathcal{S}}) - (\boldsymbol{z}^{\perp} - \boldsymbol{y}_k^{\perp}) \,\middle|\, (\boldsymbol{z}^{\mathcal{S}} - \boldsymbol{y}_k^{\mathcal{S}}) - (\boldsymbol{u}^{\perp} - \boldsymbol{u}_k^{\perp}) \right\rangle \\
&\qquad = \left\langle \boldsymbol{u}^{\mathcal{S}} - \boldsymbol{u}_k^{\mathcal{S}} \,\middle|\, \boldsymbol{z}^{\mathcal{S}} - \boldsymbol{y}_k^{\mathcal{S}} \right\rangle + \left\langle \boldsymbol{z}^{\perp} - \boldsymbol{y}_k^{\perp} \,\middle|\, \boldsymbol{u}^{\perp} - \boldsymbol{u}_k^{\perp} \right\rangle = \left\langle \boldsymbol{u} - \boldsymbol{u}_k \,\middle|\, \boldsymbol{z} - \boldsymbol{y}_k \right\rangle .
\end{aligned}$$

Moreover,

$$\begin{aligned}
\phi\big(\|(\boldsymbol{z}^{\mathcal{S}} - \boldsymbol{u}^{\perp}) - (\boldsymbol{y}_k^{\mathcal{S}} - \boldsymbol{u}_k^{\perp})\|\big) &= \phi\big(\|(\boldsymbol{z}^{\mathcal{S}} - \boldsymbol{y}_k^{\mathcal{S}}) - (\boldsymbol{u}^{\perp} - \boldsymbol{u}_k^{\perp})\|\big) \\
&= \phi\left(\sqrt{\|\boldsymbol{z}^{\mathcal{S}} - \boldsymbol{y}_k^{\mathcal{S}}\|^2 + \|\boldsymbol{u}^{\perp} - \boldsymbol{u}_k^{\perp}\|^2}\right) \\
(\phi \text{ is nondecreasing}) \quad &\geq \phi\big(\|\boldsymbol{z}^{\mathcal{S}} - \boldsymbol{y}_k^{\mathcal{S}}\|\big)
\end{aligned}$$

Altogether, we arrive at $\phi\big(\|\boldsymbol{z}^{\mathcal{S}} - \boldsymbol{y}_k^{\mathcal{S}}\|\big) \leq \left\langle \boldsymbol{u} - \boldsymbol{u}_k \,\middle|\, \boldsymbol{z} - \boldsymbol{y}_k \right\rangle$. By (a) and (b), $\boldsymbol{y}_k$ converges weakly to $\boldsymbol{z}$ and we have shown that $\boldsymbol{u}_k$ converges strongly to $\boldsymbol{u}$. We deduce then that $\left\langle \boldsymbol{u} - \boldsymbol{u}_k \,\middle|\, \boldsymbol{z} - \boldsymbol{y}_k \right\rangle \to 0$ and therefore $\boldsymbol{y}_k^{\mathcal{S}}$ converges strongly to $\boldsymbol{z}^{\mathcal{S}} = x$ in view of the properties of ϕ. The latter in conjunction with (a) implies that $\boldsymbol{z}_k^{\mathcal{S}} = x_k$ converges strongly to x.

It remains to show the special cases implying uniform monotonicity in (2). Indeed, if for all $i \in \{1, \ldots, n\}$, A_i is uniformly monotone with the same modulus ϕ which is also

convex, then for $(\boldsymbol{x},\boldsymbol{u}),(\boldsymbol{y},\boldsymbol{v}) \in \operatorname{gra} \gamma\cdot\boldsymbol{A}$,

$$\begin{aligned}
\langle \boldsymbol{u}-\boldsymbol{v} \,|\, \boldsymbol{x}-\boldsymbol{y}\rangle &= \sum_{i=1}^{n} w_i \langle u_i - v_i \,|\, x_i - y_i\rangle \,, \\
&\geq \sum_{i=1}^{n} w_i \gamma_i \phi(\|x_i - y_i\|) \,, \\
&\geq (\min_i \gamma_i) \sum_{i=1}^{n} w_i \phi(\|x_i - y_i\|) \,, \\
(\phi \text{ is convex}) &\geq (\min_i \gamma_i)\, \phi\Bigg(\sum_{i=1}^{n} w_i \|x_i - y_i\|\Bigg) \,, \\
(\phi \text{ is nondecreasing}) &\geq (\min_i \gamma_i)\, \phi\Bigg((\min_i w_i)\sqrt{\sum_{i=1}^{n} \|x_i - y_i\|^2}\Bigg) \,, \\
(w_i \in]0,1]) &\geq (\min_i \gamma_i)\, \phi\Bigg((\min_i w_i)\sqrt{\sum_{i=1}^{n} w_i \|x_i - y_i\|^2}\Bigg) \,,
\end{aligned}$$

so that one finally obtains $\langle \boldsymbol{u}-\boldsymbol{v} \,|\, \boldsymbol{x}-\boldsymbol{y}\rangle \geq (\min_i \gamma_i)\, \phi\big((\min_i w_i)\|\boldsymbol{x}-\boldsymbol{y}\|\big)$. The proof for ϕ subadditive follows the same lines using subadditivity instead of convexity in the inequalities, and replacing $\min_i \gamma_i$ by γ and $\min_i w_i$ by 1. ■

Remark 3.1 (strong convergence)**.** We have proved strong convergence of the sequence $(x_k)_{k\in\mathbb{N}}$, but we did not elaborate on strong convergence of $(\boldsymbol{z}_k)_{k\in\mathbb{N}}$. It turns out that the sequence $(\boldsymbol{z}_k)_{k\in\mathbb{N}}$ is indeed quasi-Fejér monotone with respect to $\operatorname{fix} \boldsymbol{T}$. Thus, by Combettes (2004, Lemma 2.8(iv)), if $\operatorname{int}(\operatorname{fix} \boldsymbol{T}) \neq \emptyset$ then $(\boldsymbol{z}_k)_{k\in\mathbb{N}}$ converges strongly, and so does $(x_k)_{k\in\mathbb{N}}$. An alternative sufficient condition is that $\boldsymbol{A}'_\gamma$ is demiregular; see Attouch *et al.* (2010, Definition 2.3) and Combettes and Wajs (2005, Condition 3.2) in the case of convex optimization. Demiregularity occurs for instance if the operator has a boundedly relatively compact domain (the intersection of its closure with any closed ball is compact); see Attouch *et al.* (2010, Proposition 2.4). However, this condition is rather abstract and it is not easy to translate it in terms of the properties of each A_i involved in problem (1).

Finally, let us explicit the derivation of the claims of § 2.1 from Theorem 3.1.

Proof of Theorem 2.1. It is straightforward to see that the vector whose coordinates are the sequences $(z_{i,k})_{k\in\mathbb{N}}$ defined in (7) follows iterations (13), with $\boldsymbol{\varepsilon}_{1,k} = (\varepsilon_{1,k,i})_i$ and $\boldsymbol{\varepsilon}_{2,k} = \boldsymbol{C}(-\gamma\varepsilon_{2,k})$, which are summable under the required assumptions. Applying Theorem 3.1, the claimed convergence properties follow. ■

Proof of Corollary 2.1. Since it is continuously differentiable, f has full domain, so that under (i) and (D), Lemma 1.3 provides $\operatorname{argmin}(f + \sum_i g_i) = \operatorname{zer}(\nabla f + \sum_i \partial g_i) \neq \emptyset$. Furthermore, in Lemma 1.4, (i) shows that ∇f is β-cocoercive, and for all $i \in \{1,\dots,n\}$, (ii) shows that ∂g_i is maximal monotone and (iii) shows that $J_{\frac{\gamma}{w_i}A_i} = \operatorname{prox}_{\frac{\gamma}{w_i}g_i}$. Hence, weak convergence of $(x_k)_{k\in\mathbb{N}}$ towards a minimizer of (4) follows from Theorem 3.1 (c).

The proof of strong convergence is a consequence of Theorem 3.1 (d) together with the fact that uniform convexity of a function in $\Gamma_0(\mathcal{H})$ with modulus ϕ implies uniform monotonicity of its subdifferential with modulus 2ϕ (Bauschke and Combettes, 2011, Example 22.3(iii)). ■

4 Conclusion and Perspectives

We proved convergence in a general setting of a novel inexact proximal algorithm, which extends the forward-backward splitting algorithm to the more general case where the operator that is not cocoercive is split into an arbitrary number of simpler maximal monotone operators.

In a recent work, Liang *et al.* (2014) were able to prove iteration-complexity bounds for the inexact relaxed GFB. In particular, if the sequences defined in Theorem 3.1 satisfy

$$\inf_{k\in\mathbb{N}} \rho_k\left(\tfrac{4\beta-\gamma}{2\beta} - \rho_k\right) > 0 \quad \text{and} \quad \sum_{k\in\mathbb{N}} k(\|\boldsymbol{\varepsilon}_{1,k}\| + \|\boldsymbol{\varepsilon}_{2,k}\|) < +\infty\,,$$

then the *pointwise* iteration-complexity bound ensures the existence of a constant $C \in \mathbb{R}_{+*}$ such that

$$\forall\, k \in \mathbb{N}, \quad \|\boldsymbol{z}_{k+1} - \boldsymbol{z}_k\| \leq \frac{C}{\sqrt{k+1}}\,.$$

In addition, they propose a nonstationary version of our GFB, *i.e.* with parameter γ varying along iterations.

As mentioned in the introduction, the forward-backward has revealed useful for many practical purposes, and we believe that the GFB unlocks the possibility to address efficiently increasingly complex monotone inclusion and convex optimization problems. In particular it seems to be the best candidate to deal with the inverse problem (II.6) within our SMCS framework. In the next chapter, we further illustrate those claims, both theoretically and numerically.

References

K. J. Arrow, L. Hurwicz, and H. Uzawa. *Studies in linear and nonlinear programming*. Stanford University Press, 1958.

H. Attouch, L. M. Briceño-Arias, and P. L. Combettes. A parallel splitting method for coupled monotone inclusions. *SIAM Journal on Control and Optimization*, 48(5): 3246–3270, 2010.

J.-B. Baillon and G. Haddad. Quelques propriétés des opérateurs angle-bornés et n-cycliquement monotones. *Israel Journal of Mathematics*, 26(2):137–150, 1977.

H. H. Bauschke and P. L. Combettes. *Convex Analysis and Monotone Operator Theory in Hilbert Spaces*. Springer, New York, NY, USA, 2011.

A. Beck and M. Teboulle. A fast iterative shrinkage-thresholding algorithm for linear inverse problems. *SIAM Journal on Imaging Sciences*, 2(1):183–202, 2009.

K. Bredies and D. A. Lorenz. Linear convergence of iterative soft-thresholding. *Journal of Fourier Analysis and Applications*, 14(5-6):813–837, 2008.

P. L. Combettes. Solving monotone inclusions via compositions of nonexpansive averaged operators. *Optimization*, 53(5-6):475–504, 2004.

P. L. Combettes. Iterative construction of the resolvent of a sum of maximal monotone operators. *Journal of Convex Analysis*, 16(4):727–748, 2009.

P. L. Combettes and J.-C. Pesquet. A proximal decomposition method for solving convex variational inverse problems. *Inverse Problems*, 24(6):065014, 2008.

P. L. Combettes and J.-C. Pesquet. Primal-dual splitting algorithm for solving inclusions with mixtures of composite, Lipschitzian, and parallel-sum monotone operators. *Set-Valued and Variational Analysis*, 20(2):307–330, 2012.

P. L. Combettes and V. R. Wajs. Signal recovery by proximal forward-backward splitting. *SIAM Multiscale Modeling and Simulation*, 4(4):1168, 2005.

L. Condat. A primal–dual splitting method for convex optimization involving lipschitzian, proximable and linear composite terms. *Journal of Optimization Theory and Applications*, 158(2):460–479, 2013.

F. Deutsch. *Best Approximation in Inner Product Spaces*. CMS Books in Mathematics. Springer, New York, NY, USA, 2001.

B. He and X. Yuan. Convergence analysis of primal-dual algorithms for a saddle-point problem: From contraction perspective. *SIAM Journal on Imaging Sciences*, 5(1):119–149, 2012.

J. Liang, J. M. Fadili, and G. Peyré. Convergence rates with inexact nonexpansive operators. *preprint arXiv:1404.4837*, 2014.

O. J. Minty. Montone (nonlinear) operators in Hilbert space. *Duke Mathematical Journal*, 29(3):341–346, 1962.

R. Monteiro and B. Svaiter. Iteration-complexity of block-decomposition algorithms and the alternating direction method of multipliers. *SIAM Journal on Optimization*, 23(1):475–507, 2013.

J.-J. Moreau. Proximité et dualité dans un espace hilbertien. *Bulletin de la Société Mathématique de France*, 93:273–299, 1965.

Y. Nesterov. Gradient methods for minimizing composite functions. *Mathematical Programming*, 140(1):125–161, 2013.

N. Ogura and I. Yamada. Nonstrictly convex minimization over the fixed point set of an asymptotically shrinking nonexpansive mapping. *Numerical Functional Analisys and Optimization*, 23(1-2):113–137, 2002.

R. R. Phelps. *Convex Functions, Monotone Operators and Differentiability*, volume 1364 of *Lecture Notes in Mathematics*. Springer Berlin Heidelberg, second edition, 1993.

R. T. Rockafellar. *Convex Analysis*. Princeton University Press, 1970.

J. E. Spingarn. Partial inverse of a monotone operator. *Applied Mathematics and Optimization*, 10(1):247–265, 1983.

P. Tseng. A modified forward-backward splitting method for maximal monotone mapping. *SIAM Journal on Control and Optimization*, 38(2):431–446, 2000.

B. C. Vũ. A splitting algorithm for dual monotone inclusions involving cocoercive operators. *Advances in Computational Mathematics*, 38(3):667–681, 2013.

E. H. Zarantonello. Projections on convex sets, contributions to nonlinear functional analysis. In *Projections on convex sets in Hilbert space and spectral theory*, pages 237–341. Academic Press, 1971.

▪ IV ▪

Splitting Spatially Structured Penalizations for Signal Processing

The previous chapter presented and analysed a generalized forward-backward algorithm, enabling notably the minimization of functionals structured as $F \stackrel{\text{def}}{=} f + \sum_{i=1}^{n} g_i$, where all considered functions are convex, f is smooth and each g_i is simple. However, concerning the optimization problem in our spatially structured sparse morphological components separation presented in Chapter II, two points remain to be addressed; first, how our variational problem can be split into the right structure, and second, why is the generalized forward-backward the most adapted algorithm to date for solving it.

This chapter deals with those questions in a more general perspective. On the one hand, we derive proximity operators and splitting methods that covers many problems encountered in signal processing; note that for didactic purpose, we re-establish some basic results of convex analysis and extend some others. On the other hand, we demonstrate the advantage of the proposed methods in comparison to other proximal splitting algorithms.

In this purpose, we define rigorously the penalizations introduced in § II.3, and explain how they can be split into sums of simpler penalizations. Note that at this occasion, we introduce a simple formalisation for dealing with spatially structured penalizations, and propose a new total variation penalization.

Then, we give some practical hints for truly efficient implementations of proximal splitting algorithms.

Finally we design inverse problems inspired by classical models of image processing, delibarately chosen in such a way that other proximal splitting algorithms can be applied and compared fairly.

Although our numerical results are reported only on imaging applications, it should be kept in mind that the functionals defined here, and their minimization with the generalized forward-backward, may prove useful for many other applications such as machine learning, statistical estimation or optimal control.

Contents

1 Norms and Sets in a Structured Euclidean Space

Sparsity promoting penalizations for regularizing inverse problems have been presented in the introduction of this thesis. The underlying sparsity property is illustrated

in Figure 1(b). It represents the coefficients of a natural image in an orthogonal wavelet frame, where it can be seen that most of the coefficients have small amplitude, or to state it otherwise, most of the information is captured by a few coefficients. Then in the schematic view of Figure 1(c), we illustrate the concept of structured sparsity, where it is assumed that the nonzero coefficients satisfies specific spatial structure. Although it is used here for the sake of illustration, it can be motivated by the presence of edges or textures within natural images, leading to local dependencies in their wavelet coefficients. A way to enforce sparsity while taking into account those local dependencies is to replace the famous ℓ_1-norm on the coefficients by a structured $\ell_{1,2}$-norm by blocks. Let us first define such norms in a general setting.

In all the following, P is a strictly positive integer, and we consider the Euclidean space $\mathbb{R}^P$, which can be the linear space where lies either a given signal, or its coefficients within a linear representation operator.

1.1 Groups of Coordinates over an Euclidean Space

Definition 1.1 (group, subvector, group structure)**.** Over the Euclidean space $\mathbb{R}^P$, a *group of coordinates* is a nonempty subset $b \subseteq \{1, \dots, P\}$. For such a group and for $x \in \mathbb{R}^P$, it is convenient to define the *subvector* $x_b = (x_p)_{p \in b} \in \mathbb{R}^{|b|}$. Then, a *group structure* is a nonempty, finite family of groups, $B \overset{\text{def}}{=} (b_i)_{i \in I}$.

Note that when manipulating group structures, the indexing set I is usually implicit. By abuse of notation, we also use B for the *disjoint union* of the elements of B so that one can index the groups by $b \in B$ instead of $i \in I$; and the *cardinal* of B is $|B| \overset{\text{def}}{=} |I|$. Finally, if $(B^{(i)})_{i \in I}$ is a nonempty family of group structures, their *concatenation*, also abusively denoted $(B^{(i)})_{i \in I}$, is the group structure $(b_{i,b_i})_{(i,b_i) \in \cup_{i \in I} \{i\} \times B_i}$, where for all $(i, b_i) \in \cup_{i \in I} \{i\} \times B_i$, $b_{(i,b_i)} \overset{\text{def}}{=} b_i$.

Definition 1.2 (nonoverlapping, covering group structures)**.** A group structure B over the Euclidean space $\mathbb{R}^P$, is *nonoverlapping* if $\forall\, b, b' \in B, b \neq b' \Rightarrow b \cap b' = \emptyset$, and *covering* if $\forall\, p \in \{1, \dots, P\}, \exists\, b \in B, p \in b$.

1.2 The $\ell_{1,2}$-Norm

Definition 1.3 ($\ell_{1,2}$-norm)**.** Given a group structure B and a family of nonnegative weights indexed by B, $\Lambda \overset{\text{def}}{=} (\lambda_b)_{b \in B}$, the *$\ell_{1,2}$-norm of parameter* $\Lambda_B \overset{\text{def}}{=} \{B, \Lambda\}$ is

$$\|\cdot\|_{\ell,\Lambda_B} : \begin{array}{ccc} \mathbb{R}^P & \longrightarrow & \mathbb{R}_+ \\ x & \longmapsto & \|x\|_{\ell,\Lambda_B} \overset{\text{def}}{=} \sum_{b \in B} \lambda_b \|x_b\|_2 \,, \end{array} \tag{1}$$

where for a group b, $\|x_b\|_2$ is the Euclidean norm of the subvector x_b in $\mathbb{R}^{|b|}$.

Remark 1.1 (ℓ_1-norm, ℓ_2-norm)**.** Note that in the particular case where B comprises all groups restrained to individual coordinates, *i.e.* $B \overset{\text{set}}{=} (\{p\})_{1 \leq p \leq P}$, then the $\ell_{1,2}$-norm amounts to the classical ℓ_1-norm; whereas in the particular case where B comprises a single group covering all coordinates, *i.e.* $B \overset{\text{set}}{=} (\{1, \dots, P\})$, then the $\ell_{1,2}$-norm boils down to the ℓ_2-norm, *i.e.* the Euclidean norm over $\mathbb{R}^P$.

(a) La Boute, $y^{(0)}$.

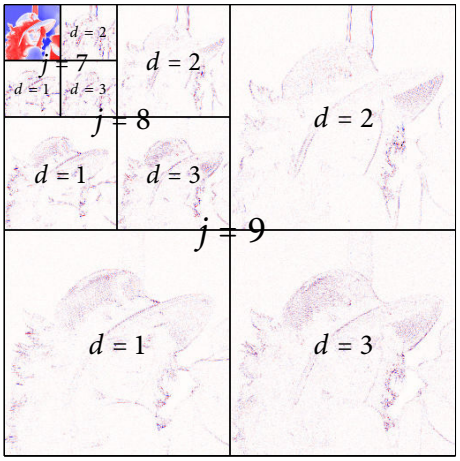

(b) $x^{(w)} = D^{(w)^{-1}} y^{(0)}$.

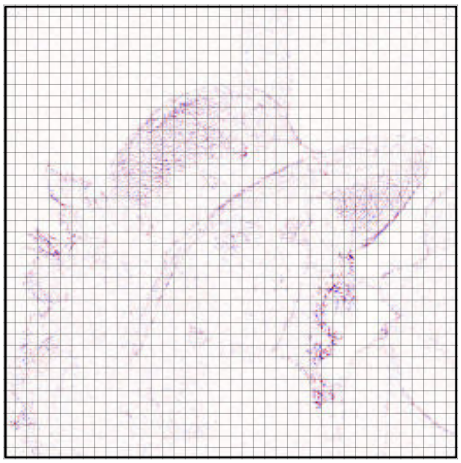

(c) $B^{(j,d,i)}$.

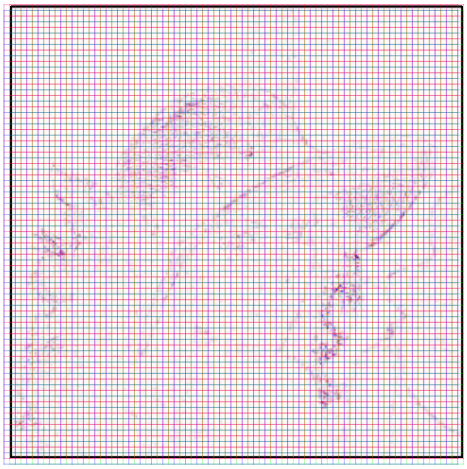

(d) $(B^{(j,d,1)}, B^{(j,d,2)}, B^{(j,d,3)}, B^{(j,d,4)})$.

Figure 1: Illustration of sparsity and spatial block structure over two-dimensional wavelet coefficients. (a) A natural image. (b) Schematic view of the coefficients of (a) in an orthogonal wavelet frame. Positive values are in red, negative values are in blue, and white pixels indicate coefficients with low absolute value: we can see that most coefficients are close to zero. Three levels of decomposition are represented, regrouped by scale j, direction d and in coherence with their spatial positions p. (c) Close up on the coefficients of scale $j = 9$ and direction $d = 3$, superposed with a *block grid*, *i.e.* a set of adjacent, nonoverlapping blocks of coefficients covering the whole domain. One can see that the meaningful coefficients are enclosed within a limited number of blocks, illustrating spatially structured sparsity. The block side length is approximatively $s^{(j,d)} = 8$. (d) The same coefficients, superposed with a block structure decomposed into four block grids, in which each spatial position belongs to exactly four different blocks.

Remark 1.2. By continuity and convexity of each Euclidean norm $\|\cdot\|_2$ over $\mathbb{R}^{|b|}$, any $\ell_{1,2}$-norm belongs to the class $\Gamma_0(\mathbb{R}^P)$. Moreover, each norm is in particular a *semi-norm*, it is thus straightforward to establish that a $\ell_{1,2}$-norm is also a semi-norm, and that it is a norm over $\mathbb{R}^P$ if, and only if, B is covering with nonnegative weights. For convenience, we keep the name $\ell_{1,2}$-norm in the general case.

1.3 The $\delta_{1,2}$-Semi-Norm

Sometimes sparsity is assumed over the *discrepancies* between coefficients rather than on the coefficients themselves. This enforces signals with entire groups of coefficients that are homogeneous, with only a few "jumps" within groups. This is in particular the case of the *total variation semi-norm* (TV) prior, also mentioned in the introduction. We develop here the more general $\delta_{1,2}$-*semi-norm*, well suited to our structured Euclidean space framework.

Definition 1.4 (first bisector, deviation operator)**.** Given a group of coordinates b, the *first bisector of* $\mathbb{R}^{|b|}$ is the unidimensional subspace $\mathcal{S}_b \overset{\text{def}}{=} \left\{x \in \mathbb{R}^{|b|} \;\middle|\; \forall\, p, q \in b,\ x_p = x_q\right\}$. Its orthogonal complement is denoted $\mathcal{S}_b^{\perp} \overset{\text{def}}{=} \left\{x \in \mathbb{R}^{|b|} \;\middle|\; \sum_{p\in b} x_p = 0\right\}$.
Then, the *deviation operator over* b is the linear operator

$$\Delta^{(b)}\colon \begin{array}{ccc} \mathbb{R}^{|b|} & \longrightarrow & \mathbb{R}^{|b|} \\ x & \longmapsto & \operatorname{proj}_{\mathcal{S}_b^{\perp}}(x) \end{array} .$$

The first bisector in $\mathbb{R}^{|b|}$ is thus the space of subvectors x_b that are constants, and the deviation operator extracts in a subvector the contribution orthogonal to this space. The $\delta_{1,2}$-semi-norm simply measures the amplitude of this contribution, within each block.

Definition 1.5 ($\delta_{1,2}$-semi-norm)**.** Given a block structure B, and a family of nonnegative weights indexed by B, $\Lambda \overset{\text{def}}{=} \left(\lambda_b\right)_{b\in B}$, the $\delta_{1,2}$-*semi-norm with parameter* $\Lambda_B \overset{\text{def}}{=} \{B, \Lambda\}$ is

$$\|\cdot\|_{\delta,\Lambda_B}\colon \begin{array}{ccc} \mathbb{R}^P & \longrightarrow & \mathbb{R}_+ \\ x & \longmapsto & \|x\|_{\delta,\Lambda_B} \overset{\text{def}}{=} \sum_{b\in B} \|\Delta^{(b)} x_b\|_2 \end{array} . \tag{2}$$

where for a group b, $\|\Delta^{(b)} x_b\|_2$ is the Euclidean norm of $\Delta^{(b)} x_b$ in $\mathbb{R}^{|b|}$.

Remark 1.3. By continuity and convexity of each Euclidean norm $\|\cdot\|_2$ over $\mathbb{R}^{|b|}$, and by continuity and linearity of each operator $\Delta^{(b)}$ over $\mathbb{R}^{|b|}$, any $\delta_{1,2}$-semi-norm belongs to the class $\Gamma_0(\mathbb{R}^P)$. Moreover, as for Remark 1.2, it is straightforward to establish that a $\delta_{1,2}$-semi-norm is indeed a semi-norm.

Remark 1.4 (orthogonal projection, statistical interpretation)**.** Given a group b, recall from Lemma III.3.1 (i) that for all $x \in \mathbb{R}^P$, $\operatorname{proj}_{\mathcal{S}_b}(x_b)$ is the constant vector of $\mathbb{R}^{|b|}$ whose coordinates are equal to the mean of the coordinates of x_b. Defining then $\overline{x_b} \overset{\text{def}}{=} \frac{1}{|b|}\sum_{p\in b} x_p$ and $\overrightarrow{x_b} \overset{\text{def}}{=} (\overline{x_b}, \ldots, \overline{x_b}) \in \mathbb{R}^{|b|}$, and since $\mathcal{S}_b$ and $\mathcal{S}_b^{\perp}$ are orthogonal complements in $\mathbb{R}^{|b|}$, we get

$$\Delta^{(b)} x_b = x_b - \overrightarrow{x_b} = \left(x_p - \overline{x_b}\right)_{p\in b} .$$

Thus, $\|\Delta^{(b)} x_b\|_2$ is essentially the *empirical standard deviation* of the coefficients in x_b.

1.4 Spatially Structured Euclidean Space

As introduced above, our specific interest is on groups that are spatial blocks, *i.e.* spatially and locally structured, according to a spatial topology conditioning the signals or its coefficients. In all the following, D is a strictly positive integer, representing the dimensionality of this spatial topology.

Definition 1.6 (spatial structure, cuboid, block, block structure)**.** The Euclidean space $\mathbb{R}^P$ is said to be *spatially structured in dimension* D by (Z, ϕ) if $\mathsf{Z} \subset \mathbb{Z}^{\mathsf{D}}$, and $\phi\colon \mathsf{Z} \to \{1, \dots, P\}$ is *bijective*. Note that we have $|\mathsf{Z}| = P$.
Given $\mathsf{v} \in \mathbb{Z}^{\mathsf{D}}$ and $\mathsf{s} \in {\mathbb{N}_*}^{\mathsf{D}}$, the *cuboid* of *lower vertex* v and *size* s is the subset

$$\mathsf{C}(\mathsf{v}, \mathsf{s}) \stackrel{\text{def}}{=} \left\{ \mathsf{z} \in \mathbb{Z}^{\mathsf{D}} \;\middle|\; \forall\, \mathsf{d} \in \{1, \dots, \mathsf{D}\}, \mathsf{v}_\mathsf{d} \leq \mathsf{z}_\mathsf{d} < \mathsf{v}_\mathsf{d} + \mathsf{s}_\mathsf{d} \right\} .$$

Then, given a cuboid $\mathsf{C} \in \mathbb{Z}^{\mathsf{D}}$, such that $\mathsf{C} \cap \mathsf{Z} \neq \emptyset$, the *block* of coordinates of *support* C is the group

$$b(\mathsf{C}) \stackrel{\text{def}}{=} \phi(\mathsf{C}(\mathsf{v}, \mathsf{s}) \cap \mathsf{Z}) .$$

Finally, a *block structure* is a group structure in which all groups are blocks.

A block is thus the intersection of Z with a cuboid in $\mathbb{Z}^{\mathsf{D}}$; this allows to gather local information of a spatially structured signal. Since cuboids tile the space $\mathbb{Z}^{\mathsf{D}}$, a natural tool for handling block structures is the intersection of Z with each cuboid within a tiling of $\mathbb{Z}^{\mathsf{D}}$, as defined below, and illustrated in Figure 1(c) in dimension $\mathsf{D} \stackrel{\text{set}}{=} 2$.

Definition 1.7 (tile grid, block grid)**.** Let $\mathbb{R}^P$ be spatially structured in dimension D, $\mathsf{v} \in \mathbb{Z}^{\mathsf{D}}$ and $\mathsf{s} \in {\mathbb{N}_*}^{\mathsf{D}}$. The *tile grid* of $\mathbb{Z}^{\mathsf{D}}$ generated by the *lower vertex* v and *size* s is the set of cuboids

$$\mathsf{T}(\mathsf{v}, \mathsf{s}) \stackrel{\text{def}}{=} \left\{ \mathsf{C}(\mathsf{v} + \mathsf{k}\mathsf{s}, \mathsf{s}) \;\middle|\; \mathsf{k} \in \mathbb{Z}^{\mathsf{D}} \right\} .$$

where for $\mathsf{k} \in \mathbb{Z}^{\mathsf{D}}$, $\mathsf{k}\mathsf{s} \stackrel{\text{def}}{=} (\mathsf{k}_\mathsf{d}\mathsf{s}_\mathsf{d})_{1 \leq \mathsf{d} \leq \mathsf{D}} \in \mathbb{Z}^{\mathsf{D}}$. Then, the *block grid* of *lower vertex* v and *size* s is the block structure

$$B(\mathsf{v}, \mathsf{s}) \stackrel{\text{def}}{=} \big(b(\mathsf{C})\big)_{\mathsf{C} \in \mathsf{T}(\mathsf{v}, \mathsf{s}) : \mathsf{C} \cap \mathsf{Z} \neq \emptyset} .$$

Tile grids and block grids have the following fundamental properties.

Lemma 1.1. *Let* $\mathsf{u}, \mathsf{v} \in \mathbb{Z}^{\mathsf{D}}$ *and* $\mathsf{s}, \mathsf{t} \in {\mathbb{N}_*}^{\mathsf{D}}$. *Then,*

(i) $\mathsf{C}(\mathsf{u}, \mathsf{s}) = \mathsf{C}(\mathsf{v}, \mathsf{t})$, *if, and only if,* $\mathsf{u} = \mathsf{v}$ *and* $\mathsf{s} = \mathsf{t}$;

(ii) *there exists a unique* $\mathsf{z} \in \mathsf{C}(\mathsf{v}, \mathsf{s})$ *such that* $\mathsf{C}(\mathsf{u}, \mathsf{s}) \in \mathsf{T}(\mathsf{z}, \mathsf{s})$;

(iii) $\mathsf{C}(\mathsf{u}, \mathsf{s}) \in \mathsf{T}(\mathsf{v}, \mathsf{s})$, *if, and only if,* $\mathsf{T}(\mathsf{u}, \mathsf{s}) = \mathsf{T}(\mathsf{v}, \mathsf{s})$;

(iv) *there exists a unique* $\mathsf{z} \in \mathsf{C}(\mathsf{v}, \mathsf{s})$ *such that* $\mathsf{T}(\mathsf{u}, \mathsf{s}) = \mathsf{T}(\mathsf{z}, \mathsf{s})$.

Proof. (i). If $C \overset{\text{def}}{=} C(u,s)$, then u and s are uniquely defined, with for all $d \in \{1,\dots,D\}$, $u_d = \min\{z_d \mid z \in C\}$ and $s_d = \max\{z_d - u_d + 1 \mid z \in C\}$. The reciprocal is immediate. (ii). Let $z \in \mathbb{Z}^D$, and define $r \overset{\text{def}}{=} z - v$.

$$\begin{aligned} C(u,s) \in T(z,s) &\Leftrightarrow \exists k \in \mathbb{Z}^D,\ C(u,s) = C(z+ks,s)\ , \\ \text{by (i)} &\Leftrightarrow \exists k \in \mathbb{Z}^D,\ u = z + ks\ , \\ &\Leftrightarrow \exists k \in \mathbb{Z}^D,\ u - v = r + ks\ . \end{aligned}$$

We deduce that $(C(u,s) \in T(z,s) \text{ and } z \in C(v,s)) \Leftrightarrow \forall d \in \{1,\dots,D\}, \exists k_d \in \mathbb{Z}, u_d - v_d = k_d s_d + r_d$ and $0 \le r_d < s_d$. Existence and uniqueness of such a $z = r + v$ is ensured by Euclidean division in $\mathbb{Z}$. (iii). Suppose $C(u,s) \in T(v,s)$, and fix $k \in \mathbb{Z}^D$ such that $C(u,s) = C(v+ks,s)$. By (i), $u = v + ks$, so that $T(u,s) = \{C(u+k's,s) \mid k' \in \mathbb{Z}^D\} = \{C(v+(k+k')s,s) \mid k' \in \mathbb{Z}^D\} = T(v,s)$, since $\{(k+k') \mid k' \in \mathbb{Z}^D\} = \mathbb{Z}^D$. For the reciprocal, observe that $C(u,s) \in T(u,s)$. (iv). Combine (ii) with (iii). ∎

Proposition 1.1. *Let $\mathbb{R}^P$ be spatially structured in dimension D, $v \in \mathbb{Z}^D$ and $s \in {\mathbb{N}_*}^D$. Then,*

(i) *$T(v,s)$ is a partition of $\mathbb{Z}^D$, i.e. for all $z \in \mathbb{Z}^D$, there exists a unique cuboid $C \in T(v,s)$ such that $z \in C$;*

(ii) *$B(v,s)$ is nonoverlapping;*

(iii) *$B(v,s)$ is covering.*

Proof. (i). Let $z \in \mathbb{Z}^D$, and C be a cuboid in $\mathbb{Z}^D$.

$$\begin{aligned} z \in C \text{ and } C \in T(v,s) &\Leftrightarrow \exists k \in \mathbb{Z}^D, && C = C(v+ks,s) \text{ and } z \in C(v+ks,s)\ , \\ &\Leftrightarrow \exists k \in \mathbb{Z}^D, && C = C(v+ks,s) \text{ and } \forall d \in \{1,\dots,D\}, \\ & && \quad 0 \le z_d - v_d - k_d s_d < s_d\ , \\ &\Leftrightarrow \exists k, r \in \mathbb{Z}^D, && C = C(v+ks,s) \text{ and } \forall d \in \{1,\dots,D\}, \\ & && \quad z_d - v_d = k_d s_d + r_d \text{ and } 0 \le r_d < s_d\ . \end{aligned}$$

Existence and uniqueness of such a C is ensured by Euclidean division in $\mathbb{Z}$. (ii) and (iii) follow directly from (i). ∎

Properties (ii) and (iii) of Proposition 1.1 actually mean that a block grid constitutes a partition of $\{1,\dots,P\}$. This is an interesting property for constructing homogeneous block structures that weight each coordinate equally. Indeed, for $n \in \mathbb{N}_*$, the concatenation of n block grids results in a block structure in which each coordinate belongs to n blocks. This is illustrated in Figure 1(d).

Now, a natural question is how to construct a given block structure as the concatenation of block grids. The following proposition addresses the special case when all the blocks have the same size, *e.g.* when it is a characteristic of the spatial scale of the underlying signal.

Proposition 1.2. *Let $\mathbb{R}^P$ be spatially structured in dimension D by (Z, ϕ), $\mathsf{v} \in \mathbb{Z}^{\mathsf{D}}$, $\mathsf{s} \in {\mathbb{N}_*}^{\mathsf{D}}$, and define $n_{\mathsf{s}} \overset{\text{def}}{=} \prod_{\mathsf{d}=1}^{\mathsf{D}} \mathsf{s}_{\mathsf{d}} \in \mathbb{N}_*$. Then,*

(i) *there exists exactly n_{s} different tile grids of size s in $\mathbb{Z}^{\mathsf{D}}$, and their concatenation constitutes a partition of the set of all possible cuboids of size s in $\mathbb{Z}^{\mathsf{D}}$;*

(ii) *there exists at most n_{s} different block grids of size s over $\mathbb{R}^P$, and their concatenation contains all possible blocks of size s over $\mathbb{R}^P$;*

(iii) *if moreover $\mathsf{C}(\mathsf{v}, \mathsf{s}) \subseteq \mathsf{Z}$, then there exists exactly n_{s} different block grids of size s over $\mathbb{R}^P$, and their concatenation constitutes the smallest block grid containing all possible blocks of size s over $\mathbb{R}^P$.*

Proof. (i). In Lemma 1.1 (iv), the existence statements proves that any tile grid of size s is of the form $\mathsf{T}(\mathsf{z}, \mathsf{s})$ for some $\mathsf{z} \in \mathsf{C}(\mathsf{v}, \mathsf{s})$, and the uniqueness statement proves that if z, z' are in $\mathsf{C}(\mathsf{v}, \mathsf{s})$ such that $\mathsf{z} \neq \mathsf{z}'$, then $\mathsf{T}(\mathsf{z}, \mathsf{s}) \neq \mathsf{T}(\mathsf{z}, \mathsf{s})$. Thus, there exists exactly $|\mathsf{C}(\mathsf{v}, \mathsf{s})| = n_{\mathsf{s}}$ different block grids of size s. Now, combining Lemma 1.1 (ii) (iii) shows that any cuboid of size s belongs to a unique block grid of size s. (ii). This is a direct consequence of (i). (iii). Suppose now that $\mathsf{C}(\mathsf{v}, \mathsf{s}) \subseteq \mathsf{Z}$ and let $\mathsf{z} \in \mathsf{C}(\mathsf{v}, \mathsf{s})$.
First, let $\mathsf{z}' \in \mathsf{C}(\mathsf{v}, \mathsf{s}) \setminus \{\mathsf{z}\}$. There exists $\mathsf{d} \in \{1, \dots, \mathsf{D}\}$ such that either $\mathsf{z}_{\mathsf{d}} < \mathsf{z}'_{\mathsf{d}}$ or $\mathsf{z}'_{\mathsf{d}} < \mathsf{z}_{\mathsf{d}}$, implying either $\mathsf{z} \notin \mathsf{C}(\mathsf{z}', \mathsf{s})$ or $\mathsf{z}' \notin \mathsf{C}(\mathsf{z}, \mathsf{s})$. Since $\mathsf{z}, \mathsf{z}' \in \mathsf{Z}$, we deduce $b(\mathsf{z}, \mathsf{s}) \neq b(\mathsf{z}', \mathsf{s})$. However, defining $\mathsf{u} \overset{\text{def}}{=} \mathsf{v} + \mathsf{s} - (1, \dots, 1)$, it is easy to verify $\mathsf{u} \in \mathsf{C}(\mathsf{v}, \mathsf{s}) \cap \mathsf{C}(\mathsf{z}, \mathsf{s}) \cap \mathsf{C}(\mathsf{z}', \mathsf{s})$, so that $\phi(\mathsf{u}) \in b(\mathsf{z}, \mathsf{s}) \cap b(\mathsf{z}', \mathsf{s})$, in particular $b(\mathsf{z}, \mathsf{s}) \cap b(\mathsf{z}', \mathsf{s}) \neq \emptyset$. Recalling $b(\mathsf{z}', \mathsf{s}) \in B(\mathsf{z}', \mathsf{s})$, we conclude from Proposition 1.1 (ii) that

$$\mathsf{z}' \in \mathsf{C}(\mathsf{v}, \mathsf{s}) \setminus \{\mathsf{z}\} \Rightarrow b(\mathsf{z}, \mathsf{s}) \notin B(\mathsf{z}', \mathsf{s}) \,. \tag{3}$$

Recalling also $b(\mathsf{z}, \mathsf{s}) \in B(\mathsf{z}, \mathsf{s})$, we have $\forall\ \mathsf{z}, \mathsf{z}' \in \mathsf{C}(\mathsf{v}, \mathsf{s}),\ \mathsf{z} \neq \mathsf{z}' \Rightarrow B(\mathsf{z}, \mathsf{s}) \neq B(\mathsf{z}', \mathsf{s})$, and with (ii) we conclude that there exists exactly n_{s} different block grids of size s. Finally, let B be a block grid of size s. By definition and Lemma 1.1 (iv), $B = B(\mathsf{z}', \mathsf{s})$ for a unique $\mathsf{z}' \in \mathsf{C}(\mathsf{v}, \mathsf{s})$. By contraposition of (3), we get $b(\mathsf{z}, \mathsf{s}) \in B \Rightarrow \mathsf{z}' = \mathsf{z}$, *i.e.* if a concatenation of several block grids contain $b(\mathsf{z}, \mathsf{s})$, then $B(\mathsf{z}, \mathsf{s})$ is one of those block grids; this proves the last statement. ∎

1.5 Convex Hard Constraints

It is often the case in signal processing that one knows in advance that the signal interest lies in a specific subset of the Euclidean space $\mathbb{R}^P$. For instance, some signals might be, because of their physical origins, always nonnegative. It is possible to incorporate such priors in variational reconstructions, by the mean of *hard constraints*. Some are used in our SMCS model, § II.3.4; we write them here in a more general setting.

First, we define useful subsets of $\mathbb{R}^P$ that do not assume any structure.

Definition 1.8 (orthant and box in $\mathbb{R}^P$)**.** Let $(v, \epsilon) \in \mathbb{R}^P \times \{-1, +1\}^P$, and $(\underline{v}, \overline{v}) \in \mathbb{R}^P \times \mathbb{R}^P$ such that for all $p \in \mathbb{R}^P$, $\underline{v}_p \leq \overline{v}_p$.
The *orthant of $\mathbb{R}^P$ of vertex v and direction ϵ* is the set

$$[v, \epsilon) \overset{\text{def}}{=} \left\{ x \in \mathbb{R}^P \;\middle|\; \forall\ p \in \{1, \dots, P\},\ \epsilon\big(x_p - v_p\big) \geq 0 \right\} .$$

In particular, $[0, (+1, \dots, +1)) = \mathbb{R}^P_+$ is the *nonnegative* or *first orthant of* $\mathbb{R}^P$.
Then, the *box in* $\mathbb{R}^P$ *of lower vertex* $\underline{v}$ *and upper vertex* $\overline{v}$ is the set

$$[\underline{v}, \overline{v}] \stackrel{\text{def}}{=} \left\{ x \in \mathbb{R}^P \;\middle|\; \forall\, p \in \{1, \dots, P\}, \underline{v}_p \leq x_p \leq \overline{v}_p \right\}.$$

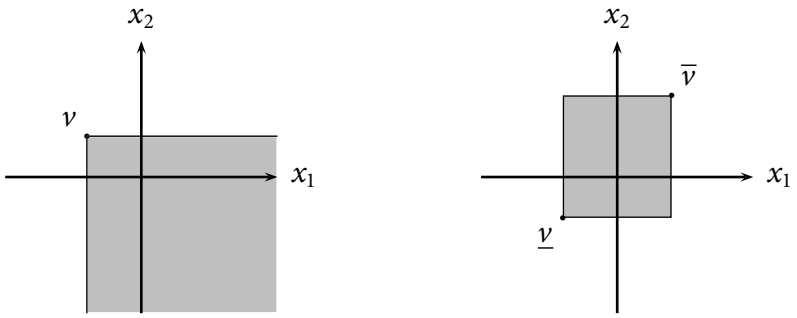

(a) Orthant $[v, (+1, -1))$. (b) Box $[\underline{v}, \overline{v}]$.

Figure 2: Illustration of an orthant and a box in $\mathbb{R}^2$.

Note that, for instance, $v \in [v, \epsilon)$, and $\underline{v} \in [\underline{v}, \overline{v}]$, so that these sets are nonempty. Moreover, they are defined by linear, large inequalities, so that they are closed and convex. Hence, their indicator functions (see § III.1.8) belongs to $\Gamma_0(\mathbb{R}^P)$. In particular, when no confusion is possible, we shall denote $\iota_+ \stackrel{\text{def}}{=} \iota_{\mathbb{R}^P_+}$, and $\text{proj}_+ \stackrel{\text{def}}{=} \text{prox}_{\iota_+}$.

Now, the following subsets of $\mathbb{R}^P$ are defined with help of group norms.

Definition 1.9 (bounded amplitude and bounded deviation)**.** Let B be a group structure over $\mathbb{R}^P$, and $\Lambda_B \stackrel{\text{def}}{=} \{B, \Lambda\}$ where $\Lambda \stackrel{\text{def}}{=} \left(\lambda_b\right)_{b \in B}$ is a family of nonnegative weights indexed by B.
The *set of bounded amplitudes* Λ_B is

$${}^{\ell}\overline{\Lambda_B} \stackrel{\text{def}}{=} \left\{ x \in \mathbb{R}^P \;\middle|\; \forall\, b \in B, \|x_b\|_2 \leq \lambda_b \right\},$$

and the *set of bounded deviations* Λ_B is

$${}^{\delta}\overline{\Lambda_B} \stackrel{\text{def}}{=} \left\{ x \in \mathbb{R}^P \;\middle|\; \forall\, b \in B, \|\Delta^{(b)} x_b\|_2 \leq \lambda_b \right\}.$$

Since $0 \in {}^{\ell}\overline{\Lambda_B}$ and $0 \in {}^{\delta}\overline{\Lambda_B}$, these sets are also nonempty. By continuity and convexity of the Euclidean norms over each $\mathbb{R}^{|b|}$, they are intersections of closed and convex sets, so that they are closed and convex. Once again, their indicator functions belongs to $\Gamma_0(\mathbb{R}^P)$; we call them *bounded amplitude* (respectively *bounded deviation*) *constraints parameterized by* Λ_B.

2 Yet Another Discrete Total Variation Semi-Norm

Roughly speaking, the total variation (TV) semi-norm of a scalar field is defined as the sum, over all spatial positions, of the norms of its spatial gradients. Because of its popularity in various field of applied mathematics and particularly in signal processing, this section is devoted to the analysis of a special case of a spatially structured $\delta_{1,2}$-semi-norm which can be seen as a discrete TV semi-norm.

Indeed, if b is a block of size $(2,\dots,2)$, the deviation operator $\Delta^{(b)}$ resembles a spatial gradient operator at the center of b, whose coordinates are linear combinations of spatial derivatives approximated by finite differences, in the directions of the vertices of b, as illustrated in dimension $\mathsf{D} \overset{\text{set}}{=} 2$ on the diagram (7). Defining B_{TV} as the block structure containing one exemplary of each possible block of size $(2,\dots,2)$, the $\delta_{1,2}$-semi-norm associated to B_{TV} plays the role of a TV semi-norm over $\mathbb{R}^P$.

In the literature, many choices have been proposed for discretizing the spatial gradient and defining the TV semi-norm. One usually expects the spatial gradient to have only one coordinate per spatial dimension, while ours necessitates in most cases $|b| = 2^{\mathsf{D}}$ coordinates. However, and this is what motivated the introduction of the $\delta_{1,2}$-semi-norm in this work in the first place, the resulting TV semi-norm can be efficiently split into simple functions, as explained along § 3 and illustrated in Figure 5.

Moreover, it is superior to other choices in several respects. First of all, dealing with boundary conditions and regions of interest is straightforward within our spatially structured Euclidean space framework: some blocks in B_{TV} contain less that 2^{D} coordinates but the deviation operator over those blocks is still well-defined and relevant to our purpose. Second, gradients discretized along grids always present *anisotropy*, *i.e.* they are more sensitive in certain directions than in others, resulting in directional bias on the corresponding TV semi-norm. We demonstrate below that our gradient is less anisotropic than more classical ones.

2.1 Some Usual Discrete Spatial Gradients

When dealing with spatially structured signals, there is a choice to be made on the underlying spatial structure over which the signals take their values. Most often, if not all the time, it is assumed that the samples are regularly spaced over a multidimensional square grid, analogous to the space $\mathbb{Z}^{\mathsf{D}}$ like we did all along this chapter. Indeed, most measurement devices follow such structure; consider for instance, any numeric photo or video camera, where the sensors are regularly arranged along a grid. This choice is made for practical engineering reasons, but a major drawback is that the distance between spatially neighboring samples depends on the direction defined by those samples. For two-dimensional grids, the (Euclidean) distance between diagonally neighboring pixels is $\sqrt{2}$-fold the distance between laterally neighboring pixels. This goes up to $\sqrt{3}$ for three-dimensional grids.

Now, taking into account this phenomenon, for instance by using anisotropic distances, introduces significant theoretical and computational overhead; and measurement devices in which all neighboring samples are at the same distance (hexagonal

grids in dimension two…) are far from being the standard. Thus, this matter is rarely discussed. However, it can become significant when it comes to estimate spatial derivatives of the signal, as it is the case for the TV semi-norm. In the following, we shade light on this problematic, and show the advantages in that respect of our deviation gradient operator over other spatial gradient discretizations.

We first introduce the discretized gradients that we compare. For simplicity and for graphical representation, we perform the analysis in dimension two; let then the Euclidean space $\mathbb{R}^P$ be structured in dimension $\mathsf{D} \overset{\text{set}}{=} 2$ by (Z, ϕ) as defined in § 1.4.

One-sided discrete gradient $\Delta_{\llcorner}$. The *one-sided* discrete gradient is the most common discretization in the literature. It approximates spatial derivatives according to the diagram in (4). Ignoring boundary conditions, it is defined for $x \in \mathbb{R}^P$ and all $p \in \{1, \dots, P\}$ as

$$\left(\Delta_{\llcorner}(x)\right)_p \overset{\text{def}}{=} \left(x_q - x_p, x_r - x_p\right), \qquad \begin{array}{|c|c|}\hline r & \\ \hline p & q \\ \hline \end{array} \tag{4}$$

where we defined the pixels $q \overset{\text{def}}{=} \phi(\phi^{-1}(p) + (1,0))$ and $r \overset{\text{def}}{=} \phi(\phi^{-1}(p) + (0,1))$.

Central difference discrete gradient Δ_{+}. The *central difference* discrete gradient is another common discretization, with better symmetry than the one-sided discrete gradient, but less spatial resolution. It approximates spatial derivatives according to the diagram in (5). Ignoring boundary conditions, it is defined for $x \in \mathbb{R}^P$ and all $p \in \{1, \dots, P\}$ as

$$\left(\Delta_{+}(x)\right)_p \overset{\text{def}}{=} \left(x_q - x_r, x_s - x_t\right), \qquad \begin{array}{|c|c|c|}\hline & s & \\ \hline r & p & q \\ \hline & t & \\ \hline \end{array} \tag{5}$$

where $q \overset{\text{def}}{=} \phi(\phi^{-1}(p) + (1,0))$, $r \overset{\text{def}}{=} \phi(\phi^{-1}(p) - (1,0))$, $s \overset{\text{def}}{=} \phi(\phi^{-1}(p) + (0,1))$, and $t \overset{\text{def}}{=} \phi(\phi^{-1}(p) - (0,1))$.

Note that the TV semi-norm derived from this gradient, like our $\delta_{1,2}$-semi-norm, can be split into simple functions.

Roberts cross discrete gradient $\Delta_{\times}$. This gradient was originally developed in the context of *edge detection*, but was considered for TV regularizations in Combettes and Pesquet (2008); Pustelnik *et al.* (2011), because the resulting TV semi-norm can also be split into simple functions, and has more spatial resolution than the central difference discrete gradient. It approximates spatial derivatives according to the diagram in (6). Ignoring boundary conditions, it is defined for $x \in \mathbb{R}^P$ and all $p \in \{1, \dots, P\}$ as

$$\left(\Delta_{\times}(x)\right)_p \overset{\text{def}}{=} \left(x_s - x_p, x_q - x_r\right), \qquad \begin{array}{|c|c|}\hline r & s \\ \hline p & q \\ \hline \end{array} \tag{6}$$

where $q \overset{\text{def}}{=} \phi(\phi^{-1}(p) + (1,0))$, $r \overset{\text{def}}{=} \phi(\phi^{-1}(p) + (0,1))$ and $s \overset{\text{def}}{=} \phi(\phi^{-1}(p) + (1,1))$.

Deviation discrete gradient $\Delta_{\times}$. Finally, let us specify in dimension $\mathsf{D} \overset{\text{set}}{=} 2$ the expression of our deviation gradient operator. Recalling Remark 1.4, it yields for $x \in \mathbb{R}^P$ and all $p \in \{1, \dots, P\}$,

$$\left(\Delta_{\times}(x)\right)_p \overset{\text{def}}{=} \left(x_p - \overline{x_b}, x_q - \overline{x_b}, x_r - \overline{x_b}, x_s - \overline{x_b}\right), \qquad (7)$$

where q, r and s are defined with respect to p as in (6), and $\overline{x_b} \overset{\text{def}}{=} \frac{1}{4}\left(x_p + x_q + x_r + x_s\right)$.

2.2 Spectral Analysis

Ignoring boundary effects, a spatial gradient is *translation invariant*, *i.e.* the gradient of a translated signal is the gradient of the signal, translated by the same translation. Since it is linear, each coordinate amounts to a *convolution* operator. Now, a convolution boils down to a multiplication in the Fourier domain (see for instance Mallat (2008, Theorem 3.9)). Hence, singular vectors of a gradient constitutes a Fourier basis, and the corresponding singular values characterize the influence of each spatial frequency on the gradient operator.

In order to have access to those singular values, we symmetrize the gradient operator by composing it by its adjoint, yielding a spatial Laplacian. The eigenvalues of the Laplacian are the squared singular values of the corresponding gradient. Once again, the Laplacian is a translation invariant linear operator, so its amount to a convolution with a certain *filter*; the eigenvalues are thus the coefficients of the *discrete Fourier transform* (DFT) of this filter. For each discrete spatial gradient Δ considered here, we compute the convolution filter of the corresponding Laplacian $\Delta^*\Delta$ by applying it to a discrete *dirac*, *i.e.* an image with null values everywhere but on a single pixel. Then, we apply a DFT to this filter, and the modulus of the resulting map is represented in Figure 3.

In the center of each map, corresponding to null spatial frequencies, *i.e.* constant signal, the eigenvalue is null for each gradient, as expected. Then, the general tendency is that the eigenvalues increase with the spatial frequency, what is also expected since more oscillations correspond to higher gradients. Now, if the gradients operator were *isotropic*, the level sets of those maps would be concentric circles. One can see that the one-sided gradient weights more diagonal gradients than vertical or horizontal gradients. This is the contrary for the Roberts cross gradient, which exhibits an even worst phenomenon: the eigenvalues in the diagonal directions starts to *decrease* with the frequency after a certain value, reaching null value at the highest diagonal frequencies. Indeed, checkerboard features, alternating high and low values, actually lie in the kernel of this gradient. In that respect, the central difference gradient is the worst, since this phenomenon appears also along vertical and horizontal directions, *i.e.* high frequency vertical or horizontal stripes lie also in its kernel. At last, our deviation gradient operator presents the best spectral properties of all four gradients introduced here, even though not fully isotropic.

Finally, let us mention that, motivated by similar concerns, Moisan (2007) introduces a specific *spectral* TV semi-norm, computed as a Riemann sum of norms of the

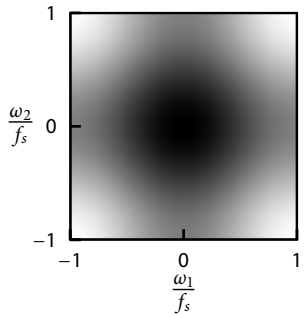

(a) One-sided, $\Delta_{\llcorner}^{*}\Delta_{\llcorner}$.

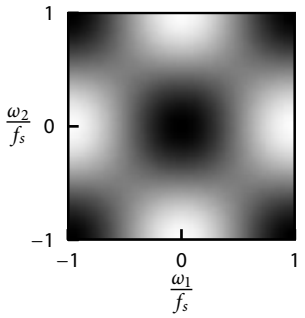

(b) Roberts cross, $\Delta_{\times}^{*}\Delta_{\times}$.

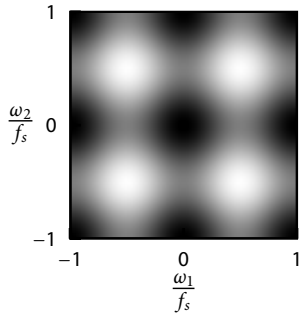

(c) Central difference, $\Delta_{+}^{*}\Delta_{+}$.

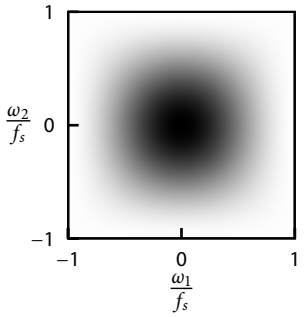

(d) Deviation, $\Delta_{\times}^{*}\Delta_{\times}$.

Figure 3: Anisotropies in eigenvalues of discrete two-dimensional Laplacians, derived from various finite differences schemes. Eigenvectors constitute a Fourier basis, so that they are indexed by spatial frequencies (ω_1, ω_2), normalized by the spatial sampling frequency f_s. Each colormap is linearly scaled between black (null modulus), and white (highest eigenvalue modulus).

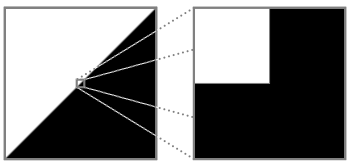

(a) $\|x\|_{\llcorner} = 2$.

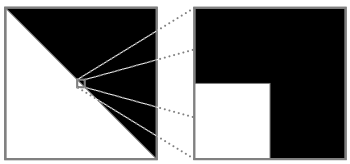

(b) $\|x\|_{\llcorner} = \sqrt{2}$.

Figure 4: Example of two edge orientations that are weighted differently by one-sided discretization. On each figure, the edge is represented on the left side, and a schematic view of the discretization is shown on the right side. The values of the resulting one-sided TV semi-norms, defined as $\|x\|_{\llcorner} \overset{\text{def}}{=} \sum_p \left\|\left(\Delta_{\llcorner}(x)\right)_p\right\|_2$, are given after normalization by the side length of the square.

analytical derivatives of the *Shannon interpolate* of the discrete signals. In spite of ideal spectral properties, this TV semi-norm is rarely used to our knowledge, in particular because of complexity overhead.

2.3 Anisotropies in Edge Orientations

Another important direction bias in common discretized gradients is due to their lack of spatial symmetry. This cannot be revealed by the previous spectral analysis, because gradient operators are symmetrized when computing their Laplacian. However, as pointed out by Chambolle *et al.* (2009), it can induce drastic differences between the TV semi-norms of an edge and of the same edge rotated by 90°. This is illustrated in Figure 4 for the TV semi-norm derived from the one-sided discrete gradient.

In contrast, our deviation TV semi-norm is invariant by rotations of 90°. Note that such rotation invariance can be imposed by adding coordinates to the gradient, as proposed in Chambolle *et al.* (2009) in the case of the one-sided discrete gradient; this, however, does not cope with the spectral anisotropies described in § 2.2.

2.4 Consistency With the Bounded Variation Semi-Norm

It could be interesting to study the consistency of our discretization with the original, continuous formulation of the TV semi-norm, the *bounded variation* (BV) semi-norm (see for instance Ambrosio *et al.* (2000)). Supposing that a discrete signal is a sampling of an underlying continuous one, it is possible to show that our TV semi-norm actually Γ-converges to the BV semi-norm of the continuous signal, as the discrete sampling tends to infinity. This is however beyond the scope of the present thesis, and we leave it for a future publication. For now, keep in mind that the answer to this question has little impact on the concrete applications of our discrete TV semi-norm, which, as one can see along the pages of this chapter, serves our purpose: favoring piecewise-constant solutions of variational signal reconstructions.

3 Proximal Splitting for Signal Processing

It is now time to derive the proximal splitting of all the functionals that we defined along the previous pages of this thesis. The aim of this section is to provide the tools for applying first-order proximal methods to minimization problems, arising in particular from inverse problems in signal processing; for the sake of completeness, we present already known results together with elementary proofs, alongside our contributions. Of course, we do not pretend to exhaustivity, since we restrain ourselves only to the functionals that are of interest to us; however the formulations in the current chapter are fairly general, and should already cover a large class of situations, where complex structured penalizations are relevant. For a more general review of proximal calculus, particularly in the context of signal processing, we refer the reader to Combettes and Pesquet (2011) and references therein.

In the continuity of the previous chapter, theoretical results are formulated in infinite dimensional settings, though practical results concern finite dimension. Throughout this chapter, we use the notations introduced in § III.1.1; $\mathcal{H}$ and $\mathcal{H}'$ are real Hilbert spaces, and $\|\cdot\|$, $\langle\cdot\,|\,\cdot\rangle$ and Id are respectively the norm, inner product and the identity operator over the appropriate space to be understood from the context.

3.1 Quadratic Functionals

We first address the case of functionals of the form $f(x) \stackrel{\text{def}}{=} \frac{1}{2}\|y - \Phi x\|^2$, where Φ is a linear operator and y is a given vector. This is probably the most common term appearing in linear inverse problems, usually motivated as a data-fidelity term as explained in the introduction, where observations are supposed to be corrupted by white Gaussian noise. Let us derive the gradient and proximity operators of f.

Proposition 3.1. *Let $\Phi : \mathcal{H} \to \mathcal{H}'$ be a bounded linear operator, let $y \in \mathcal{H}'$ and define $f : \mathcal{H} \to \mathbb{R} : x \mapsto \frac{1}{2}\|y - \Phi x\|^2$. The function f is differentiable everywhere, and its gradient is the affine function*

$$\nabla f : x \mapsto \Phi^*(\Phi x - y)\,, \tag{8}$$

which is Lipschitz continuous, with constant $\beta^{-1} = \|\Phi\|^2$.

Proof. For any $x, h \in \mathcal{H}$, we have $f(x+h) = \frac{1}{2}\langle \Phi(x+h) - y \,|\, \Phi(x+h) - y\rangle = f(x) + \frac{2}{2}\langle \Phi x - y \,|\, \Phi h\rangle + \frac{1}{2}\|h\|^2 = f(x) + \langle \Phi^*(\Phi x - y) \,|\, h\rangle + o(\|h\|^2)$, which is the definition of the gradient. Finally, for any $x_1, x_2 \in \mathcal{H}$, $\|\nabla f(x_1) - \nabla f(x_2)\| = \|\Phi^*\Phi(x_1 - x_2)\| \leq \|\Phi^*\|\|\Phi\|\|x_1 - x_2\| = \|\Phi\|^2\|x_1 - x_2\|$. ∎

Proposition 3.2. *With the hypothesis of Proposition 3.1, $f \in \Gamma_0(\mathcal{H})$, $(\mathrm{Id} + \gamma\Phi^*\Phi)$ is invertible, and for any $\gamma \in \mathbb{R}_{+*}$ and $x \in \mathcal{H}$,*

$$\mathrm{prox}_{\gamma f}(x) = (\mathrm{Id} + \gamma\Phi^*\Phi)^{-1}(x + \gamma\Phi^* y)\,. \tag{9}$$

Proof. The first statement follows from the facts that Φ is linear and continuous and that the squared norm is over $\mathcal{H}'$ a function of $\Gamma_0(\mathcal{H}')$ with full domain. Now, for $\gamma \in \mathbb{R}_{+*}$ and $x \in \mathcal{H}$, considering the variational problem (III.2) defining the proximity operator, and using Lemma III.1.3 (i)-(ii) and Proposition 3.1, we obtain for all $\xi \in \mathcal{H}$,

$$\begin{aligned} \mathrm{prox}_{\gamma f}(x) = \xi &\Leftrightarrow \xi - x + \gamma\Phi^*(\Phi\xi - y) = 0\,, \\ &\Leftrightarrow (\mathrm{Id} + \gamma\Phi^*\Phi)\xi = x + \gamma\Phi^* y\,. \end{aligned} \tag{10}$$

By *strong convexity* of the squared norm, $\mathrm{prox}_{\gamma f}(x)$ exists in $\mathcal{H}$ and is unique. Since $\gamma\Phi^* y$ is a fixed vector in $\mathcal{H}$, we deduce from (10) that $(\mathrm{Id} + \gamma\Phi^*\Phi)$ is bijective, hence invertible. The expression of $\mathrm{prox}_{\gamma f}(x)$ follows. ∎

Remark 3.1. By Lemma III.1.4 (ii)-(iii), the subdifferential of $f \in \Gamma_0(\mathcal{H})$ is a maximal monotone operator whose resolvent is the proximity operator of f; the existence of $\mathrm{prox}_{\gamma f}$ can then be established with Minty's theorem, Lemma III.1.2 (i) ⇔ (iv).

Remark 3.2. Noticing that $(\mathrm{Id}+\gamma\Phi^*\Phi)$ is self-adjoint, bounded from below and injective, it is easy to establish invertibility using the *closed range theorem* in functional analysis. Interestingly, we retrieve here this result using only classical arguments of convex analysis.

In a computational point of view, for repeated computations of the proximity operator of f given in (9), the vector $\Phi^* y$ can be precomputed, but inverting $(\mathrm{Id}+\gamma\Phi^*\Phi)$ in (9) may be in general demanding; see our concrete examples in § 5.2.1. In the following, we derive some important special cases that are useful for proximal algorithms.

3.1.1 Switching Φ and Φ^*

It often happens that the composition $\Phi\Phi^*$ is easier to handle that $\Phi^*\Phi$. In this case, consider the following proposition.

Proposition 3.3. *Let $\Phi\colon\mathcal{H}\to\mathcal{H}'$ be a bounded linear operator. Then, for any $\gamma\in\mathbb{R}_{+*}$, $(\mathrm{Id}+\gamma\Phi\Phi^*)$ is invertible, and*[1]

$$(\mathrm{Id}+\gamma\Phi^*\Phi)^{-1} = \mathrm{Id}-\gamma\Phi^*(\mathrm{Id}+\gamma\Phi\Phi^*)^{-1}\Phi\,. \tag{11}$$

Proof. This is a special case of the Sherman-Morrison-Woodbury formula, which holds true in infinite-dimension. Invertibility of $(\mathrm{Id}+\gamma\Phi\Phi^*)$ is ensured by Proposition 3.2 because boundedness of Φ implies boundedness of Φ^*. Then, for $\gamma\in\mathbb{R}_{+*}$,

$$\begin{aligned}\big(\mathrm{Id}-\gamma\Phi^*(\mathrm{Id}+\gamma\Phi\Phi^*)^{-1}\Phi\big)\big(\mathrm{Id}+\gamma\Phi^*\Phi\big)&\\ = \mathrm{Id}+\gamma\Phi^*\Phi-\gamma\Phi^*(\mathrm{Id}+\gamma\Phi\Phi^*)^{-1}(\mathrm{Id}+\gamma\Phi\Phi^*)\Phi\,,&\\ = \mathrm{Id}+\gamma\Phi^*\Phi-\gamma\Phi^*\Phi = \mathrm{Id}\,.&\end{aligned}$$

■

3.1.2 Augmenting the Dimensionality

Another interesting situation is when neither $\Phi^*\Phi$ nor $\Phi\Phi^*$ are easy to handle, but the linear operator can be decomposed as $\Phi \overset{\text{def}}{=} \Phi_1\Phi_2$, where both Φ_1 and Φ_2 have nicer computational properties. In such a case, a possible workaround, that has been used for instance in Briceño-Arias *et al.* (2011), is to introduce an auxiliary variable, augmenting $\mathcal{H}$ to $\tilde{\mathcal{H}} \overset{\text{def}}{=} \mathcal{H}\times\mathcal{H}'$, replacing $f\colon\mathcal{H}\to\mathbb{R}$ by $\tilde{f}\colon\tilde{\mathcal{H}}\to]-\infty,+\infty]$, defined by

$$\tilde{f}(x,u) \overset{\text{def}}{=} g_1(\tilde{x}) + g_2(\tilde{x})\,, \tag{12}$$

where $\tilde{x} \overset{\text{def}}{=} (x,u)\in\mathcal{H}\times\mathcal{H}'$, $g_1(\tilde{x}) \overset{\text{def}}{=} \frac{1}{2}\|y-\Phi_1 u\|^2$, and $g_2\colon\tilde{\mathcal{H}}\to]-\infty,+\infty]$ is defined by

$$g_2(\tilde{x}) \overset{\text{def}}{=} \begin{cases} 0 & \text{if } \Phi_2 x = u\,,\\ +\infty & \text{otherwise}\,. \end{cases}$$

[1] in Raguet *et al.* (2013, (3.3)), a factor γ has been forgotten in the formula.

In turn, a minimization problem of the form $\min_{x\in\mathcal{H}} \left\{F(x) \overset{\text{def}}{=} f(x) + \Psi(x)\right\}$ is equivalent to $\min_{\tilde{x}\overset{\text{def}}{=}(x,u)\in\tilde{\mathcal{H}}} \left\{\tilde{F}(\tilde{x}) \overset{\text{def}}{=} \tilde{f}(\tilde{x}) + \Psi(\tilde{x})\right\}$, where Ψ does not depend on u.

Since g_1 defined above does not depend on x, Proposition 3.2 provides directly

$$\operatorname{prox}_{\gamma g_1}(x,u) = \left(x,\ (\mathrm{Id} + \gamma\Phi_1{}^*\Phi_1)^{-1}(u + \gamma\Phi_1{}^* y)\right) . \tag{13}$$

Now by defining the linear operator $\tilde{\Phi}_2 : \tilde{\mathcal{H}} \to \mathcal{H}' : \tilde{x} \mapsto \Phi_2 x - u$, observe that g_2 is the indicator function of the set $\{\tilde{x} \overset{\text{def}}{=} (x,u) \in \tilde{\mathcal{H}} \,|\, \Phi_2 x = u\} = \ker\tilde{\Phi}_2$, which is closed and convex. Thus, $\operatorname{prox}_{\gamma g_2}$ is the orthogonal projector on the closed subspace $\ker\tilde{\Phi}_2$. Such projection is addressed in the following section, Proposition 3.4 .

3.2 Linear Constraints

The function $\iota_{\ker\tilde{\Phi}_2}$ defined above is a special instance of the class of functionals imposing *linear constraints* over solutions of optimization problems, also widely used in linear reconstructions. Consider first the following lemma.

Lemma 3.1. *Let $\Phi : \mathcal{H} \to \mathcal{H}'$ be a bounded linear operator with closed range. Then,*

(i) *Φ^* has closed range and $\operatorname{proj}_{\ker\Phi} = \mathrm{Id} - \operatorname{proj}_{\operatorname{ran}\Phi^*}$;*

(ii) *we have $\forall\, x \in \mathcal{H}, \forall\, v \in \mathcal{H}'$, $\operatorname{proj}_{\operatorname{ran}\Phi^*}(x) = \Phi^* v \Leftrightarrow \Phi\Phi^* v = \Phi x$.*

Proof. (i). By the closed range theorem, $(\ker\Phi)^\perp = \operatorname{ran}\Phi^*$, and the result follows. (ii). Let $x \in \mathcal{H}$. By definition $\operatorname{proj}_{\operatorname{ran}\Phi^*}(x) = \operatorname{argmin}_{\xi\in\operatorname{ran}\Phi^*} \frac{1}{2}\|x-\xi\|^2$. Since $\operatorname{ran}\Phi^* = \{\xi \in \mathcal{H} \,|\, \exists\, u \in \mathcal{H}',\ \xi = \Phi^* u\}$, we have

$$\begin{aligned} \operatorname{proj}_{\operatorname{ran}\Phi^*}(x) = \xi &\Leftrightarrow \exists\, v \in \operatorname{argmin}_{u\in\mathcal{H}'} \tfrac{1}{2}\|x - \Phi^* u\|^2,\ \xi = \Phi^* v\ , \\ &\Leftrightarrow \exists\, v \in \mathcal{H}',\ \Phi(\Phi^* v - x) = 0 \text{ and } \xi = \Phi^* v\ , \end{aligned} \tag{14}$$

where we derived the second equivalence using Lemma III.1.3 (i)-(ii) and Proposition 3.1. Establishing (ii) from (14) is straightforward. ∎

The above lemma shows that one can compute the projection of a vector x on the kernel of a linear operator Φ if one can find a vector v such that $\Phi\Phi^* v = \Phi x$. Let us precise some important special cases.

First, we derive the projection over the linear equality imposed with an auxiliary variable, as introduced above in § 3.1.2.

Proposition 3.4. *Let $\Phi : \mathcal{H} \to \mathcal{H}'$ be a bounded linear operator with closed range. Define the Hilbert space $\tilde{\mathcal{H}} \overset{\text{def}}{=} \mathcal{H} \times \mathcal{H}'$ endowed with the canonical inner product of the Cartesian product of Hilbert spaces, and $\tilde{\Phi} : \tilde{\mathcal{H}} \to \mathcal{H}' : (x,u) \mapsto \Phi x - u$. Then,*

(i) *$\tilde{\Phi}$ is a bounded linear operator with closed range, and its adjoint is $\tilde{\Phi}^* : \mathcal{H}' \to \tilde{\mathcal{H}} : v \mapsto (\Phi^* v, -v)$.*

(ii) *we have* $\forall\, \tilde{x} \overset{\text{def}}{=} (x,u) \in \tilde{\mathcal{H}}$, $\operatorname{proj}_{\ker\tilde{\Phi}}(\tilde{x}) = (x - \Phi^* v, u + v)$, *where the vector* v *is defined by* $v \overset{\text{def}}{=} (\mathrm{Id} + \Phi\Phi^*)^{-1}(\Phi x - u)$.

Proof. Let $\tilde{x} \overset{\text{def}}{=} (x,u) \in \tilde{\mathcal{H}}$ and $v \in \mathcal{H}'$.
(i). $\tilde{\Phi}$ is obviously linear, and we have $\|\tilde{\Phi}\tilde{x}\| \leq \|\Phi x\| + \|u\| \leq (\|\Phi\|+1)\|\tilde{x}\|$, so $\tilde{\Phi}$ is bounded. Then, $(0,-v) \in \tilde{\mathcal{H}}$, and $\tilde{\Phi}(0,-v) = v$, showing that $\tilde{\Phi}$ is surjective, and in particular has closed range. Finally, $\tilde{\Phi}^*$ as defined above is obviously linear, and $\langle \tilde{\Phi}\tilde{x} | v \rangle = \langle \Phi x \,|\, v \rangle - \langle u \,|\, v \rangle = \langle x \,|\, \Phi^* v \rangle + \langle u \,|\, -v \rangle = \langle \tilde{x} | \tilde{\Phi}^* v \rangle$.
(ii). We have $\tilde{\Phi}\tilde{\Phi}^* v = \tilde{\Phi}(\Phi^* v, -v) = \Phi\Phi^* v + v$, showing that $\tilde{\Phi}\tilde{\Phi}^* = \mathrm{Id} + \Phi\Phi^*$. We know from Proposition 3.3 with $\gamma \overset{\text{set}}{=} 1$ that the latter operator is invertible, and applying Lemma 3.1 (ii) gives $\operatorname{proj}_{\operatorname{ran}\tilde{\Phi}^*}(\tilde{x}) = \tilde{\Phi}^*\big(\tilde{\Phi}\tilde{\Phi}^*\big)^{-1}\tilde{\Phi}\tilde{x} = \tilde{\Phi}^* v = (\Phi^* v, -v)$, with v defined as above. Invoking Lemma 3.1 (i) terminates the proof. ∎

Remark 3.3. If $\mathrm{Id} + \Phi^*\Phi$ is easier to invert than $\mathrm{Id} + \Phi\Phi^*$, it is still possible in (ii) to call on Proposition 3.3 by switching the roles of Φ and Φ^*.

Now, a general linear *equality* constraint is the indicator function of a set $\Phi^{-}(\{u\}) \overset{\text{def}}{=} \{x \in \mathcal{H} \mid \Phi x = u\}$ for some $\Phi\colon \mathcal{H} \to \mathcal{H}'$ and $u \in \mathcal{H}'$. Such a set is closed and convex, and nonempty as soon as $u \in \operatorname{ran}\Phi$, *i.e.* there exists $y \in \mathcal{H}$, such that $\Phi y = u$. Assuming that such a vector y is known and that $\operatorname{proj}_{\ker\Phi}$ can be computed (for instance when $\Phi\Phi^*$ is invertible), the following proposition gives the projection over a linear equality constraint.

Proposition 3.5. *Let* $\Phi\colon \mathcal{H} \to \mathcal{H}'$ *be a bounded linear operator with closed range,* $y \in \mathcal{H}$ *and* $u \in \mathcal{H}'$ *such that* $\Phi y = u$. *Then, for all* $x \in \mathcal{H}$, $\operatorname{proj}_{\Phi^{-}(\{u\})}(x) = y + \operatorname{proj}_{\ker\Phi}(x - y)$.

Proof. For $z \in \mathcal{H}$, we have $z = \operatorname*{argmin}_{\xi \in \Phi^{-}(\{u\})} \|x - \xi\| \Leftrightarrow z - y = \operatorname*{argmin}_{\xi \in \Phi^{-}(\{0\})} \|(x-y) - \xi\|$. ∎

Finally, when the linear operator Φ is a functional, *i.e.* takes values in $\mathbb{R}$, then linear equality constraint can be naturally extended to inequality. A linear *inequality* constraint is the indicator function of a set $\Phi^{-}(]-\infty, u]) \overset{\text{def}}{=} \{x \in \mathcal{H} \mid \Phi x \leq u\}$, for some $\Phi\colon \mathcal{H} \to \mathbb{R}$ and $u \in \mathbb{R}$. The following proposition explicits the projection over a linear inequality constraint. Recall that by *Riesz representation theorem*, there exists $\phi \in \mathcal{H}$ such that for all $x \in \mathcal{H}$, $\Phi(x) = \langle \phi \,|\, x \rangle$; it is easy to see that for such a vector ϕ, we have $\Phi^*\colon \mathbb{R} \to \mathcal{H}\colon u \mapsto u\phi$.

Proposition 3.6 (projection on a half-space)**.** *Let* $\phi \in \mathcal{H}$ *be a nonzero vector,* $u \in \mathbb{R}$, *and define* $\Phi\colon \mathcal{H} \to \mathbb{R}$ *such that for all* $x \in \mathcal{H}$, $\Phi(x) \overset{\text{def}}{=} \langle \phi \,|\, x \rangle$. *Then for all* $x \in \mathcal{H}$,

(i) *if* $\Phi(x) \leq u$, *then* $\operatorname{proj}_{\Phi^{-}(]-\infty,u])}(x) = x$;

and if $\Phi(x) > u$, *then*

(ii) $\Phi\Big(\operatorname{proj}_{\Phi^{-}(]-\infty,u])}(x)\Big) = u$, *and*

(iii) $\operatorname{proj}_{\Phi^{-}(]-\infty,u])}(x) = x - \frac{\langle \phi \,|\, x \rangle}{\|\phi\|^2}\phi + \frac{u}{\|\phi\|^2}\phi$.

Proof. (i). Obvious. (ii). Let $x, z \in \mathcal{H}$, such that $\Phi(x) > u$ and $\Phi(z) < u$. Then, defining $\xi = \frac{u-\Phi(z)}{\Phi(x)-\Phi(z)}x + \frac{\Phi(x)-u}{\Phi(x)-\Phi(z)}z$, we have $\Phi(\xi) = u$, hence $\xi \in \Phi^-(]-\infty, u])$, and it is easy to verify that $\|x-\xi\| < \|x-z\|$, implying $z \neq \mathrm{proj}_{\Phi^-(]-\infty,u])}(x)$. The result follows by contraposition and the definition of $\mathrm{proj}_{\Phi^-(]-\infty,u])}(x)$. (iii). We deduce from (ii) that if $\Phi(x) > u$, then $\mathrm{proj}_{\Phi^-(]-\infty,u])}(x) = \mathrm{proj}_{\Phi^-(\{u\})}(x)$. Now, observe that $\Phi\Phi^*\colon \mathbb{R} \to \mathbb{R}\colon u \mapsto \langle \phi \,|\, u\phi \rangle = \|\phi\|^2 u$ is invertible, and that $y \stackrel{\text{def}}{=} \frac{u}{\|\phi\|^2}\phi$ satisfies $\Phi(y) = u$. Applying Proposition 3.5 with Lemma 3.1 yields the given expression. ∎

Remark 3.4 (projection on a polytope)**.** The point (ii) above justifies the term "half-space": the affine hyperplane $\Phi^-(\{u\})$ separate the space $\mathcal{H}$ in two domains, one of which is $\Phi^-(]-\infty, u])$. A *polytope in* $\mathcal{H}$ is defined as a (nonempty) intersection of half-spaces. Proposition 3.6 shows that any polytope constraint can be tackled with proximal splitting algorithms by introducing as many auxiliary variables as the number of half-spaces defining the polytope. In particular, we can show that the method of Llanas and Moreno (1996) for computing an orthogonal projection over a polytope is a particular instance of GFB for solving $\mathrm{argmin}_\xi \frac{1}{2}\|x-\xi\|^2 + \sum_{i=1}^n \iota_{\Phi^-(]-\infty,u])}(\xi)$.

However, it should be noted that, as the number of inequality constraints grows, the number of auxiliary variables required can become prohibitively large, and many polytope constraints have specific structure that can be better exploited. For instance, the orthant and box constraints defined in § 1.5 are actually polytope constraints, but the corresponding projections are addressed specifically in § 3.5.

3.3 Proximal Calculus with the Tight Frame Property

When a functional g is simple and Φ is a linear operator, Proposition 3.4 shows that in many circumstances, proximal splitting of the functional $g \circ \Phi$ can be achieved at the cost of augmenting the dimensionality of the problem by the dimension of $\mathrm{ran}\,\Phi$, following the technique described in § 3.1.2. This allows to deal with simple functions composed with linear operator, using primal-only (as opposed to primal-dual, mentioned in the introduction) proximal algorithms. This section is devoted to an important special case, where the introduction of an auxiliary variable is not required; such case is characterized by the following property.

Definition 3.1 (tight frame property)**.** We say that a linear operator $\Phi\colon \mathcal{H} \to \mathcal{H}'$ has the *tight frame property* with squared norm $\nu \in \mathbb{R}_{+*}$, if $\Phi\Phi^* = \nu\,\mathrm{proj}_{\mathrm{ran}\,\Phi}$.

Remark 3.5. One can show that an operator Φ has the tight frame property, if, and only if, for all $u \in \mathrm{ran}\,\Phi$, $\Phi\Phi^* u = \nu u$. In finite dimension (or more generally over separable Hilbert spaces), an operator which has the tight frame property can indeed be associated to a *tight frame* of its range (see for instance Mallat (2008) for the concept of tight frame).

Tight frames are extensively used in signal processing; for instance, any concatenation of orthogonal dictionaries results in a tight frame. For that reason, the following proposition is of importance in the context of proximal algorithms.

Proposition 3.7. *Let $\Phi\colon \mathcal{H} \to \mathcal{H}'$ be a bounded linear operator with closed range which has the tight frame property with squared norm $\nu \in \mathbb{R}_{+*}$, and $g \in \Gamma_0(\mathcal{H}')$ such that* $\operatorname{dom} g \cap \operatorname{ran}\Phi \neq \emptyset$. *Then,*

(i) $\operatorname{proj}_{\operatorname{ran}\Phi^*} = \frac{1}{\nu}\Phi^*\Phi$;

(ii) $g \circ \Phi \in \Gamma_0(\mathcal{H})$;

(iii) $\forall\, x \in \mathcal{H}$, $\operatorname{prox}_{\nu g}(\Phi x) \in \operatorname{ran}\Phi \Rightarrow \operatorname{prox}_{g\circ\Phi}(x) = x + \frac{1}{\nu}\Phi^*\big(\operatorname{prox}_{\nu g} - \mathrm{Id}\big)\Phi x$.

Proof. Let $x \in \mathcal{H}$. (i). Obviously $u \overset{\text{def}}{=} \Phi x \in \operatorname{ran}\Phi$, so that $\Phi\Phi^* u = \nu u$. We deduce $\frac{1}{\nu}\Phi\Phi^* u = \Phi x$, and Lemma 3.1 (ii) proves $\operatorname{proj}_{\operatorname{ran}\Phi^*}(x) = \frac{1}{\nu}\Phi^* u$. (ii). Since $\operatorname{dom} g \cap \operatorname{ran}\Phi \neq \emptyset$, $g \circ \Phi$ is proper. Lower semicontinuity and convexity of $g \circ \Phi$ follows respectively from lower semicontinuity of g and continuity of Φ, and convexity of g and linearity of Φ. (iii). We know from Lemma 3.1 that $\mathcal{H}$ is the orthogonal sum of $\ker\Phi$ and $\operatorname{ran}\Phi^*$. For $\xi \in \mathcal{H}$, denote then $\xi_{\ker\Phi} \overset{\text{def}}{=} \operatorname{proj}_{\ker\Phi}(\xi)$ and $\xi_{\operatorname{ran}\Phi^*} \overset{\text{def}}{=} \operatorname{proj}_{\operatorname{ran}\Phi^*}(\xi)$. Noticing that $\Phi\xi = \Phi\xi_{\operatorname{ran}\Phi^*}$, we get

$$\operatorname{prox}_{g\circ\Phi}(x) = \operatorname*{argmin}_{\xi\in\mathcal{H}} \tfrac{1}{2}\|x_{\ker\Phi} - \xi_{\ker\Phi}\|^2 + \tfrac{1}{2}\|x_{\operatorname{ran}\Phi^*} - \xi_{\operatorname{ran}\Phi^*}\|^2 + g(\Phi\xi_{\operatorname{ran}\Phi^*})\ .$$

Thus, the problem is separable along the complementary subspaces $\ker\Phi$ and $\operatorname{ran}\Phi^*$, and we deduce for $\hat{\xi} \in \mathcal{H}$, $\hat{\xi} = \hat{\xi}_{\ker\Phi} + \hat{\xi}_{\operatorname{ran}\Phi^*}$ and

$$\hat{\xi} = \operatorname{prox}_{g\circ\Phi}(x) \Leftrightarrow \begin{cases} \hat{\xi}_{\ker\Phi} = x_{\ker\Phi}\ , & \text{(15a)} \\ \hat{\xi}_{\operatorname{ran}\Phi^*} = \operatorname{argmin}_{\xi\in\operatorname{ran}\Phi^*} \tfrac{1}{2}\|x_{\operatorname{ran}\Phi^*} - \xi\|^2 + g(\Phi\xi)\ . & \text{(15b)} \end{cases}$$

Using (i), we get both (15a) $\Leftrightarrow \hat{\xi}_{\ker\Phi} = x - \frac{1}{\nu}\Phi^*\Phi x$, and

$$\begin{aligned} \text{(15b)} &\Leftrightarrow \exists\, \hat{v} \in \operatorname*{argmin}_{v\in\mathcal{H}'} \tfrac{1}{2}\|x_{\operatorname{ran}\Phi^*} - \Phi^* v\|^2 + g(\Phi\Phi^* v),\ \hat{\xi}_{\operatorname{ran}\Phi^*} = \Phi^*\hat{v}\ , \\ &\Leftrightarrow \exists\, \hat{v} \in \operatorname*{argmin}_{v\in\mathcal{H}'} \tfrac{1}{2}\|\tfrac{1}{\nu}\Phi^*\Phi x - \Phi^* v\|^2 + g(\Phi\Phi^* v),\ \hat{\xi}_{\operatorname{ran}\Phi^*} = \Phi^*\hat{v}\ . \qquad \text{(16)} \end{aligned}$$

Notice that the right-hand side of (16) is independent from the component of v along $\ker\Phi^* = (\operatorname{ran}\Phi)^\perp$. In particular, if $\hat{v}$ satisfies it, then so does $\operatorname{proj}_{\operatorname{ran}\Phi}(\hat{v})$, hence the minimization can be carried over $\operatorname{ran}\Phi$ instead of $\mathcal{H}'$. Now, developing for any $v \in \operatorname{ran}\Phi$, $\|\frac{1}{\nu}\Phi^*\Phi x - \Phi^* v\|^2 = \frac{1}{\nu}\big\langle \Phi^*\Phi x - \nu\Phi^* v \,\big|\, \frac{1}{\nu}\Phi^*\Phi x - \Phi^* v\big\rangle = \frac{1}{\nu}\langle \Phi x - \nu v \,|\, \Phi x - \nu v\rangle = \frac{1}{\nu}\|\Phi x - \nu v\|^2$, noticing that $g(\Phi\Phi^* v) = g(\nu v)$, and substituting $\hat{v}$ to $\nu\hat{v}$ in (16) yields

$$\text{(15b)} \Leftrightarrow \exists\, \hat{v} \in \operatorname*{argmin}_{v\in\operatorname{ran}\Phi} \tfrac{1}{2}\|\Phi x - v\|^2 + \nu g(v),\ \hat{\xi}_{\operatorname{ran}\Phi^*} = \tfrac{1}{\nu}\Phi^*\hat{v}\ .$$

Finally, if $\operatorname{prox}_{\nu g}(\Phi x) \in \operatorname{ran}\Phi$, then $\operatorname*{argmin}_{v\in\operatorname{ran}\Phi} \frac{1}{2}\|\Phi x - v\|^2 + \nu g(v) = \operatorname{prox}_{\nu g}(\Phi x)$, and the result follows. ∎

Remark 3.6 (surjective operator)**.** If Φ is surjective, then Φ has closed range, $\operatorname{dom} g \cap \operatorname{ran}\Phi \neq \emptyset$, and the condition $\operatorname{prox}_{\nu g}(\Phi x) \in \operatorname{ran}\Phi$ is satisfied for all $x \in \mathcal{H}$. One retrieves Combettes and Pesquet (2007, Proposition 11), where their hypothesis $\Phi\Phi^* = \nu \operatorname{Id}$ implies surjectivity of Φ. In their proof, the authors make use of the fact that $\partial(g \circ \Phi) = \Phi^* \circ \partial g \circ \Phi$. In the nonsurjective case, this condition is not sufficient anymore, as can be seen in Example 3.1 below.

Example 3.1. To see that the requirement $\operatorname{prox}_{\nu g}(\Phi x) \in \operatorname{ran}\Phi$ is necessary, set $\mathcal{H} \stackrel{\text{def}}{=} \mathcal{H}' \stackrel{\text{def}}{=} \mathbb{R}^2$, $\Phi \stackrel{\text{def}}{=} \operatorname{proj}_{\mathcal{D}_1}$ and $g \stackrel{\text{def}}{=} \iota_{\mathcal{D}_2}$, where the subspaces $\mathcal{D}_1$ and $\mathcal{D}_2$ are defined by $\mathcal{D}_1 \stackrel{\text{def}}{=} \{(x_1, x_2) \in \mathbb{R}^2 \,|\, x_2 = 0\}$ and $\mathcal{D}_2 \stackrel{\text{def}}{=} \{(x_1, x_2) \in \mathbb{R}^2 \,|\, x_1 = x_2\}$. We have $\operatorname{ran}\Phi = \mathcal{D}_1$, and Φ has obviously the tight frame property with squared norm $\nu \stackrel{\text{def}}{=} 1$. Moreover, $\operatorname{dom} g = \mathcal{D}_2$, so that $\operatorname{dom} g \cap \operatorname{ran}\Phi = \{(0,0)\} \neq \emptyset$. Then, it is easy to see that $g \circ \Phi = \iota_{\mathcal{D}_3}$, with $\mathcal{D}_3 \stackrel{\text{def}}{=} \{(x_1, x_2) \in \mathbb{R}^2 \,|\, x_1 = 0\}$. Note moreover that for all $x \in \mathbb{R}^2$,

$$\partial\iota_{\mathcal{D}_3}(x) = \begin{cases} \mathcal{D}_1 & \text{if } x \in \mathcal{D}_3 \\ \emptyset & \text{otherwise} \end{cases} = \left\{ \operatorname{proj}_{\mathcal{D}_1}(u) \,\middle|\, u \in \partial\iota_{\mathcal{D}_2}(\operatorname{proj}_{\mathcal{D}_1}(x)) \right\},$$

so that we have $\partial(g \circ \Phi) = \Phi^* \circ \partial g \circ \Phi$. However, considering for instance $x \stackrel{\text{set}}{=} (1,1)$, we have $\operatorname{prox}_{g\circ\Phi}(x) = \operatorname{proj}_{\mathcal{D}_3}(x) = (0,1)$, but

$$\begin{aligned} x + \Phi^*(\operatorname{prox}_g - \operatorname{Id})\Phi x &= (1,1) + \operatorname{proj}_{\mathcal{D}_1}\big(\operatorname{proj}_{\mathcal{D}_2} - \operatorname{Id}\big)(1,0) \\ &= (1,1) + \operatorname{proj}_{\mathcal{D}_1}\left(\left(\tfrac{1}{2}, \tfrac{1}{2}\right) - (1,0)\right) \\ &= (1,1) + \left(\tfrac{1}{2} - 1, 0\right) = \left(\tfrac{1}{2}, 1\right). \end{aligned}$$

Remark 3.7 (separability in singular vector basis)**.** For simplicity, we consider here the finite dimensional case. Suppose in Proposition 3.7 that Φ does *not* have the time frame property. Still, $M\colon \operatorname{ran}\Phi \to \operatorname{ran}\Phi\colon u \mapsto \Phi\Phi^* u$, is bijective and self-adjoint. With the *spectral theorem*, $M \stackrel{\text{def}}{=} UNU^*$, where U is orthogonal and $N \stackrel{\text{def}}{=} \operatorname{diag}(\nu_1, \ldots, \nu_r)$, with $r \stackrel{\text{def}}{=} \operatorname{rank}\Phi$ and for all $i \in \{1, \ldots, r\}$, $\nu_i \in \mathbb{R}_{+*}$. Define now $\tilde{\Phi} \stackrel{\text{def}}{=} M^{-\frac{1}{2}}\Phi$ and $\tilde{g}\colon \mathcal{H}' \to]-\infty, +\infty]$ with for all $u \in \mathcal{H}'$,

$$\tilde{g}(u) = \begin{cases} g\big(M^{\frac{1}{2}}u\big) & \text{if } u \in \operatorname{ran}\Phi, \\ +\infty & \text{otherwise}. \end{cases}$$

Observe that $g \circ \Phi = \tilde{g} \circ \tilde{\Phi}$, that $\tilde{\Phi}$ has the tight frame property with squared norm $\nu \stackrel{\text{set}}{=} 1$, and that $\tilde{g} \in \Gamma_0(\mathcal{H}')$ and $\operatorname{dom}\tilde{g} \cap \operatorname{ran}\tilde{\Phi} \neq \emptyset$. Let $x \in \mathcal{H}$; by definition of $\tilde{g}$, it is obvious that $\operatorname{prox}_{\tilde{g}}(\tilde{\Phi}x) \in \operatorname{ran}\Phi$. Since $\operatorname{ran}\Phi = \operatorname{ran}\tilde{\Phi}$, Proposition 3.7 gives

$$\begin{aligned} \operatorname{prox}_{g\circ\Phi}(x) = \operatorname{prox}_{\tilde{g}\circ\tilde{\Phi}}(x) &= x + \tilde{\Phi}^*\big(\operatorname{prox}_{\tilde{g}} - \operatorname{Id}\big)\tilde{\Phi}x, \\ &= x + \Phi^* M^{-\frac{1}{2}}\big(\operatorname{prox}_{\tilde{g}} - \operatorname{Id}\big)M^{-\frac{1}{2}}\Phi x. \end{aligned}$$

Unfortunately, computing $\operatorname{prox}_{\tilde{g}}$ is not easier than $\operatorname{prox}_{g\circ\Phi}$ in the general case. However, using that $M^{\frac{1}{2}}$ is bijective and U is an isometry (over $\operatorname{ran}\Phi$), we have

$$\begin{aligned}\operatorname{prox}_{\tilde{g}}(M^{-\frac{1}{2}}\Phi x) &= \operatorname*{argmin}_{v\in\operatorname{ran}\Phi} \tfrac{1}{2}\|M^{-\frac{1}{2}}\Phi x - v\|^2 + g\big(M^{\frac{1}{2}}v\big)\,,\\ &= M^{-\frac{1}{2}} \operatorname*{argmin}_{v\in\operatorname{ran}\Phi} \tfrac{1}{2}\|M^{-\frac{1}{2}}\Phi x - M^{-\frac{1}{2}}v\|^2 + g(v)\,,\\ &= M^{-\frac{1}{2}} \operatorname*{argmin}_{v\in\operatorname{ran}\Phi} \tfrac{1}{2}\|N^{-\frac{1}{2}}U^*(\Phi x - v)\|^2 + g(v)\,,\end{aligned}$$

where U is associated to an orthonormal basis $(u_i)_{1\leq i\leq r}$ of $\operatorname{ran}\Phi$; these are actually the left singular vectors of Φ, associated to nonzero singular values. Suppose now that the function g is separable according to the basis U over $\operatorname{ran}\Phi$, *i.e.* there exists r functions $g_i \in \Gamma_0(\mathbb{R})$ such that for all $v \in \operatorname{ran}\Phi$, $g(v) = \sum_{i=1}^r g_i(\langle u_i \,|\, v\rangle)$. We get for $\hat{v} \in \mathcal{H}'$,

$$\begin{aligned}\operatorname{prox}_{\tilde{g}}(M^{-\frac{1}{2}}\Phi x) = M^{-\frac{1}{2}}\hat{v} \Leftrightarrow \hat{v} &= \operatorname*{argmin}_{v\in\operatorname{ran}\Phi} \sum_{i=1}^r \tfrac{1}{2\nu_i}\langle u_i \,|\, \Phi x - v\rangle^2 + g_i(\langle u_i \,|\, v\rangle)\,,\\ \Leftrightarrow \hat{v} &= \sum_{i=1}^r \operatorname{prox}_{\nu_i g_i}(\langle u_i \,|\, \Phi x\rangle) u_i\,.\end{aligned}$$

Altogether, we established

$$\operatorname{prox}_{g\circ\Phi}(x) = x + \Phi^*\left(\sum_{i=1}^r \frac{1}{\nu_i}\big(\operatorname{prox}_{\nu_i g_i} - \mathrm{Id}\big)\Big(\langle u_i \,|\, \Phi x\rangle\Big)u_i\right),$$

extending Pustelnik *et al.* (2011, Proposition III.4) to non necessarily surjective Φ.

3.4 Proximal Splitting of Structured Penalizations

The formalization introduced in § 1 simplifies the manipulation of structured functionals over the Euclidean space $\mathbb{R}^P$. We hereby make use of the same formalization to describe a systematic proximal splitting approach that allows to take them into account with primal, first-order proximal algorithms.

Beyond those that are of direct interest to us and presented here, the same framework is actually suitable for many other functionals. In particular, let us mention the immediate extension of the $\ell_{1,2}$-norm (respectively $\delta_{1,2}$-norm) to the $\ell_{1,q}$-norm (respectively $\delta_{1,q}$-norm), where $0 < q \leq \infty$, by substituting a ℓ_q norm to the euclidean norm in (1) (respectively (2)). In particular, the specific case $q \overset{\text{set}}{=} \infty$ presents computational properties similar to the Euclidean case $q \overset{\text{set}}{=} 2$ developed below, and can be addressed following the same lines with few modifications.

Structured penalizations are useful for sufficiently many applications, especially in the sparsity framework, so that specific convex optimization techniques have been considered in the literature. Before mentioning some of them, we first describe our approach, because of its simplicity and generality. The technical results are stated subsequently.

3.4.1 Our Approach

It is well known that the proximity operators of the $\ell_{1,2}$- and $\ell_{1,\infty}$-norms can be computed efficiently, as long as they are defined over nonoverlapping group structures; see references in § 3.4.2, and developments in § 3.4.3, where we prove the same property for the $\delta_{1,2}$-semi-norm and the bounded amplitude and bounded deviation constraints.

Let now B be a group structure which is the concatenation of $n \in \mathbb{N}_*$ nonoverlapping group structures, *i.e.* $B \overset{\text{def}}{=} (B^{(i)})_{1\leq i\leq n}$. The key point is that, if g_{Λ_B} is any structured functional defined in § 1, parameterized by $\Lambda_B \overset{\text{def}}{=} \{B, (\lambda_b)_{b\in B}\}$, then we have

$$g_{\Lambda_B} = \sum_{i=1}^{n} g_{\Lambda_B^{(i)}} , \tag{17}$$

where for each $i \in \{1,\dots,n\}$, $g_{\Lambda_B^{(i)}}$ is the same structured functional but parameterized by $\Lambda_B^{(i)} \overset{\text{def}}{=} \{B^{(i)}, (\lambda_b)_{b\in B^{(i)}}\}$.

Since each $B^{(i)}$ is nonoverlapping, (17) constitute a splitting of the structured functional g_{Λ_B} into simple functions. Now, it easy to see that any group structure can be split as above; in the worst case with $n = |B|$ as $B = (b)_{b\in B}$, *i.e.* each single group in B is considered as a separate group structure. In the general case, notice that a group structure in which a given coordinate belongs to n different groups cannot be split into less than n nonoverlapping group structures. In the special case of block structures containing only blocks of a given size, which is of special interest to us, Proposition 1.2 gives an optimal splitting in terms of number of nonoverlapping block structures.

3.4.2 Different Proximal Approaches

Although surprisingly simple, the above proximal splitting of structured functional was never written, to our knowledge, in such generality. However, it is not the only approach possible. In direct continuity with § 3.2, consider that if B is any group structure, it is possible to decouple the interactions between overlapping groups by introducing the linear *grouping operator*

$$\Phi^{(B)}\colon \begin{array}{ccc} \mathbb{R}^P & \longrightarrow & \mathbb{R}^B \\ x & \longmapsto & (x_b)_{b\in B} \end{array} . \tag{18}$$

where we define the Euclidean space $\mathbb{R}^B \overset{\text{def}}{=} \underset{b\in B}{\times} \mathbb{R}^{|b|}$ endowed with the inner product naturally induced on the Cartesian product. Note that this space is indexed directly by groups of coordinates. In brief, $\tilde{B} \overset{\text{def}}{=} (b)_{b\in B}$ is thus a nonoverlapping group structure over $\mathbb{R}^B$, and one can define the structured functional $\tilde{g}_{\Lambda_{\tilde{B}}}$ parameterized by $\Lambda_{\tilde{B}} \overset{\text{def}}{=} \left\{\tilde{B}, (\lambda_b)_{b\in\tilde{B}}\right\}$, such that $g_{\Lambda_B} = \tilde{g}_{\Lambda_{\tilde{B}}} \circ \Phi^{(B)}$. Since $\tilde{g}_{\Lambda_{\tilde{B}}}$ is simple, one can resort either to primal proximal algorithms over the augmented space $\tilde{\mathcal{H}}$ as defined in § 3.1.2, with help of Proposition 3.4 and Remark 3.3 (note that $\mathrm{Id} + \Phi^{(B)*}\Phi^{(B)}$ is diagonal), or to primal-dual proximal algorithms. We prefer the splitting (17) over this approach because the former yields more symmetrical schemes, and require less auxiliary variables when applying primal methods.

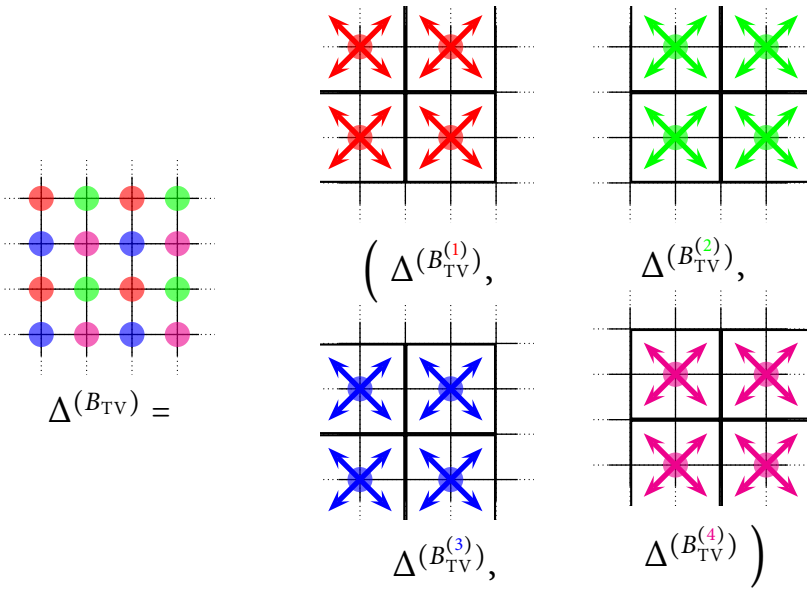

Figure 5: Illustration of the splitting of the deviation spatial gradient in dimension $\mathsf{D} \overset{\text{set}}{=} 2$, into four deviation operators over nonoverlapping block structures. On the left side, each dot is the center of a block of size 2×2; their color indicates which block grid they belong to in the splitting. We can see that all possible blocks of size 2×2 are taken into account.

Other approaches have been considered for tackling structured penalization with proximal methods. In particular, Jenatton *et al.* (2011) derive the proximity operators of $\ell_{1,2}$- and $\ell_{1,\infty}$-norms defined over *hierarchical* group structures, *i.e.* satisfying $\forall\, b, b' \in B,\ b \cap b' \neq \emptyset \Rightarrow b \subseteq b'$ or $b' \subseteq b$. The same group of authors subsequently developed in Mairal *et al.* (2011) a procedure for computing the proximity operator of a $\ell_{1,\infty}$-norm defined over an arbitrary group structure; though at the cost of significant theoretical and computational complexity overheads.

Their approach is different than ours, in the sense that they derive procedures for computing the proximity operators of structured norms, while we propose to split those norms into simpler functionals whose proximity operators are easy to compute. The main advantage of their approach lies in problems where a structured norm regularizes a smooth functional, with no other nonsmooth penalizations. Since their methods enable the computation of the proximity operator without further splitting, it is possible to call on accelerated schemes of the forward-backward algorithm (as mentioned in the introduction), which currently only allows for a single nonsmooth part in the splitting of the objective functional, and do not apply in general to our GFB. It would be interesting to compare the performances of both approaches over classical problems of signal processing or machine learning. However, we leave this to a future work, especially because the proximity operator of the $\ell_{1,2}$-norm over an overlapping group structure, which is the one of interest to us in the present work, is not available. On this point let us precise that in the case of a $\ell_{1,2}$-norm defined over an overlapping group structure, Mairal *et al.* (2011) actually propose the splitting approach involving the grouping operator (18),

solved with a primal-dual proximal algorithm.

Finally, a last approach that should be mentioned here is proposed by Chen *et al.* (2012), who apply the smoothing technique of Nesterov (2005) to the dual formulations of originally nonsmooth sparsity inducing penalizations. To ensure that the solution of the approximated problem is still sparse, they add a ℓ_1-norm term to the objective functional and solve it with a proximal splitting method. We did not investigate further this approach for two main reasons. First, the smoothing technique involves specific parameters that might have strong influence on the recovered solutions. Second, the introduction of the additional ℓ_1-norm in the objective seems rather arbitrary, and also increases the number of parameters.

3.4.3 Proximity Operators over Non-Overlapping Group Structures

For $\lambda \in \mathbb{R}_+$, we define the *closed ball of radius* λ of $\mathcal{H}$ by $\mathcal{B}_\lambda \stackrel{\text{def}}{=} \{u \in \mathcal{H} \,|\, \|u\| \leq \lambda\}$, and denote $\lambda\|\cdot\|$ the functional $x \mapsto \lambda\|x\|$. Let us first re-establish the following fundamental lemma; note that more general versions of it can be found for instance in Combettes and Pesquet (2008).

Lemma 3.2. *Let $\lambda \in \mathbb{R}_+$. For all $x \in \mathcal{H}$,*

$$\text{(i)}\quad \mathrm{prox}_{\lambda\|\cdot\|}(x) = \begin{cases} \left(1 - \frac{\lambda}{\|x\|}\right)x & \text{if } \|x\| > \lambda\,, \\ 0 & \text{if } \|x\| \leq \lambda\,. \end{cases}$$

$$\text{(ii)}\quad \mathrm{proj}_{\mathcal{B}_\lambda}(x) = \begin{cases} \frac{\lambda}{\|x\|}x & \text{if } \|x\| > \lambda\,, \\ x & \text{if } \|x\| \leq \lambda\,. \end{cases}$$

Proof. Since the norm is proper, continuous and convex, and $\mathcal{B}_\lambda$ is nonempty, closed and convex, those proximity operators are well defined. Take then $x \in \mathcal{H}$.
(i). We have $\mathrm{prox}_{\lambda\|\cdot\|}(x) = \mathrm{argmin}_{z\in\mathcal{H}} \left\{F(z) \stackrel{\text{def}}{=} \frac{1}{2}\langle x - z \,|\, x - z\rangle + \lambda\sqrt{\langle z \,|\, z\rangle}\right\}$. For $z \neq 0$, $\langle z \,|\, z\rangle > 0$ so that F is differentiable in z, with for all $h \in \mathcal{H}$, $\mathrm{d}F(z)(h) = \langle z - x \,|\, h\rangle + \lambda\frac{2\langle z \,|\, h\rangle}{2\sqrt{\langle z \,|\, z\rangle}} = \left\langle \left(1 + \frac{\lambda}{\|z\|}\right)z - x \,\middle|\, h\right\rangle$. Now if $\|x\| > \lambda$, define $\xi \stackrel{\text{def}}{=} \left(1 - \frac{\lambda}{\|x\|}\right)x$ and observe that $\|\xi\| = (\|x\| - \lambda) > 0$. Developing $\left(1 + \frac{\lambda}{\|\xi\|}\right)\xi = \left(1 + \frac{\lambda}{\|x\|-\lambda}\right)\left(1 - \frac{\lambda}{\|x\|}\right)x = x$ shows that $\mathrm{d}F(\xi) = 0$, and we deduce by convexity of F that $\xi = \mathrm{prox}_{\lambda\|\cdot\|}(x)$. Otherwise, if $\|x\| \leq \lambda$, then for all $z \in \mathcal{H}$, $F(x) = \frac{1}{2}\|x\|^2 + \frac{1}{2}\|z\|^2 - \langle x \,|\, z\rangle + \lambda\|z\|$. By Cauchy-Schwartz inequality, $\langle x \,|\, z\rangle \leq \lambda\|z\|$, so that $F(z) \leq \frac{1}{2}\|x\|^2 = F(0)$, hence $\mathrm{prox}_{\lambda\|\cdot\|}(x) = 0$.
(ii). If $\|x\| \leq \lambda$, then $x \in \mathcal{B}_\lambda$ and $\mathrm{proj}_{\mathcal{B}_\lambda}(x) = x$. Otherwise, define $\xi \stackrel{\text{def}}{=} \frac{\lambda}{\|x\|}x$, and observe that $\|\xi\| = \lambda$. Then, for all $z \in \mathcal{B}_\lambda$, $\|x - z\|^2 = \|x - \xi\|^2 + \|\xi - z\|^2 + 2\langle x - \xi \,|\, \xi\rangle - 2\langle x - \xi \,|\, z\rangle$. Again by Cauchy-Schwartz inequality, we have $\langle x - \xi \,|\, z\rangle \leq \left(1 - \frac{\lambda}{\|x\|}\right)\|x\|\lambda = \langle x - \xi \,|\, \xi\rangle$, and we deduce for all $z \in \mathcal{B}_\lambda$, $\|x - z\|^2 \geq \|x - \xi\|^2$, that is to say $\xi = \mathrm{proj}_{\mathcal{B}_\lambda}(x)$. ∎

Remark 3.8. In the proof, we voluntarily used only basic arguments. Interestingly, with the identity $\mathrm{prox}_g(x) = \xi \Leftrightarrow x \in \xi + \partial g(\xi)$, one can deduce from (i) that $\partial(\lambda\|\cdot\|)(0) =$

$\mathcal{B}_\lambda$, and from (ii) that if $\|x\| = \lambda$, then $\partial \iota_{\mathcal{B}_\lambda}(x) = \{\mu x \mid \mu \in \mathbb{R}_+\}$. Moreover, observe that we have $\operatorname{prox}_{\lambda\|\cdot\|} + \operatorname{proj}_{\mathcal{B}_\lambda} = \mathrm{Id}$. This is a particular instance of Moreau's identity (Moreau, 1962), $\iota_{\mathcal{B}_\lambda}$ being the *Fenchel conjugate* of $\lambda\|\cdot\|$ (see for instance Boyd and Vandenberghe (2004, Example 3.26)).

From now on, B is a nonoverlapping group structure over the Euclidean space $\mathbb{R}^P$ and $\Lambda \overset{\text{def}}{=} (\lambda_b)_{b\in B}$ is a family of nonnegative weights indexed by B. Then, we define the group of coordinates *complementary* to B, as $b^c \overset{\text{def}}{=} \{1,\dots,P\} \setminus \cup_{b\in B} b$; note that the concatenation (B, b^c) is nonoverlapping and covering, so that any vector $x \in \mathbb{R}^P$ can be indexed uniquely as $x \overset{\text{def}}{=} ((x_b)_{b\in B}, x_{b^c})$.

It is now straightforward to establish the proximity operator of the $\ell_{1,2}$-norm parameterized by Λ_B and of the corresponding bounded amplitude constraint.

Proposition 3.8. *For all* $x, \xi \in \mathbb{R}^P$,

$$\text{(i)}\quad \operatorname{prox}_{\|\cdot\|_{\ell,\Lambda_B}}(x) = \xi \Leftrightarrow \xi_{b^c} = x_{b^c} \text{ and } \forall\, b \in B,\ \xi_b = \begin{cases} \left(1 - \frac{\lambda_b}{\|x_b\|_2}\right) x_b & \text{if } \|x_b\|_2 > \lambda_b\,, \\ 0 & \text{if } \|x_b\|_2 \le \lambda_b\,; \end{cases}$$

$$\text{(ii)}\quad \operatorname{proj}_{\ell^{\infty}_{\Lambda_B}}(x) = \xi \Leftrightarrow \xi_{b^c} = x_{b^c} \text{ and } \forall\, b \in B,\ \xi_b = \begin{cases} \frac{\lambda_b}{\|x_b\|_2} x_b & \text{if } \|x_b\|_2 > \lambda_b\,, \\ x_b & \text{if } \|x_b\|_2 \le \lambda_b\,. \end{cases}$$

Proof. Let $x \in \mathbb{R}^P$. (i). Since (B, b^c) constitutes a partition of $\{1,\dots,P\}$, we have for all $\xi \in \mathbb{R}^P$, $\|\xi\|_2^2 = \sum_{p\in\{1,\dots,P\}} \xi_p^2 = \sum_{b\in(B,b^c)} \sum_{p\in b} \xi_p^2 = \sum_{b\in(B,b^c)} \|\xi_b\|_2^2$. Thus, we can write $\operatorname{prox}_{\|\cdot\|_{\ell,\Lambda_B}}(x) = \operatorname{argmin}_{\xi\in\mathbb{R}^P} \frac{1}{2}\|x_{b^c} - \xi_{b^c}\|_2^2 + \sum_{b\in B} \left(\frac{1}{2}\|x_b - \xi_b\|_2^2 + \lambda_b \|\xi_b\|_2\right)$. Since (B, b^c) is nonoverlapping, the problem is separable along the groups, and we get for all $\xi \in \mathbb{R}^P$, $\operatorname{prox}_{\|\cdot\|_{\ell,\Lambda_B}}(x) = \xi \Rightarrow \xi_{b^c} = x_{b^c}$ and $\forall\, b \in B,\ \xi_b = \operatorname{prox}_{\lambda_b\|\cdot\|_2}(x_b)$. Reciprocally, (B, b^c) is covering, so that this condition defines a unique vector in $\mathbb{R}^P$; by existence of the proximity operator (Remark 1.2) this vector is equal to $\operatorname{prox}_{\|\cdot\|_{\ell,\Lambda_B}}(x)$. Lemma 3.2 (i) over each separated group with $\mathcal{H} \overset{\text{set}}{=} \mathbb{R}^{|b|}$ completes the proof.
(ii). It is easy to verify that for all $\xi \in \mathbb{R}^P$, $\iota_{\ell^{\infty}_{\Lambda_B}}(\xi) = \sum_{b\in B} \iota_{\mathcal{B}_{\lambda_b}}(\xi_b)$, where for all $b \in B$, $\mathcal{B}_{\lambda_b}$ is the closed ball of radius λ_b in $\mathbb{R}^{|b|}$. Then, $\operatorname{proj}_{\ell^{\infty}_{\Lambda_B}}(x) = \operatorname{argmin}_{\xi\in\mathbb{R}^P} \frac{1}{2}\|x_{b^c} - \xi_{b^c}\|_2^2 + \sum_{b\in B} \left(\frac{1}{2}\|x_b - \xi_b\|_2^2 + \iota_{\mathcal{B}_{\lambda_b}}(\xi_b)\right)$. We conclude as above, with Lemma 3.2 (ii). ∎

Remark 3.9 (soft-thresholding)**.** Recall from Remark 1.1 that the ℓ_1-norm is a special case of the $\ell_{1,2}$-norm, with groups restrained to individual coefficients. In this case, the proximity operator reduces to the celebrated *soft-thresholding*.

The proximity operator of the $\delta_{1,2}$-semi-norm parameterized by Λ_B and of the corresponding bounded deviation constraint can now be established, following almost the same lines. Recall from Remark 1.4 that, given $x \in \mathbb{R}^P$ and $b \in B$, defining in $\mathbb{R}^{|b|}$, $\overrightarrow{x_b} \overset{\text{def}}{=} (\overline{x_b}, \dots, \overline{x_b})$, where $\overline{x_b} = \frac{1}{|b|}\sum_{p\in b} x_p$, we have $\Delta^{(b)} x_b = x_b - \overrightarrow{x_b}$.

Proposition 3.9. *For all* $x, \xi \in \mathbb{R}^P$,

(i) $\operatorname{prox}_{\|\cdot\|_{\delta,\Lambda_B}}(x) = \xi \Leftrightarrow \xi_{b^c} = x_{b^c}$ *and* $\forall\, b \in B$,

$$\xi_b = \begin{cases} \overrightarrow{x_b} + \left(1 - \frac{\lambda_b}{\|x_b - \overrightarrow{x_b}\|_2}\right)\left(x_b - \overrightarrow{x_b}\right) & \text{if } \|x_b - \overrightarrow{x_b}\|_2 > \lambda_b\,, \\ \overrightarrow{x_b} & \text{if } \|x_b - \overrightarrow{x_b}\|_2 \leq \lambda_b\,; \end{cases}$$

(ii) $\operatorname{proj}_{\delta\overline{\Lambda_B}}(x) = \xi \Leftrightarrow \xi_{b^c} = x_{b^c}$ *and* $\forall\, b \in B$,

$$\xi_b = \begin{cases} \overrightarrow{x_b} + \frac{\lambda_b}{\|x_b - \overrightarrow{x_b}\|_2}\left(x_b - \overrightarrow{x_b}\right) & \text{if } \|x_b - \overrightarrow{x_b}\|_2 > \lambda_b\,, \\ x_b & \text{if } \|x_b - \overrightarrow{x_b}\|_2 \leq \lambda_b\,. \end{cases}$$

Proof. Let $x \in \mathbb{R}^P$. (i). Following the proof of Proposition 3.8 (i), we can first write $\operatorname{prox}_{\|\cdot\|_{\delta,\Lambda_B}}(x) = \operatorname{argmin}_{\xi\in\mathbb{R}^P} \frac{1}{2}\|x_{b^c} - \xi_{b^c}\|_2^2 + \sum_{b\in B}\left(\frac{1}{2}\|x_b - \xi_b\|_2^2 + \lambda_b\|\Delta^{(b)}\xi_b\|_2\right)$, and deduce for all $\xi \in \mathbb{R}^P$, $\operatorname{prox}_{\|\cdot\|_{\delta,\Lambda_B}}(x) = \xi \Leftrightarrow \xi_{b^c} = x_{b^c}$ and $\forall\, b \in B$, $\xi_b = \operatorname{prox}_{\lambda_b\|\cdot\|_2\circ\Delta^{(b)}}(x_b)$. Now, for all $b \in B$, the linear operator $\Delta^{(b)}$ is self-adjoint and idempotent (Proposition III.1.1), hence $\Delta^{(b)}\Delta^{(b)*} = \operatorname{proj}_{\mathcal{S}_b^\perp}$; since $\operatorname{ran}\Delta^{(b)} = \mathcal{S}_b^\perp$, it has the tight frame property over its range, with squared norm 1. Moreover, we see from Lemma 3.2 (i) that for all $b \in B$, $\operatorname{prox}_{\lambda_b\|\cdot\|_2}(\Delta^{(b)}x_b)$ and $\Delta^{(b)}x_b$ are colinear, hence $\operatorname{prox}_{\lambda_b\|\cdot\|_2}(\Delta^{(b)}x_b) \in \mathcal{S}_b^\perp$. Altogether, applying Proposition 3.7 (iii) provides that for all $b \in B$,

$$\begin{aligned} \operatorname{prox}_{\lambda_b\|\cdot\|_2\circ\Delta^{(b)}}(x_b) &= x_b + \Delta^{(b)*}\left(\operatorname{prox}_{\lambda_b\|\cdot\|_2}(\Delta^{(b)}x_b) - \Delta^{(b)}x_b\right) \\ &= x_b + \operatorname{prox}_{\lambda_b\|\cdot\|_2}(x_b - \overrightarrow{x_b}) - (x_b - \overrightarrow{x_b}) \\ &= \overrightarrow{x_b} + \operatorname{prox}_{\lambda_b\|\cdot\|_2}(x_b - \overrightarrow{x_b}), \end{aligned}$$

and we conclude again with Lemma 3.2 (i).
(ii). Now, as for the proof of Proposition 3.8 (ii), $\operatorname{proj}_{\delta\overline{\Lambda_B}}(x) = \operatorname{argmin}_{\xi\in\mathbb{R}^P} \frac{1}{2}\|x_{b^c} - \xi_{b^c}\|_2^2 + \sum_{b\in B}\left(\frac{1}{2}\|x_b - \xi_b\|_2^2 + \iota_{\mathcal{B}_{\lambda_b}}(\Delta^{(b)}\xi_b)\right)$. Similarly as above, we see from Lemma 3.2 (ii) that $\operatorname{proj}_{\mathcal{B}_{\lambda_b}}(\Delta^{(b)}x_b) \in \mathcal{S}_b^\perp$, and Proposition 3.7 (iii) gives for all $b \in B$, $\operatorname{prox}_{\iota_{\mathcal{B}_{\lambda_b}}\circ\Delta^{(b)}}(x_b) = \overrightarrow{x_b} + \operatorname{proj}_{\mathcal{B}_{\lambda_b}}(x_b - \overrightarrow{x_b})$, and we conclude with Lemma 3.2 (ii). ∎

3.4.4 Proximity Operators of Composite Structured Penalizations

In many applications, different structured penalizations are considered within the same functional to be minimized, in order to benefit from various priors one can have on the problem at hand. It is the case in our SMCS model for VSDOI, § II.3, where the coefficients of the periodic artifacts are penalized by both a $\ell_{1,2}$-norm and a bounded amplitude constraint, and the coefficients of the neuronal activity are penalized simultaneously by a $\ell_{1,2}$-norm, a $\delta_{1,2}$-semi-norm and a bounded deviation constraint. Another example is the so-called *fused LASSO* penalization, which is nothing but the combination of a $\ell_{1,2}$-norm and a $\delta_{1,2}$-semi-norm. Introduced in dimension $\mathsf{D} \overset{\text{set}}{=} 1$ in the context of statistics by Tibshirani *et al.* (2005), it has been since used under different versions in other areas, see for instance Friedman *et al.* (2007); Liu *et al.* (2010); Nowak *et al.* (2011); Nelson (2013).

Our work generalizes such composite structured penalizations in any spatial dimension D, and propose state-of-the-art approaches for efficient, large scale minimizations. So far, we demonstrated that any structured penalization as defined in § 1 can be split into a certain number of simple functionals; obviously, it is still the case for any sum of such penalizations. However, for limiting the computational load of an iterative proximal algorithm applied to such splitting, one should always reduce as much as possible the number of simple functionals involved in the splitting. For this reason, we demonstrate here that under the right hypothesis, the proximity operator of a sum of structured functionals can be efficiently computed without further splitting. The key point of this result lie in the following lemma.

Lemma 3.3. *Let $\Phi\colon \mathcal{H} \to \mathcal{H}'$ be a linear operator, and $g\colon \mathcal{H} \to \mathbb{R}\colon x \mapsto \|\Phi x\|$. Then, for all $x, \xi \in \mathcal{H}$ and $\rho \in \mathbb{R}_+$ such that $\Phi\xi = \rho\Phi x$, $\partial g(x) \subseteq \partial g(\xi)$.*

Proof. Let $x, \xi \in \mathcal{H}$, and $u \in \partial g(x)$. First, suppose that $\Phi\xi = 0$. For all $h \in \mathcal{H}$, on one hand, using the triangular inequality we have $g(x) + g(h) \geq g(x+h) \geq g(x) + \langle u \,|\, h\rangle$, so that $g(h) \geq \langle u \,|\, h\rangle$, and on the other hand, $g(\xi + h) = \|\Phi(\xi + h)\| = \|\Phi h\| = g(h)$. Since $g(\xi) = 0$, we have thus for all $h \in \mathcal{H}$, $g(\xi + h) \geq g(\xi) + \langle u \,|\, h\rangle$, *i.e.* $u \in \partial g(\xi)$. Now, suppose that there exists $\rho \in \mathbb{R}_{+*}$ such that $\Phi\xi = \rho\Phi x$. For all $h \in \mathcal{H}$, we have $g(\xi + h) = \|\rho\Phi x + \Phi h\| = \rho\|\Phi x + \Phi\frac{1}{\rho}h\| = \rho g(x + \frac{1}{\rho}h) \geq \rho\Big(g(x) + \Big\langle u \,\Big|\, \frac{1}{\rho}h\Big\rangle\Big)$, and thus $g(\xi + h) \geq g(\xi) + \langle u \,|\, h\rangle$. ∎

We have seen in § 3.4.3 that proximity operators of $\ell_{1,2}$-norm and bounded constraints over nonoverlapping group structures are groupwise shrinkage operators. Using the above lemma, we can show that proximity operators of sums of some structured functionals reduce to *compositions* of proximity operators, provided that the functionals are defined over suitable block structures. Namely, in Proposition 3.10 below, (i) requires block structures which are *mutually hierarchical*, while (ii) requires block structures which are identical.

Proposition 3.10. *Let B, B' and B'' be nonoverlapping block structures over $\mathbb{R}^P$, such that for any $b \in B$, $b' \in B'$ and $b'' \in B''$, $b \cap b' \neq \emptyset \Rightarrow b \subseteq b'$ and $b' \cap b'' \neq \emptyset \Rightarrow b' \subseteq b''$. Moreover, let $\Lambda \stackrel{\text{def}}{=} (\lambda_b)_{b\in B}$, $\Lambda' \stackrel{\text{def}}{=} \big(\lambda'_{b'}\big)_{b'\in B'}$ and $\Lambda'' \stackrel{\text{def}}{=} \big(\lambda''_{b''}\big)_{b''\in B''}$ be families of nonnegative weights indexed respectively by B, B' and B''; denote finally the parameters $\Lambda_B \stackrel{\text{def}}{=} \{B, \Lambda\}$, $\Lambda'_B \stackrel{\text{def}}{=} \{B', \Lambda'\}$ and $\Lambda''_B \stackrel{\text{def}}{=} \{B'', \Lambda''\}$. Then,*

(i) $$\operatorname{prox}_{\iota_{\ell\overline{\Lambda''_B}} + \|\cdot\|_{\ell,\Lambda'_B} + \|\cdot\|_{\delta,\Lambda_B}} = \operatorname{proj}_{\ell\overline{\Lambda''_B}} \circ \operatorname{prox}_{\|\cdot\|_{\ell,\Lambda'_B}} \circ \operatorname{prox}_{\|\cdot\|_{\delta,\Lambda_B}},$$

in particular, $\operatorname{prox}_{\iota_{\ell\overline{\Lambda''_B}} + \|\cdot\|_{\ell,\Lambda'_B}} = \operatorname{proj}_{\ell\overline{\Lambda''_B}} \circ \operatorname{prox}_{\|\cdot\|_{\ell,\Lambda'_B}}$, $\operatorname{prox}_{\iota_{\ell\overline{\Lambda''_B}} + \|\cdot\|_{\delta,\Lambda_B}} = \operatorname{proj}_{\ell\overline{\Lambda''_B}} \circ \operatorname{prox}_{\|\cdot\|_{\delta,\Lambda_B}}$, *and* $\operatorname{prox}_{\|\cdot\|_{\ell,\Lambda'_B} + \|\cdot\|_{\delta,\Lambda_B}} = \operatorname{prox}_{\|\cdot\|_{\ell,\Lambda'_B}} \circ \operatorname{prox}_{\|\cdot\|_{\delta,\Lambda_B}}$.

(ii) $$\operatorname{prox}_{\iota_{\delta\overline{\Lambda_B}} + \|\cdot\|_{\delta,\Lambda_B}} = \operatorname{proj}_{\delta\overline{\Lambda_B}} \circ \operatorname{prox}_{\|\cdot\|_{\delta,\Lambda_B}}.$$

Proof. We denote by $b^c \overset{\text{def}}{=} \{1,\dots,P\} \setminus \cup_{b\in B} b$, $b^{c\prime} \overset{\text{def}}{=} \{1,\dots,P\} \setminus \cup_{b'\in B'} b'$ and $b^{c\prime\prime} \overset{\text{def}}{=} \{1,\dots,P\} \setminus \cup_{b''\in B''} b''$ complementary to B, B' and B'', respectively. Let then $x \in \mathcal{H}$.
(i). Define first $\xi \overset{\text{def}}{=} \mathrm{prox}_{\|\cdot\|_{\delta,\Lambda_B}}(x)$. Following the proof of Proposition 3.9 (i), we have $\xi_{b^c} = x_{b^c}$ and for all $b \in B$, $\xi_b = \mathrm{prox}_{\lambda_b\|\cdot\|_2\circ\Delta^{(b)}}(x_b)$. Defining $u \overset{\text{def}}{=} x - \xi$, the characterization of the proximity operator in terms of subdifferential shows that

$$u_{b^c} = 0 \quad \text{and} \quad \forall\, b \in B,\ u_b \in \partial(\lambda_b\|\cdot\|_2 \circ \Delta^{(b)})(\xi_b)\ . \tag{19}$$

Now, define $\xi' \overset{\text{def}}{=} \mathrm{prox}_{\|\cdot\|_{\ell,\Lambda'_B}}(\xi)$. On one hand, similarly as above, we can establish from Proposition 3.8 (i) that with $u' \overset{\text{def}}{=} \xi - \xi'$, we have

$$u'_{b^{c\prime}} = 0 \quad \text{and} \quad \forall\, b' \in B',\ u'_{b'} \in \partial(\lambda'_{b'}\|\cdot\|_2)(\xi'_{b'})\ . \tag{20}$$

On the other hand, observe also with Proposition 3.8 (i) that for all $b' \in (B', b^{c\prime})$, there exists $\rho_{b'} \in \mathbb{R}_+$ such that $\xi'_{b'} = \rho_{b'}\xi_{b'}$. Taking any $b \in (B, b^c)$, according to the properties of B and B', there exists a unique $b' \in (B', b^{c\prime})$ such that $b \subseteq b'$, so that $\xi'_b = \rho_{b'}\xi_b$. Using, for each $b \in B$, Lemma 3.3 with $\mathcal{H} \overset{\text{set}}{=} \mathbb{R}^{|b|}$ and $\Phi \overset{\text{set}}{=} \mathrm{Id}$, we get from (19)

$$u_{b^c} = 0 \quad \text{and} \quad \forall\, b \in B,\ u_b \in \partial(\lambda_b\|\cdot\|_2 \circ \Delta^{(b)})(\xi'_b)\ . \tag{21}$$

Finally, define $\xi'' \overset{\text{def}}{=} \mathrm{proj}_{\ell^{\overline{\Lambda''_B}}}(\xi')$. Similarly, we get from Proposition 3.8 (ii) that with $u'' \overset{\text{def}}{=} \xi' - \xi''$,

$$u''_{b^{c\prime\prime}} = 0 \quad \text{and} \quad \forall\, b'' \in B'',\ u''_{b''} \in \partial\iota_{\mathcal{B}_{\lambda''_b}}(\xi''_{b''})\ , \tag{22}$$

and that for all $b'' \in (B'', b^{c\prime\prime})$, there exists $\rho_{b''} \in \mathbb{R}_+$ such that $\xi''_{b''} = \rho_{b''}\xi'_{b''}$. Using again Lemma 3.3 with (20) and (21) gives respectively

$$u'_{b^{c\prime}} = 0 \quad \text{and} \quad \forall\, b' \in B',\ u'_{b'} \in \partial(\lambda'_{b'}\|\cdot\|_2)(\xi''_{b'})\ , \tag{23}$$

and

$$u_{b^c} = 0 \quad \text{and} \quad \forall\, b \in B,\ u_b \in \partial(\lambda_b\|\cdot\|_2 \circ \Delta^{(b)})(\xi''_b)\ . \tag{24}$$

Using separability of the structured functionals along the blocks, it is now straightforward to establish that $u'' \in \partial\iota_{\ell^{\overline{\Lambda''_B}}}(\xi'')$, $u' \in \partial(\|\cdot\|_{\ell,\Lambda'_B})(\xi'')$, and $u \in \partial(\|\cdot\|_{\delta,\Lambda_B})(\xi'')$, from (22), (23) and (24), respectively. Recalling Lemma III.1.3 (iii) on the subdifferential of sums, $\|\cdot\|_{\ell,\Lambda'_B}$ and $\|\cdot\|_{\delta,\Lambda_B}$ having full domain, we deduce $u'' + u' + u \in \partial(\iota_{\ell^{\overline{\Lambda''_B}}} + \|\cdot\|_{\ell,\Lambda'_B} + \|\cdot\|_{\delta,\Lambda_B})(\xi'')$; and with $\xi'' + u'' + u' + u = x$ we conclude $\xi'' = \mathrm{prox}_{\iota_{\ell^{\overline{\Lambda''_B}}}+\|\cdot\|_{\ell,\Lambda'_B}+\|\cdot\|_{\delta,\Lambda_B}}(x)$.
The particular cases can be established with, respectively, for all $b \in B$, $\lambda_b = 0$, for all $b' \in B'$, $\lambda'_{b'} = 0$, and for all $b'' \in B''$, $\lambda''_{b''} \to \infty$.
(ii). As previously, we define $\xi \overset{\text{def}}{=} \mathrm{prox}_{\|\cdot\|_{\delta,\Lambda_B}}(x)$ and $u = x - \xi$. However, we define now $\xi' = \mathrm{proj}_{\delta^{\overline{\Lambda_B}}}(\xi)$ and the proof of Proposition 3.9 (ii) shows that, for all $b \in (B, b^c)$, there exists $\rho_b \in \mathbb{R}_+$ such that $\Delta^{(b)}\xi'_b = \rho_b\Delta^{(b)}\xi_b$. Using this time, for each $b \in B$, Lemma 3.3 with $\mathcal{H} \overset{\text{set}}{=} \mathbb{R}^{|b|}$ and $\Phi \overset{\text{set}}{=} \Delta^{(b)}$, we get from (19) that $u \in \partial(\|\cdot\|_{\delta,\Lambda_B})(\xi')$. With $u' \overset{\text{def}}{=} \xi - \xi' \in \partial\iota_{\delta^{\overline{\Lambda_B}}}(\xi')$ and $\xi' + u' + u = x$, we conclude as above $\xi' = \mathrm{prox}_{\iota_{\delta^{\overline{\Lambda_B}}}+\|\cdot\|_{\delta,\Lambda_B}}(x)$. ∎

3.5 Projection on Simple Convex Sets

At last, let us explicit the simple projections over the orthant and box constraints, making use, as in the previous section, of the separability of the Euclidean norm along the coordinates.

Proposition 3.11. *Let* $(v, \epsilon) \in \mathbb{R}^P \times \{-1, +1\}^P$, *and* $(\underline{v}, \overline{v}) \in \mathbb{R}^P \times \mathbb{R}^P$ *such that for all* $p \in \mathbb{R}^P$, $\underline{v}_p \leq \overline{v}_p$. *Then for all* $x \in \mathbb{R}^P$,

(i) $\operatorname{proj}_{[v,\epsilon)}(x) = \big(\epsilon_p \max(\epsilon_p v_p, \epsilon_p x_p)\big)_{1\leq p\leq P}$;

(ii) $\operatorname{proj}_{[\underline{v},\overline{v}]}(x) = \Big(\max\big(\underline{v}_p, \min(\overline{v}_p, x_p)\big)\Big)_{1\leq p\leq P}$.

In particular, $\operatorname{proj}_{+}(x) = \big(\max(0, x_p)\big)_{1\leq p\leq P}$.

Proof. Let $x \in \mathbb{R}^P$. (i). The separation yields $\operatorname{proj}_{[v,\epsilon)}(x) = \operatorname*{argmin}_{\xi\in\mathbb{R}^P} \sum_{p=1}^P \Big(\frac{1}{2}\big(x_p - \xi_p\big)^2 + \iota_{[v_p,\epsilon_p)}(\xi_p)\Big) = \Big(\operatorname{proj}_{[v_p,\epsilon_p)}(x_p)\Big)_{1\leq p\leq P}$. For all $p \in \{1, \dots, P\}$, if $\epsilon_p = +1$, then $[v_p, \epsilon_p) = [v_p, +\infty[$. By cases analysis, $\operatorname{proj}_{[v_p,+\infty[}(x_p) = \begin{cases} x_p & \text{if } x_p \geq v_p \\ v_p & \text{if } x_p < v_p \end{cases}$, *i.e.* $\operatorname{proj}_{[v_p,+\infty[}(x_p) = \max\big(v_p, x_p\big)$. Similarly if $\epsilon_p = -1$, $\operatorname{proj}_{]-\infty,v_p]}(x_p) = \min\big(v_p, x_p\big) = -\max\big(-v_p, -x_p\big)$.
(ii). $\operatorname{proj}_{[\underline{v},\overline{v}]}(x) = \operatorname*{argmin}_{\xi\in\mathbb{R}^P} \sum_{p=1}^P \Big(\frac{1}{2}\big(x_p - \xi_p\big)^2 + \iota_{[\underline{v}_p,\overline{v}_p]}(\xi_p)\Big) = \Big(\operatorname{proj}_{[\underline{v}_p,\overline{v}_p]}(x_p)\Big)_{1\leq p\leq P}$. For $p \in \{1, \dots, P\}$, by cases analysis, $\operatorname{proj}_{[\underline{v}_p,\overline{v}_p]}(x_p) = \begin{cases} \underline{v}_p & \text{if } x_p < \underline{v}_p \\ x_p & \text{if } \underline{v}_p \leq x_p \leq \overline{v}_p \\ \overline{v}_p & \text{if } x_p > \overline{v}_p \end{cases}$, and we deduce $\operatorname{proj}_{[v_p,+\infty[}(x_p) = \max\big(\underline{v}_p, \min(\overline{v}_p, x_p)\big)$. ∎

4 Efficient Implementation of Splitting Algorithms

The theoretical developments of the previous section enables the application of proximal splitting algorithms to a wide range of convex optimization problems. As underlined in the introduction, such algorithms are especially interesting thanks to their relative simplicity of implementation. However, for generality of exposition and ease of analysis, algorithms are written in abstract form, as we did for instance on Figure III.1. This might hide the structure of the specific problem at hand, so that a naive implementation is often suboptimal.

In this section, we expose situations that are common in variational problems for signal processing, and we give some practical implementation considerations that may reduce significantly the computational load of proximal splitting methods. We specify here the case of the generalized forward-backward algorithm for minimizing

$$\min_{x\in\mathcal{H}} \Big\{ F(x) \stackrel{\text{def}}{=} f(x) + \sum_{i=1}^n g_i(x) \Big\}\,, \tag{25}$$

though the following techniques can be adapted to other proximal splitting algorithms.

Let us first rewrite the main iteration of Algorithm III.2, where we use an auxiliary variable $p \in \mathcal{H}$ to avoid computing n times the gradient of f per iterations.

$$\begin{aligned} &p \leftarrow 2x - \gamma \nabla f(x)\,; \\ &\textbf{for } i \in \{1,\dots,n\} \textbf{ do} \\ &\quad z_i \leftarrow z_i + \rho_k\big(\operatorname{prox}_{\frac{\gamma}{w_i} g_i}\big(p - z_i\big) - x\big)\,; \\ &x \leftarrow \textstyle\sum_{i=1}^n w_i z_i\,. \end{aligned} \tag{26}$$

4.1 GFB with Tight Frames

We have shown that, under suitable hypothesis, the composition of a simple functional with a linear operator with the tight frame property is also a simple functional, its proximity operator being given by Proposition 3.7 (iii).

Let now $I \subseteq \{1,\dots,n\}$, define $I^c \stackrel{\text{def}}{=} \{1,\dots,n\} \smallsetminus I$, and extend the problem (25) to

$$\min_{x\in\mathcal{H}} \Big\{ F(x) \stackrel{\text{def}}{=} f(x) + \sum_{i\in I} g_i(L_i(x)) + \sum_{i\in I^c} g_i(x) \Big\}\,, \tag{27}$$

where for each $i \in I$, $L_i\colon \mathcal{H} \to \mathcal{H}_i$ is a linear operator (bounded, with closed range[2]), $g_i \in \Gamma_0(\mathcal{H}_i)$ such that $\operatorname{ran} L_i \cap \operatorname{dom} g_i \neq \emptyset$, and there exists $\nu_i \in \mathbb{R}_{+*}$ such that for all $u \in \operatorname{ran} L_i$, $L_i L_i^* u = \nu_i u$ and $\operatorname{prox}_{\frac{\nu_i\gamma}{w_i} g_i}(u) \in \operatorname{ran} L_i$.

Using Proposition 3.7 (iii), for all $i \in I$, the update (26) becomes

$$z_i \leftarrow z_i + \rho_k(p - z_i - x) + \frac{\rho_k}{\nu_i} L_i^*\big(\operatorname{prox}_{\frac{\nu_i\gamma}{w_i} g_i} - \mathrm{Id}\big) L_i(p - z_i)\,. \tag{28}$$

The following computational tricks rely on the same observation: the nonlinear part in this update involves the knowledge of $L_i z_i$ but not of z_i. Hence, it is possible to store only the values of $L_i z_i$, at the expense of a few auxiliary variables keeping track of the missing information over $\ker L_i$. We detail here some circumstances where this can be useful. Note that we suppose here that proper implementation does not necessitate auxiliary variables for additions and/or applications of linear operators.

4.1.1 The General Case

Define $z_I \stackrel{\text{def}}{=} \sum_{i\in I} w_i z_i \in \mathcal{H}$, and for all $i \in I$, $\zeta_i \stackrel{\text{def}}{=} L_i z_i \in \mathcal{H}_i$. Note that, according to the properties of g_i and L_i, $\big(\operatorname{prox}_{\frac{\nu_i\gamma}{w_i} g_i} - \mathrm{Id}\big) L_i(p - z_i) \in \operatorname{ran} L_i$ so that the update of ζ_i can be reduced to

$$\zeta_i \leftarrow \zeta_i - \rho_k L_i x + \rho_k \operatorname{prox}_{\frac{\nu_i\gamma}{w_i} g_i}(L_i p - \zeta_i)\,. \tag{29}$$

In the same time, in view of (28), the updates of z_I can be ensured with an additional auxiliary variable $\zeta \in \mathcal{H}_i$ within the scope of the loop over $i \in I$, according to the following main iteration[3]

[2] in a computational context, the dimension is always finite...

[3] the initialization must satisfy $z_I = \sum_{i\in I} w_i z_i \in \mathcal{H}$, this can be done typically by initializing all variables to zero.

$$
\begin{aligned}
&p \leftarrow 2x - \gamma \nabla f(x) \,; \\
&z_I \leftarrow (1-\rho_k) z_I + \rho_k \big(\textstyle\sum_{i\in I} w_i\big)(p - x) \,; \\
&\textbf{for } i \in I \textbf{ do} \\
&\quad \pi \leftarrow L_i p \,; \\
&\quad \zeta \leftarrow \operatorname{prox}_{\frac{v_i \gamma}{w_i} g_i} (\pi - \zeta_i) \,; \\
&\quad z_I \leftarrow z_I + \rho_k \tfrac{w_i}{v_i} L_i^* (\zeta - (\pi - \zeta_i)) \,; \\
&\quad \zeta_i \leftarrow \zeta_i + \rho_k (\zeta - L_i x) \,; \\
&\textbf{for } i \in I^c \textbf{ do} \\
&\quad z_i \leftarrow z_i + \rho_k \Big(\operatorname{prox}_{\frac{\gamma}{w_i} g_i} \big(p - z_i\big) - x \Big) \,; \\
&x \leftarrow z_I + \textstyle\sum_{i\in I^c} w_i z_i \,.
\end{aligned}
$$

We also introduced the auxiliary variable $\pi \in \mathcal{H}_i$ within the scope of the loop over $i \in I$, to avoid computing $L_i p$ twice.

The above implementation is useful when, for each $i \in I$, the dimension of $\mathcal{H}_i$ is much lower than the dimension of $\mathcal{H}$: indeed, at the expense of storing z_I and ζ, each auxiliary variables z_i is replaced by its image through L_i. This is particularly interesting for dealing with highly redundant representations such as the undecimated wavelet transform that we use for the neuronal activity component in our SMCS model (see § II.2.2.3).

4.1.2 No Relaxation

If we set for all $k \in \mathbb{N}$, $\rho_k \overset{\text{set}}{=} 1$, one can get rid of the auxiliary variable ζ. The main iteration becomes

$$
\begin{aligned}
&p \leftarrow 2x - \gamma \nabla f(x) \,; \\
&z_I \leftarrow \big(\textstyle\sum_{i\in I} w_i\big)(p - x) \,; \\
&\textbf{for } i \in I \textbf{ do} \\
&\quad \pi \leftarrow L_i p \,; \\
&\quad \zeta_i \leftarrow \zeta_i + \operatorname{prox}_{\frac{v_i \gamma}{w_i} g_i} (\pi - \zeta_i) \,; \\
&\quad z_I \leftarrow z_I + \tfrac{w_i}{v_i} L_i^* (\zeta_i - \pi) \,; \\
&\quad \zeta_i \leftarrow \zeta_i - L_i x \,; \\
&\textbf{for } i \in I^c \textbf{ do} \\
&\quad z_i \leftarrow z_i + \operatorname{prox}_{\frac{\gamma}{w_i} g_i} \big(p - z_i\big) - x \,; \\
&x \leftarrow z_I + \textstyle\sum_{i\in I^c} w_i z_i \,.
\end{aligned}
$$

4.1.3 Identical Operators

The last and most interesting case is when the linear operators are the same, *i.e.* there exists $\mathcal{H}'$, $L : \mathcal{H} \to \mathcal{H}'$ and $v \in \mathbb{R}_{+*}$ such that for all $i \in I$, $\mathcal{H}_i = \mathcal{H}'$, $L_i = L$ and $v_i = v$. It is then easy to derive the following main iteration

$p \leftarrow \gamma \nabla f(x)$;
$\pi \leftarrow Lp$;
$\xi \leftarrow Lx$;
$\zeta_I \leftarrow 0$;
for $i \in I$ **do**
  $\zeta \leftarrow \operatorname{prox}_{\frac{\nu\gamma}{w_i} g_i}(2\xi - \pi - \zeta_i)$;
  $\zeta_I \leftarrow \zeta_I + \rho_k \frac{w_i}{\nu}(\zeta - (2\xi - \pi - \zeta_i))$;
  $\zeta_i \leftarrow \zeta_i + \rho_k(\zeta - \xi)$;
$z_I \leftarrow (1 - \rho_k) z_I + \rho_k (\sum_{i \in I} w_i)(x - p) + L^* \zeta_I$;
for $i \in I^c$ **do**
  $z_i \leftarrow z_i + \rho_k \big(\operatorname{prox}_{\frac{\gamma}{w_i} g_i} \big(2x - p - z_i\big) - x \big)$;
$x \leftarrow z_I + \sum_{i \in I^c} w_i z_i$.

Note that we introduced two additional variables $\xi, \zeta_I \in \mathcal{H}'$. However, this implementation requires, per iteration, only two calls to the operator L and only one call to its adjoint. Moreover, setting as in the above case, for all $k \in \mathbb{N}$, $\rho_k \overset{\text{set}}{=} 1$, one can get rid of the auxiliary variables ζ and z_I.

Note also that p stores only the gradient step, so as to isolate the application of L to $\nabla f(x)$, for two reasons. First, this kind of situation where several functions are composed with a given linear operator often arises when the target signal is represented in a synthesis operator L and several terms in the objective functional apply in the signal domain. For instance in our variational problem (31), this is the case of the data-fidelity term, the total variation penalization and the hard constraint term. When the smooth term f is a quadratic data-fidelity term, (8) shows that $\nabla f(x) = L^* u$ for some $u \in \mathcal{H}'$. In this case, provided that $u \in \operatorname{ran} L$, the above variable π reduces to $\gamma L L^* u = \gamma \nu u$, so that only one call to L is necessary per iteration. Second, recall that the relaxed Douglas-Rachford algorithm is a special case of GFB with $f \overset{\text{set}}{=} 0$. In this case, the variables p and π disappear, and, again, only one call to L is necessary per iteration. This is a significant improvement over Pustelnik *et al.* (2011, Algorithm 3), which requires two calls to L per iteration, and much more auxiliary variables than the implementation proposed here.

4.2 Different Splitting Numbers Along Coordinates

In a computational context, one usually minimizes the functional over a given number P of coordinates, *i.e.* one can explicit $\mathcal{H} \overset{\text{set}}{=} \mathbb{R}^P$. It often happens that some terms in the functional F does not depend on all the P coordinates, but only a subset of them. Different terms can require different numbers of functionals in a proximal splitting, but a naive implementation of the GFB does not take this into account; let us precise here good practices regarding this aspect.

4.2.1 General Case

Let $b \subseteq \{1, \dots, P\}$ be a group of coordinates, and $b^c \overset{\text{def}}{=} \{1, \dots, P\} \setminus b$ it's complementary. Suppose that some functionals in (25) does not depend on the coordinates in b, *i.e.* there exists $I \subseteq \{1, \dots, n\}$ such that $F(x) = f(x) + \sum_{i \in I} g(x) + \sum_{i \in I^c} g_i(x_{b^c})$, where

$I^c \overset{\text{def}}{=} \{1,\dots,n\} \setminus I$. In that case, for all $i \in I^c$, the update (26) can be particularized according to the coordinates, as

$$\begin{aligned}(z_i)_{b^c} &\leftarrow (z_i)_{b^c} + \rho_k\Big(\operatorname{prox}_{\frac{\gamma}{w_i} g_i}\left(p_{b^c} - (z_i)_{b^c}\right) - x_{b^c}\Big)\,,\\ (z_i)_b &\leftarrow (1-\rho_k)(z_i)_b + \rho_k(p_b - x_b)\,.\end{aligned}$$

One sees in particular that the update of $(z_i)_b$ is the same for all $i \in I^c$, so that if they are all initialized to the same value (and there is no reason not to), only one variable $(z_{I^c})_b$ is necessary for keeping track of all updates. Each iteration of GFB becomes

$$\begin{aligned}&p \leftarrow 2x - \gamma\nabla f(x)\,;\\ &\textbf{for } i \in I \textbf{ do}\\ &\quad z_i \leftarrow z_i + \rho_k\Big(\operatorname{prox}_{\frac{\gamma}{w_i} g_i}\left(p - z_i\right) - x\Big)\,;\\ &\textbf{for } i \in I^c \textbf{ do}\\ &\quad (z_i)_{b^c} \leftarrow (z_i)_{b^c} + \rho_k\Big(\operatorname{prox}_{\frac{\gamma}{w_i} g_i}\left(p_{b^c} - (z_i)_{b^c}\right) - x_{b^c}\Big)\,;\\ &(z_{I^c})_b \leftarrow (1-\rho_k)(z_{I^c})_b + \rho_k(p_b - x_b)\,;\\ &x_{b^c} \leftarrow \textstyle\sum_{i=1}^n w_i (z_i)_{b^c}\,;\\ &x_b \leftarrow \textstyle\sum_{i\in I} w_i (z_i)_b + \left(\sum_{i\in I^c} w_i\right)(z_{I^c})_b\,.\end{aligned}$$

Moreover, without relaxation (*i.e.* $\forall\, k \in \mathbb{N}$, $\rho_k \overset{\text{set}}{=} 1$), one can get rid of the auxiliary variable $(z_{I^c})_b$ since it is always equal to $p_b - x_b$.

Note also that we particularized here only one group of coordinates b, but this can be extended to any number of groups and any configuration.

4.2.2 Separable Case

A particular case arises when a given functional is separable along several groups of coordinates, each group requiring different splitting numbers; see for instance the structured penalizations over the wavelet and cosine coefficients proposed in § 5.2.2. In that case, we show here that, in contrast to the technique presented above, the auxiliary variable $(z_{I^c})_b$ is not necessary, and more importantly, the update of x_b only involves variables that underwent a proximal step.

For simplicity of exposition, consider first $F \overset{\text{def}}{=} f + g$, where the functional g is separable according to a nonoverlapping group structure B, *i.e.* for all $x \in \mathbb{R}^P$, $g(x) = \sum_{b\in B} g_b(x_b)$, and that for each $b \in B$, there exists $n_b \in \mathbb{N}_*$ such that the functional g_b can be split into n_b simple functions, as $g_b = \sum_{j=1}^{n_b} g_{b,j}$. Note that, up to adding in B its complementary group of coordinates, we can suppose B covering without loss of generality. A naive implementation of GFB would require to introduce $n \overset{\text{set}}{=} \max_{b\in B} n_b$ auxiliary variables and as many updates per iterations. We show however that for each $b \in B$, one only needs n_b auxiliary subvectors of the size of x_b, and only these are involved in the update of x_b at each iteration.

Define $n_B = \prod_{b\in B} n_b$, and note that for all $b \in B$, $g_b = \sum_{j'=1}^{n_B/n_b} \sum_{j=1}^{n_b} \frac{n_b}{n_B} g_{b,j}$ constitutes a splitting of g_b in a sum of n_B simple functions indexed by $j \in \{1,\dots,n_b\}$ and $j' \in \{1,\dots,n_B/n_b\}$, and that one can re-index arbitrarily by $(g_{b,i'})_{1\le i'\le n_B}$. For all

$i' \in \{1,\dots,n_B\}$, define then $g_{i'}(x) \overset{\text{def}}{=} \sum_{b\in B} g_{b,i'}(x_b)$, and observe that $F = f + \sum_{i'=1}^{n_B} g_{i'}$ is now of the form (25) with $n \overset{\text{set}}{=} n_B$. The key point here is that by separability along the groups in B, and setting equal weights, *i.e.* for all $i' \in \{1,\dots,n_B\}$, $w_{i'} \overset{\text{set}}{=} \frac{1}{n_B}$, one can apply GFB without making explicit the indexing over i'. The main iteration becomes

$$
\begin{aligned}
&p \leftarrow 2x - \gamma\nabla f(x)\,;\\
&\textbf{for } b \in B,\ j \in \{1,\dots,n_b\},\ j' \in \{1,\dots,n_B/n_b\} \textbf{ do}\\
&\quad \left(z_{j,j'}\right)_b \leftarrow \left(z_{j,j'}\right)_b + \rho_k\Big(\operatorname{prox}_{\gamma n_b g_{b,j}}\left(p_b - \left(z_{j,j'}\right)_b\right) - x_b\Big)\,;\\
&\textbf{for } b \in \{1,\dots,B\} \textbf{ do}\\
&\quad x_b \leftarrow \sum_{j=1}^{n_b} \tfrac{1}{n_B} \sum_{j'=1}^{n_B/n_b} \left(z_{j,j'}\right)_b\,.
\end{aligned}
\tag{30}
$$

So far, we only increased the number of auxiliary variables, since n_B is much greater than $\max_{b\in B} n_b$. However for all $b \in B$ and $j \in \{1,\dots,n_b\}$, the update of $\left(z_{j,j'}\right)_b$ in (30) is the same for all $j' \in \{1,\dots,n_B/n_b\}$, so that by initializing them to the same value, only one variable $\left(z_j\right)_b$ is necessary for keeping track of all updates.

Extending this technique to the problem $F \overset{\text{def}}{=} f + \sum_{i=1}^{n} g_i$ where for all $i \in \{1,\dots,n\}$, g_i is separable according to a nonoverlapping (and covering) group structure B_i, is straightforward. With obvious notations, the main iteration reads

$$
\begin{aligned}
&p \leftarrow 2x - \gamma\nabla f(x)\,;\\
&\textbf{for } i \in \{1,\dots,n\},\ b \in B_i,\ j \in \{1,\dots,n_b\} \textbf{ do}\\
&\quad \left(z_{i,j}\right)_b \leftarrow \left(z_{i,j}\right)_b + \rho_k\Big(\operatorname{prox}_{\frac{\gamma n_b}{w_i} g_{i,b,j}}\left(p_b - \left(z_{i,j}\right)_b\right) - x_b\Big)\,;\\
&x \leftarrow 0\,;\\
&\textbf{for } i \in \{1,\dots,n\},\ b \in B_i \textbf{ do}\\
&\quad x_b \leftarrow x_b + \tfrac{w_i}{n_b} \sum_{j=1}^{n_b} \left(z_{i,j}\right)_b\,.
\end{aligned}
$$

5 Illustration and Experiments

In this section, we illustrate the previously defined penalizations in classical image processing settings, and we investigate the use of several first-order proximal splitting algorithms for solving the resulting variational problems.

5.1 Variational Image Restoration

Over the set $\mathcal{I} \sim \mathbb{R}^P$ of gray level images comprising P pixels, we consider a class of regularized inverse problems, where one wants to recover a high resolution image $y^{(0)} \in \mathcal{I}$, from noisy low resolution observations $y = Ly^{(0)} + v \in \mathcal{I}$. The values of $y^{(0)}$ lie in the range $[0,1]$, the noise vector $v \in \mathcal{I}$ is a realization of an additive white Gaussian noise of variance ${\sigma_v}^2$, and the linear operator $L\colon \mathcal{I} \to \mathcal{I}$ models the observation process; we focus our attention on convolution and masking operators, and their combination.

The *inpainting* inverse problem deals with a masking operator $M\colon \mathcal{I} \to \mathcal{I}$, defined for each pixel p as

$$
(My)_p \overset{\text{def}}{=} \begin{cases} y_p & \text{if } p \in \Omega\,,\\ 0 & \text{otherwise}\,, \end{cases}
$$

where $\Omega \subseteq \{1, \dots, P\}$ is a set of pixels. This simulates for instance missing or defective sensors in an image acquisition (see Figure 7, upper left). It is an orthogonal projector, diagonal in the pixel domain. Then, the *deblurring* inverse problem deals with a convolution operator, $K : \mathcal{I} \to \mathcal{I} : y \mapsto G_{\sigma_K} * y$, where G_{σ_K} is a discrete Gaussian filter of width σ_K and normalized to unit mass. This simulates scattering or out-of-focus pixels in the image acquisition (see Figure 7, upper middle). Boundary conditions of the two-dimensional convolution $*$ are periodic, so that K is a diagonal operator in Fourier domain. The operator L will be either M or K, or the composition of both, MK.

We represent the restored image $\hat{y} \in \mathcal{I}$ within the concatenation of two dictionaries adapted to image compression and denoising, namely a discrete wavelet frame $D^{(\mathrm{W})}$ and a discrete cosine frame $D^{(\mathrm{C})}$. They are complementary in the sense that the former handles best local features, while the latter is nonlocal; see Mallat (2008) for details. To deal with boundary conditions of the wavelet transform, the image is mirrored prior to the wavelet transform; in this setting, the coefficients of $\hat{y}$ are vectors $\hat{x} \in \mathcal{H} \overset{\text{set}}{=} \mathcal{I}^4 \times \mathcal{I} \sim \mathbb{R}^{5P}$ ($4P$ wavelet coefficients, and P cosine coefficients), and the synthesis operator reads

$$D : \begin{array}{ccc} \mathcal{H} & \longrightarrow & \mathcal{I} \\ x \overset{\text{def}}{=} (x^{(\mathrm{W})}, x^{(\mathrm{C})}) & \longmapsto & D^{(\mathrm{W})} x^{(\mathrm{W})} + D^{(\mathrm{C})} x^{(\mathrm{C})} \end{array} .$$

The wavelet and cosine atoms are normalized so that D is a *Parseval tight frame*, *i.e.* it satisfies $DD^* = \mathrm{Id}$.

Our general variational problem for the recovery reads

$$\min_{x \in \mathcal{H}} \left\{ F(x) \overset{\text{def}}{=} \tfrac{1}{2} \|y - LDx\|_2^2 + \Psi^{(\Lambda)}(x) \right\} . \tag{31}$$

The first term in the summand is the data fidelity term, which is taken as the squared ℓ_2-norm motivated by the additive white Gaussian noise, while the second term is a regularization, enforcing priors assumed to be satisfied by the original image. Note that it closely resembles the variational problem (II.6) in our SMCS model; for the sake of illustration, we use penalizations also inspired by our SMCS model,

$$\Psi^{(\Lambda)}(x) \overset{\text{def}}{=} \|x^{(\mathrm{W})}\|_{\ell, \Lambda_B^{(\mathrm{W})}} + \|x^{(\mathrm{C})}\|_{\ell, \Lambda_B^{(\mathrm{C})}} + \|Dx\|_{\delta, \Lambda_{\mathrm{TV}}} + \iota_{[0,1]}(Dx) . \tag{32}$$

The first two regularizations enforces sparsity on the coefficients, with a block-structured $\ell_{1,2}$-norm over the wavelet coefficients and a weighted ℓ_1-norm on the cosine coefficients. The third regularization induces sparsity on the spatial gradient of the restored image through the discrete total variation semi-norm. The fourth and last term forces the values of the restored image to lie in the range $[0, 1]$, by mean of a box constraint.

Remark 5.1. Though the link between the present variational problem and the one introduced in our SMCS model is obvious (compare (31) and (32) to (II.6) and (II.16)), they should not be confused. The goal here is to retrieve only one image, in a linear representation that happens to be a concatenation of complementary dictionaries, *i.e.* the distribution of the representation between those dictionaries does not matter. In contrast, the goal of the SMCS model is to separate different components represented by different dictionaries. Moreover, VSDOI data are spatiotemporal: the dictionaries are temporal (*i.e.* unidimensional) and the penalization are spatially structured. Here, the dictionaries are spatial (*i.e.* two-dimensional, see for instance Figure 1).

5.2 Details On the Variational Problem

In the following, we detail each term of (31) and (32), and explicit their proximal splitting properties as derived in a general settings along § 3.

5.2.1 Data Fidelity $\frac{1}{2}\|y - LDx\|_2^2$

Denoting $\Phi \overset{\text{set}}{=} LD$, the data fidelity term reads $f(x) \overset{\text{set}}{=} \frac{1}{2}\|y - \Phi x\|_2^2$. It is a smooth functional whose gradient can be directly deduced from Proposition 3.1 and can be computed efficiently, $\nabla f(x) = D^* L^* (LDx - y)$. Moreover, a Lipschitz constant of ∇f is $\beta^{-1} = \|LD\|^2$; one can estimate it numerically using the *power method* (Von Mises and Pollaczek-Geiringer, 1929).

Now, the proximity operator of f cannot be directly computed from Proposition 3.2, since $\Phi^*\Phi = D^* L^* LD$ has no interesting properties for computing the required inverse. However, applying Proposition 3.3 and using the fact that D is a Parseval tight frame, the right-hand side of (11) becomes $\mathrm{Id} - \gamma D^* L^* (\mathrm{Id} + \gamma LL^*)^{-1} LD$. For inpainting or deblurring alone, since M (resp. K) is a diagonal operator in the pixel domain (resp. Fourier domain), the inversion can be computed efficiently.

Finally, one can deal with the composite case $L \overset{\text{set}}{=} MK$ by augmenting the dimensionality from $\mathcal{H}$ to $\mathcal{H} \times \mathcal{I}$, following § 3.1.2, with $\Phi_1 \overset{\text{set}}{=} M$ and $\Phi_2 \overset{\text{set}}{=} KD$. Accordingly, (13) becomes

$$\mathrm{prox}_{\gamma g_1}(x, u) = \left(x,\ (\mathrm{Id} + \gamma M)^{-1}(u + \gamma My)\right), \tag{33}$$

and using Proposition 3.4, we get

$$\mathrm{prox}_{\gamma g_2}(x, u) = (x - D^* K^* v,\ u + v), \tag{34}$$

where $v = (\mathrm{Id} + KK^*)^{-1}(KDx - u)$ can be computed efficiently.

5.2.2 Sparsity Enforcing Penalizations $\|x^{(\mathrm{W})}\|_{\ell,\Lambda_B^{(\mathrm{W})}} + \|x^{(\mathrm{C})}\|_{\ell,\Lambda_B^{(\mathrm{C})}}$

Block structures over two-dimensional wavelet coefficients. As illustrated on the schematic view of Figure 1(b), the k-th atom in a two-dimensional wavelet dictionary is characterized by its *spatial position* p_k, its *scale* j_k, and its *direction* d_k (which can be horizontal, vertical or diagonal). Within each scale j and direction d, the spatial positions are naturally organized along a grid in $\mathbb{Z}^2$, over which we define a block structure $B^{(j,d)}$. The whole $\ell_{1,2}$-norm by blocks is then $\|x^{(\mathrm{W})}\|_{\ell,\Lambda_B^{(\mathrm{W})}} \overset{\text{def}}{=} \sum_{j=j_{\min}}^{j_{\max}} \sum_{d=1}^{3} \|x^{(\mathrm{W})}\|_{\ell,\Lambda_B^{(j,d)}}$, parameterized by $\Lambda_B^{(\mathrm{W})} \overset{\text{def}}{=} \left\{ \Lambda_B^{(j,d)} \overset{\text{def}}{=} \{\Lambda^{(j,d)}, B^{(j,d)}\} \;\middle|\; \substack{j_{\min} \le j \le j_{\max} \\ 1 \le d \le 3} \right\}$. Of course, such group structure over wavelet coefficients can be generalized to any spatial dimension D.

In practice, for each scale j and direction d, the block structure $B^{(j,d)}$ is defined as follows. We choose a block side length $\mathsf{s}^{(j,d)}$ and a number of grids $n^{(j,d)} \in \mathbb{N}_*$, $1 \le n^{(j,d)} \le \mathsf{s}^{(j,d)^2}$. Then, $B^{(j,d)} \overset{\text{def}}{=} \left(B^{(j,d,i)}\right)_{1 \le i \le n^{(j,d)}}$ is the concatenation of $n^{(j,d)}$ different block grids of size $\mathsf{s} \overset{\text{def}}{=} (\mathsf{s}^{(j,d)}, \mathsf{s}^{(j,d)})$. Note that setting $n^{(j,d)} \overset{\text{set}}{=} 1$ can give too much importance to a specific grid, while $n^{(j,d)} \overset{\text{set}}{=} \mathsf{s}^{(j,d)^2}$ leads to heavy structures for large block side length (consider that for blocks of size 10×10, there exists already 100

different grids!). The actual setting of $\mathsf{s}^{(j,b)}$ and of the weights in $\Lambda_B^{(\mathrm{W})}$ is discussed in the next chapter, § V.5.

Now, we have $\|x^{(\mathrm{W})}\|_{\ell,\Lambda_B^{(j,d)}} = \sum_{i=1}^{n^{(j,d)}} \|x^{(\mathrm{W})}\|_{\ell,\Lambda_B^{(j,d,i)}}$, which is a splitting into simple functionals, as shown by Proposition 3.8 (i). Note that $n^{(j,d)}$, the number of functionals in the splitting, might vary according to directions and scales. See § 4.2.2 for proper implementation of proximal splitting algorithms in that case.

Finally, $\|x^{(\mathrm{C})}\|_{\ell,\Lambda_B^{(\mathrm{C})}}$ is a simple weighted ℓ_1-norm, whose proximity operator is a soft-thresholding.

5.2.3 Penalizations Over the Restored Image $\|Dx\|_{\delta,\Lambda_{\mathrm{TV}}} + \iota_{[0,1]}(Dx)$

The specificity of those last two penalizations is that they do not apply to the coefficients x but to the resulting image Dx; they illustrate well the advantage of the tight frame property for proximity operators. Here, D is surjective so that the minor premise of Proposition 3.7 (iii) is always satisfied with $\Phi \overset{\text{set}}{=} D$. In consequence, $\sum_{i=1}^{4} \|\cdot\|_{\delta,\Lambda_{\mathrm{TV}}^{(i)}} \circ D$, where for each $i \in \{1,\dots,4\}$, $\Lambda_{\mathrm{TV}}^{(i)} \overset{\text{def}}{=} \left\{\Lambda^{(i)}, B_{\mathrm{TV}}^{(i)}\right\}$, constitutes a splitting of the functional $\|\cdot\|_{\delta,\Lambda_{\mathrm{TV}}} \circ D$ into simple functions; and $\iota_{[0,1]} \circ D$ is also simple.

Here, several functionals are composed with the same operator with the tight frame property. In such a case, consider § 4.1.3 for efficient implementation.

5.3 Numerical Experiments

We derived all the proximity and gradient operators required to apply various first-order proximal algorithms to our variational image restoration (31). This allows us to compare the performance of several splitting strategies and algorithms for minimizing a functional in high dimension involving usual tools of signal processing. The competing algorithms, already presented in § III.2.3, are summed up in Table 1. Note that GFB and DR are only primal algorithms, while the others are primal-dual; note also that DR and ChPo do not make use of the smoothness of any term.

GFB	generalized forward-backward,	see Algorithm III.2,
DR	relaxed Douglas-Rachford,	set $f \overset{\text{set}}{=} 0$ in Algorithm III.2,
CoPe	Combettes and Pesquet (2012),	see Algorithm III.3,
CoVu	Condat (2013) and Vũ (2013),	see Algorithm III.4,
ChPo	Chambolle and Pock (2011),	set $f \overset{\text{set}}{=} 0$ in Algorithm III.4,
BD-HPE	Monteiro and Svaiter (2013),	see Algorithm III.5.

Table 1: List of competing algorithms for solving (31).

5.3.1 Methodology

We implemented the numerical experiments using Matlab, with some linear and proximity operators in C interfaced with Mex. Each algorithm has been optimized as much as possible for a fair comparison[4]. In particular for the concerned algorithms, the smooth term f in the splitting is the data-fidelity term. Note also that we adapted as much as possible the implementation techniques described in § 4. Finally, let us mention that we considered the diagonal preconditioning of ChPo proposed by Pock and Chambolle (2011). However, this requires to compute the norms of rows and columns of the matrix representation of the linear operators involved in the functional; this is not adapted to linear operators implemented implicitly by successive filtering, such as the wavelet or cosine transforms that we use here.

Six different experiments are performed: three different tasks (inpainting, deblurring, composite) and two different penalizations (coefficients sparsity only, and coefficients sparsity jointly with total variation). For each experiment, we initialize all main and auxiliary variables to zero and run five hundred iterations of each considered optimization method.

Each run is performed twice, once for recording the evolution of the functional F, and once for recording the elapsed computational time t. Then, we want to compare the distance between the current value of the functional and its minimum. For each experiment, this minimum is approximated by running five thousand iterations of the best method (this was always GFB). Since for any nonzero observation the value of the objective functional is strictly positive, it is convenient to normalize the distance by the value of the minimum to obtain similar order of magnitudes. The results are plotted against time on a logarithmic scale in Figure 6. Note that we did not use in practice the penalization $\iota_{[0,1]}(Dx)$ because it would yield a functional value of $+\infty$ as soon as the box constraint is not fully satisfied, preventing proper comparison along iterations.

5.3.2 Results

The observations y and restored image $\hat{y} = D\hat{x}$ (recovered with GFB) are plotted in Figure 7, together with their *signal-to-noise ratio* relative to the original image $y^{(0)}$, computed in decibels for any $y \in \mathbb{R}^P$ by

$$\mathrm{SNR}(y, y^{(0)}) \stackrel{\text{def}}{=} 20 \log_{10} \left(\frac{\|y^{(0)}\|_2}{\|y - y^{(0)}\|_2} \right).$$

In all cases, introducing the total variation penalization in the variational problem improves the quality of the restoration. Qualitatively, it reduces the "ringing artifacts" that often appears when denoising natural images with sparse wavelet and cosine representations (see in particular the composite task, right column of Figure 7). Quantitatively, we observe an improvement of almost 1 dB. This is an empirical argument in favor of combined penalizations.

As underlined in § III.2.3, the primal-dual algorithms designed to handle the composition of each functional in the splitting with any linear operator (CoPe, CoVu, ChPo)

[4] source code is available on request to the author.

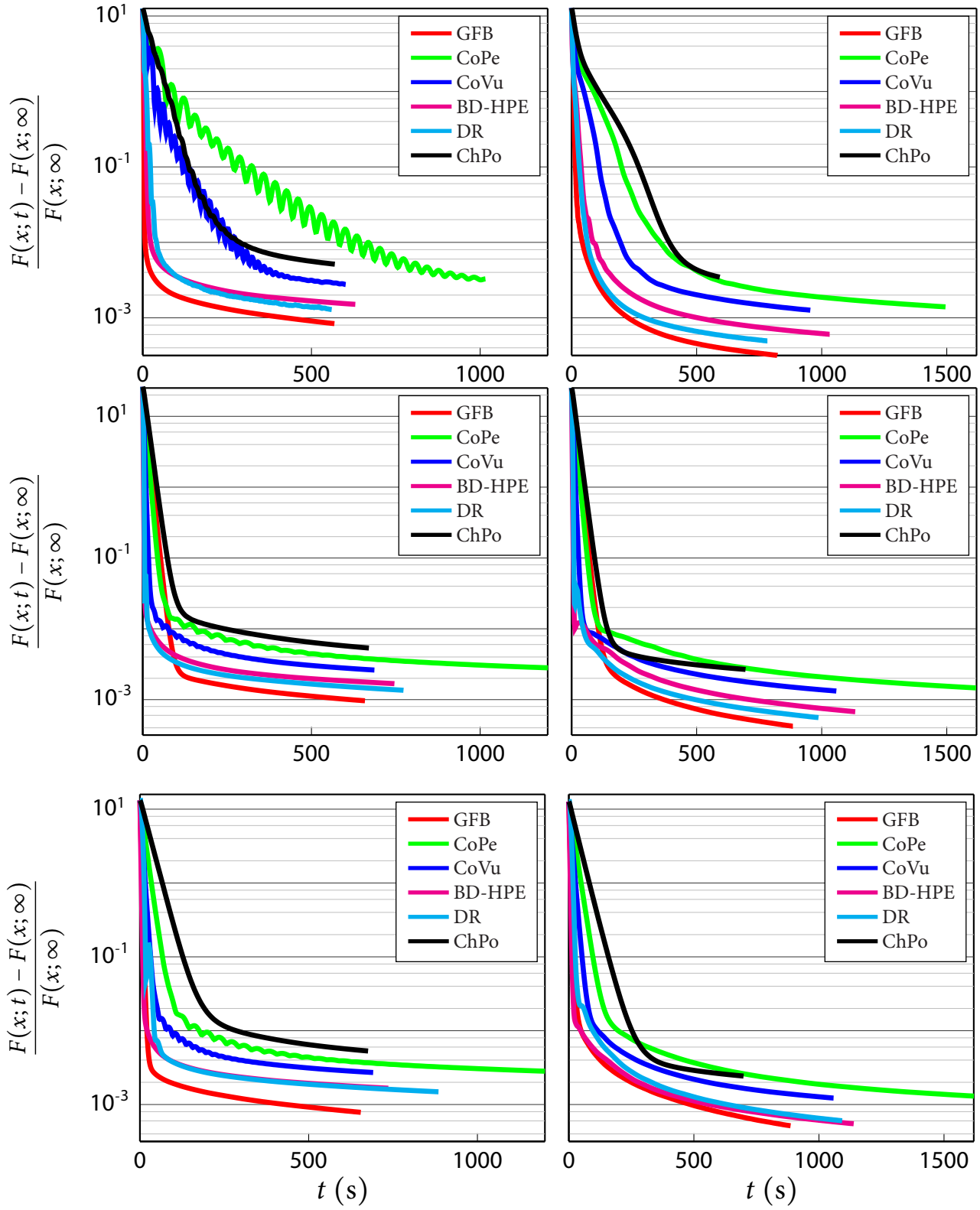

Figure 6: Results of the numerical experiments. See *opposite*.

Figure 6, *opposite*: Results of the numerical experiments. Tasks, from top to bottom: inpainting, deblurring, composite. Regularizations, left: only coefficients sparsity, right: coefficients sparsity jointly with total variation.

have more restrictive range of parameters ensuring convergence. This might be the reason why the objective functional decay is slower for them in all our experiments. However, note that when introducing the composition of simple functions with linear operators (in our case, the total variation functional), the computational load of ChPo is less affected than the other methods (see the black curves in the right column of Figure 6); nevertheless, in our experiments this is not sufficient to make it more interesting. CoVu enjoys less of this property (because of the call to the gradient of the data-fidelity f, two calls of the synthesis operator D are still required per iterations). CoPe, which requires two calls of the gradient of f and two calls of the adjoint of each involved linear operators per iterations, has always the biggest computational load.

Then, we see that the algorithms using the smoothness of the data-fidelity (*i.e.* the gradient of f) are more efficient than their counterparts which use only proximity operators (see GFB versus DR, and CoVu versus ChPo). This constitutes an empirical arguments in favor of the use of the gradient of any smooth part of an objective functional to be minimized, even when the corresponding proximity operator is available.

Finally, each iteration of BD-HPE are slightly more costly and less efficient than the ones of GFB; moreover, as observed in § III.2.3, the former requires more computational memory.

5.4 Conclusion

We motivated and described some of the most popular convex penalizations used to regularize inverse problems for signal processing. Their popularity can be explained notably by their convenience for proximal splitting method, as exposed all along this chapter. We also presented some empirical evidence that it is possible to combine several priors about a problem at hand, by summing several such penalizations. Finally in the context of first-order proximal splitting algorithm for minimizing objective functionals involving a smooth part, we have shown two interests of using an explicit gradient descent step rather than an implicit proximity operators. First, computing the gradient of a smooth functional might be easier than computing its proximity operator. Second, the resulting optimization scheme might be more efficient.

Concerning the original problem which motivated Chapter III and the current chapter of this thesis, recall that the SMCS synthesis dictionary D within the data-fidelity term of (6) is the concatenation of a variety of possibly redundant sub-dictionaries, some of them being implemented implicitly through successive filtering. Therefore, the operator inversions required for computing the proximity operator of the data-fidelity (see § 3.1) are computationaly too demanding. Our numerical experiments confirms our guess that GFB is the best candidate for retrieving efficiently the coefficients within our SMCS model for noisy components separation in voltage-sensitive dye optical imaging.

	Inpainting $L \overset{\text{set}}{=} M$	Deblurring $L \overset{\text{set}}{=} K$	Composite $L \overset{\text{set}}{=} MK$
Observations $y = Ly^{(0)} + v$	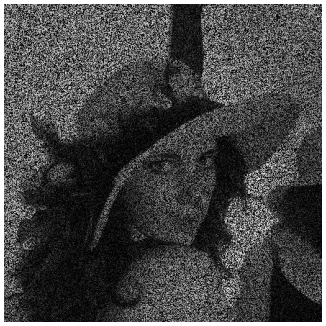		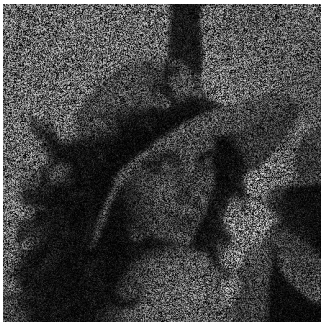
$\mathrm{SNR}(y, y^{(0)})$	2.7 dB	13.7 dB	2.7 dB
Recovery $\Psi^{(\Lambda)}(x) \overset{\text{set}}{=} \|x^{(\mathrm{W})}\|_{\ell,\Lambda_B^{(\mathrm{W})}} + \|x^{(\mathrm{C})}\|_{\ell,\Lambda_B^{(\mathrm{C})}}$			
$\mathrm{SNR}(\hat{y}, y^{(0)})$	22.6 dB	21.7 dB	21.0 dB
Recovery $\Psi^{(\Lambda)}(x) \overset{\text{set}}{=} \|x^{(\mathrm{W})}\|_{\ell,\Lambda_B^{(\mathrm{W})}} + \|x^{(\mathrm{C})}\|_{\ell,\Lambda_B^{(\mathrm{C})}} + \|Dx\|_{\delta,\Lambda_{\mathrm{TV}}}$			
$\mathrm{SNR}(\hat{y}, y^{(0)})$	23.8 dB	22.6 dB	21.9 dB

Figure 7: Observations and restored images of the numerical experiments. See *opposite*.

Figure 7, *opposite*: Observations and restored images of our example problem. For the masking operator M, the set of observed pixel Ω is drawn at random such that $|\Omega| \approx P/2$; for the blur operator K, the width of the Gaussian filter is $\sigma_K \overset{\text{set}}{=} 3$ (in pixels); the standard deviation of the noise v is $\sigma_v \overset{\text{set}}{=} 10^{-1}$ (recall that $y^{(0)}$ is scaled between 0 and 1). The choice of the penalizations parameters Λ is detailed in the next chapter, § V.4.

Before detailing the practical application of GFB to the SMCS model in Chapter II, the crucial question on the actual selection of the values of the many parameters involved in the model remains to be answered. This is the subject of the next chapter.

References

L. Ambrosio, N. Fucso, and D. Pallara. *Functions of Bounded Variation and Free Discontinuity Problems*. Oxford Mathematical Monographs. Oxford University Press, 2000.

S. Boyd and L. Vandenberghe. *Convex Optimization*. Cambridge University Press, New York, NY, USA, 2004.

L. M. Briceño-Arias, P. L. Combettes, J.-C. Pesquet, and N. Pustelnik. Proximal algorithms for multicomponent image recovery problems. *Journal of Mathematical Imaging and Vision*, 41(1-2):3–22, 2011.

A. Chambolle and T. Pock. A first-order primal-dual algorithm for convex problems with applications to imaging. *Journal of Mathematical Imaging and Vision*, 40(1): 120–145, 2011.

A. Chambolle, S. Levine, and B. Lucier. Some variations on total variation–based image smoothing. 2009. URL http://hal.archives-ouvertes.fr/hal-00370195.

Xi Chen, Qihang Lin, Seyoung Kim, Jaime G. Carbonell, and Eric P. Xing. Smoothing proximal gradient method for general structured sparse regression. *The Annals of Applied Statistics*, 6(2):719–752, 2012.

P. L. Combettes and J.-C. Pesquet. A Douglas-Rachford splitting approach to nonsmooth convex variational signal recovery. *IEEE Journal of Selected Topics in Signal Processing*, 1(4):564–574, 2007.

P. L. Combettes and J.-C. Pesquet. A proximal decomposition method for solving convex variational inverse problems. *Inverse Problems*, 24(6):065014, 2008.

P. L. Combettes and J.-C. Pesquet. *Proximal Splitting Methods in Signal Processing*, volume 49 of *Optimization and Its Applications*, chapter 10, pages 185–212. Springer, New York, NY, USA, 2011.

P. L. Combettes and J.-C. Pesquet. Primal-dual splitting algorithm for solving inclusions with mixtures of composite, Lipschitzian, and parallel-sum monotone operators. *Set-Valued and Variational Analysis*, 20(2):307–330, 2012.

L. Condat. A primal–dual splitting method for convex optimization involving lipschitzian, proximable and linear composite terms. *Journal of Optimization Theory and Applications*, 158(2):460–479, 2013.

J. Friedman, T. Hastie, H. Höfling, and R. Tibshirani. Pathwise coordinate optimization. *The Annals of Applied Statistics*, 1(2):302–332, 2007.

R. Jenatton, J.-Y. Audibert, and F. Bach. Structured variable selection with sparsity-inducing norms. *Journal of Machine Learning Research*, 12(oct):2777–2824, 2011.

J. Liu, L. Yuan, and J. Ye. An efficient algorithm for a class of fused lasso problems. In *Proceedings of the 16th ACM SIGKDD International Conference on Knowledge Discovery and Data Mining*, KDD '10, pages 323–332, New York, NY, USA, 2010. ACM.

B. Llanas and C. Moreno. Finding the projection on a polytope: An iterative method. *Computers & Mathematics with Applications*, 32(8):33–39, 1996.

J. Mairal, R. Jenatton, G. Obozinski, and F. Bach. Convex and network flow optimization for structured sparsity. *Journal of Machine Learning Research*, 12(nov):2681–2720, 2011.

S. Mallat. *A Wavelet Tour of Signal Processing, Third Edition: The Sparse Way*. Academic Press, 3rd edition, 2008.

L. Moisan. How to discretize the total variation of an image? *Proceedings in Applied Mathematics and Mechanics*, 7(1):1041907–1041908, 2007.

R. Monteiro and B. Svaiter. Iteration-complexity of block-decomposition algorithms and the alternating direction method of multipliers. *SIAM Journal on Optimization*, 23(1):475–507, 2013.

J.-J. Moreau. Fonctions convexes duales et points proximaux dans un espace hilbertien. *Comptes Rendus de l'Académie des Sciences de Paris Série A MathÁľmatiques*, 255:2897–2899, 1962.

J.D.B. Nelson. Fused lasso and rotation invariant autoregressive models for texture classification. *Pattern Recognition Letters*, 34(16):2166–2172, 2013.

Y. Nesterov. Smooth minimization of nonsmooth functions. *Mathematical Programming*, 103(1):127–152, 2005.

G. Nowak, T. Hastie, J. R. Pollack, and R. Tibshirani. A fused lasso latent feature model for analyzing multi-sample acgh data. *Biostatistics*, 12(4):776–791, 2011.

T. Pock and A. Chambolle. Diagonal preconditioning for first order primal-dual algorithms in convex optimization. pages 1762–1769, 2011.

N. Pustelnik, C. Chaux, and J.-C. Pesquet. Parallel ProXimal algorithm for image restoration using hybrid regularization. *IEEE Transactions on Image Processing*, 20 (9):2450–2462, 2011.

H. Raguet, J. M. Fadili, and G. Peyré. A generalized forward-backward splitting. *SIAM Journal on Imaging Sciences*, 6(3):1199–1226, 2013.

R. Tibshirani, M. Saunders, S. Rosset, J. Zhu, and K. Knight. Sparsity and smoothness via the fused lasso. *Journal of the Royal Statistical Society B*, 67:91–108, 2005.

R. Von Mises and H. Pollaczek-Geiringer. Praktische verfahren der gleichungsauflösung. *Zeitschrift für Angewandte Mathematik und Mechanik*, 9(2):152–164, 1929.

B. C. Vũ. A splitting algorithm for dual monotone inclusions involving cocoercive operators. *Advances in Computational Mathematics*, 38(3):667–681, 2013.

V

Risk Estimation for Parameter Selection in Proximal Denoising

All along previous chapters, we motivated and exemplified the use of variational problems for signal reconstruction. Such problems always involve parameters balancing the influence between terms, and these should be set carefully. In fact, parameter selection is at least as important as optimization methods, as far as the relevance of the solution to the problem at hand is concerned. However, while (convex) optimization methods can all be discussed within the same mathematical framework (to which belong the two previous chapters), parameter selection is more problem-dependent.

As discussed in more details in the introduction, there have been numerous *model selection* approaches developed in the literature, particularly in the context of statistical learning, where automatic parameter selections apply more naturally. However, they often do not apply directly to inverse problems in signal processing, and more importantly, they usually require to solve the problem many times, what is computationaly too expensive for large scale problems.

Recall from previous chapters that proximal splitting algorithms are good candidates for solving complex, large scale problems, by splitting them into "subproblems" that are easily tractable. These subproblems are proximity operators that can be efficiently computed, and as we will see, they can be seen as *denoising problems* of their own; and when they are treated as such, it is much easier to find relevant values of their parameters. Therefore in this chapter, we focus our attention on a statistical tool which seems the most adapted to such situations, namely *Stein's unbiased risk estimate*, and investigate its use for signal processing applications.

Contents

Within this chapter, P is a positive integer, and $y^{(0)} \in \mathbb{R}^P$ is a certain signal of interest. Suppose that $N \overset{\text{def}}{\sim} \mathcal{N}(0, C)$ follows a Gaussian noise with zero mean and *variance-covariance* $C \overset{\text{def}}{=} \left(c_{p,q}\right)_{\substack{1\le p\le P\\ 1\le q\le P}} \in \mathbb{R}^{P\times P}$; then, an *observation* of $y^{(0)}$ corrupted additively by N is a realization y of the random variable $Y \overset{\text{def}}{=} y^{(0)} + N$.

1 Stein's Unbiased Risk Estimate for Denoising

1.1 Denoising Problem and Risk of an Estimator

The *denoising problem* is the problem of retrieving $y^{(0)}$ given the observation y. An *estimator* of $y^{(0)}$ parameterized by Λ is a function $\hat{y}^{(\Lambda)}\colon \mathbb{R}^P \to \mathbb{R}^P\colon y \mapsto \hat{y}^{(\Lambda)}(y)$. In this

context, considering an estimator $\hat{y}^{(\Lambda)}$ and several possible values for its parameter Λ, one wishes to select the values of Λ which minimizes the *risk* of this estimator, defined as the expected value of the squared error,

$$\operatorname{risk}\left(\hat{y}^{(\Lambda)}\right) \stackrel{\text{def}}{=} \mathbb{E}_N \left\| y^{(0)} - \hat{y}^{(\Lambda)}(Y) \right\|^2 . \tag{1}$$

Unfortunately, one does not have access to the target signal $y^{(0)}$, so that the risk (1) cannot be estimated directly. However, one can develop $\left\| y^{(0)} - \hat{y}^{(\Lambda)}(Y) \right\|^2 = \left\| y^{(0)} - Y + Y - \hat{y}^{(\Lambda)}(Y) \right\|^2 = \|N\|^2 + \left\| Y - \hat{y}^{(\Lambda)}(Y) \right\|^2 + 2\left\langle -N \,\middle|\, Y - \hat{y}^{(\Lambda)}(Y) \right\rangle$, so that taking the expectation over N provides

$$\operatorname{risk}\left(\hat{y}^{(\Lambda)}\right) = \mathbb{E}_N \left\| Y - \hat{y}^{(\Lambda)}(Y) \right\|^2 + 2\mathbb{E}_N \left\langle N \,\middle|\, \hat{y}^{(\Lambda)}(Y) \right\rangle - \mathbb{E}_N \|N\|^2 . \tag{2}$$

The first term in the right hand side of (2) accounts for the distance between the observations and the corresponding estimations. The second term is the covariance between the noise and the estimator; in the risk, it accounts for the sensitivity of the estimator $\hat{y}^{(\Lambda)}$ to the noise. From a statistical point of view, it corresponds to the *degrees of freedom* of the estimator (see in particular Efron (2004) and references therein); this quantifies the complexity of an estimator, hence its susceptibility to overfitting. The last term depends only on the statistics of the noise, as $\mathbb{E}_N \|N\|^2 = \operatorname{tra} C$; in particular, it is independent from the estimator $\hat{y}^{(\Lambda)}$.

Altogether, minimizing the risk according to Λ amounts to find the best compromise between confidence on the observations and robustness to noise of the estimator, through estimates of (2). In a denoising problem, realizations of Y are observed, so that the first term can be estimated. However, one does not observe the corresponding realizations of the noise N, which would be useful for estimating the second term. Fortunately, Stein's lemma (Stein, 1981) stipulates that in the case of additive Gaussian noise, this term can still be estimated, provided that the noise's statistics are known and that the estimator $\hat{y}^{(\Lambda)}$ has sufficient regularity, as described in the following.

1.2 Stein's Unbiased Risk Estimate

Developed first for the case of an homoscedastic, white Gaussian noise, the following lemma has been extended to correlated Gaussian noise, and more generally to an arbitrary noise following an *exponential family* distribution, see in particular Eldar (2009); Pesquet *et al.* (2009). We re-establish it here properly in the case of an arbitrary Gaussian noise. In particular, we specify the required weak differentiability assumption on the estimator[1] $\hat{y}$, which are somewhat often imprecisely given in the literature. Note moreover that with our formulation, this assumption is slightly easier to check than with the original formulation of Stein (1981), though they are equivalent.

For $p \in \{1, \ldots, P\}$, we particularize the coordinate p of a vector $x \in \mathbb{R}^P$ by denoting the subvector $x_{\{p\}^c} \stackrel{\text{def}}{=} x_{\{1,\ldots,P\} \setminus \{p\}}$; such an x is then uniquely determined by $\left(x_{\{p\}^c}, x_p\right)$.

[1] for the time being, we drop the dependency of $\hat{y}$ on Λ.

Definition 1.1 (almost differentiability)**.** Let $P, Q \in \mathbb{N}_*$. A function $\hat{y}\colon \mathbb{R}^P \to \mathbb{R}^Q$ is *almost differentiable* if it is absolutely continuous over almost all line segments parallel to the coordinate directions, *i.e.* for all $p \in \{1, \dots, P\}$ and $q \in \{1, \dots, Q\}$, there exists a locally integrable function $\frac{\partial \hat{y}_q}{\partial y_p}\colon \mathbb{R}^P \to \mathbb{R}$ such that for almost all $y \in \mathbb{R}^P$ and for almost all $y'_p \in \mathbb{R}$,

$$\hat{y}_q\big(y_{\{p\}^c}, y'_p\big) = \hat{y}_q\big(y_p\big) + \int_{y_p}^{y'_p} \frac{\partial \hat{y}_q}{\partial y_p}\big(y_{\{p\}^c}, t\big)\,\mathrm{d}t\,;$$

the function $\frac{\partial \hat{y}_q}{\partial y_p}$ is called the *weak partial derivative* of $\hat{y}_q$ along direction p. We denote then $\frac{\partial \hat{y}}{\partial y}\colon \mathbb{R}^P \to \mathbb{R}^{P\times P}\colon y \mapsto \Big(\frac{\partial \hat{y}_q}{\partial y_p}(y)\Big)_{\substack{1\le q\le Q\\ 1\le p\le P}}$ the corresponding *weak Jacobian matrix*.

Lemma 1.1 (Stein's lemma)**.** *Let* $y^{(0)} \in \mathbb{R}^P$, $N \overset{\text{def}}{\sim} \mathcal{N}(0, C)$, $Y \overset{\text{def}}{=} y^{(0)} + N$, *and* $\hat{y}\colon \mathbb{R}^P \to \mathbb{R}^P$ *almost differentiable. If for all* $p, q \in \{1, \dots, P\}$, $\mathbb{E}_N\big|\frac{\partial \hat{y}_q}{\partial y_p}(Y)\big| < +\infty$, *then*

$$\mathbb{E}_N\langle N \,|\, \hat{y}(Y)\rangle = \mathbb{E}_N\Big[\operatorname{tra}\Big(C\tfrac{\partial \hat{y}}{\partial y}(Y)\Big)\Big]\,. \tag{3}$$

Proof. In Annex A, we correct the proof of Raphan and Simoncelli (2008), using the modified integration by part of Stein (1981). ∎

Remark 1.1. Following Evans and Gariepy (1992, Theorem 2 in Section 4.9.2), almost differentiable functions that are locally integrable together with their weak partial derivatives are actually the functions in the local Sobolev space $W^{1,1}_{\text{loc}}(\mathbb{R}^P)$. In view of the integrability conditions required by Stein's lemma, we conclude that (3) is valid for all functions in the Sobolev space $W^{1,1}(\mathbb{R}^P, \mathbb{P}_N)$ equipped with the probability measure induced by N. In that context, Lieb and Loss (2001, Theorem 6.9) shows that our definition of weak differentiability is equivalent to that of Stein (1981).

Remark 1.2. In the proof, it is easy to see that if the noise is uncorrelated along given directions $p, q \in \{1, \dots, P\}$, *i.e.* $c_{p,q} = c_{q,p} = 0$, then the estimator does not need to be absolutely continuous along these directions; in (3), the weak partial derivatives $\frac{\partial \hat{y}_q}{\partial y_p}$ and $\frac{\partial \hat{y}_p}{\partial y_q}$ can simply be replaced by 0.

Making use of analytic properties of the Gaussian distribution, Stein's lemma allows to replace the knowledge of the noise realizations by the knowledge of the weak partial derivatives of the estimator to obtain an *unbiased estimate* of its risk. More precisely, given one observation $y \in \mathbb{R}^P$, we define *Stein's unbiased risk estimate* (SURE) of the estimator $\hat{y}$ by

$$\operatorname{SURE}(\hat{y}, y) \overset{\text{def}}{=} \|y - \hat{y}(y)\|^2 + 2\operatorname{tra}\Big(C\tfrac{\partial \hat{y}}{\partial y}(y)\Big) - \operatorname{tra} C\,; \tag{4}$$

combining (2) with Lemma 1.1, we get immediately $\mathbb{E}_N[\operatorname{SURE}(\hat{y}, Y)] = \operatorname{risk}(\hat{y})$.

For sufficiently large observations, *i.e.* large values of P, only one observation is enough to have a good approximation of the risk of a given estimator. As shown in § 4,

this is typically the case in signal processing applications. Recall that estimators usually depend on some parameter Λ; if one can compute the SURE for sufficiently many values of the parameters, one can thus select the values minimizing the risk. This approach has two main limitations. First, one must have access to the weak partial derivatives of the estimators, which is not always the case; consider for instance that many estimators are defined as solutions of optimization problems, computed through iterative algorithms, and one does not have access to close form expressions. Second, testing for many values of the parameters can become computationaly prohibitively expensive. In particular, expressions of $\hat{y}^{(\Lambda)}(y)$ and of its weak partial derivatives must be computed efficiently in order to obtain the SURE value for thousands of parameters. Moreover, if the estimator $\hat{y}^{(\Lambda)}$ depends on several parameters, and for each parameters several values must be tested, there is a combinatorial explosions of the number of different SURE values to compute. In the following sections, we address those practical problems, illustrated by typical signal processing situations, with a focus on our SMCS model for VSDOI.

1.3 Prerequisite: Estimating the Noise Level

Before delving into specific denoising estimators, keep in mind that all the risk estimates given along this chapter require the knowledge of the noise statistics. In real-life applications, this is not known *a priori*, and has to be estimated. We describe here the most popular approach for dealing with natural signals corrupted by Gaussian noise.

Following for instance Donoho and Johnstone (1994), if the sampling resolution of a signal is high enough, one may assume that the "high frequencies" of Y are dominated by the noise N. More precisely, if $d \in \mathbb{R}^P$ is a vector presenting only transient features, such as a discretized wavelet at a high frequency scale, then the random variable of the correlation $\langle d \,|\, Y \rangle = \langle d \,|\, y^{(0)} \rangle + \langle d \,|\, N \rangle$ follows approximately the distribution of $\langle d \,|\, N \rangle \sim \mathcal{N}(0, {}^t d C d)$. Using an appropriately chosen family $(D_k)_{1 \leq k \leq K}$ of such vectors, it is then possible to use classical variance estimators in order to estimate C from the observations $(\langle D_k \,|\, y \rangle)_{1 \leq k \leq K}$.

We underline that the use of a robust estimator is recommended here, since those observations might be corrupted by actual high frequency features of $y^{(0)}$. An interesting special case is the white, homoscedastic noise, *i.e.* $C \overset{\text{set}}{=} \sigma^2 \operatorname{Id}_P$. Suppose that D is an orthonormal frame, for instance the high frequency subbands of an orthogonal wavelet frame. Then, $\left(N_k \overset{\text{def}}{=} \langle D_k \,|\, N \rangle\right)_{1 \leq k \leq K}$ are independent and identically distributed random variables following $N_0 \sim \mathcal{N}(0, \sigma^2)$. Given a realization of those variables, a popular estimator of σ is based on the *median of absolute deviations*. By definition, it is characterized by $\mathrm{m} \in \mathbb{R} : \mathbb{P}_{N_0}(|N_0| < \mathrm{m}) \overset{\text{def}}{=} \frac{1}{2}$. It satisfies

$$\mathbb{P}_{N_0}\left(\frac{|N_0|}{\sigma} < \frac{\mathrm{m}}{\sigma}\right) = \int_{-\frac{\mathrm{m}}{\sigma}}^{\frac{\mathrm{m}}{\sigma}} \phi(v)\,\mathrm{d}v = 2\Phi\left(\frac{\mathrm{m}}{\sigma}\right) = \frac{1}{2}\,,$$

where ϕ is the probability density function of the standard normal distribution, and $\Phi : \mathbb{R} \to \mathbb{R} : x \mapsto \int_0^x \phi(v)\,\mathrm{d}v$ is a strictly increasing function. Inverting Φ in the last equality yields $\frac{\mathrm{m}}{\sigma} = \Phi^{-1}\left(\frac{1}{4}\right)$. Since the *sample median* is a *consistent* estimator of the

median, and $\left(\Phi^{-1}\left(\frac{1}{4}\right)\right)^{-1} \approx 1.4826$, we deduce that

$$\hat{\sigma}\colon (v_k)_{1\le k\le K} \mapsto 1.4826 \ \operatorname{med}\left(|v_k|\right)_{1\le k\le K},$$

where med denotes the sample median, is a consistent estimator of σ. Note that the use of the sample median median for robustness of the estimator is particularly relevant when the signal is sparse in the chosen family of high frequency vectors, *i.e.* for only a few $k \in \{1,\dots,K\}$, $\langle D_k \,|\, y^{(0)}\rangle$ might have a significant value and is then considered as an outlier, with limited impact on the median.

Now and for the rest of this chapter, we suppose that the noise statistics are known with sufficient accuracy.

2 Derivation for Some Proximity Operators

As underlined in the introduction of this chapter, proximity operators can be seen as denoising estimators. More importantly, proximity operators of simple functions involving few parameters do not suffer from the computational limitations introduced above. In addition, proximity operators are nonexpansive (Lemma III.1.2 and III.1.3), and in particular Lipschitzian. The following lemma provides regularity properties for Lipschitzian functions.

Lemma 2.1. *Let $P, Q \in \mathbb{N}_*$, and $\hat{y}\colon \mathbb{R}^P \to \mathbb{R}^Q$. If $\hat{y}$ is Lipschitzian, then it is almost differentiable, with weak partial derivatives bounded almost everywhere. In particular, for all $p \in \{1,\dots,P\}$ and all $q \in \{1,\dots,Q\}$, $\mathbb{E}_N\left|\frac{\partial \hat{y}_q}{\partial y_p}(Y)\right| < +\infty$.*

Proof. According to Evans and Gariepy (1992, Theorem 5 in Section 4.2.3, Theorem 2 in Section 4.9.2 and Theorem 1 in Section 6.2), $\hat{y}$ is differentiable almost everywhere, almost differentiable, and its weak derivative equals its derivative almost everywhere. Now by definition of the derivative, for almost all $y \in \mathbb{R}^P$ and for all $p \in \{1,\dots,P\}$ and all $q \in \{1,\dots,Q\}$, we have $\frac{\partial \hat{y}_q}{\partial y_p}(y) = \lim_{y'_p \to y_p} \frac{\hat{y}_q(y_{\{p\}^c}, y'_p) - \hat{y}_q(y_{\{p\}^c}, y_p)}{y'_p - y_p}$. Thus, $\frac{\partial \hat{y}_q}{\partial y_p}$ is bounded almost everywhere by any Lipschitz constant of $\hat{y}$, hence $\mathbb{E}_N\left|\frac{\partial \hat{y}_q}{\partial y_p}(Y)\right| < +\infty$. ∎

In consequence, if a proximity operator is known in closed form, it suffices then to derive it almost everywhere to get its weak partial differentials. In this section, we derive the SURE expressions for the proximity operators of structured penalizations given in the previous chapter (§ IV.3.4.3), and discuss practical computational matters. For brevity, and since it is the case of interest in our SMCS model (recall § II.2.1), we limit the exposition to the heteroscedastic, uncorrelated noise, *i.e.* $C \overset{\text{def}}{=} \operatorname{diag}(\sigma_1{}^2,\dots,\sigma_P{}^2)$. We denote then $\sigma \overset{\text{def}}{=} (\sigma_p)_{1\le p\le P} \in \mathbb{R}^P$ and somewhat abusively $\nabla \hat{y}^{(\Lambda_B)}\colon \mathbb{R}^P \to \mathbb{R}^P : y \mapsto \left(\frac{\partial \hat{y}_p}{\partial y_p}^{(\Lambda)}(y)\right)_{1\le p\le P}$; the SURE expression (4) becomes

$$\operatorname{SURE}\left(\hat{y}^{(\Lambda)}, y\right) = \left\|\hat{y}^{(\Lambda)}(y) - y\right\|^2 + 2\left\|\sigma \cdot \nabla \hat{y}^{(\Lambda)}(y)\right\|^2 - \|\sigma\|^2 . \tag{5}$$

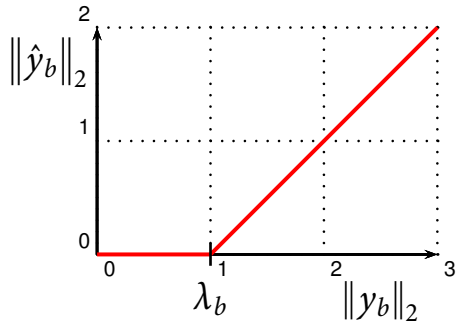

Figure 1: Group soft-thresholding; $\lambda_b \overset{\text{set}}{=} 1$.

Recall from § IV.3.4 that our structured penalizations are simple as soon as they are defined over nonoverlapping group structures; let then B be a nonoverlapping group structure over the Euclidean space $\mathbb{R}^P$, $b^c \overset{\text{def}}{=} \{1,\dots,P\} \smallsetminus \cup_{b\in B} b$ its complementary group of coordinates, and $\Lambda \overset{\text{def}}{=} (\lambda_b)_{b\in B}$ be a family of nonnegative weights indexed by B. Recall that (B, b^c) constitutes a partition of $\{1,\dots,P\}$. All the following cases are similar, hence only the $\ell_{1,2}$-norm denoising is well detailed.

2.1 $\ell_{1,2}$-Norm Denoising

Set first $\hat{y}^{(\Lambda_B)} \overset{\text{def}}{=} \operatorname{prox}_{\|\cdot\|_{\ell,\Lambda_B}} : y \mapsto \operatorname{argmin}_{x\in\mathbb{R}^P} \|y-x\|^2 + \|x\|_{\ell,\Lambda_B}$. Proposition IV.3.8(i) provides that, for all $y \in \mathbb{R}^P$, $\hat{y}^{(\Lambda_B)}_{b^c}(y) = y_{b^c}$, and for all $b \in B$,

$$\hat{y}^{(\Lambda_B)}_b(y) = \begin{cases} \left(1 - \frac{\lambda_b}{\|y_b\|_2}\right) y_b & \text{if } \|y_b\|_2 > \lambda_b\,, \\ 0 & \text{if } \|y_b\|_2 \le \lambda_b\,. \end{cases} \tag{6}$$

This estimator is sometimes called *group soft-thresholding*, canceling groups of coefficients whose amplitude is lower than the corresponding threshold λ_b, and shrinking the amplitude of the remaining groups by λ_b, as illustrated in Figure 1.

Proposition 2.1. *With the above definitions, $\hat{y}^{(\Lambda_B)}$ is almost differentiable, with for all $p \in b^c$, $\frac{\partial \hat{y}_p{}^{(\Lambda_B)}}{\partial y_p} = 1$, and for all $b \in B$, for all $p \in b$, and for almost all $y \in \mathbb{R}^P$,*

$$\frac{\partial \hat{y}_p{}^{(\Lambda_B)}}{\partial y_p}(y) = \begin{cases} \left(1 - \frac{\lambda_b}{\|y_b\|_2} + \frac{\lambda_b y_p{}^2}{\|y_b\|_2^3}\right) & \text{if } \|y_b\|_2 > \lambda_b\,, \\ 0 & \text{if } \|y_b\|_2 \le \lambda_b\,. \end{cases} \tag{7}$$

Note that expression (7) presents discontinuity at points where there exists $b \in B$ such that $\|y_b\|_2 = \lambda_b$; the partial derivative is actually not defined at those points. We set it here as 0, which its the left limit as λ_b tends to $\|y_b\|_2$. As discussed below, this indeterminacy is usually not a concern for practical applications.

Corollary 2.1. *With the above definitions,*

$$\begin{aligned}\mathrm{SURE}\left(\hat{y}^{(\Lambda_B)}, y\right) \overset{\text{def}}{=} & \sum_{\substack{b\in B:\\ |y_b|_2\le\lambda_b}} \|y_b\|_2^2 + \sum_{\substack{b\in B:\\ |y_b|_2>\lambda_b}} {\lambda_b}^2 + 2\|\sigma_{b^c}\|_2^2 - \|\sigma\|_2^2 \\ & + 2\sum_{\substack{b\in B:\\ |y_b|_2>\lambda_b}} \left(\|\sigma_b\|_2^2\left(1-\frac{\lambda_b}{\|y_b\|_2}\right) + \frac{\lambda_b}{\|y_b\|_2}\frac{\|\sigma_b\cdot y_b\|_2^2}{\|y_b\|_2^2}\right), \end{aligned} \tag{8}$$

is an unbiased estimate of the risk of $\hat{y}^{(\Lambda_B)}$.

Optimizing expression (8) separately for each λ_b, even if possible, makes no practical sense. Indeed, that would correspond to handle each subvector y_b separately, and by doing so to lose the statistical significance of the SURE computed over a single observation. A good practice here is to weight each group b by a fixed factor μ_b that depends on some prior knowledge over the group b (usually on the noise σ_b or the group size $|b|$, as we do in our SMCS model, see § II.3.5) and defining for all $b \in B$, $\lambda_b \overset{\text{set}}{=} \lambda\mu_b$ for a certain λ over which the SURE must be optimized. Denoting for each $b \in B$, $r_b \overset{\text{def}}{=} \frac{\|y_b\|_2}{\mu_b}$, the corresponding SURE (8) becomes

$$\begin{aligned}\mathrm{SURE}\left(\hat{y}^{(\lambda)}, y\right) = & \sum_{b\in B} {\mu_b}^2 \min\left(\lambda, r_b\right)^2 + 2\sum_{\substack{b\in B:\\ r_b>\lambda}} \left(\|\sigma_b\|_2^2\left(1-\frac{\lambda}{r_b}\right) + \frac{\lambda}{r_b}\frac{\|\sigma_b\cdot y_b\|_2^2}{\|y_b\|_2^2}\right) \\ & + 2\|\sigma_{b^c}\|_2^2 - \|\sigma\|_2^2 . \end{aligned} \tag{9}$$

Under that form, it is easier to see that the value of λ minimizing the estimated risk is a compromise between the first term of the right-hand side of (9), favoring a small shrinkage value to minimize bias, and the second term, favoring a large threshold value to remove the noise.

Now, by ordering the observed values of $(r_b)_{b\in B}$, say $r_{b_1} < \cdots < r_{b_{|B|}}$, observe that, for $i \in \{1, \ldots, |B|-1\}$ and λ ranging between the two consecutive values $[r_{b_i}, r_{b_{i+1}}[$, the SURE (9) is a convex and continuously differentiable function of λ, with derivative $\lambda \mapsto 2\sum_{b\in B: r_b > r_{b_i}} \left({\mu_b}^2\lambda + \frac{1}{r_b}\left(\frac{\|\sigma_b\cdot y_b\|_2^2}{\|y_b\|_2^2} - \|\sigma_b\|_2^2\right)\right)$. We deduce that the minimum of the SURE (9) over $[r_{b_i}, r_{b_{i+1}}[$ is attained at

$$\hat{\lambda}_i \overset{\text{def}}{=} \max\left(r_{b_i}, \min\left(r_{b_{i+1}}, \sum_{\substack{b\in B:\\ r_b>r_{b_i}}} \frac{1}{r_b}\left(\|\sigma_b\|_2^2 - \frac{\|\sigma_b\cdot y_b\|_2^2}{\|y_b\|_2^2}\right) \Big/ \sum_{\substack{b\in B:\\ r_b>r_{b_i}}} {\mu_b}^2\right)\right). \tag{10}$$

Defining similarly $\hat{\lambda}_0$ with $r_{b_0} \overset{\text{def}}{=} 0$, and $\hat{\lambda}_{|B|} \overset{\text{def}}{=} r_{|B|}$, it is thus possible to find the optimal λ in $O(P + |B|\log|B|)$ operations, by pre-computing norms involved in (9), ordering the ratios $(r_b)_{b\in B}$ and computing the SURE at points $\left\{\hat{\lambda}_i \,\middle|\, 0 \le i \le |B|\right\}$ using cumulative sums[2].

Recall that the points where $\lambda = r_b$ (or equivalently, $\lambda_b = \|y_b\|_2$) are precisely the ones for which the partial derivatives are not well defined. However, choosing between

[2] codes in Matlab are available at https://github.com/1a7r0ch3/SURE.

left or right limit as λ_b tends to $\|y_b\|_2$ only results in favoring one of two consecutive values of r_{b_i}, $r_{b_{i+1}}$. For sufficiently large observations, such two values are usually close enough so that the difference is insignificant in practice.

Finally, let us mention that the selection method described above is generalized in Chaux *et al.* (2008) to a large class of shrinking estimators. It is an extension of the method proposed by Donoho and Johnstone (1995) for the soft-thresholding estimator, which is the particular case where $B \overset{\text{set}}{=} (\{p\})_{1\leq p\leq P}$. Focusing on sparse wavelet denoising, they select one different threshold value for each different wavelet subband, by ordering the absolute values of the observed coefficients (note that when $|b_i| = 1$, then $\hat{\lambda}_i = r_{b_i}$) and computing the corresponding SURE. The numerical experiments in § 4.1 are in the same spirit.

2.2 Bounded Amplitude Denoising

Let then $\hat{y}^{(\Lambda_B)} \overset{\text{def}}{=} \text{proj}_{\ell^\infty_{\Lambda_B}} : y \mapsto \text{argmin}_{x\in\mathbb{R}^P} \|y - x\|^2 + \iota_{\ell^\infty_{\Lambda_B}}(x)$. Proposition IV.3.8(ii) shows that, for all $y \in \mathbb{R}^P$, $\hat{y}^{(\Lambda_B)}_{b^c}(y) = y_{b^c}$, and for all $b \in B$,

$$\hat{y}^{(\Lambda_B)}_b(y) = \begin{cases} \frac{\lambda_b}{\|y_b\|_2} y_b & \text{if } \|y_b\|_2 > \lambda_b \,, \\ y_b & \text{if } \|y_b\|_2 \leq \lambda_b \,. \end{cases}$$

Proposition 2.2. *With the above definitions, $\hat{y}^{(\Lambda_B)}$ is almost differentiable, with for all $p \in b^c$, $\frac{\partial \hat{y}_p^{(\Lambda_B)}}{\partial y_p} = 1$, and for all $b \in B$, for all $p \in b$, and for almost all $y \in \mathbb{R}^P$,*

$$\frac{\partial \hat{y}_p^{(\Lambda_B)}}{\partial y_p}(y) = \begin{cases} \frac{\lambda_b}{\|y_b\|_2}\left(1 - \frac{{y_p}^2}{\|y_b\|_2^2}\right) & \text{if } \|y_b\|_2 > \lambda_b \,, \\ 1 & \text{if } \|y_b\|_2 \leq \lambda_b \,. \end{cases}$$

Corollary 2.2. *With the above definitions,*

$$\begin{aligned} \text{SURE}\left(\hat{y}^{(\Lambda_B)}, y\right) \overset{\text{def}}{=} & \sum_{\substack{b\in B: \\ \|y_b\|_2 > \lambda_b}} \left((\|y_b\|_2 - \lambda_b)^2 + 2\frac{\lambda_b}{\|y_b\|_2}\left(\|\sigma_b\|_2^2 - \frac{\|\sigma_b \cdot y_b\|_2^2}{\|y_b\|_2^2}\right)\right) \\ & + 2 \sum_{\substack{b\in B: \\ \|y_b\|_2 \leq \lambda_b}} \|\sigma_b\|_2^2 + 2\|\sigma_{b^c}\|_2^2 - \|\sigma\|_2^2 \,, \end{aligned} \tag{11}$$

is an unbiased estimate of the risk of $\hat{y}^{(\Lambda_B)}$.

Introducing, as in § 2.1, the parameter λ, and for all $b \in B$, μ_b such that $\lambda_b \overset{\text{set}}{=} \lambda\mu_b$ and $r_b \overset{\text{def}}{=} \frac{\|y_b\|_2}{\mu_b}$, the SURE (11) becomes

$$\begin{aligned} \text{SURE}\left(\hat{y}^{(\lambda)}, y\right) = & \sum_{\substack{b\in B: \\ r_b > \lambda}} \left({\mu_b}^2 (r_b - \lambda)^2 + 2\frac{\lambda}{r_b}\left(\|\sigma_b\|_2^2 - \frac{\|\sigma_b \cdot y_b\|_2^2}{\|y_b\|_2^2}\right)\right) \\ & + 2 \sum_{\substack{b\in B: \\ r_b \leq \lambda}} \|\sigma_b\|_2^2 + 2\|\sigma_{b^c}\|_2^2 - \|\sigma\|_2^2 \,. \end{aligned}$$

Similarly to the expression (9), for all $i \in \{1,\dots,|B|-1\}$ and λ ranging between the two consecutive values $[r_{b_i}, r_{b_{i+1}}[$, this is a convex and continuously differentiable function of λ, with derivative $\lambda \mapsto 2\sum_{b\in B: r_b > r_{b_i}} \left(\mu_b{}^2(\lambda - r_b) + \frac{1}{r_b}\left(\|\sigma_b\|_2^2 - \frac{\|\sigma_b \cdot y_b\|_2^2}{\|y_b\|_2^2}\right)\right)$. We deduce that the minimum of the SURE over $[r_{b_i}, r_{b_{i+1}}[$ is attained at

$$\hat{\lambda}_i \stackrel{\text{def}}{=} \max\left(r_{b_i}, \min\left(r_{b_{i+1}}, \sum_{\substack{b\in B:\\ r_b > r_{b_i}}} \frac{1}{r_b}\left(\|y_b\|_2^2 + \frac{\|\sigma_b\cdot y_b\|_2^2}{\|y_b\|_2^2} - \|\sigma_b\|_2^2\right) \Big/ \sum_{\substack{b\in B:\\ r_b > r_{b_i}}} \mu_b{}^2\right)\right).$$

2.3 $\delta_{1,2}$-Semi-Norm Denoising

Let now $\hat{y}^{(\Lambda_B)} \stackrel{\text{def}}{=} \operatorname{prox}_{\|\cdot\|_{\delta,\Lambda_B}} : y \mapsto \operatorname{argmin}_{x\in\mathbb{R}^P} \|y-x\|^2 + \|x\|_{\delta,\Lambda_B}$. For a vector $x \in \mathbb{R}^P$ and a goup of coordinates b, we denote as in Remark IV.1.4, $\overline{x_b} \stackrel{\text{def}}{=} \frac{1}{|b|}\sum_{p\in b} x_p$ and $\overrightarrow{x_b} \stackrel{\text{def}}{=} (\overline{x_b},\dots,\overline{x_b}) \in \mathbb{R}^{|b|}$, so that $\Delta^{(b)}x_b = x_b - \overrightarrow{x_b}$. For brevity of notations, we also denote $\|x_b\|_\delta \stackrel{\text{def}}{=} \|x_b - \overrightarrow{x_b}\|_2$; in particular, by Pythagoras theorem, we get $\|x_b\|_\delta^2 = \|x_b\|_2^2 - \|\overrightarrow{x_b}\|_2^2$. According to Proposition IV.3.9(i), for all $y \in \mathbb{R}^P$, we have $\hat{y}_{b^c}^{(\Lambda_B)}(y) = y_{b^c}$ and for all $b \in B$,

$$\hat{y}_b^{(\Lambda_B)}(y) = \begin{cases} \overrightarrow{y_b} + \left(1 - \frac{\lambda_b}{\|y_b\|_\delta}\right)\left(y_b - \overrightarrow{y_b}\right) & \text{if } \|y_b\|_\delta > \lambda_b\,, \\ \overrightarrow{y_b} & \text{if } \|y_b\|_\delta \le \lambda_b\,. \end{cases}$$

Proposition 2.3. *With the above definitions, $\hat{y}^{(\Lambda_B)}$ is almost differentiable, with for all $p \in b^c$, $\frac{\partial \hat{y}_p}{\partial y_p}^{(\Lambda_B)} = 1$, and for all $b \in B$, for all $p \in b$, and for almost all $y \in \mathbb{R}^P$,*

$$\frac{\partial \hat{y}_p}{\partial y_p}^{(\Lambda_B)}(y) = \begin{cases} \frac{1}{|b|} + \left(1 - \frac{\lambda_b}{\|y_b\|_\delta}\right)\frac{|b|-1}{|b|} + \frac{\lambda_b}{\|y_b\|_\delta}\frac{(y_p - \overline{y_b})^2}{\|y_b\|_\delta^2} & \text{if } \|y_b\|_\delta > \lambda_b\,, \\ \frac{1}{|b|} & \text{if } \|y_b\|_\delta \le \lambda_b\,. \end{cases}$$

Corollary 2.3. *With the above definitions,*

$$\begin{aligned} \operatorname{SURE}\left(\hat{y}^{(\Lambda_B)}, y\right) = &\sum_{\substack{b\in B:\\ \|y_b\|_\delta \le \lambda_b}} \|y_b\|_\delta^2 + \sum_{\substack{b\in B:\\ \|y_b\|_\delta > \lambda_b}} \lambda_b{}^2 - \|\sigma\|_2^2 + 2\|\sigma_{b^c}\|_2^2 + 2\sum_{b\in B}\frac{\|\sigma_b\|_2^2}{|b|} \\ &+ 2\sum_{\substack{b\in B:\\ \|y_b\|_\delta > \lambda_b}} \left(\left(1 - \frac{\lambda_b}{\|y_b\|_\delta}\right)\frac{|b|-1}{|b|}\|\sigma_b\|_2^2 + \frac{\lambda_b}{\|y_b\|_\delta}\frac{\|\sigma_b\cdot\left(y_b - \overrightarrow{y_b}\right)\|_2^2}{\|y_b\|_\delta^2}\right), \end{aligned}$$

is an unbiased estimate of the risk of $\hat{y}^{(\Lambda_B)}$.

Similarly to § 2.1, with the parameter λ, and for all $b \in B$, μ_b such that $\lambda_b \stackrel{\text{set}}{=} \lambda\mu_b$ and $r_b \stackrel{\text{def}}{=} \frac{\|y_b\|_\delta}{\mu_b}$, we get

$$\begin{aligned} \operatorname{SURE}\left(\hat{y}^{(\lambda)}, y\right) = &\sum_{b\in B} \mu_b{}^2 \min\left(r_b, \lambda\right)^2 - \|\sigma\|_2^2 + 2\|\sigma_{b^c}\|_2^2 + 2\sum_{b\in B}\frac{\|\sigma_b\|_2^2}{|b|} \\ &+ 2\sum_{\substack{b\in B:\\ r_b > \lambda}} \left(\left(1 - \frac{\lambda}{r_b}\right)\frac{|b|-1}{|b|}\|\sigma_b\|_2^2 + \frac{\lambda}{r_b}\frac{\|\sigma_b\cdot\left(y_b - \overrightarrow{y_b}\right)\|_2^2}{\|y_b\|_\delta^2}\right); \end{aligned} \tag{12}$$

and for all $i \in \{1, \dots, |B|-1\}$, the minimum of this expression over two consecutive values $[r_{b_i}, r_{b_{i+1}}[$ is attained at

$$\hat{\lambda}_i \stackrel{\text{def}}{=} \max\left(r_{b_i}, \min\left(r_{b_{i+1}}, \sum_{\substack{b\in B:\\ r_b > r_{b_i}}} \frac{1}{r_b}\left(\frac{|b|-1}{|b|}\|\sigma_b\|_2^2 - \frac{\|\sigma_b\cdot(y_b-\overrightarrow{y_b})\|_2^2}{\|y_b\|_\delta^2}\right) \Big/ \sum_{\substack{b\in B:\\ r_b > r_{b_i}}} {\mu_b}^2\right)\right). \tag{13}$$

2.4 Bounded Deviation Denoising

Let finally $\hat{y}^{(\Lambda_B)} \stackrel{\text{def}}{=} \operatorname{proj}_{\delta\overline{\Lambda_B}}: y \mapsto \operatorname{argmin}_{x\in\mathbb{R}^P} \|y-x\|^2 + \iota_{\delta\overline{\Lambda_B}}(x)$. For all $y \in \mathbb{R}^P$, according to Proposition IV.3.9(ii), we have $\hat{y}^{(\Lambda_B)}_{b^c}(y) = y_{b^c}$, and for all $b \in B$,

$$\hat{y}^{(\Lambda_B)}_b(y) = \begin{cases} \overrightarrow{y_b} + \frac{\lambda_b}{\|y_b\|_\delta}\left(y_b - \overrightarrow{y_b}\right) & \text{if } \|y_b\|_\delta > \lambda_b\,, \\ y_b & \text{if } \|y_b\|_\delta \le \lambda_b\,. \end{cases}$$

Proposition 2.4. *With the above definitions, $\hat{y}^{(\Lambda_B)}$ is almost differentiable, with for all $p \in b^c$, $\frac{\partial \hat{y}_p}{\partial y_p}^{(\Lambda_B)} = 1$, and for all $b \in B$, for all $p \in b$, and for almost all $y \in \mathbb{R}^P$,*

$$\frac{\partial \hat{y}_p}{\partial y_p}^{(\Lambda_B)}(y) = \begin{cases} \frac{1}{|b|} + \frac{\lambda_b}{\|y_b\|_\delta}\left(\frac{|b|-1}{|b|} - \frac{\left(y_p - (\overrightarrow{y_b})_p\right)^2}{\|y_b\|_\delta^2}\right) & \text{if } \|y_b\|_\delta > \lambda_b\,, \\ 1 & \text{if } \|y_b\|_\delta \le \lambda_b\,, \end{cases}$$

Corollary 2.4. *With the above definitions,*

$$\begin{aligned} \operatorname{SURE}\left(\hat{y}^{(\Lambda_B)}, y\right) = {} & 2\|\sigma_{b^c}\|_2^2 - \|\sigma\|_2^2 + 2\sum_{\substack{b\in B:\\ \|y_b\|_\delta \le \lambda_b}} \|\sigma_b\|_2^2 \\ & + \sum_{\substack{b\in B:\\ \|y_b\|_\delta > \lambda_b}} \left(\left(\|y_b\|_\delta - \lambda_b\right)^2 + 2\frac{\|\sigma_b\|_2^2}{|b|} \right. \\ & \left. + \frac{2\lambda_b}{\|y_b\|_\delta}\left(\frac{|b|-1}{|b|}\|\sigma_b\|_2^2 - \frac{\|\sigma_b\cdot\left(y_b - \overrightarrow{y_b}\right)\|_2^2}{\|y_b\|_\delta^2}\right)\right) \end{aligned}$$

is an unbiased estimate of the risk of $\hat{y}^{(\Lambda_B)}$.

Finally, with the parameter λ, and for all $b \in B$, μ_b such that $\lambda_b \stackrel{\text{set}}{=} \lambda\mu_b$ and $r_b \stackrel{\text{def}}{=} \frac{\|y_b\|_\delta}{\mu_b}$,

$$\begin{aligned} \operatorname{SURE}\left(\hat{y}^{(\lambda)}, y\right) = {} & 2\|\sigma_{b^c}\|_2^2 - \|\sigma\|_2^2 + 2\sum_{\substack{b\in B:\\ r_b \le \lambda}} \|\sigma_b\|_2^2 \\ & + \sum_{\substack{b\in B:\\ r_b > \lambda}} \left({\mu_b}^2(r_b - \lambda)^2 + 2\frac{\|\sigma_b\|_2^2}{|b|} \right. \\ & \left. + \frac{2\lambda}{r_b}\left(\frac{|b|-1}{|b|}\|\sigma_b\|_2^2 - \frac{\|\sigma_b\cdot\left(y_b - \overrightarrow{y_b}\right)\|_2^2}{\|y_b\|_\delta^2}\right)\right); \end{aligned}$$

and for all $i \in \{1, \dots, |B|-1\}$, the minimum of this expression over two consecutive values $[r_{b_i}, r_{b_{i+1}}[$ is attained at

$$\hat{\lambda}_i \overset{\text{def}}{=} \max\left(r_{b_i}, \min\left(r_{b_{i+1}}, \sum_{\substack{b\in B:\\ r_b > r_{b_i}}} \frac{1}{r_b}\left(\|y_b\|_\delta + \frac{\|\sigma_b\cdot(y_b - \overrightarrow{y_b})\|_2^2}{\|y_b\|_\delta^2} - \frac{|b|-1}{|b|}\|\sigma_b\|_2^2\right) \Big/ \sum_{\substack{b\in B:\\ r_b > r_{b_i}}} {\mu_b}^2\right)\right). \quad (14)$$

2.5 Reweighted $\ell_{1,2}$-Norm Denoising

In § II.3.2, we introduced the reweighted $\ell_{1,2}$-norm penalization, directly inspired by the reweighted ℓ_1-norm proposed by Candès *et al.* (2008). A denoising estimator defined with this penalization is *not* an explicit proximal operator, but the derivation of its SURE is similar to the above cases. Let us first define such an estimator properly and exhibit some of its properties.

On top of B and Λ_B set as above, let $E_B \overset{\text{def}}{=} (\varepsilon_b)_{b\in B}$ be a family of nonnegative weights indexed by B. Below, we define the reweighted $\ell_{1,2}$-norm denoising estimator in Definition 2.1, with help of Proposition 2.5.

Definition 2.1 (reweighted $\ell_{1,2}$-norm denoising sequences)**.** With the above definitions, let moreover $y \in \mathbb{R}^P$. Dropping the dependencies on Λ_B, E_B and y for brevity, the *reweighted $\ell_{1,2}$-norm denoising sequences* are the sequence $(\hat{y}^{(n)})_{n\in\mathbb{N}}$ in $\mathbb{R}^P$, and the sequence $\left(\Lambda^{(n)} \overset{\text{def}}{=} \left(\lambda_b^{(n)}\right)_{b\in B}\right)_{n\in\mathbb{N}}$ of families of nonnegative weights indexed by B, defined by induction as $\hat{y}^{(0)} \overset{\text{def}}{=} 0$, and for all $n \in \mathbb{N}$,

$$\begin{cases} \forall\, b \in B,\ \lambda_b^{(n)} \overset{\text{def}}{=} \dfrac{\lambda_b}{\left\|\hat{y}_b^{(n)}\right\|_2 / \varepsilon_b \ + 1}\,, & (15a) \\ \hat{y}^{(n+1)} \overset{\text{def}}{=} \operatorname*{argmin}_{x\in\mathbb{R}^P} \frac{1}{2}\|y - x\|^2 + \|x\|_{\Lambda_B^{(n)}}\,. & (15b) \end{cases}$$

where $\Lambda_B^{(n)} \overset{\text{def}}{=} \{\Lambda^{(n)}, B\}$.

Proposition 2.5. *Any sequence $(\hat{y}^{(n)})_{n\in\mathbb{N}}$ as defined above is convergent. We can thus define the* reweighted $\ell_{1,2}$-norm denoising estimator parameterized by Λ_B and E_B, *as $\hat{y}^{(\Lambda_B,E_B)}\colon y \mapsto \lim_{n\to+\infty} \hat{y}^{(n)}$. Moreover, this estimator is characterized, for all $y \in \mathbb{R}^P$, by $\hat{y}_{b^c}^{(\Lambda_B,E_B)}(y) = y_{b^c}$ and for all $b \in B$,*

$$\hat{y}_b^{(\Lambda_B,E_B)}(y) = \begin{cases} \frac{1}{2}\left(1 - \frac{\varepsilon_b}{\|y_b\|_2} + \sqrt{\left(\frac{\varepsilon_b}{\|y_b\|_2} + 1\right)^2 - 4\frac{\lambda_b\varepsilon_b}{\|y_b\|_2^2}}\right) y_b & \text{if } \|y_b\|_2 > \lambda_b\,, \\ 0 & \text{if } \|y_b\|_2 \le \lambda_b\,. \end{cases} \quad (16)$$

Proof. Fix $y \in \mathbb{R}^P$ and $b \in B$. Obviously, $\|\hat{y}_b^{(0)}\|_2 \le \|\hat{y}_b^{(1)}\|_2$. Then, for all $n \in \mathbb{N}$, (15a) shows that $\|\hat{y}_b^{(n)}\|_2 \le \|\hat{y}_b^{(n+1)}\|_2 \Rightarrow \lambda_b^{(n)} \ge \lambda_b^{(n+1)}$, while (15b) together with (6) shows in turn that $\lambda_b^{(n)} \ge \lambda_b^{(n+1)} \Rightarrow \|\hat{y}_b^{(n+1)}\|_2 \le \|\hat{y}_b^{(n+2)}\|_2$. By induction, we have that $\left(\|\hat{y}_b^{(n)}\|_2\right)_{n\in\mathbb{N}}$ is nondecreasing and $\left(\lambda_b^{(n)}\right)_{n\in\mathbb{N}}$ is nonincreasing; the latter being bounded below by 0, it

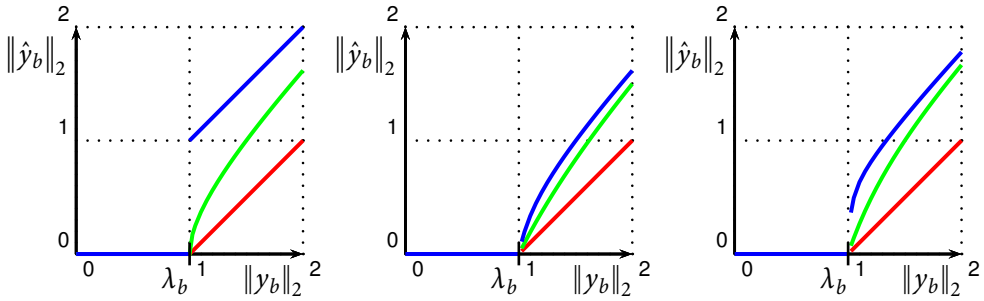

(a) $\lambda_b \overset{\text{set}}{=} 1$, $\varepsilon_b \overset{\text{set}}{=} 1$. (b) $\lambda_b \overset{\text{set}}{=} 1$, $\varepsilon_b \overset{\text{set}}{=} 1$. (c) $\lambda_b \overset{\text{set}}{=} 1$, $\varepsilon_b \overset{\text{set}}{=} 0.5$.

Figure 2: Reweighted $\ell_{1,2}$-norm denoising estimator. (a) Comparison to the soft- (red) and hard- (blue) thresholding estimators. (b) Reweighted $\ell_{1,2}$-norm denoising sequence for $n \overset{\text{set}}{=} 1$ (red), 2 (green), and 5 (blue); we see that it converges quickly to the limit estimator, in green on (a). (c) *Idem*, with $\varepsilon_b < \lambda_b$; the jump at $\pm\lambda_b$ induces instability, and the estimator is not almost differentiable.

is convergent, and by continuity of (6) with respect to λ_b, so is the sequence $\left(\hat{y}_b^{(n)}\right)_{n\in\mathbb{N}}$. Now, if $\|y_b\|_2 \leq \lambda_b$, then it follows from (6) that $\hat{y}_b^{(1)} = 0$ and from (15a) that $\lambda_b^{(1)} = \lambda_b$; by induction, for all $n \in \mathbb{N}$, $\hat{y}_b^{(n)} = 0$, so that $\hat{y}_b^{(\Lambda_B, E_B)}(y) = 0$. Suppose then $\|y_b\|_2 > \lambda_b$. By continuity of (15a) with respect to y_b, and then again by continuity of (6) with respect to λ_b, we get at convergence $\hat{y}_b^{(\Lambda_B, E_B)}(y) = \left(1 - \frac{\lambda_b}{\|\hat{y}_b^{(\Lambda_B, E_B)}(y)\|_2/\varepsilon_b + 1}\right) y_b$. Its norm satisfies thus $\|\hat{y}_b^{(\Lambda_B, E_B)}(y)\|_2^2 + (\varepsilon_b - \|y_b\|_2)\|\hat{y}_b^{(\Lambda_B, E_B)}(y)\|_2 + \varepsilon_b(\lambda_b - \|y_b\|_2) = 0$, *i.e.* it is a positive root of a second-order polynomial. The discriminant is $\Delta = (\varepsilon_b + \|y_b\|_2)^2 - 4\lambda_b\varepsilon_b > 0$ and the only positive root yields $\frac{1}{2}\left(1 - \frac{\varepsilon_b}{\|y_b\|_2} + \sqrt{\left(\frac{\varepsilon_b}{\|y_b\|_2} + 1\right)^2 - 4\frac{\lambda_b\varepsilon_b}{\|y_b\|_2^2}}\right)\|y_b\|_2$. The result follows by collinearity of $\hat{y}_b^{(\Lambda_B, E_B)}(y)$ and y_b. ∎

Recall the ℓ_0-pseudo-norm penalization mentioned in the introduction, counting the number of nonzero coefficients of a vector, thus inducing sparsity in variational reconstructions. We can define a structured version of the ℓ_0-pseudo-norm, where for all $b \in B$, the subvector defined over b is penalized by λ_b if it is nonzero. The denoising estimator that derives from this penalization is the *group hard-thresholding*, such that for all $b \in B$, $\hat{y}_b^{(\Lambda_B)} \overset{\text{def}}{=} \begin{cases} y_b & \text{if } \|y_b\|_2 > \lambda_b, \\ 0 & \text{if } \|y_b\|_2 \leq \lambda_b. \end{cases}$ On top of its nonconvexity, another drawback of the ℓ_0-pseudo-norm is its noncontinuity. As a result, the hard-thresholding estimator is not continuous either. In contrast, our reweighted $\ell_{1,2}$-norm denoising estimator is computed as successive solutions of convex problems. Moreover, we can see from (16) that it interpolates between the soft- (as $\varepsilon_b \to +\infty$) and hard- (as $\varepsilon_b \to 0$) thresholding estimators; this is also illustrated on Figure 2(a). In the following proposition, we precise under which conditions this estimator has sufficient regularity for estimating its risk with the SURE.

Proposition 2.6. *With the above definitions, $\hat{y}^{(\Lambda_B,E_b)}$ is almost differentiable if, and only if, for all $b \in B$, $\varepsilon_b \geq \lambda_b$. In that case, for all $p \in b^c$, $\frac{\partial \hat{y}_p}{\partial y_p}^{(\Lambda_B,E_B)} = 1$, and for all $b \in B$, for all $p \in b$, and for almost all $y \in \mathbb{R}^P$,*

$$\frac{\partial \hat{y}_p}{\partial y_p}^{(\Lambda_B,E_B)}(y) = \begin{cases} \frac{\|y_b\|_2^{-1}}{2}\left(\|y_b\|_2 - \varepsilon_b + \sqrt{(\varepsilon_b + \|y_b\|_2)^2 - 4\lambda_b\varepsilon_b}\right) \\ \qquad + \frac{\varepsilon_b}{2}\left(1 - \frac{(\varepsilon_b + \|y_b\|_2) - 4\lambda_b}{\sqrt{(\varepsilon_b + \|y_b\|_2)^2 - 4\lambda_b\varepsilon_b}}\right)\frac{{y_p}^2}{\|y_b\|_2^3} & \text{if } \|y_b\|_2 > \lambda_b, \quad (17a) \\ 0 & \text{if } \|y_b\|_2 \leq \lambda_b. \quad (17b) \end{cases}$$

Proof. Let $p \in \{1,\dots,P\}$, $y \in \mathbb{R}^P$, and consider $\hat{u}\colon \mathbb{R} \to \mathbb{R}\colon y'_p \mapsto \hat{y}_p^{(\Lambda_B,E_B)}(y_{\{p\}^c}, y'_p)$. If $p \in b^c$, then $\hat{u}$ reduces to the identity, and $\frac{\partial \hat{y}_p}{\partial y_p}^{(\Lambda_B)} = 1$. Otherwise, let $b \in B$ be the unique group of coordinates containing p, and denote $\{p\}_b^c \stackrel{\text{def}}{=} b \setminus \{p\}$. Then for all $y'_p \in \mathbb{R}$, we develop $\hat{u}(y'_p) =$

$$\begin{cases} \frac{y'_p}{2} - \frac{1}{2}\left[\|y_{\{p\}_b^c}\|_2^2 + {y'_p}^2\right]^{-\frac{1}{2}}\left(\varepsilon_b - \sqrt{\left(\varepsilon_b + \sqrt{\|y_{\{p\}_b^c}\|_2^2 + {y'_p}^2}\right)^2 - 4\lambda_b\varepsilon_b}\right)y'_p \\ \qquad\qquad \text{if } \|y_{\{p\}_b^c}\|_2^2 + {y'_p}^2 > {\lambda_b}^2, \\ 0 \qquad\qquad \text{if } \|y_{\{p\}_b^c}\|_2^2 + {y'_p}^2 \leq {\lambda_b}^2, \end{cases}$$

where $\|y_{\{p\}_b^c}\|_2$ is the Euclidean norm of $y_{\{p\}_b^c} \in \mathbb{R}^{|b|-1}$ if $|b| > 1$, and is 0 otherwise. If $\|y_{\{p\}_b^c}\|_2^2 > {\lambda_b}^2$, then for all $y'_p \in \mathbb{R}$, $\left(\varepsilon_b + \sqrt{\|y_{\{p\}_b^c}\|_2^2 + {y'_p}^2}\right)^2 - 4\lambda_b\varepsilon_b > 0$, so that $\hat{u}$ is continuously differentiable over $\mathbb{R}$, hence absolutely continuous. If $\|y_{\{p\}_b^c}\|_2^2 \leq {\lambda_b}^2$, define $z \stackrel{\text{def}}{=} \sqrt{{\lambda_b}^2 - \|y_{\{p\}_b^c}\|_2^2}$; $\hat{u}$ is obviously absolutely continuous over $[-z,z]$. Moreover, $\hat{u}$ is continuously differentiable over $]z,+\infty[$, so that for all $y'_p, y''_p \in]z,+\infty[$, we have $\hat{u}(y''_p) = \hat{u}(y'_p) + \int_{y'_p}^{y''_p} \frac{\partial \hat{u}}{\partial y'_p}(t)\,\mathrm{d}t$, where the weak derivative $\frac{\partial \hat{u}}{\partial y'_p}(t)$ is given by (17a) by substituing $(y_{\{p\}^c}, t)$ to y_b and t to y_p. Provided that the limit exists, we get the improper integral $\hat{u}(y''_p) = \lim_{y'_p \to z^+} \hat{u}(y'_p) + \int_z^{y''_p} \frac{\partial \hat{u}}{\partial y'_p}(t)\,\mathrm{d}t$; verifying that $\frac{\partial \hat{u}}{\partial y'_p}$ is nonnegative, it is then integrable over $[z, y''_p]$ and its integral is equal to the above improper integral. Now, if $\lambda_b > 0$, then we have $\lim_{y'_p \to z^+} \hat{u}(y'_p) = \frac{1}{2\lambda_b}\left(\lambda_b - \varepsilon_b + |\varepsilon_b - \lambda_b|\right)z$ and if $\lambda_b = 0$, then $\lim_{y'_p \to z^+} = 0$. In any case, if $\varepsilon_b \geq \lambda_b$, then $\lim_{y'_p \to z^+} \hat{u}(y'_p) = 0 = \lim_{y'_p \to z^-} \hat{u}(z)$, and we deduce that $\hat{u}$ is absolutely continuous over all line segments in $[z,+\infty[$. Noticing that it is an odd function, we deduce by symmetry that it is absolutely continuous over all line segments in $\mathbb{R}$. Conversely, if $\varepsilon_b < \lambda_b$, then for all $y \in \left\{y \in \mathbb{R} \,\middle|\, \|y_{\{p\}_b^c}\|_2 < \lambda_b\right\}$, $\lim_{y'_p \to z^+} \hat{u}(y'_p) > \lim_{y'_p \to z^-} \hat{u}(y'_p)$, hence for all $y''_p \in]z,+\infty[$, $\hat{u}$ is not absolutely continuous over $[z, y''_p]$. Since the sets $y \in \left\{y \in \mathbb{R}^P \,\middle|\, \|y_{\{p\}_b^c}\|_2 < \lambda_b\right\}$ and $]z,+\infty[$ have nonzero measure (for the Lebesgue measures over $\mathbb{R}^P$ and $\mathbb{R}$, respectively), we conclude that $\hat{y}^{(\Lambda_B,E_b)}$ is not almost differentiable. ∎

Remark 2.1. Strictly speaking, one should also check the existence of the weak partial derivatives $\frac{\partial \hat{y}_q}{\partial y_p}^{(\Lambda_B, E_B)}$ for $q \neq p$ to establish almost differentiability; this follows the same lines as the case $q = p$. Note however that, in the case of uncorrelated noise, in view of Remark 1.2, the existence and integrability of $\frac{\partial \hat{y}_p}{\partial y_p}^{(\Lambda_B, E_B)}$ for $p \in \{1, \dots, P\}$ is sufficient for (5) to be an unbiased estimate of the risk of $\hat{y}^{(\Lambda_B, E_B)}$.

Corollary 2.5. *With the above definitions, if for all $b \in B$, $\varepsilon_b \geq \lambda_b$, then*

$$\begin{aligned}
\mathrm{SURE}\left(\hat{y}^{(\Lambda_B, E_B)}, y\right) \overset{\text{def}}{=} & \sum_{\substack{b \in B: \\ \|y_b\|_2 \leq \lambda_b}} \|y_b\|_2^2 + 2\|\sigma_{b^c}\|_2^2 - \|\sigma\|_2^2 \\
& + \sum_{\substack{b \in B: \\ \|y_b\|_2 > \lambda_b}} \left(\frac{1}{4}\left((\varepsilon_b + \|y_b\|_2) - \sqrt{(\varepsilon_b + \|y_b\|_2)^2 - 4\lambda_b \varepsilon_b} \right)^2 \right. \\
& \qquad + \frac{\|\sigma_b\|_2^2}{\|y_b\|_2} \left(\|y_b\|_2 - \varepsilon_b + \sqrt{(\varepsilon_b + \|y_b\|_2)^2 - 4\lambda_b \varepsilon_b} \right) \\
& \qquad \left. + \frac{\varepsilon_b}{\|y_b\|_2} \left(1 - \frac{(\varepsilon_b + \|y_b\|_2) - 4\lambda_b}{\sqrt{(\varepsilon_b + \|y_b\|_2)^2 - 4\lambda_b \varepsilon_b}} \right) \frac{\|\sigma_b \cdot y_b\|_2^2}{\|y_b\|_2^2} \right)
\end{aligned} \tag{18}$$

is an unbiased estimate of the risk of $\hat{y}^{(\Lambda_B, E_B)}$.

Proof. If for all $b \in B$, $\varepsilon_b \geq \lambda_b$, then according to Proposition 2.6, $\hat{y}^{(\Lambda_B, E_B)}$ is almost differentiable, and in view of (17), its weak partial derivatives are nonnegative. In particular, for all $p \in \{1, \dots, P\}$, $\left| \frac{\partial \hat{y}_p}{\partial y_p}^{(\Lambda_B, E_B)} \right|$ is locally integrable. Moreover, we see from (17a) that $\lim_{\|y_b\|_2 \to +\infty} \frac{\partial \hat{y}_p}{\partial y_p}^{(\Lambda_B, E_B)}(y) = 1$, so that it is bounded outside a ball of sufficiently large radius. Since the probability density of N is bounded over $\mathbb{R}$ and has finite mass, we conclude that $\mathbb{E}_N \left| \frac{\partial \hat{y}_p}{\partial y_p}^{(\Lambda_B, E_B)}(Y) \right| < +\infty$. The result follows by injecting (16) and (17) in (5). ∎

Whenever the reweighted $\ell_{1,2}$-norm penalization seems relevant, one can set for all $b \in B$, $\varepsilon_b \overset{\text{set}}{=} \lambda_b$. As illustrated on Figure 2, it is the best compromise between influence of the reweighting process, and regularity of the resulting denoising estimator. For optimizing the SURE efficiently for only one parameter, one can then follow once again the previous approach, introducing the parameter λ and for all $b \in B$, the factor μ_b such that $\lambda_b \overset{\text{set}}{=} \lambda \mu_b$, and the ratios $r_b \overset{\text{def}}{=} \frac{\|y_b\|_2}{\mu_b}$. The SURE (18) becomes

$$\begin{aligned}
\mathrm{SURE}\left(\hat{y}^{(\lambda)}, y\right) \overset{\text{def}}{=} & \sum_{\substack{b \in B: \\ r_b \leq \lambda}} {\mu_b}^2 {r_b}^2 + 2\|\sigma_{b^c}\|_2^2 - \|\sigma\|_2^2 \\
& + \sum_{\substack{b \in B: \\ r_b > \lambda}} \left(\frac{{\mu_b}^2}{4}\left((\lambda + r_b) - \sqrt{(\lambda + r_b)^2 - 4\lambda^2} \right)^2 \right. \\
& \qquad + \frac{\|\sigma_b\|_2^2}{r_b} \left(r_b - \lambda + \sqrt{(\lambda + r_b)^2 - 4\lambda^2} \right) \\
& \qquad \left. + \frac{\lambda}{r_b} \left(1 - \frac{(\lambda + r_b) - 4\lambda}{\sqrt{(\lambda + r_b)^2 - 4\lambda^2}} \right) \frac{\|\sigma_b \cdot y_b\|_2^2}{\|y_b\|_2^2} \right).
\end{aligned}$$

In comparison to (9), finding the λ at which this expression reached its minimum over two consecutive values $[r_{b_i}, r_{b_{i+1}}[$ is more involved. However, simply testing for each observed values, *i.e.* $\hat{\lambda}_i \overset{\text{set}}{=} r_{b_i}$, is a good strategy in practice. Note also that it is computationaly more expensive than for the simple $\ell_{1,2}$-norm denoising, because for all $b \in B$, the factor $\sqrt{(\lambda + r_b)^2 - 4\lambda^2}$ must be computed for each tested $\hat{\lambda}_i$, and cumulative sums cannot be used anymore; the total cost scales then as $O(P + |B|^3)$ operations. In consequences, it is also a good practice to discard irrelevant observed values $\hat{\lambda}_i$, and to subsample the remaining ones[3]

Remark 2.2. The reweighting scheme presented along this section can be adapted without much modifications to a $\delta_{1,2}$-norm penalization; corresponding conditions of weak differentiability and SURE expressions can be similarly derived.

3 Beyond Proximity Operators

As explained in the introduction of this thesis, in the variational framework, denoising estimators are written as solutions of minimization problems. However, the data-fidelity term is not necessarily reduced to a ℓ_2-norm; alternatively, the penalizations are not necessarily simple functionals. In such cases, the SURE (4) cannot necessarily be computed efficiently. In this section, we present some usual situations, and propose practical workarounds.

3.1 Sum of Simple Penalizations

First, let us consider a direct extension of the estimators in § 2, namely denoising estimators defined as the proximity operator of a given convex penalization $g \in \Gamma_0(\mathbb{R}^P)$ which is not simple, *i.e.* $\hat{y} \overset{\text{def}}{=} \text{prox}_g$ is not known as a closed form expression. We assume however that g can be split as a sum of simple penalizations, as $g \overset{\text{def}}{=} \sum_{i=1}^n g_i$ with $n \in \mathbb{N}_*$, so that, as explained in the introduction, $y \in \mathbb{R}^P$ being given, many iterative proximal algorithms are available for computing the minimization problem $\hat{y}(y) \overset{\text{def}}{=} \text{argmin}_{x \in \mathbb{R}^P} \frac{1}{2}\|y - x\|^2 + \sum_{i=1}^n g_i(x)$ at reasonable cost.

3.1.1 Partly Smooth Penalizations

Assuming that the computational cost of computing $\hat{y}(y)$ is affordable, it remains only to estimate the trace of its weak Jacobian in order to compute its SURE (4). Several papers address this problem for different penalizations; the most general result to date can be found in Vaiter *et al.* (2014), unveiling the expression of the weak derivative of $\hat{y}$ for any functional g which is a *piecewise regular gauge*. Without delving into details, this encompasses all the penalizations presented in this work, at the notable exception of the indicator functions.

[3] codes in Matlab and C interfaced with Mex are available at https://github.com/1a7r0ch3/SURE.

A practical drawback of this approach is that the solution of the minimization problem defining $\hat{y}(y)$ must be computed with high precision. In brief, the functional g defines certain subspaces of interest, and one must identify which of those subspaces contains the solution $\hat{y}(y)$ in order to compute the weak derivatives; and the dependencies of the weak derivatives on those subspaces are highly unstable. A typical example is the $\ell_{1,2}$-norm (and in general any sparsity promoting regularization), for which, as can be seen in (7), the partial derivatives depends on the support (the nonzero groups of coefficients) of the solution. For a problem comprising such sparsity promoting penalizations mixed with other penalizations, iterative proximal algorithms often provides solutions with coefficients which are numerically of very small amplitudes, but not exactly zero. Therefore, identification of the support will fail, impacting drastically the risk estimate.

3.1.2 Iterative SURE and Monte Carlo SURE

When $\hat{y}$ is computed as the output of an iterative algorithm, an other approach that necessitates less precision than above consists in estimating iteratively the degrees of freedom of the estimator. Choosing $m \in \mathbb{N}_*$, one replaces $\hat{y}$ by an approximation $\hat{y}^{(m)}$ defined as the output of the algorithm, initialized at a given point $\hat{y}^{(0)}$, after m iterations.

For most proximal splitting algorithms, $\hat{y}^{(m)}$ is a composition of Lipschitzian operators (essentially proximity operators and linear operators), and thus is itself Lipschitzian. Moreover, we show in Proposition 5.1 that one can compute the weak partial derivatives of the composition using the *chain rule*, provided than one knows the weak partial derivatives of each individual functionals in an appropriate orthonormal basis (see Annex B for details). More precisely, suppose that the algorithm is defined as, for all $l \in \mathbb{N}$, $\hat{y}^{(l+1)}(y) = T^{(l)}(\hat{y}^{(l)}(y), y)$, where $T^{(l)} \colon \mathbb{R}^P \times \mathbb{R}^P \to \mathbb{R}^P$ is Lipschitzian. Then we have for all $l \in \mathbb{N}$ and almost all $y \in \mathbb{R}^P$, in obvious matrix notations,

$$\frac{\partial \hat{y}^{(l+1)}}{\partial y}(y) = \left(\frac{\partial T^{(l)}}{\partial \hat{y}}\left(\hat{y}^{(l)}(y), y\right)\right)\left(\frac{\partial \hat{y}^{(l)}}{\partial y}(y)\right) + \frac{\partial T^{(l)}}{\partial y}\left(\hat{y}^{(l)}(y), y\right).$$

Now, even if one has access, for each $l \in \{1, \dots, m\}$, to the derivatives of $T^{(l)}$ in closed form, the analytic expression of the derivatives of $\hat{y}^{(m)}$ becomes prohibitively complicated as the number of iterations m is increasing. However, recall that the weak Jacobian matrix is involved in the SURE expression (4) only through its trace. Following for instance Deledalle *et al.* (2012), a workaround relies on the *Monte Carlo implicit matrix trace estimator*: if $A \in \mathbb{R}^{P \times P}$ is a given matrix and H is a random vector in $\mathbb{R}^P$ following a convenient distribution (*e.g.* $H \sim \mathcal{N}(0, \mathrm{Id}_P)$), then $\mathrm{tra}(A) = \mathbb{E}_H\langle H \,|\, AH \rangle$; see Roosta-Khorasani and Ascher (2013) and references therein for details. Thus, one can compute an empirical estimate of the term $\mathrm{tra}\left(C\frac{\partial \hat{y}^{(m)}}{\partial y}(y)\right)$ by computing iteratively the products $\left(\frac{\partial \hat{y}^{(l)}}{\partial y}(y)\right)h$ for given random realizations h of H. For sufficiently large observations, just as one can get acceptable estimate of $\mathbb{E}_N\|\hat{y}(Y) - Y\|^2$ from a single observation $\|\hat{y}(y) - y\|^2$, a single realization h is usually sufficient for estimating of $\mathbb{E}_{N,H}\langle H \,|\, C\left(\frac{\partial \hat{y}^{(m)}}{\partial y}(Y)\right)H \rangle$ from $\langle h \,|\, C\left(\frac{\partial \hat{y}^{(m)}}{\partial y}(y)\right)h \rangle$.

In a similar spirit, let us mention the Monte Carlo SURE proposed by Ramani *et al.* (2008), where the degrees of freedom is estimated by *random finite differences*: under

suitable regularity conditions, for all $y \in \mathbb{R}$, $\mathbb{E}_H \lim_{\epsilon \to 0} \frac{1}{\epsilon} \langle H \mid \hat{y}(y + \epsilon H) - \hat{y}(y) \rangle = \operatorname{tra}\left(\frac{\partial \hat{y}}{\partial y}(y)\right)$. Approximating the limit with a "sufficiently small" value of ϵ, this approach presents the advantage of using the estimator as a black box, *i.e.* there is no need to compute any actual weak partial derivative.

3.1.3 Fast Approximations

Unfortunately, in many cases one cannot afford many computations of $\hat{y}$. In order to select efficiently the parameters of the model, we propose crude heuristics that depends on the nature of the penalizations $(g_i)_{1 \leq i \leq n}$. Indeed, mixed penalizations in a variational problem usually enforces different priors on the signal; the idea is simply to select each individual penalization g_i by using the SURE of the estimator $\hat{y}^{(i)} \stackrel{\text{def}}{=} \operatorname{prox}_{g_i}$, and to scale them roughly according to their possible interactions.

Certain penalizations are independent from the others, as it the case for indicator functions, constraining the estimator to lie in a certain convex set without any regards to other penalizations or to the noise intensity. If g_i enforces such a prior, it can be selected considering $\hat{y}^{(i)}$ alone.

In contrast, different penalizations can sometimes interfere one with the other, for instance the ones which aim at capturing the noise. It is the case of the $\ell_{1,2}$-norm and of the $\delta_{1,2}$-norm, which both tend to shrink the amplitude of the signal. If each individual $\hat{g}_i$ is selected as above, then $g \stackrel{\text{set}}{=} \sum_{i=1}^n \hat{g}_i$ would tend to overpenalize the denoising problem. If one still wants to enjoy from a variety of priors, each one of them being selected adaptively to the signal, a natural approach is to consider a convex combinations of them, in particular $\hat{g} \stackrel{\text{set}}{=} \frac{1}{n} \sum_{i=1}^n \hat{g}_i$. We underline here that each $\hat{y}^{(i)}$ is usually a nonlinear function of its parameters, so that no theoretical guarantee can be given over the resulting estimator. However, as illustrated numerically with experiment 4.2.2, this approach can be successful in simple cases.

A specific instance of the latter situation arises when a given penalization is split into several simple terms, all parameterized by the same single parameter. For example, a $\ell_{1,2}$-norm defined over a complex block structure can be split over arbitrary nonoverlapping block structures, but the scaling parameter should be optimized over all of them simultaneously. In this example, assuming that the signal of interest are spatially statistically stationary, observe that the functions $(g_i)_{1 \leq i \leq n}$ are close to each other. In turn, for each $i \in \{1, \dots, n\}$, $\hat{y}^{(i)}$ is close to $\operatorname{prox}_{\frac{1}{n} g}$; and up to small variations, it is relevant to approximate the latter by $\tilde{y} \stackrel{\text{def}}{=} \frac{1}{n} \sum_{i=1}^n \hat{y}^{(i)}$.

Interestingly, it is easy to see that $\tilde{y}$ is exactly $\hat{y}^{(1)}$ defined in § 3.1.2 for approximating $\operatorname{prox}_{\frac{1}{n} g}$, using a specific instance of our generalized forward-backward algorithm. In contrast to the previous section, with only one iteration, weak partial derivatives of $\tilde{y}$ can be directly deduced from the ones of each $\hat{y}^{(i)}$ by linearity. Developing for all $y \in \mathbb{R}^P$, $\frac{1}{n} \sum_{i=1}^n \left\| y - \hat{y}^{(i)}(y) \right\|^2 = \left\| y - \tilde{y}(y) \right\|^2 + \frac{1}{n} \sum_{i=1}^n \left\| \tilde{y}(y) - \hat{y}^{(i)}(y) \right\|^2$, we deduce from (4) that

$$\operatorname{SURE}(\tilde{y}, y) = \frac{1}{n} \operatorname{SURE}(\hat{y}^{(i)}) - \frac{1}{n} \sum_{i=1}^n \left\| \tilde{y}(y) - \hat{y}^{(i)}(y) \right\|^2 . \tag{19}$$

One retrieves the fact that the risk of the average of several estimators is the average of the risk of each one of them, reduced by the variance across them. Note that since $\tilde{y}$ approximates $\operatorname{prox}_{\frac{1}{n}g}$, if all functions $(\hat{g}_i)_{1\leq i\leq n}$ are selected simultaneously by minimizing (19), the corresponding optimal penalization is $\hat{g} \overset{\text{set}}{=} \frac{1}{n}\sum_{i=1}^{n}\hat{g}_i$. Selecting g that way rather than selecting each g_i individually seems more accurate; in particular, the correction by the variance might sometimes prove useful, as illustrated numerically in experiment 4.2.1.

3.2 Denoising in a Synthesis Frame

We have seen that convex penalizations in variational denoising estimators are supposed to enforce known priors about the signal one wants to recover. In many situations, such priors are not directly relevant over the signal domain, but rather over the coefficients of the signal within a certain linear representation. Recall for instance that $\ell_{1,2}$-norm penalization enforces sparsity; natural signals are not sparse in the pixel domain, but usually admit good sparse approximations in the wavelet domain (see again the introduction). Let $K \in \mathbb{N}_*$, and $D\colon \mathbb{R}^K \to \mathbb{R}^P$ be a linear operator represented by a dictionary of K atoms in $\mathbb{R}^P$ (a so-called *frame*, abusively also denoted D), and $g \in \Gamma_0(\mathbb{R}^K)$ be a convex penalization. The *denoising estimator with synthesis frame D and penalization g* is defined as $\hat{y}\colon \mathbb{R}^P \to \mathbb{R}^P\colon y \mapsto D\hat{x}$ where

$$\hat{x} \in \operatorname*{argmin}_{x\in\mathbb{R}^K} \tfrac{1}{2}\|y - Dx\|^2 + g(x)\ . \tag{20}$$

We assume that the set of minimizers in (20) is nonempty (it is the case for instance if g is *coercive*, or if D is injective). In that case, note that all minimizers have the same image by the operator D. Indeed, if two minimizers had different images by D, then by strict convexity of the squared norm, any strictly convex combination of them would achieve a lower value of the objective, contradicting the fact that they are minimizers. Thus, $\hat{y}$ is a well defined one-to-one mapping.

3.2.1 Orthonormal Frame

Let us first specify the important case of an orthonormal frame, *i.e.* $D^*D = \mathrm{Id}$ (over $\mathbb{R}^K$), or in matrix notations, for all $k, k' \in \{1,\dots,K\}$, ${}^tD_kD_{k'} = 1$ if $k = k'$, 0 otherwise. Note that the operator D is itself orthogonal if, and only if, $\operatorname{ran} D = \mathbb{R}^P$, *i.e.* $K = P$. Applying Lemma IV.3.1 (ii) to D^*, we have $\operatorname{proj}_{\operatorname{ran} D} = DD^*$. Then, for all $y \in \mathbb{R}^P$ and $x \in \mathbb{R}^K$, we have by orthogonality $\|y - Dx\|^2 = \|DD^*y - Dx\|^2 + \|y - DD^*y\|^2$. Developing and using the properties of the adjoint, $\|DD^*y - Dx\|^2 = \langle DD^*y - Dx \,|\, DD^*y - Dx\rangle = \langle D^*y - x \,|\, D^*DD^*y - D^*Dx\rangle$, we finally get

$$\|y - Dx\|^2 = \|D^*y - x\|^2 + \|y - DD^*y\|^2\ . \tag{21}$$

The term $\|y - DD^*y\|^2$ in (21) is the square distance between y and $\operatorname{ran} D$, and represents the part of the signal that cannot be represented within the dictionary D. In particular, it is independent from the coefficients x. Injecting (21) in (20), we get for all $y \in \mathbb{R}^P$

$\hat{y}(y) = D\hat{x}(D^*y)$, where $\hat{x}\colon \mathbb{R}^K \to \mathbb{R}^K \colon x \mapsto \mathrm{prox}_g(x)$ is now a well defined one-to-one mapping. Note that D^*y is a realization of $D^*Y = D^*y^{(0)} + D^*N$, and we have moved the denoising problem from the signal domain to the transformed domain, where the target signal $D^*y^{(0)}$ is corrupted additively by the transformed noise $D^*N \sim \mathcal{N}(0, D^*CD)$. Following (4), the SURE for the estimator $\hat{x}$, which is now a proximity operator as in § 2, is

$$\mathrm{SURE}\left(\hat{x}, D^*y\right) = \left\|D^*y - \hat{x}(D^*y)\right\|^2 + 2\,\mathrm{tra}\left(D^*CD\tfrac{\partial\hat{x}}{\partial x}(D^*y)\right) - \mathrm{tra}\left(D^*CD\right), \qquad (22)$$

Now, it is easy to see that $\hat{y} = D\circ\hat{x}\circ D^*$ is also almost differentiable and by Proposition 5.1, its weak Jacobian is for all $y \in \mathbb{R}$, $\frac{\partial\hat{y}}{\partial y}(y) = D\frac{\partial\hat{x}}{\partial x}(D^*y)D^*$. By commuting the arguments in the trace in (22) and reusing (21), we get $\mathrm{SURE}\left(\hat{x}, D^*y\right) = \mathrm{SURE}\left(\hat{y}, y\right) - \|y - DD^*y\|^2$. Altogether, we have established that the SURE for the denoising estimator in the transformed domain is equal, up to a factor that depends only on the observed signal y and the dictionary D, to the SURE of the denoising estimator in the signal domain. Optimizing parameters for the penalization function g can then be performed directly in the transformed domain, over the observation $D^*y \in \mathbb{R}^K$, which is nothing but the vector of correlations of y with each element of the frame D; in matrix notations, $({}^tD_k y)_{1\le k\le K}$.

3.2.2 Orthogonal Approximation

If the frame is not orthonormal, previous considerations fail and we cannot resort to the SURE of the proximity operator of g anymore. First, observe that a denoising estimator in an arbitrary frame still falls within the frameworks discussed along § 3.1.1 and 3.1.2, so that on can resort to the approaches described therein.

Once again, in practice this is often computationaly too expensive. For fast parameter selection, we simply propose to select the penalization g using (22) *as if* the frame D was orthonormal. Such an approximation might be surprising, especially for redundant frames containing highly correlated atoms, but keep in mind that any frame can be seen, up to normalization, as the concatenation of several orthonormal frames. Based on that, Raphan and Simoncelli (2008) consider estimators of the form $y \mapsto D\hat{x}(D^*y)$, where $\hat{x}\colon \mathbb{R}^K \to \mathbb{R}^K$ is a given estimator acting over the transformed domain of an orthonormal frame, and their natural extensions to a redundant frame. Under stationary noise assumption, they show that such an estimator presents lower risk within the redundant frame than within any individual orthonormal frame composing it.

Though this does not apply directly to estimators defined as (20), let us mention that, in the particular but important case of the sparsity framework, reconstructing a signal with as few atoms as possible tends to select uncorrelated atoms. If g is separable according to coefficients corresponding to different orthonormal frame, it seems reasonable to select each separable part for the corresponding denoising in the orthonormal frame; chances are that aggregating them in a redundant frame denoising will perform at least as good as each orthonormal frame denoising. Following this rationale, recall that in our SMCS model, some components are reconstructed within redundant temporal frames. Since we penalize the coefficients corresponding to each atom separately (see § II.3), we

can thus select those penalizations separately for each atom $k \in \{1, \dots, K\}$. Note that this is rendered possible because we observe the correlations of a given atom with the time course of each spatial locations, in the notations of Chapter II, $\left({}^{\mathrm{t}}D_k^{(c)} Y_p\right)_{1 \leq p \leq P}$; this provides statistical significance of the SURE of each denoising of Y within the dictionary $D_k^{(c)}$ reduced to a single temporal atom.

The orthogonal approximation for sparse denoising within a redundant frame is illustrated numerically on experiment 4.1.3.

4 Numerical Experiments

This section is devoted to numerics illustrations of previous theoretical and computational considerations. All experiments deal with the same denoising task, where $y^{(0)} \in \mathbb{R}^P$ is a gray level natural image comprising $P \overset{\text{set}}{=} 512 \times 512$ pixels, corrupted by a realization of an additive white Gaussian noise $N \overset{\text{set}}{\sim} \mathcal{N}(0, C \overset{\text{set}}{=} \sigma^2 \mathrm{Id}_P)$, see Figure 5(a) and (b); the values of $y^{(0)}$ are normalized in the range $[0,1]$, while the standard deviation of the noise is $\sigma \overset{\text{set}}{=} 10^{-1}$. Note that with the single realization y of our experiments, using the method described in § 1.3, the relative error between our estimate $\hat{\sigma}$ and the actual σ lie below 10^{-2}.

We test for relevance and accuracy of the previous developments by comparing, for each estimator that we consider and various values of the parameters tuning it, the approximation of the risk together with the actual squared error $\|y - y^{(0)}\|^2$. For the sake of comparison, all denoising results are depicted in Figure 5, together with their respective signal-to-noise ratio, as defined by (IV.5.3.2).

4.1 Block Sparse Wavelet Denoising

The first set of experiments deals with the denoising within a two-dimensional wavelet frame, in the sparsity framework. We use Daubechies wavelets with four vanishing moments (Daubechies, 1992), over four decomposition levels.

4.1.1 Block $\ell_{1,2}$-Norm Denoising in an Orthogonal Wavelet Frame

Estimators and parameters. The block structured $\ell_{1,2}$-norm penalization that we use to enforce spatially structured sparsity over the coefficients of a two-dimensional orthogonal wavelet frame is described in details within the previous chapter, § IV.5.2.2. In brief, the wavelet frame is the concatenations of *subbands* as $D = \left(D^{(j,d)}\right)_{\substack{j_{\min} \leq j \leq j_{\max} \\ 1 \leq d \leq 3}}$, each one being characterized by its scale j and direction d. For each subband, one must select a block size $\mathsf{s}^{(j,d)}$ that will determine the block structure $B^{(j,d)}$, and set the corresponding weights $\Lambda^{(j,d)}$. Following the strategy described within § 2.1, the latter depends only on one scalar $\lambda^{(j,d)} \in \mathbb{R}$, defining for all $b \in B^{(j,d)}$, $\lambda_b \overset{\text{set}}{=} \lambda^{(j,d)} \mu_b$, where $\mu_b \overset{\text{set}}{=} \sqrt{|b|}\hat{\sigma}$ scales the weight of the block b according to the estimated $\ell_{1,2}$-amplitude of the noise within the block.

Since the frame is orthogonal and the penalization is separable along the subbands, the parameters $(\mathsf{s}^{(j,d)}, \lambda^{(j,d)})$ can be selected within each subband independently, using $\mathrm{SURE}(\hat{x}^{(j,d,\mathsf{s},\lambda)}, D^* y)$ as described by (22). In addition, we have $\|D\hat{x}(y) - y^{(0)}\|^2 = \sum_{j=j_{\min}}^{j_{\max}} \sum_{d=1}^{3} \|(\hat{x}^{(j,d)}(y) - {}^{\mathrm{t}}D^{(j,d)} y^{(0)})\|_2^2$, so that the squared error can also be decomposed along the subbands.

We consider two denoising estimators. The first one is penalized by a $\ell_{1,2}$-norm defined over a only one block grid per subband, *i.e.* $B^{(j,d)}$ is nonoverlapping. Hence, its SURE can be computed exactly thanks to (9). In contrast, the penalization of the second one defined over several block grids, and we approximate its SURE following (19), by splitting the $\ell_{1,2}$-norm along the grids.

block size $\mathsf{s}^{(j,d)}$	1	2	3	4	6	8	10	12
separation between grids	1	1	1	1	2	2	3	3
resulting number of grids $n^{(j,d)}$	1	4	9	16	9	16	9	16

Table 1: Tested block structures in experiments 4.1.1 and 4.1.2.

Results. We compute, within each subband (j, d) and for each block size $\mathsf{s}^{(j,d)}$ listed in Table 1, the risk estimate and the squared error for values of $\lambda^{(j,d)}$ running across the optimal values $\left(\hat{\lambda}_i\right)_{0 \le i \le |B^{(j,d)}|}$ defined by (10) (more precisely, a regularly spaced subset of them, for subbands containing too many coefficients). Then on Figure 3(a), we give for each subband the block size achieving the minimum of the risk estimate, and for this block size we plot the risk estimate (in transparency) and the squared error (in opacity) as functions of λ. The results concerning the estimator penalized over a single block grid (respectively over multiple block grids) are given in blue (respectively in red).

The overall shapes of the curves are similar across subbands, but their minima are not attained for the same values of λ. In particular, the optimal penalization is increasing with the scale j of the subband. This is consistent with the hypothesis that the highest frequencies in the observations are dominated by noise (see § 1.3). The selected block sizes also tend to increase with the scale j, certainly because the support of the wavelets decreases with their scale j, so that a given spatially localized feature concerns more spatially neighboring wavelet coefficients.

In general, the risk estimates are in good accordance with the squared error. More importantly, on each graph their minima are attained at values of λ which are close to each others, *i.e.* the proposed risk estimates allows to select near optimal penalization values. Now, the approximated SURE of the estimator penalized over multiple grids nearly coincides with the exact SURE of the estimator penalized over a single grid. This indicates that the proximity operators of the $\ell_{1,2}$-norm over two different block grids are so similar that the correction by the variance across grids in (19) is negligible. Incidentally, on that particular denoising problem, using overlapping block structures does not improve much the denoising performance, as can be seen by comparing Figure 5(e) and (f).

4.1.2 Reweighted Version

Estimators and parameters. The setting is the same as experiment 4.1.1, except that we use the reweighted version of the $\ell_{1,2}$-norm. For the estimator penalized over a single block grid, we set for all $b \in B^{(j,d)}$, $\varepsilon_b \overset{\text{set}}{=} \lambda_b$. Note however that for the estimator penalized over multiple block grids, since each coefficient is penalized within exactly $n^{(j,d)}$ different blocks, the order of magnitude of each penalization tends to be decreased by a factor $n^{(j,d)}$, compared to the nonoverlapping case. Thus, we consider the above reweighting parameters when computing the approximated SURE (19), but in the final estimator, we set for all $b \in B^{(j,d)}$, $\varepsilon_b \overset{\text{set}}{=} n^{(j,d)}\lambda_b$.

Results. The results are comparable to the above nonreweighted $\ell_{1,2}$-norm penalization case. Note however that the curves of the risk estimates on Figure 5(b) are more irregular. This is due to the fact that the derivative of the estimator tends to infinity when for any block b, λ_b tends to $\|y_b\|_2$ from below, as can be seen on Figure 2. Though, as long as the estimator is weakly differentiable (*i.e.* for all $b \in B^{(j,d)}$, $\varepsilon_b \geq \lambda_b$), in spite of irregular fluctuations, its SURE enables relevant selection of penalization parameters. As expected, they are in general greater than for the corresponding nonreweighted $\ell_{1,2}$-norm denoising estimator, allowing for higher sparsity. In our experiments, this translates to slightly better denoising, as shown in Figure 5(g) and (h).

4.1.3 ℓ_1-Norm Denoising in a Redundant Wavelet Frame

Estimators and parameters. In the same setting as experiment 4.1.1, we consider only blocks of size $\mathsf{s} \overset{\text{set}}{=} 1$ (*i.e.* the penalization is a weighted ℓ_1-norm) and investigate the denoising in a redundant frame. More precisely, we use a *nondecimated* version of the orthogonal wavelet frame, which can be seen as the concatenation of all its possible spatial shifts. Atoms are normalized within each scale so as to obtain a tight frame, and penalizations weights are normalized accordingly. Similarly to the orthogonal case, we select one penalization parameter per subband, independently from the other subbands, following the orthogonal approximation discussed in § 3.2.2.

Results. As expected, the risk estimate and squared error curves within each subbands closely resemble those of experiment 4.1.1 (data not shown); in particular, risk estimates of orthogonal and redundant versions almost coincide, in coherence with the stationarity assumption of the statistics of our image. As shown in Figure 5(c) and (d), using the redundant version slightly improves the denoising performance.

At this occasion, note by comparing Figure 5(c) with (e) or (f), that using spatially structured penalizations also improves the denoising.

4.2 Total Variation and Composite Denoising

We now turn to denoising estimators penalized by $\delta_{1,2}$-norms defined over the pixel domain. For brevity, we consider in the block structure B only blocks of size $\mathsf{s} \overset{\text{set}}{=} 2$; recall

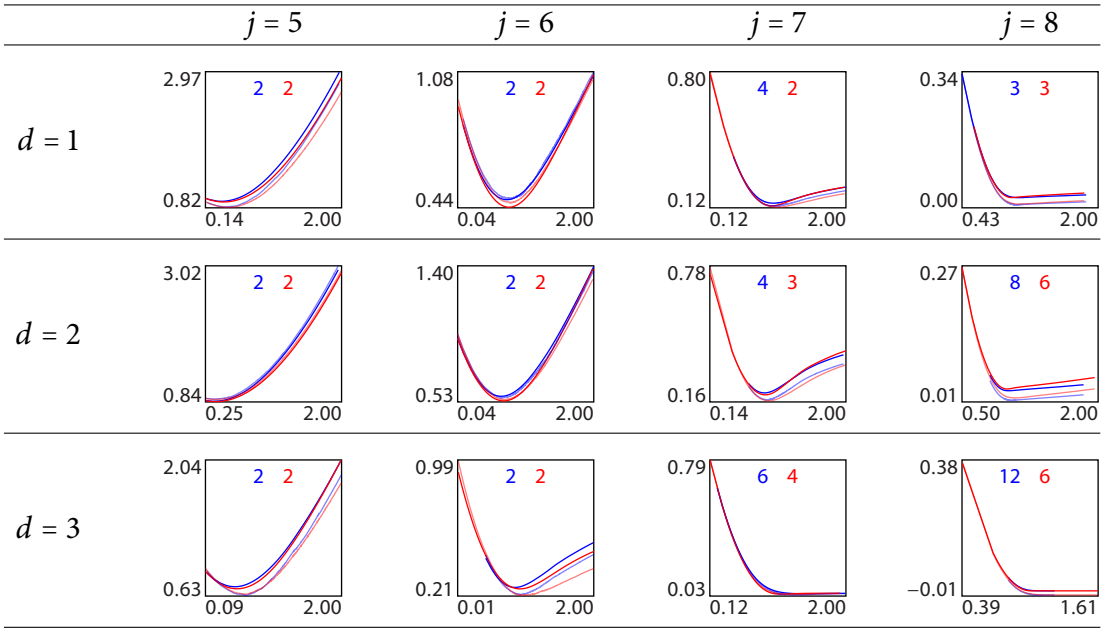

(a) $\ell_{1,2}$-Norm

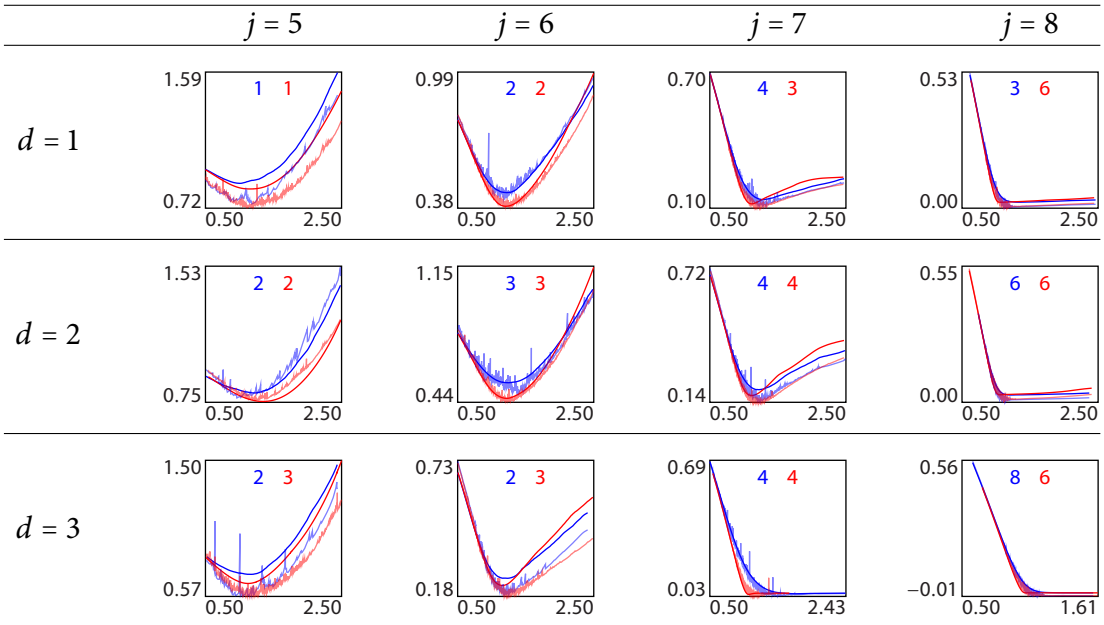

(b) Reweighted $\ell_{1,2}$-Norm

Figure 3: Experiments 4.1.1 and 4.1.2: risk estimates (in transparency) and squared error (in opacity), as functions of the parameter $\lambda^{(j,d)}$, plotted for each subband (j,d) of the orthogonal wavelet transform. The selected block sizes are indicated on top of each corresponding graph. Both risk estimates and squared error are normalized by the noise variance σ^2 and the number of coefficients within the considered subband, while $\lambda^{(j,d)}$ is multiplied by the number of block grids defining the penalization. The results concerning the estimator penalized over a single block grid (respectively over multiple block grids) are given in blue (respectively in red).

from § IV.2 that a $\delta_{1,2}$-norm defined over the four different possible block grids yields a discretized two-dimensional total variation semi-norm.

4.2.1 $\delta_{1,2}$-Norm Denoising

Estimators and parameters. Following again the strategy described within § 2.1, only one penalization scalar $\lambda \in \mathbb{R}$ must be selected by defining for all b in the block structure B, $\lambda_b \overset{\text{set}}{=} \lambda\mu_b$, where $\mu_b \overset{\text{set}}{=} \sqrt{|b|-1}\hat{\sigma}$ scales the weight of the block b according to the estimated $\delta_{1,2}$-amplitude of the noise within the block.

Again, we consider an estimator penalized over only one block grid, *i.e.* B is nonoverlapping and its SURE can be computed exactly following (12), and an estimator penalized by the total variation. We estimate the risk of the latter, both with the average approximation (19) by splitting the $\ell_{d,2}$-norm along the four different grids, and with the iterative SURE described in § 3.1.2.

Results. We compute the risk estimates and the squared error for values of λ running across (an equally spaced subset of) the optimal values $\left(\hat{\lambda}_i\right)_{0\leq i\leq |B|}$ defined in (13). On Figure 4, the results for the estimator penalized over a single grid (respectively penalized by the total variation) are plotted in blue (respectively in red).

As expected, the SURE of the estimator penalized over a single grid estimates accurately the squared error. However, even at the parameter achieving its best performance, this estimator performs poorly (21.8 dB, output image not shown). This is not surprising, since there is no reason for the edges of the image to be aligned with the block grid, and even so, averaging over blocks of size 2 would not be statistically enough to cancel out noise.

A more interesting result is that the iterative SURE (dashed curve) of the total variation denoising estimator is close to its squared error, providing an accurate way of tuning the total variation penalization.

Now, and in contrast to what we observed for $\ell_{1,2}$-norm denoising, the approximated SURE (solid transparent red curve) is significantly different than the SURE of the estimator penalized over a single block grid. Indeed, the proximity operators of the $\delta_{1,2}$-norm over two different block grids can yield drastically different results on images presenting sharp edges. Unfortunately, the approximation fails to give a good estimate of the actual squared error of the total variation denoising estimator. However, recall that one is actually interested in the value of λ achieving the minimum of the risk estimate, regardless of the actual value of the risk. In that respect, we see on Figure 5(j) and (k) that selecting λ with the fast SURE approximation yields as good an estimator as with the iterative SURE. Finally, we check for the usefulness of the correction by the variance across grids within the average approximation, by selecting λ without this correction. We see on Figure 5(i) that the resulting denoising is less efficient.

4.2.2 Composite Denoising

At last, we experiment the possibility of using efficiently the SURE approach for denoising with composite penalizations, involving several parameters.

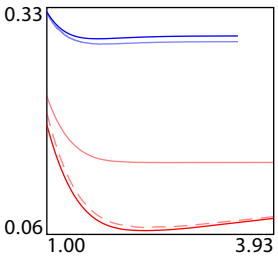

Figure 4: Experiment 4.2.1: risk estimates (in transparency) and squared error (in opacity), both normalized by σ^2 and the number of pixels, as functions of λ times the number of block grids de. Single grid $\ell_{1,2}$-norm in blue, total variation in red. The solid red transparent curve is the risk estimated with the average approximation (19), while the dashed curve is the risk estimated with the iterative SURE.

Estimators and parameters. We consider a denoising estimator penalized by both the weighted ℓ_1-norm over the coefficients of an orthogonal wavelet frame, and the total variation semi-norm. We select the parameters of the former as in experiment 4.1.3, and of the latter with the approximated SURE as in experiment 4.2.1. However, following the heuristic advocated in § 3.1.3, each parameter is then halved to account for mixture of two penalizations which tend to shrink the coefficients amplitudes.

Results. As can be seen on Figure 5(l), the resulting estimator outperforms all other estimators considered in those numerical experiments. Still, our parameter selection might be far from optimal. Note however that, in order to evaluate optimality, testing the estimator for one thousand values of each parameter would require to solve the optimization problem defining it one million times…

With our fast approach, in spite of its simplicity and lack of theoretical guarantee, the resulting estimator enjoys the advantages of both penalizations, getting rid of the "ringing artifacts" that can be seen along contours on all sparse wavelet denoising ((c)-(h)), and reducing the "cartoon effect" induced by the total variation penalization ((i)-(k)).

(a) Paulette, $y^{(0)}$.

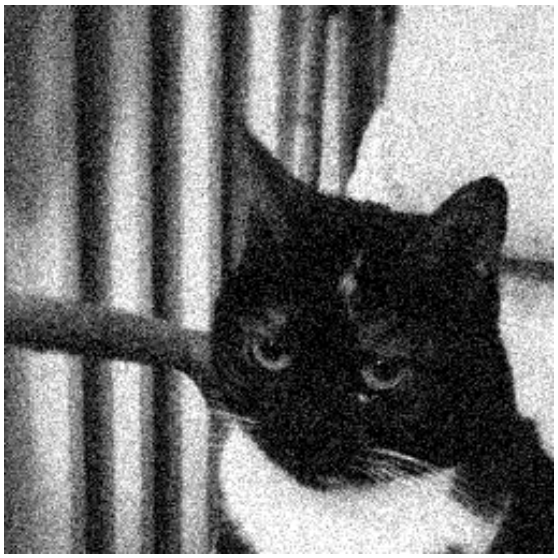

(b) Observation, y; 16.5 dB.

(c) ℓ_1 orthogonal wavelet frame; 27.0 dB.

(d) ℓ_1 redundant wavelet frame; 27.4 dB.

Figure 5: Original image and zoom over the noisy observation and the output of the various estimators of the numerical experiments.

(e) $\ell_{1,2}$ ortho. wav., single grid; 27.7 dB.

(f) $\ell_{1,2}$ ortho. wav., multiple grids; 27.8 dB.

(g) RW $\ell_{1,2}$ ortho. wav., single grid; 27.8 dB.

(h) RW $\ell_{1,2}$ ortho. wav., multiple grids; 28.1 dB.

Figure 5: (continued) original image and zoom over the noisy observation and the output of the various estimators of the numerical experiments.

(i) TV, selected with approximate SURE, *not* corrected by variance across grids; 27.6 dB.

(j) TV, selected with approximate SURE, corrected by variance across grids; 28.3 dB.

(k) TV, selected with iterative SURE; 28.3 dB.

(l) Composite TV and ℓ_1 ortho. wav.; 28.6 dB.

Figure 5: (continued) original image and zoom over the noisy observation and the output of the various estimators of the numerical experiments.

5 Risk Estimate Beyond Denoising

In this chapter, we have reviewed the most popular uses of Stein's unbiased risk estimate for fairly simple denoising estimators, and we have introduced fast methods for dealing with more complex ones, together with some empirical validations.

Now, in inverse problems the signal of interest is not only corrupted by noise, but also undergoes noninvertible transformations during the observation process. This situation is illustrated in § IV.5, where the linear operator L models blurring and/or masking transformation. At this occasion, we claimed that the parameters in the variational problem were selected using methods presented within the current chapter; this is in fact both *unrealistic* and *suboptimal*. Indeed, we computed various risk estimates over a noisy version of the original image while such information was not supposed to be available. More importantly, depending on the degradation operator L, parameters that are optimal for a denoising task might be irrelevant for an inverse problem, even over the same original signal and under the same noise conditions.[4]

In such cases, one can call on the *projected generalized* SURE (Eldar, 2009, Section IV), which gives an unbiased estimate of the risk projected over the orthogonal complement of the nullspace of the degradation operator L. This also requires to solve the variational problem for each value of the parameters one wishes to test, but the fast approximations proposed along this chapter could be adapted to the projected generalized SURE by considering the denoising over $(\ker L)^{\perp}$.

Unfortunately, the inverse problem which motivates our work is a component separation problem. Here, the operator L is simply the sum of the components, and the information that we are trying to recover, namely the distribution of the observation amongst the components, lie precisely in the nullspace of L. In the next chapter, we show that, using the specificity of VSDOI acquisitions and further approximations, the parameters of our SMCS model might still be automatically selected using the methods developed here.

Appendix

A Proof of Stein's Lemma

Proof of Lemma 1.1. Let ϕ be the probability density function of N, *i.e.* for all $v \in \mathbb{R}^P$, $\phi(v) = \frac{1}{\sqrt{(2\pi)^P |C|}} \exp\left(-\frac{1}{2}\langle v \,|\, C^{-1}v\rangle\right)$. Since C is a symmetric matrix, we have for all $y \in \mathbb{R}^P$, $\operatorname{tra}\left(C\frac{\partial \hat{y}}{\partial y}(y)\right) = \sum_{1\leq p,q\leq P} c_{p,q}\frac{\partial \hat{y}_q}{\partial y_p}(y)$. For all $p, q \in \{1,\dots,P\}$, $\mathbb{E}_N\left|\frac{\partial \hat{y}_q}{\partial y_p}(Y)\right| <$

[4] we did not address those limitations since the main purpose was to compare optimization algorithms rather than solving accurately the inverse problem.

$+\infty$, hence $\operatorname{tra}\left(C\frac{\partial\hat{y}}{\partial y}(Y)\right)$ has finite expectation; using Fubini's theorem for each $p, q \in \{1,\dots,P\}$, it expands to

$$\mathbb{E}_N\Big[\operatorname{tra}\left(C\tfrac{\partial\hat{y}}{\partial y}(Y)\right)\Big] = \sum_{1\le p,q\le P} \int_{\mathbb{R}^{P-1}} \int_{\mathbb{R}} c_{p,q}\tfrac{\partial\hat{y}_q}{\partial y_p}(y)\phi(v)\,\mathrm{d}v_p\,\mathrm{d}v_{\{p\}^c}\,, \tag{23}$$

where in the integral, $y \overset{\text{def}}{=} y^{(0)} + v$. Fix now $p, q \in \{1,\dots,P\}$. For all $v \in \mathbb{R}^P$, observe that $\frac{\partial\phi}{\partial v_p}(v) = -\left(C^{-1}v\right)_p \phi(v)$ and $\lim_{|v'_p|\to\infty} \phi\left(v_{\{p\}^c}, v'_p\right) = 0$, hence we can rewrite $\phi(v) = \int_{v_p}^{+\infty} \left(C^{-1}\left(v_{\{p\}^c}, v'_p\right)\right)_p \phi\left(v_{\{p\}^c}, v'_p\right)\mathrm{d}v'_p = \int_{-\infty}^{v_p} -\left(C^{-1}\left(v_{\{p\}^c}, v'_p\right)\right)_p \phi\left(v_{\{p\}^c}, v'_p\right)\mathrm{d}v'_p$. Up to the factor $c_{p,q}$, the inner integral over v_p in (23) can in turn be written, for any $\alpha \in \mathbb{R}$,

$$\begin{aligned}\int_{\mathbb{R}} \tfrac{\partial\hat{y}_q}{\partial y_p}(y)\phi(v)\,\mathrm{d}v_p = &\int_{\alpha}^{+\infty}\int_{v_p}^{+\infty} \tfrac{\partial\hat{y}_q}{\partial y_p}(y)\left(C^{-1}\left(v_{\{p\}^c}, v'_p\right)\right)_p \phi\left(v_{\{p\}^c}, v'_p\right)\mathrm{d}v'_p\,\mathrm{d}v_p \\ &- \int_{-\infty}^{\alpha}\int_{-\infty}^{v_p} \tfrac{\partial\hat{y}_q}{\partial y_p}(y)\left(C^{-1}\left(v_{\{p\}^c}, v'_p\right)\right)_p \phi\left(v_{\{p\}^c}, v'_p\right)\mathrm{d}v'_p\,\mathrm{d}v_p\,,\end{aligned}$$

and then switching the integrals with Fubini's theorem

$$\begin{aligned}= &\int_{\alpha}^{+\infty}\int_{\alpha}^{v'_p} \tfrac{\partial\hat{y}_q}{\partial y_p}\left(y_{\{p\}^c}, y_p\right)\left(C^{-1}\left(v_{\{p\}^c}, v'_p\right)\right)_p \phi\left(v_{\{p\}^c}, v'_p\right)\mathrm{d}v_p\,\mathrm{d}v'_p \\ &- \int_{-\infty}^{\alpha}\int_{v'_p}^{\alpha} \tfrac{\partial\hat{y}_q}{\partial y_p}\left(y_{\{p\}^c}, y_p\right)\left(C^{-1}\left(v_{\{p\}^c}, v'_p\right)\right)_p \phi\left(v_{\{p\}^c}, v'_p\right)\mathrm{d}v_p\,\mathrm{d}v'_p\,.\end{aligned}$$

For almost all $v_{\{p\}^c} \in \mathbb{R}^{P-1}$ and almost all $v'_p \in \mathbb{R}$, we can choose $\alpha \in \mathbb{R}$ such that we can integrate the weak differential $\frac{\partial\hat{y}_q}{\partial y_p}$ over v_p to get

$$\begin{aligned}= &\int_{\alpha}^{+\infty} \left(\hat{y}_q\left(y_{\{p\}^c}, y'_p\right) - \hat{y}_q\left(y_{\{p\}^c}, y_p^{(0)} + \alpha\right)\right)\left(C^{-1}\left(v_{\{p\}^c}, v'_p\right)\right)_p \phi\left(v_{\{p\}^c}, v'_p\right)\mathrm{d}v'_p \\ &+ \int_{-\infty}^{\alpha} \left(\hat{y}_q\left(y_{\{p\}^c}, y'_p\right) - \hat{y}_q\left(y_{\{p\}^c}, y_p^{(0)} + \alpha\right)\right)\left(C^{-1}\left(v_{\{p\}^c}, v'_p\right)\right)_p \phi\left(v_{\{p\}^c}, v'_p\right)\mathrm{d}v'_p\,,\end{aligned}$$

where $y'_p \overset{\text{def}}{=} y_p^{(0)} + v'_p$. Now, we have $\int_{-\infty}^{+\infty} -\hat{y}_q\left(y_{\{p\}^c}, y_p^{(0)} + \alpha\right)\left(C^{-1}\left(v_{\{p\}^c}, v'_p\right)\right)_p \phi\left(v_{\{p\}^c}, v'_p\right)\mathrm{d}v'_p = \hat{y}_q\left(y_{\{p\}^c}, y_p^{(0)} + \alpha\right)\left[\phi\left(v_{\{p\}^c}, v'_p\right)\right]_{v'_p=-\infty}^{v'_p=+\infty} = 0$, so that we finally obtain for almost all $v_{\{p\}^c} \in \mathbb{R}^{P-1}$,

$$\int_{\mathbb{R}} \tfrac{\partial\hat{y}_q}{\partial y_p}(y) f(v)\,\mathrm{d}v_p = \int_{\mathbb{R}} \hat{y}_q\left(y_{\{p\}^c}, y'_p\right)\left(C^{-1}\left(v_{\{p\}^c}, v'_p\right)\right)_p \phi\left(v_{\{p\}^c}, v'_p\right)\mathrm{d}v'_p\,.$$

At last, injecting this in (23) leads to

$$\begin{aligned}\mathbb{E}_N\Big[\operatorname{tra}\left(C\tfrac{\partial\hat{y}}{\partial y}(Y)\right)\Big] &= \sum_{\substack{1\le q\le P\\ 1\le p\le P}} \int_{\mathbb{R}^{P-1}}\int_{\mathbb{R}} c_{p,q}\hat{y}_q(y)\left(C^{-1}v\right)_p \phi(v)\,\mathrm{d}v_p\,\mathrm{d}v_{\{p\}^c}\,, \\ &= \int_{\mathbb{R}^P} \sum_{1\le q\le P}\sum_{1\le p\le P} c_{p,q}\left(C^{-1}v\right)_p \hat{y}_q(y)\phi(v)\,\mathrm{d}v\,, \\ &= \int_{\mathbb{R}^P} \sum_{1\le q\le P} v_q\hat{y}_q(y)\,\phi(v)\,\mathrm{d}w = \mathbb{E}_N\left\langle N \,\middle|\, \hat{y}_q(Y)\right\rangle\,. \qquad \blacksquare\end{aligned}$$

B Chain Rule for Lipschitzian Operators

Proposition 5.1. *Let $P, Q, R \in \mathbb{N}_*$, $f\colon \mathbb{R}^P \to \mathbb{R}^Q$ be differentiable almost everywhere, $g\colon \mathbb{R}^Q \to \mathbb{R}^R$ be locally Lipschitzian, such that $g \circ f\colon \mathbb{R}^P \to \mathbb{R}^R$ is also differentiable almost everywhere. Then, for all $x \in \mathbb{R}^P$ such that f and $g \circ f$ are both differentiable at x, g is differentiable at $f(x)$ along direction $\operatorname{ran}\left(\frac{\partial f}{\partial x}(x)\right)$, i.e. the operator*

$$\mathrm{D}g(f(x))\colon \begin{array}{ccc} \operatorname{ran}\left(\frac{\partial f}{\partial x}(x)\right) & \longrightarrow & \mathbb{R}^R \\ d & \longmapsto & \lim\limits_{\epsilon \to 0} \frac{1}{\epsilon}\big(g(f(x)+\epsilon d) - g(f(x))\big) \end{array} \tag{24}$$

is well-defined and linear; moreover $\frac{\partial (g\circ f)}{\partial x}(x) = \mathrm{D}g(f(x))\frac{\partial f}{\partial x}(x)$. In particular, for almost all $x \in \mathbb{R}^P$, within any orthonormal basis of $\operatorname{ran}\left(\frac{\partial f}{\partial x}(x)\right)$ completed into an orthonormal basis of $\mathbb{R}^Q$, the chain rule holds, i.e. for all $p \in \{1, \dots, P\}$ and $r \in \{1, \dots, R\}$,

$$\frac{\partial (g\circ f)_r}{\partial x_p}(x) = \sum_{q=1}^{Q} \frac{\partial g_r}{\partial y_q}(f(x))\frac{\partial f_q}{\partial x_p}(x)\,, \tag{25}$$

with the convention that for all $q \in \{1, \dots, Q\}$, $\frac{\partial g_r}{\partial y_q}(f(x))$ is the partial derivative of g_r in direction q at $f(x)$ if it is well defined, and can be any real number otherwise.

Proof. Let $x \in \mathbb{R}^P$ be a point of differentiability of f. Observe that for any $d \in \mathbb{R}^P$ and $\epsilon \in \mathbb{R}_*$,

$$\begin{aligned} g\big(f(x) + \epsilon \tfrac{\partial f}{\partial x}(x)d\big) - g\big(f(x)\big) = {} & g\big(f(x) + \epsilon \tfrac{\partial f}{\partial x}(x)d\big) - g\big(f(x+\epsilon d)\big) \\ & + g\big(f(x+\epsilon d)\big) - g\big(f(x)\big)\,. \end{aligned}$$

Then, we have $\left\| g\big(f(x) + \epsilon \frac{\partial f}{\partial x}(x)d\big) - g\big(f(x+\epsilon d)\big)\right\| \le L\left\|f(x) + \epsilon \frac{\partial f}{\partial x}(x)d - f(x+\epsilon d)\right\|$, where $L \in \mathbb{R}_{+,*}$ is any local Lipschitz constant of g, and by definition of the differentiability of f at x we can deduce $\lim_{\epsilon\to 0} \frac{1}{\epsilon}\Big(g\big(f(x) + \epsilon \frac{\partial f}{\partial x}(x)d\big) - g\big(f(x+\epsilon d)\big)\Big) = 0$. Thus, if x is also a point of differentiability of $g \circ f$, we get

$$\begin{aligned} \lim_{\epsilon\to 0} \frac{1}{\epsilon}\Big(g\big(f(x) + \epsilon \tfrac{\partial f}{\partial x}(x)d\big) - g\big(f(x)\big)\Big) &= \lim_{\epsilon\to 0} \frac{1}{\epsilon}(g\circ f(x+\epsilon d) - g\circ f(x)) \\ &= \frac{\partial (g\circ f)}{\partial x}(x)d\,. \end{aligned}$$

This shows that $\mathrm{D}g(f(x))$ given in (24) is well-defined, and by linearity of both $\frac{\partial f}{\partial x}(x)$ and $\frac{\partial (g\circ f)}{\partial x}(x)$, it is linear; the expression of $\frac{\partial (g\circ f)}{\partial x}(x)$ follows. Finally, by Lipschitzianity of f, for almost all $x \in \mathbb{R}^P$, both f and $g \circ f$ are differentiable at x. Fix such an x and let, up to reordering, $(e'_q)_{1\le q\le \operatorname{rank}\left(\frac{\partial f}{\partial x}(x)\right)}$ be any orthonormal basis of $\operatorname{ran}\left(\frac{\partial f}{\partial x}(x)\right)$ completed as $(e'_q)_{1\le q\le Q}$ into an orthonormal basis of $\mathbb{R}^Q$. For all $q \in \{1, \dots, Q\}$, if $q \le \operatorname{rank}\left(\frac{\partial f}{\partial x}(x)\right)$, then $e'_q \in \operatorname{ran}\left(\frac{\partial f}{\partial x}(x)\right)$ and we have seen that for all $r \in \{1, \dots, R\}$, $\frac{\partial g_r}{\partial y_q}(f(x))$ exists. If now $q > \operatorname{rank}\left(\frac{\partial f}{\partial x}(x)\right)$, then e'_q is orthogonal to $\operatorname{ran}\left(\frac{\partial f}{\partial x}(x)\right)$, so that for all $p \in \{1, \dots, P\}$, $\frac{\partial f_q}{\partial x_p}(x) = \left\langle \frac{\partial f}{\partial x}(x)e_p \,|\, e'_q\right\rangle = 0$, where we denoted $\left(e_p\right)_{1\le p\le P}$ the canonical basis of $\mathbb{R}^P$. Altogether, developing the expression of $\mathrm{D}g(f(x))\frac{\partial f}{\partial x}(x)$ in those bases yields the chain rule (25). ∎

Example 5.1. The need for an orthonormal basis of $\operatorname{ran}\left(\frac{\partial f}{\partial x}(x)\right)$, completed into an orthonormal basis of $\mathbb{R}^Q$, is illustrated by the example given by Marcus and Mizel (1971, Remark after Theorem 3, p. 40). Let $f\colon \mathbb{R} \to \mathbb{R}^2 \colon x \mapsto (x, x)$, and $g\colon \mathbb{R}^2 \to \mathbb{R} \colon (y_1, y_2) \mapsto \max(y_1, y_2)$. Both functions are Lipschitzian, and $g \circ f$ is the identity over $\mathbb{R}$, differentiable everywhere. However, g is nowhere differentiable on the first diagonal, so that the chain rule (25) is nowhere defined within the canonical basis. Nevertheless, let us mention that in this basis we have for all $x \in \mathbb{R}$, $\frac{\partial f}{\partial x}(x) = (1,1)$. Thus, using the basis $\left(e_1' \overset{\text{set}}{=} \frac{1}{\sqrt{2}}(1,1), e_2' \overset{\text{set}}{=} \frac{1}{\sqrt{2}}(-1,1)\right)$ of $\mathbb{R}^2$, we have for all $x \in \mathbb{R}$, $\frac{\partial f_1}{\partial x}(x) = \sqrt{2}$, $\frac{\partial f_2}{\partial x}(x) = 0$, and $\frac{\partial g}{\partial y_1}(f(x)) \overset{\text{def}}{=} \lim_{\epsilon \to 0} \frac{1}{\epsilon}\left(\max(x + \frac{\epsilon}{\sqrt{2}}, x + \frac{\epsilon}{\sqrt{2}}) - \max(x, x)\right) = \frac{1}{\sqrt{2}}$; attributing any value to $\frac{\partial g}{\partial y_2}(f(x))$, we get $\frac{\partial g}{\partial y_1}(f(x))\frac{\partial f_1}{\partial x}(x) + \frac{\partial g}{\partial y_2}(f(x))\frac{\partial f_2}{\partial x}(x) = 1 = \frac{\partial (g \circ f)}{\partial x}(x)$.

References

E. J. Candès, M. B. Wakin, and S. P. Boyd. Enhancing sparsity by reweighted ℓ_1 minimization. *Journal of Fourier Analysis and Applications*, 14(5):877–905, 2008.

C. Chaux, L. Duval, A. Benazza-Benyahia, and J.-C. Pesquet. A nonlinear Stein-based estimator for multichannel image denoising. *IEEE Transactions on Signal Processing*, 56(8):3855–3870, 2008.

I. Daubechies. *Ten Lectures on Wavelets*. Society for Industrial and Applied Mathematics, 1992.

C.-A. Deledalle, S. Vaiter, G. Peyré, J. M. Fadili, and C. Dossal. Proximal splitting derivatives for risk estimation. *Journal of Physics: Conference Series*, 386(1):012003, 2012.

D. L. Donoho and I. M. Johnstone. Ideal spatial adaptation by wavelet shrinkage. *Biometrika*, 81(3):425–455, 1994.

D. L. Donoho and I. M. Johnstone. Adapting to unknown smoothness via wavelet shrinkage. *Journal of the American Statistical Association*, 90(432):1200–1224, 1995.

B. Efron. The estimation of prediction error. *Journal of the American Statistical Association*, 99(467):619–632, 2004.

Y. C. Eldar. Generalized SURE for exponential families: Applications to regularization. *Signal Processing, IEEE Transactions on*, 57(2):471–481, 2009.

L. C. Evans and R. F. Gariepy. *Measure Theory and Fine Properties of Functions*. Studies in Advanced Mathematics. Taylor & Francis, 1992.

E. H. Lieb and M. Loss. *Analysis*. CRM Proceedings & Lecture Notes. American Mathematical Society, 2001.

M. Marcus and V. J. Mizel. Functional composition on Sobolev spaces. *Bulletin of the American Mathematical Society*, 78(1):38–42, 1971.

J.-C. Pesquet, A. Benazza-Benyahia, and C. Chaux. A SURE approach for digital signal/image deconvolution problems. *IEEE Transactions on Signal Processing*, 57(12): 4616–4632, 2009.

S. Ramani, T. Blu, and M. Unser. Monte-Carlo SURE: A black-box optimization of regularization parameters for general denoising algorithms. *IEEE Transactions on Image Processing*, 17(9):1540–1554, 2008.

M. Raphan and E. P. Simoncelli. Optimal denoising in redundant representations. *IEEE Transactions on Image Processing*, 17(8):1342–1352, 2008.

F. Roosta-Khorasani and U. M. Ascher. Improved bounds on sample size for implicit matrix trace estimators. *CoRR*, abs/1308.2475, 2013.

C. M. Stein. Estimation of the mean of a multivariate normal distribution. *The Annals of Statistics*, 9(6):1135–1151, 1981.

S. Vaiter, C.-A. Deledalle, G. Peyré, J. M. Fadili, and C. Dossal. The degrees of freedom of partly smooth regularizers. 2014. URL http://hal.archives-ouvertes.fr/hal-00981634.

▪ VI ▪

A Full Component Separation Method for Voltage-Sensitive Dye Optical Imaging

Thanks to the developments of the three previous chapters, we are now able to address each one of the practical concerns raised in § II.4.2, in order to use our spatially structured sparse morphological model. Within this chapter, we expose in details the concrete application of this model to voltage-sensitive dye optical imaging.

Recall that the component separation defined by our model is given by the solution of the convex minimization problem (II.6). The optimization problem *per se* has already been discussed extensively, and all necessary ingredients for efficient implementation can be found along Chapter IV. Therefore, the present chapter deals essentially with the automatic setting of the numerous parameters involved in the penalizations. First, we establish the simple theoretical rationale underlying our approach, consisting in a series of approximations of the components involved in the problem. Only then, we detail the practical conditions which make it suitable for applications to VSDOI acquisitions.

The full method presented here is implemented in Matlab, together with the minimization algorithms in C interfaced with Mex, in an integrated environment, simplifying notably display and analysis of the data. The code is available on request; unfortunately, due to the complexity of the method, the actual implementation cannot be used without technical assistance by the author of this work.

Contents

1 Scaling Penalizations for Noisy Component Separation

Recall that the data-fidelity term in (II.6) is normalized by the noise level at each spatial positions, in order to account for differences of confidence one can have on the observations. Prior to all other considerations, we assume that this information can actually be captured within the parameters of the penalization Ψ. Hence, we recast the problem by rescaling the data-fidelity term so as to obtain

$$\text{find } \hat{X} \text{ in } \left\{ \operatorname*{argmin}_{X \in \mathbb{C}^{K \times P}} \tfrac{1}{2} \|Y - DX\|_2^2 + \Psi^{(\Lambda)}(X) \right\}. \tag{1}$$

Note that the scaling rules of the parameters in Λ depending on the noise level, originally given in § II.3.5, must be set accordingly. In this section, we justify our choices concerning this question, and motivate the subsequent approximations, enabling eventually parameter selection for noisy component separation problems.

For brevity, as long as the relationship between Ψ and its parameter Λ is not made explicit, we drop the dependency on Λ.

1.1 Scaling an Ideal Frame Denoising

Supposing the presence of only one component in the SMCS model, *i.e.* $Y = Y^{(0)} + R$, then (1) reduces to a denoising estimator with synthesis frame D and penalization Ψ. As we have seen in § V.3.2, $\hat{X}$ might not be unique but all minimizers define a unique estimation $\hat{Y} = D\hat{X}$ of the component $Y^{(0)}$. Differentiating (1) with help of Proposition IV.3.1, and applying Fermat's rule § III.3, a necessary and sufficient condition for $\hat{X}$ to be a minimizer is

$$ {}^{\mathrm{t}}D\big(Y - D\hat{X}\big) \in \partial\Psi(\hat{X}) \,. \tag{2} $$

Now, we say that the denoising is *ideal* if the dictionary D and the penalization Ψ are such that one retrieves exactly the component, *i.e.* $\hat{Y} = Y^{(0)}$. In view of (2), the denoising is ideal if, and only if, $Y^{(0)} = D\hat{X}$ and ${}^{\mathrm{t}}DR \in \partial\Psi(\hat{X})$.

Now for all $\sigma \in \mathbb{R}_{+*}$, we have $\partial(\sigma\Psi) = \sigma\partial\Psi$. An immediate consequence is that, if D and Ψ are ideal for separating $Y^{(0)}$ from the residual R, then for all $\sigma \in \mathbb{R}_{+*}$, D and $\sigma\Psi$ are ideal for separating $Y^{(0)}$ from the residual σR.

Unfortunately, this optimality relation only holds in the ideal case. Given a statistical distribution over the residual R, D and Ψ are in general not ideal for all its realizations, so that in terms of risk of the denoising estimator (see Chapter 4), the optimality of Ψ for the noise R do not necessarily imply optimality of $\sigma\Psi$ for the noise σR. Nonetheless, in absence of any other information, this justifies to scale a penalization that aims at capturing additive Gaussian noise proportionally to its standard deviation.

In accordance with the structure over the parameters defined in § II.3.5, when a penalization over a given regressor $k \in \{1, \dots, K\}$ is spatially structured according to a block structure B_k, we adapt the weights over each block $b \in B_k$ as $\lambda_{k,b} \overset{\text{set}}{=} \lambda_k \mathbb{E}_R[\Psi^{(b)}(R)]$, where λ_k scales the whole block structure, $\Psi^{(b)}$ is the penalization restrained to the block b with unit weight, and the expectation is taken over the noise model for the residual R. In particular, for our heteroscedastic white Gaussian noise model and with the notations of § II.3.5, if Ψ is a $\ell_{1,2}$-norm then $\mathbb{E}_R[\Psi^{(b)}(R)] = \|\Sigma_b\|_2$, and if Ψ is a $\delta_{1,2}$-norm then $\mathbb{E}_R[\Psi^{(b)}(R)] = \sqrt{\frac{|b|-1}{|b|}}\|\Sigma_b\|_2$.

A notable exception to the above rule concerns the hard constraints, for which $\Psi^{(b)}$ takes values only in $\{0, +\infty\}$; this is not surprising, since hard constraints do not scale with the noise. With no other knowledge over the underlying signal, a natural criterion is to suppose an homogeneous signal; and to scale each hard constraint penalization so as to allow for the same constant value of the signal over each block. Recalling the above instances, if Ψ is a bounded amplitude constraint this translates to $\mu_{k,b} \overset{\text{set}}{=} \mu_k\sqrt{|b|}$, and if Ψ a bounded deviation constraint we get $\mu_{k,b} \overset{\text{set}}{=} \mu_k\sqrt{|b|-1}$.

1.2 From Denoising to Component Separation

We now turn back to the component separation setting. Since the penalization Ψ is separable along components, *i.e.* $\Psi(X) = \sum_c \Psi^{(c)}\big(X^{(c)}\big)$, we deduce that $\partial\Psi(X) =$

$\times_c \partial\Psi^{(c)}\left(X^{(c)}\right)$, and the condition (2) translates to

$$\forall\,(c),\ {}^{\mathrm{t}}D^{(c)}\left(Y - D\hat{X}\right) \in \partial\Psi^{(c)}\left(\hat{X}^{(c)}\right). \tag{3}$$

Hence, if for all component (c), $D^{(c)}$ and $\Psi^{(c)}$ define an ideal estimator for denoising $Y^{(c)}$ corrupted by R, *i.e.* there exists $\hat{X}^{(c)} \in \mathbb{C}^{K_c \times P}$ such that $Y^{(c)} = D^{(c)}\hat{X}^{(c)}$ and ${}^{\mathrm{t}}D^{(c)}R \in \partial\Psi\left(\hat{X}^{(c)}\right)$, then $\hat{X} = \left(X^{(c)}\right)_c \in \mathbb{C}^{K \times P}$ is a minimizer of the variational problem (1), achieving ideal component separation.

Although there might be other solutions of (1) yielding different component separations, the above observation motivates the following approach for applying our SMCS model to VSDOI data. By approximating the whole separation problem in a series of isolated denoising steps, all parameters can be learnt adaptively on the data using the SURE presented in Chapter V.

2 Component Approximations for Parameters Selection

Within this section, we detail each step of the full method for applying the SMCS model to VSDOI data; they are summarized in Table 1. We make extensive use of the notations introduced in § II.1; moreover, when dealing with *approximations* of components, we will substitute Z to the notation Y.

Those approximations involve notably a processing on a blank VSDOI acquisition, where only few neuronal activities are expected; the blank and stimulus conditions are indexed by the respective superscripts (b) and (s). Considering that the blank acquisition contains no significant neuronal activity component, *i.e.* $\tilde{Y}^{(\mathrm{b,P})} \approx 0$, the model (II.1) yields

$$\tilde{Y}^{(\mathrm{b})} = G^{(\mathrm{b})} \cdot \left(Y^{(\mathrm{b,B})} + Y^{(\mathrm{b,P})}\right) + \tilde{R}^{(\mathrm{b})}. \tag{4}$$

2.1 Gain and Bleaching Approximation on Blank

Since the bleaching component presents constrained temporal dynamic and has high amplitude comparatively to the periodic artifacts, it is possible to get a rough estimation of the former by neglecting the latter. Once the number K_{B} of bleaching regressors has been chosen (usually one or two decreasing exponentials, on top of the constant regressor), the bleaching time constants are fitted over all pixels of all the available blank acquisitions $\left\{\tilde{Y}^{(\mathrm{b})}\right\}_{\mathrm{b}}$ simultaneously, as

$$\mathcal{T} \in \underset{\tau \overset{\text{def}}{=} \{\tau_k\}_{1\le k\le K_{\mathrm{B}}}}{\operatorname{argmin}} \left(\sum_{\mathrm{b}} \min_{X \in \mathbb{R}^{K_{\mathrm{B}} \times P}} \left\| \tilde{Y}^{(\mathrm{b})} - D^{(\mathrm{B},\tau)}X \right\|_2^2 \right), \tag{5}$$

where $D^{(\mathrm{B},\tau)}$ depends on the time constants according to (II.2). Note that given a matrix $D^{(\mathrm{B},\tau)}$, the optimal coefficients $X \in \mathbb{R}^{K_{\mathrm{B}} \times P}$ in (5) is given in closed form by $\tilde{X}^{(\mathrm{b,B},\tau)} = \left({}^{\mathrm{t}}D^{(\mathrm{B},\tau)}D^{(\mathrm{B},\tau)}\right)^{-1}{}^{\mathrm{t}}D^{(\mathrm{B},\tau)}\tilde{Y}^{(\mathrm{b})}$. The resulting objective function in (5) is differentiable and

Table 1: Overview of the full method.

Input
Blank acquisitions $\left\{\tilde{Y}^{(\mathrm{b})}\right\}_{\mathrm{b}}$; stimulus condition acquisitions $\left\{\tilde{Y}^{(\mathrm{s})}\right\}_{\mathrm{s}}$;
Number of bleaching time constants K_{B} in $\mathcal{T}$ (see § II.2.2.1);
Set of periodic artifacts frequencies $\mathcal{F}$ (see § II.2.2.2);
Neuronal activity wavelet filter and minimum scale $j_{\min}$ (see § II.2.2.3);
Set of block sizes $\mathcal{S}$ for $\ell_{1,2}$-norm penalizations (see § II.3.5).

Processing Steps

1.	Estimate $\mathcal{T}$, $Z^{(\mathrm{b},\mathrm{B})}$ and $G^{(\mathrm{b})}$	§ 2.1
2.	Estimate $\Sigma^{(\mathrm{b})}$	§ 2.2
3.	Select the ROI	§ 2.3
4.	For all $k \in \{1..K_{\mathrm{P}}\}$, select $B_k^{(\mathrm{b})}$ and $\lambda_k^{(\mathrm{b},\mathrm{P})}$	§ 2.4
5.	Estimate $Y^{(\mathrm{b},\mathrm{B})}$, $Y^{(\mathrm{b},\mathrm{P})}$ and $R^{(\mathrm{b})}$	§ 2.5
6.	Estimate $Z^{(\mathrm{s},\mathrm{B})}$ and $G^{(\mathrm{s})}$	§ 2.7
7.	For all $k \in \{1..K_{\mathrm{A}}\}$, select $B_k^{(\mathrm{b})}$, $\lambda_k^{(\mathrm{s},\mathrm{A},\ell)}$, $\lambda_k^{(\mathrm{s},\mathrm{A},\delta)}$ and $\mu_k^{(\mathrm{s},\mathrm{A})}$	§ 2.8
8.	For all $k \in \{1..K_{\mathrm{P}}\}$, select $B_k^{(\mathrm{s})}$, $\lambda_k^{(\mathrm{s},\mathrm{P})}$ and $\mu_k^{(\mathrm{s},\mathrm{P})}$	§ 2.9
9.	Estimate $Y^{(\mathrm{s},\mathrm{B})}$, $Y^{(\mathrm{s},\mathrm{P})}$, $Y^{(\mathrm{s},\mathrm{A})}$, $R^{(\mathrm{s})}$	§ 2.10

Output
Estimated gain G, components $Y^{(\mathrm{B})}$, $Y^{(\mathrm{P})}$, $Y^{(\mathrm{A})}$, and residual R over all blank and stimulus condition acquisitions.

thus is minimized typically by gradient descent with line search. It is however nonconvex, hence sensitive to initialization. Typical values suitable for most VSDOI acquisitions are 100 ms for the first time constant and 1 000 ms when a second one is required (see also the numerical experiments in Chapter VII).

Recall that the bleaching component in our model accounts also for the baseline fluorescence, which dominates all other components in the signal. Hence, we consider that the optimal $\tilde{Z}^{(\mathrm{b},\mathrm{B})} \overset{\text{def}}{=} D^{(\mathrm{B})}\tilde{X}^{(\mathrm{b},\mathrm{B})}$ corresponding to the optimal $\mathcal{T}$ in (5) gives a good approximation of the bleaching dynamic, multiplied by the gain $G^{(\mathrm{b})}$. Following our hypothesis on the gain (see § II.2.1 and Annex I.A), we estimate the latter, at each pixel $p \in \{1,\dots,P\}$, as the average over time of $\tilde{Z}^{(\mathrm{b},\mathrm{B})}$

$$g_p^{(\mathrm{b})} = \frac{1}{T}\sum_{t=1}^{T} \tilde{z}_{t,p}^{(\mathrm{b},\mathrm{B})} \,. \tag{6}$$

2.2 Noise Level on Blank

Recall (§ II.2.1) that the residual $\tilde{R}^{(\mathrm{b})}$ is modeled as a white heteroscedastic Gaussian noise, and that the matrix $\tilde{\Sigma}^{(\mathrm{b})}$ of its standard deviations is supposed to be constant along time. Thanks to the high sampling frequency of VSDOI acquisitions, the highest frequencies observed are dominated by the noise, and it is possible to evaluate the noise level as explained in § V.1.3. For more accuracy, we remove the already estimated bleaching component from the acquisition. Using the highest frequency temporal variations of the resulting signal, the median of absolute deviation standard deviation estimator yields at each spatial positions $p \in \{1,\dots,P\}$,

$$\hat{\sigma}_p^{(\mathrm{b})} = 1.4826 \ \operatorname{med}\left(\left|\left(\tilde{y}_{t+1,p}^{(\mathrm{b})} - \tilde{z}_{t+1,p}^{(\mathrm{b},\mathrm{B})}\right) - \left(\tilde{y}_{t,p}^{(\mathrm{b})} - \tilde{z}_{t,p}^{(\mathrm{b},\mathrm{B})}\right)\right|\right)_{1\le t\le T-1} . \tag{7}$$

However, some high frequency contributions in the signal might not be due to noise, and one needs to make the estimation more robust to outliers. In this purpose, recall that our model assumes that the variance is an affine function of the gain along space, *i.e.* there exists $\alpha^{(\mathrm{b})}, \beta^{(\mathrm{b})} \in \mathbb{R}$ such that for all pixel $p \in \{1,\dots,P\}$, $\left(\tilde{\sigma}_p^{(\mathrm{b})}\right)^2 = \alpha^{(\mathrm{b})} + \beta^{(\mathrm{b})} g_p^{(\mathrm{b})}$. As demonstrated in Annex A, the following are consistent estimators of $\alpha^{(\mathrm{b})}$ and $\beta^{(\mathrm{b})}$, making use of the values given in (7)

$$\begin{aligned}
\hat{\beta}^{(\mathrm{b})} &= \frac{\sum_{p=1}^{P}\left(\hat{\sigma}_p^{(\mathrm{b})}\right)^2 g_p^{(\mathrm{b})} - \frac{1}{P}\left(\sum_{p=1}^{P}\left(\hat{\sigma}_p^{(\mathrm{b})}\right)^2\right)\left(\sum_{p=1}^{P} g_p^{(\mathrm{b})}\right)}{\sum_{p=1}^{P}\left(g_p^{(\mathrm{b})}\right)^2 - \frac{1}{P}\left(\sum_{p=1}^{P} g_p^{(\mathrm{b})}\right)^2} \,, \\
\hat{\alpha}^{(\mathrm{b})} &= \frac{1}{P}\sum_{p=1}^{P}\left(\left(\hat{\sigma}_p^{(\mathrm{b})}\right)^2 - \beta^{(\mathrm{b})} g_p^{(\mathrm{b})}\right) .
\end{aligned} \tag{8}$$

Note that this amounts to perform a *linear regression* with quadratic loss, explaining the values $\left(\left(\hat{\sigma}_p^{(\mathrm{b})}\right)^2\right)_{1\le p\le P}$ from the values $\left(g_p^{(\mathrm{b})}\right)_{1\le p\le P}$; this allows to test the coherence of the

noise model with actual VSDOI data, see § VII.1. At last, we retrieve $\tilde{\Sigma}^{(\mathrm{b})}$ and $\Sigma^{(\mathrm{b})}$ with for all $p \in \{1, \dots, P\}$,

$$\tilde{\sigma}_p^{(\mathrm{b})} = \sqrt{\hat{\alpha}^{(\mathrm{b})} + \hat{\beta}^{(\mathrm{b})} g_p^{(\mathrm{b})}}\,, \quad \text{and} \quad \sigma_p^{(\mathrm{b})} = \frac{\tilde{\sigma}_p^{(\mathrm{b})}}{g_p^{(\mathrm{b})}}\,. \tag{9}$$

2.3 Selection of Clean Blank Acquisitions and Region of Interest

Let us precise that the estimation of the bleaching time constants and of the noise level condition the accuracy of the subsequent processing. Once the first bleaching approximation and the gain are computed, we get for each blank acquisition

$$\left(\tilde{Y}^{(\mathrm{b})} - \tilde{Z}^{(\mathrm{b},\mathrm{B})}\right)/G^{(\mathrm{b})} \approx Y^{(\mathrm{b},\mathrm{P})} + R^{(\mathrm{b})}\,. \tag{10}$$

At this stage, one must check visually these approximations in order to identify blank acquisitions presenting strong patterns of spontaneous neuronal activity. Such blank acquisition should be discarded from the set of blanks $\left\{Y^{(\mathrm{b})}\right\}_{\mathrm{b}}$, because high amplitude spontaneous neuronal activity would bias each processing proposed here. Moreover, these blank acquisitions can be processed later for extraction of spontaneous neuronal activity.

In addition, it is possible to identify, across the remaining blank acquisitions, the spatial positions which are irrelevant for analysis, for instance because the gain is too low or the noise is too high.

As a result, we get, for a given experimental protocol, a region of interest (ROI) and a set of "clean" blank acquisitions, that we abusively still index respectively by (b) and by $p \in \{1, \dots, P\}$. For improved accuracy, it is recommended to perform the processing of § 2.1 and 2.2 all over again on the restrained data.

2.4 Selection of $B^{(\mathrm{b},\mathrm{P})}$ and $\Lambda^{(\mathrm{b},\mathrm{P})}$

Equation (10) shows that, thanks to the bleaching and gain first approximations, we can get a noisy observation of the periodic artifacts components $Y^{(\mathrm{b},\mathrm{P})}$. This constitutes indeed a *denoising problem* analogous to the framework of Chapter V, where we identify $Y^{(\mathrm{b},\mathrm{P})}$ as the target signal $y^{(0)}$, $\left(\tilde{Y}^{(\mathrm{b})} - \tilde{Z}^{(\mathrm{b},\mathrm{B})}\right)/G^{(\mathrm{b})}$ as the observation y, and $R^{(\mathrm{b})}$ the realization of the noise N.

Ignoring the bleaching and neuronal activity components in the SMCS recovery leads to the periodic artifacts estimator, parameterized by $\Lambda_B^{(\mathrm{P})}$ and $M_B^{(\mathrm{P})}$, and defined as $\hat{Y}^{(\Lambda_B^{(\mathrm{P})}, M_B^{(\mathrm{P})})} : Y \mapsto D^{(\mathrm{P})}\hat{X}$, where

$$\hat{X} \in \operatorname*{argmin}_{X \in \mathbb{C}^{K_{\mathrm{P}} \times P}} \tfrac{1}{2}\left\|Y - D^{(\mathrm{P})}X\right\|_2^2 + \left\|X\right\|_{\ell,\Lambda_B^{(\mathrm{P})}} + \iota_{\overline{\ell_{M_B^{(\mathrm{P})}}}}(X)\,. \tag{11}$$

In the terms of Chapter V, this is a denoising estimator with synthesis frame $D^{(\mathrm{P})}$ and penalization $X \mapsto \left\|X\right\|_{\ell,\Lambda_B^{(\mathrm{P})}} + \iota_{\overline{\ell_{M_B^{(\mathrm{P})}}}}(X)$.

First, since there is no neuronal activity in the blank acquisitions, there is no need for the bounded amplitude constraint; we thus only have to select the parameters $\Lambda_B^{(\mathrm{P})}$ for the $\ell_{1,2}$-norm by blocks.

For each blank acquisition, thanks to the estimated noise statistics $\Sigma^{(\mathrm{b})}$, we can consider using the SURE of $\hat{Y}^{(\Lambda_B^{(\mathrm{b},\mathrm{P})})}$ in order to set $B^{(\mathrm{b},\mathrm{P})}$ and $\Lambda^{(\mathrm{b},\mathrm{P})}$. Using the orthogonal approximation § V.3.2.2, we select the parameters separately for each regressor $k \in \{1, \dots, K_{\mathrm{P}}\}$. For each possible block size $\mathsf{s} \in \mathcal{S}$ we compute the average SURE approximation described in § V.3.1.3 applied to the resulting $\ell_{1,2}$-norm denoising estimator decomposed along the block grids; we select the block size $\mathsf{s}_k^{(\mathrm{b},\mathrm{P})}$ and the scaling parameter $\lambda_k^{(\mathrm{b},\mathrm{P})}$ minimizing the estimated risk.

Note that, as suggested by the numerical experiment § V.4.1.1, one can neglect the variance across grids when computing the average SURE approximation (V.19).

2.5 SMCS on Blank

Altogether, we can now solve the spatially structured sparse morphological component separation adapted to the blank acquisition, *i.e.* without significant neuronal activity component. In the variational problem (1), this translates to $K \overset{\text{set}}{=} K_{\mathrm{B}} + K_{\mathrm{P}}$, $D \overset{\text{set}}{=} \left(D^{(\mathrm{B})}, D^{(\mathrm{P})}\right)$, $X \overset{\text{set}}{=} \left(X^{(\mathrm{B})}, X^{(\mathrm{P})}\right)$, and the penalization reduces to

$$\Psi^{(\Lambda)}(X) \overset{\text{set}}{=} \iota_+\left(X^{(\mathrm{B})}\right) + \left\|X^{(\mathrm{P})}\right\|_{\ell,\Lambda_B^{(\mathrm{b},\mathrm{P})}} . \tag{12}$$

We mention also that for using the reweighted version of the $\ell_{1,2}$-norm penalization defined over an overlapping block structure, the reweighting parameters E_B should be set adapted to the number of overlaps, as explained in § V.4.1.1.

Finally, the output of the algorithm provides us with the final estimations of the components $Y^{(\mathrm{b},\mathrm{B})}$ and $Y^{(\mathrm{b},\mathrm{P})}$, and of the residual $R^{(\mathrm{b})}$, for each blank acquisition (b).

2.6 Stimulus and Spontaneous Neuronal Activity Condition

Assuming that all blank acquisitions of the protocol have been processed according to the previous section, we now describe the processing of acquisitions containing neuronal activity component. As introduced earlier, this comprises stimulus condition, as well as blank acquisitions containing important spontaneous neuronal activity. Nonetheless, unless stated explicitly otherwise, we will refer to both cases with the term *stimulus condition*, and index them by the superscript (s).

2.7 Gain and Bleaching Approximation

Since large neuronal activity can be expected, in contrast to the blank acquisitions case § 2.1, it is not possible to estimate accurately the bleaching approximation $\tilde{Z}^{(\mathrm{s},\mathrm{B})}$ directly on the raw traces $Y^{(\mathrm{s})}$. However, we suppose that it changes only slowly along time, so that it should be close to the bleaching dynamic found on the last blank recorded. Still,

the gain may have changed between the stimulus condition acquisition and its corresponding blank. In order to adjust it, we must then find for each pixel $p \in \{1, \dots, P\}$, a scaling $s \in \mathbb{R}_{+*}$ such that $\tilde{Z}_p^{(\mathrm{s,B})} = s_p \tilde{Y}_p^{(\mathrm{b,B})}$. In order to evaluate this scaling without being influenced by the neuronal activity component, we propose a weighted least-square regression

$$s_p \overset{\text{def}}{=} \operatorname*{argmin}_{s \in \mathbb{R}} \sum_{t=1}^{T} w_{t,p} \big(y_{t,p}^{(\mathrm{s})} - s \tilde{y}_{t,p}^{(\mathrm{b,B})} \big)^2 , \tag{13}$$

where for each pixel p and time frame t, the weight $w_{t,p} \in \mathbb{R}_{+*}$ quantifies the confidence one has on the observation $y_{t,p}^{(\mathrm{s})}$ for estimating the bleaching. We set the weights by evaluating how well the dynamic of $Y_p^{(\mathrm{s})}$ can be retrieved by $Y_p^{(\mathrm{b,B})}$, locally around the time frame t, following

$$w_{t,p} \overset{\text{set}}{=} \exp\Big(- \min_{s \in \mathbb{R}} \sum_{t'=t_1}^{t_2} \Big(y_{t',p}^{(\mathrm{s})} - s \tilde{y}_{t',p}^{(\mathrm{b,B})} \Big)^2 \Big/ \Big((t_2 - t_1 + 1) \big(\tilde{\sigma}_p^{(\mathrm{b})} \big)^2 \Big) \Big) , \tag{14}$$

where $t_1 \overset{\text{def}}{=} \max(1, t - t_{\mathrm{loc}}/2)$ and $t_2 \overset{\text{def}}{=} \min(T, t + t_{\mathrm{loc}}/2)$. The parameter t_{loc} defines the number of time frames locally taken into account (we use 100 ms), the minimum mean squared error is normalized by the noise variance estimated on the blank, and the exponential function penalizes specifically values below -1. Note also that if the acquisition is stimulus-locked, it is also possible to set $w_{t,p} \overset{\text{set}}{=} 0$ for time frames t from stimulus onset up to a certain delay.

The minimizations in (14) and then in (13) can be easily written in closed form, and we obtain this way a robust first approximation of the bleaching component $\tilde{Z}^{(\mathrm{s,P})}$. From that we estimate the gain $G^{(\mathrm{s})}$ as in (6), with for all $p \in \{1, \dots, P\}$, $g_p^{(\mathrm{s})} = \frac{1}{T} \sum_{t=1}^{T} \tilde{z}_{t,p}^{(\mathrm{s,P})}$.

2.8 Selection of $\Lambda_B^{(\mathrm{s,A})}$, $\Lambda_{\mathrm{TV}}^{(\mathrm{s,A})}$ and $M_{\mathrm{TV}}^{(\mathrm{s,A})}$

Similarly to (10), we get now

$$\big(\tilde{Y}^{(\mathrm{s})} - \tilde{Z}^{(\mathrm{s,B})} \big) / G^{(\mathrm{s})} \approx Y^{(\mathrm{s,P})} + Y^{(\mathrm{s,A})} + R^{(\mathrm{s})} . \tag{15}$$

In that signal, there remains two significant components, on top of the residual, so that it does not reduce to a denoising setting.

Here, we make a significant difference between VSDOI acquisitions that are synchronized on the heartbeat of the animal (see § I.3.1), and those that are not. Indeed, the strongest contribution in the periodic artifacts component is often due to heartbeat. In the synchronized case, we have then the approximation $Y^{(\mathrm{s,P})} \approx Y^{(\mathrm{b,P})}$, and we can simply subtract the periodic artifacts component already found on the blank from both sides of (15) to get a noisy approximation of the neuronal activity component. In the nonsynchronized case however, periodic artifacts can be drastically different from one acquisition to another, and (15) is the best approximation that we can get so far.

SURE on single trial. In each case, we estimate the neuronal activity penalization parameters similarly to § 2.4 by considering the neuronal activity estimator, parameterized by $\Lambda_B^{(\mathrm{A})}$, $\Lambda_{\mathrm{TV}}^{(\mathrm{A})}$ and $M_{\mathrm{TV}}^{(\mathrm{A})}$, and defined as $\hat{Y}^{(\Lambda_B^{(\mathrm{A})},\Lambda_{\mathrm{TV}}^{(\mathrm{A})},M_{\mathrm{TV}}^{(\mathrm{A})})}\colon Y \mapsto D^{(\mathrm{A})}\hat{X}$, where

$$\hat{X} \in \underset{X\in\mathbb{C}^{K_{\mathrm{P}}\times P}}{\operatorname{argmin}} \tfrac{1}{2}\left\|Y - D^{(\mathrm{A})}X\right\|_2^2 + \left\|X\right\|_{\ell,\Lambda_B^{(\mathrm{A})}} + \left\|X\right\|_{\delta,\Lambda_{\mathrm{TV}}^{(\mathrm{A})}} + \iota_{\overline{\delta_{M_B^{(\mathrm{P})}}}}(X)\,. \tag{16}$$

Note that, since we are provided with the residual $R^{(\mathrm{b})}$ found on the blank, we can get an accurate estimate of the noise level. Moreover, recall from § II.2.2.3 that the neuronal activity component is captured within a dictionary of temporal wavelet regressors. It is then possible to refine the white noise model, allowing for different noise levels along different wavelet scales. Within each scale $j \in \{j_{\min},\dots,j_{\max}\}$, we compute the risk estimation by setting the noise level at each pixel $p \in \{1,\dots,P\}$ as

$$\left(\sigma_{p,j}^{(\mathrm{s})}\right)^2 = \frac{1}{\left|\{k : j_k = j\}\right|}\sum_{k:j_k=j}\left\langle R_p^{(\mathrm{b})} \,\middle|\, D_k^{(\mathrm{A})}\right\rangle^2, \tag{17}$$

where it is assumed that each regressor has unit norm.

As advocated in § V.3.1.3, we actually select the parameters for each penalization term involved in (16) separately. Noticing that the bounded deviation constraint does not interfere with the two others, we keep it as-is. However, the two others tend to shrink coefficients in the reconstruction, and should be scaled accordingly. In practice, we found out that it is better *not* to scale them, but rather to substitute the $\ell_{1,2}$- and $\delta_{1,2}$-norm penalizations by their reweighted versions (§ II.3.2, § V.2.5), reducing the final bias; see also § 2.10 for details.

SURE on average. In the specific case of stimulus-locked acquisitions, it is common to consider that a reproducible pattern of neuronal activity will be evoked on all trials with the same stimulus (see however § I.1.3.2). Although such a reproducible pattern is influenced by many sources of variability, we believe that this could provide reliable information over the neuronal activity approximation, in order to refine the corresponding penalization parameters.

Hence, when acquisitions are stimulus-locked, we apply the above risk estimation of the estimator (16), but on observations constituted by the average of expressions (15) across repetitions of the same stimulus. Note that in particular, the noise level is then reduced by a factor equal to the number of trials in the average.

For each parameter involved in the penalizations, we are thus provided with two values. We select eventually the value which imposes *the less restrictive* constraint on the neuronal activity component. That way, the final estimation keeps significant features of the average signal, without reducing the single trial variability.

2.9 Selection of $\Lambda_B^{(\mathrm{s,P})}$ and $M_B^{(\mathrm{s,P})}$

As underlined in § 2.8, the periodic artifacts can be different from one acquisition to another. However, their biophysical origins are supposed to stay approximately the

same overtime. It is thus reasonable to assume that on two consecutive acquisitions, a given spatial position is affected, at a given frequency, with the same *amplitude*; the differences being essentially due to changes of *phase*.

Now, recall that for estimating the risk of the periodic artifacts estimator (16), the orthogonal approximation allows to work at the single regressor level, by considering the correlations between the observations and the regressor. Moreover, the SURE expression for the $\ell_{1,2}$-norm denoising estimator (V.8) only involves the norms of the observed correlations. Thus, the risk estimation only takes into account amplitudes of the observations, regardless to their phase. In particular, task of separating $Y^{(\mathrm{s,p})}$ from the residual $R^{(\mathrm{s})}$, is statistically the same as separating $Y^{(\mathrm{b,p})}$ from $R^{(\mathrm{b})}$.

In consequence, we select the parameter $\Lambda_B^{(\mathrm{s,p})}$ by estimating the risk of (16) (ignoring again the bounded amplitude constraint) over the observation $Y^{(\mathrm{b,p})} + R^{(\mathrm{b})}$. In addition, since this actual denoising instance is known, it is again possible to refine the noise estimation in the same spirit as for the wavelet regressors (17), with for all $k \in \{1, \dots, K_P\}$, for all $p \in \{1, \dots, P\}$, $\left(\sigma_{k,p}^{(\mathrm{s})}\right)^2 = \left|\left\langle D_k^{(\mathrm{p})} \,\middle|\, R_p^{(\mathrm{b})} \right\rangle\right|^2$, assuming again that the regressors are normalized.

Finally, following again the assumption that the amplitudes of the periodic artifacts are the same in the stimulus condition acquisition and in the corresponding blank acquisition, it is straightforward to estimate an upper bound over the coefficients amplitude. For all $k \in \{1, \dots, K_P\}$, the block structure $B_k^{(\mathrm{s,p})}$ being chosen thanks to the above, we directly set for all $b \in B_k^{(\mathrm{s,p})}$,

$$\mu_{k,b}^{(\mathrm{s,p})} = \max\left(\left\| \left(\left\langle D_k^{(\mathrm{p})} \,\middle|\, Y_p^{(\mathrm{b})} \right\rangle \right)_{p \in b} \right\|_2, \left\| \left(X_{k,p}^{(\mathrm{b})} \right)_{p \in b} \right\|_2 \right);$$

note that the two values in the right-hand-side might be different because the regressors in $D^{(\mathrm{p})}$ are not exactly orthogonal.

2.10 SMCS on Stimulus Condition

At last, we are now provided with every parameters tuning the penalization Ψ, written in full in (II.16), and we can solve the variational problem (1) to obtain the final component separation. Again, it is advised to use the reweighted version of the block norms penalizations. As discussed in § 2.8, this is an interesting way of debiasing penalizations which shrinks coefficients amplitude, while keeping the $\ell_{1,2}$-norms over the competing periodic artifacts and activity components approximately at the same level.

The next chapter studies concrete applications of the entire method to VSDOI data. In particular, § VII.5 precises important considerations on its overall computational cost, and discusses some crucial steps described here.

Appendix

A Consistent Estimator for the Affine Noise Model

Proposition 2.1. *Let $P \in \mathbb{N}_*$ and R be a P-dimensional random vector with zero mean and covariance matrix $\mathbb{E}[R\,{}^tR] = \alpha\Gamma + \beta\,\mathrm{Id}_P$, where $\alpha, \beta \in \mathbb{R}_+$ and $\Gamma \overset{\text{def}}{=} \left(\gamma_{p,q}\right)_{\substack{1\le p\le P\\ 1\le q\le P}}$ is a given symmetric matrix. Let A and B be defined as*

$$A \overset{\text{def}}{=} \frac{{}^tR\Gamma R - \frac{1}{P}{}^tR1_PR\,\mathrm{tra}(1_P\Gamma)}{\mathrm{tra}(\Gamma^2) - \frac{1}{P}\mathrm{tra}(1_P\Gamma)^2}\,, \qquad B \overset{\text{def}}{=} \tfrac{1}{P}({}^tR1_PR - A\,\mathrm{tra}(1_P\Gamma))\,, \tag{18}$$

where 1_P is the $P\times P$ matrix whose all terms are equal to 1. Then, $\mathbb{E}[A] = \alpha$, and $\mathbb{E}[B] = \beta$.

Proof. Develop $\mathbb{E}[{}^tR\Gamma R] = \sum_{p,q}\gamma_{p,q}\mathbb{E}\left[R_pR_q\right] = \sum_{p,q}\gamma_{p,q}(\alpha\gamma_{p,q} + \beta) = \alpha\sum_{p,q}{\gamma_{p,q}}^2 + \beta\sum_{p,q}\gamma_{p,q} = \alpha\,\mathrm{tra}(\Gamma^2) + \beta\,\mathrm{tra}(1_P\Gamma)$, and $\mathbb{E}[{}^tR1_PR] = \sum_{p,q}\mathbb{E}\left[R_pR_q\right] = \alpha\,\mathrm{tra}(1_P\Gamma) + \beta P$. Injecting this in (18) gives the desired result. ∎

When Γ is diagonal, *i.e.* for $p \neq q$, $\mathbb{E}\left[R_pR_q\right] = 0$, then 1_P can be replaced by Id_P in (18). Applying this with $\Gamma \overset{\text{set}}{=} \mathrm{diag}\left(\left(g_p^{(\mathrm{b})}\right)_{1\le p\le P}\right)$, and since for all $p \in \{1,\dots,P\}$, the sample variances ${\hat\sigma_p}^2$ is a consistent estimators of ${\tilde\sigma_p}^2 \overset{\text{def}}{=} \mathbb{E}\left[{R_p}^2\right]$, we deduce that the expressions given in (8) are consistent estimators of α and β of the affine noise model.

▪ VII ▪

Exploration of Voltage-Sensitive Dye Optical Imaging With Our Method

We are now set for applying our noisy component separation method to voltage-sensitive dye optical imaging data. Due to the difficulty of the task (recall Chapter I) and the lack of *ground truth*, *i.e.* prior knowledge of what the neuronal signal should look like through voltage-sensitive dye optical imaging, this work remains essentially exploratory. We test the fundamental hypothesis of our spatially structured sparse morphological model presented in Chapter II, and after analyzing various data sets, we discuss the potential of our method for revealing *in-vivo* spatiotemporal cortical dynamics which are up to now out of reach. In particular, we provide some comparisons with the blank subtraction and general linear model approaches, both described in Chapter II.

We investigate four different data sets, acquired in various experimental conditions. Two of them are *in-vivo* recordings of the *visual* cortex in the cat, acquired by Cyril Monier at the UNIC laboratory. The data set `Cat_Gratings` contains neuronal responses to *full-field luminance gratings* of different orientations, drifting along different directions, and the data set `Cat_Long` consists in long acquisitions (more than five seconds) with *drifting gratings*, *dense noise* and *natural images* stimuli. The two others are *in-vivo* recordings of the *somatosensory* cortex in the mouse, acquired by Isabelle Férézou at the ESPCI ParisTech and UNIC laboratories. The data set `Mouse_All` contains neuronal responses to *deflections of all whiskers*, while the data set `Mouse_Single` investigates *deflections of a single whisker* along different directions. Each stimulus condition is recorded for several trials, together with a corresponding *blank* acquisition. Details concerning experimental protocols are given in Annex A.

Finally, concerning both the development and the applications of our method, which require extensive computations, we are very grateful to Laurent Demanet for providing us access to the *Wave* computing server at the Massachusetts Institute of Technology.

Contents

This chapter makes use of the notations introduced in § II.1. Note however that the notation t indexing the time frames (discrete, $1 \leq t \leq T$) will also be used abusively to represent physical time (continuous, starting at 0 at the beginning of the acquisition, in seconds). When both conventions appears in the same expression, it is implied that the latter is converted into time frames, according to

$$t_{\text{frames}} = 1 + \lfloor t_{\text{physical}}\, f_s \rfloor \quad \text{for temporal instants,}$$

and

$$s_{\text{frames}} = \lfloor s_{\text{physical}}\, f_s \rfloor \quad \text{for durations,}$$

where f_s is the sampling frequency of the acquisition (in Hz).

1 Fluorescence, Gain, Noise

One of the most important aspects conditioning the application of the SMCS model to VSDOI is the *generative model* of the signal, motivated all along § I.2 and exposed in § II.2. Apart from the actual dynamics of the components, this model relies on a few fundamental assumptions described in § II.2.1 which can be summarized as

(H1) the recorded signal is the sum of a baseline fluorescence, of different components scaled by a gain, and a residual;

(H2) the gain can be determined from the baseline fluorescence, varies from pixel to pixel and stay constant for the duration of an acquisition;

(H3) the residual is a random noise whose variance is an affine function of the gain.

Notably, we formulate the hypotheses (H2) and (H3) from the fact that it has been reported that the signal-to-noise ratio, which is the amplitude of the recovered components divided by the standard deviation of the residual, roughly evolves as the *square root* of the overall illumination intensity (Grinvald *et al.*, 1999, §5.). This is mostly due to the statistical nature of the shot noise (see § I.1.2.2), modeled here as a Gaussian noise whose variance is proportional to the gain.

1.1 Testing the Hypotheses

The coherence of the hypotheses (H1)-(H3) with VSDOI data can be easily tested. Recall from § VI.2.2 that we evaluate the noise level, over a given blank acquisition (b), by performing a linear regression of a first estimated variance of the highest temporal variations at each pixel, $\left(\left(\hat{\sigma}_p^{(\mathrm{b})}\right)^2\right)_{1\leq p\leq P}$, against an estimate of the gain at those pixels, $\left(g_p^{(\mathrm{b})}\right)_{1\leq p\leq P}$. More precisely, we evaluate the coefficients

$$\left(\hat{\alpha}_\ell^{(\mathrm{b})}, \hat{\beta}_\ell^{(\mathrm{b})}\right) \overset{\text{def}}{=} \underset{(\alpha,\beta)\in\mathbb{R}^2}{\operatorname{argmin}} \sum_{p=1}^{P} \left(\alpha + \beta g_p^{(\mathrm{b})} - \left(\hat{\sigma}_p^{(\mathrm{b})}\right)^2\right)^2, \tag{1}$$

and we finally estimate the noise variance at each pixel $p \in \{1,\dots,P\}$ as $\left(\tilde{\sigma}_p^{(\mathrm{b},\ell)}\right)^2 = \hat{\alpha}_\ell^{(\mathrm{b})} + \hat{\beta}_\ell^{(\mathrm{b})} g_p^{(\mathrm{b})}$. Resulting regressions are plotted on Figure 1 for a single blank acquisition of each acquisition protocol. The correlation between the model and the first estimated values is

$$r_\ell^{(\mathrm{b})} \overset{\text{def}}{=} \frac{\sum_{p=1}^{P}\left(\hat{\sigma}_p^{(\mathrm{b})}\right)^2\left(\tilde{\sigma}_p^{(\mathrm{b},\ell)}\right)^2}{\sqrt{\sum_{p=1}^{P}\left(\hat{\sigma}_p^{(\mathrm{b})}\right)^4}\sqrt{\sum_{p=1}^{P}\left(\tilde{\sigma}_p^{(\mathrm{b},\ell)}\right)^4}}. \tag{2}$$

The distribution of those correlations and of the coefficients $\hat{\alpha}_\ell^{(\mathrm{b})}$ and $\hat{\beta}_\ell^{((\mathrm{b}))}$ along the blank acquisitions are reported on Figure 2. We can see that the noise model is accurate: the correlations are high, and the values of the coefficients lie in a narrow range, indicating that they might have physical meaning, as further explained in § 1.2.

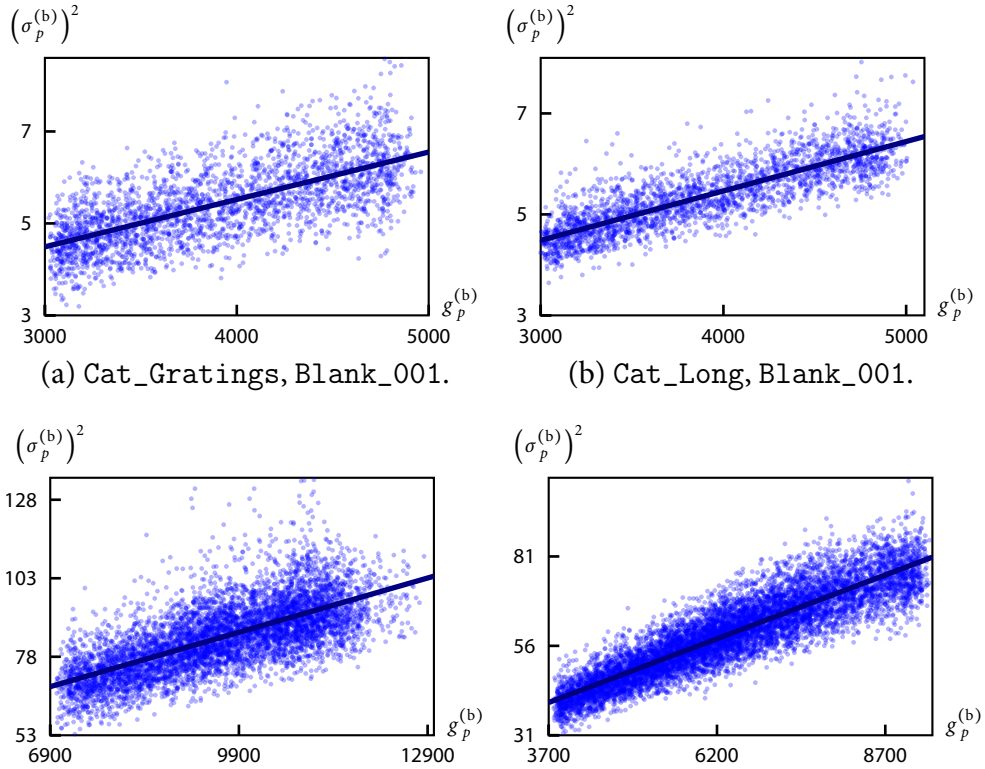

(a) `Cat_Gratings`, `Blank_001`. (b) `Cat_Long`, `Blank_001`.

(c) `Mouse_All`, `Blank_003`. (d) `Mouse_Single`, `Blank_001`.

Figure 1: Least-square linear regression of the empirical high frequency variances in function of the gain at each pixel, for the first processed blank of each protocol. Values are given in units of recorded fluorescence intensity. Size of the region of interest for each protocol, in pixels: (a) 2597, (b) 2446, (c) 8871, and (d) 6109.

Note that for the protocols `Mouse_All` and `Mouse_Single`, some blank acquisitions exhibit obvious patterns of spontaneous activity (see § 4.2), with high amplitude and at a somewhat lower frequency than the high frequency fluctuations investigated here. In order to focus on those high frequency fluctuations, in the present analysis we discard blank acquisitions exhibiting such patterns; even though they qualitatively do not change the results (data not shown).

1.2 Is There Neuronal Signal in the Highest Frequencies?

In the noise model, $\hat{\beta}_\ell^{(b)} g_p^{(b)}$ is the part of the noise variance due to shot noise, while $\hat{\alpha}_\ell^{(b)}$ represents a noise source affecting the whole acquisition field, independently from the differences in illumination intensities. This term can have different origins, in particular the thermal noise of the camera.

An other important term that could also influence high frequency fluctuations within the blank acquisitions is the ongoing neuronal activity. According to (H1), such neuronal noise is supposed to be also scaled by the gain. If it is the case, then its influence

on the high frequency variance should scale *quadratically* with the gain. Hence, we also perform a quadratic regression

$$\left(\hat{\alpha}_q^{(\mathrm{b})}, \hat{\beta}_q^{(\mathrm{b})}, \hat{\gamma}_q^{(\mathrm{b})}\right) \stackrel{\text{def}}{=} \underset{(\alpha,\beta,\gamma)\in\mathbb{R}^2}{\operatorname{argmin}} \sum_{p=1}^{P} \left(\alpha + \beta g_p^{(\mathrm{b})} + \gamma\left(g_p^{(\mathrm{b})}\right)^2 - \left(\hat{\sigma}_p^{(\mathrm{b})}\right)^2\right)^2, \tag{3}$$

and compute the corresponding correlation coefficients

$$r_q^{(\mathrm{b})} \stackrel{\text{def}}{=} \frac{\sum_{p=1}^{P}\left(\hat{\sigma}_p^{(\mathrm{b})}\right)^2\left(\tilde{\sigma}_p^{(\mathrm{b},q)}\right)^2}{\sqrt{\sum_{p=1}^{P}\left(\hat{\sigma}_p^{(\mathrm{b})}\right)^4}\sqrt{\sum_{p=1}^{P}\left(\tilde{\sigma}_p^{(\mathrm{b},q)}\right)^4}}, \tag{4}$$

where for all p, $\left(\hat{\sigma}_p^{(\mathrm{b},q)}\right)^2 \stackrel{\text{def}}{=} \hat{\alpha}_q^{(\mathrm{b})} + \hat{\beta}_q^{(\mathrm{b})} g_p^{(\mathrm{b})} + \hat{\gamma}_q^{(\mathrm{b})}\left(g_p^{(\mathrm{b})}\right)^2$. The resulting coefficients α and β are not significantly different than for the simple linear regression, while the coefficients $\hat{\gamma}_q^{(\mathrm{b})}$ seem meaningless, being sometimes even negative (data not shown). Moreover, one can see on Figure 2 that adding the quadratic term did not significantly improve the correlation with the observed values.

Now, supposing that (H1) is *not* true, *i.e.* the neuronal signal does not scale with the gain, it is possible that ongoing neuronal activity contributes to the constant part of the noise variance $\hat{\alpha}_\ell^{(\mathrm{b})}$. In order to evaluate the importance of the shot noise in the total amount of high frequency noise, we compute for each blank acquisition the ratio

$$\rho^{(\mathrm{b})} \stackrel{\text{def}}{=} \frac{\hat{\beta}_\ell^{(\mathrm{b})} g_p^{(\mathrm{b})}}{\hat{\alpha}_\ell^{(\mathrm{b})} + \hat{\beta}_\ell^{(\mathrm{b})} g_p^{(\mathrm{b})}}, \tag{5}$$

and report its distribution in Figure 2. One can see that shot noise accounts for a dominant fraction of the noise level.

We conclude from those observations that

1. the high frequency noise is spatially significantly homoscedastic, and this is accurately modeled by a linear variation of the variance in function of our estimated gain;

2. the neuronal activity contributes to, at most, a minor fraction of the high frequency fluctuations in the blank acquisitions.

Given the amplitude of the high frequency fluctuations in VSDOI recordings, our opinion is that macroscopic, *in-vivo* VSDOI is not a reliable tool for investigating, at the single trial level, patterns of neuronal activity whose duration is less that 20 ms (corresponding to a characteristic frequency of 50 Hz).

2 Synthetic Data

The aim of this section is two-fold. First, we investigate the power of separability of our SMCS method, in a controlled, noisy condition. Second, this allows to illustrate the

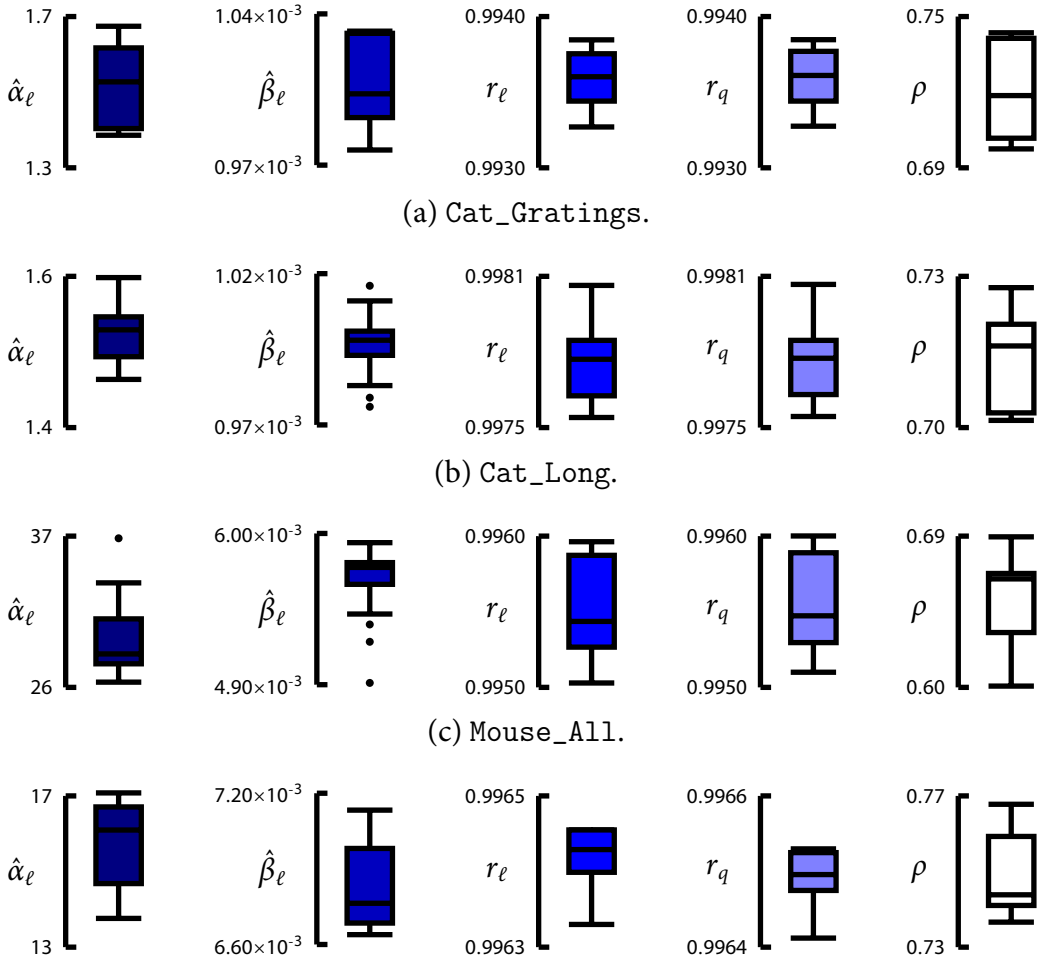

(a) `Cat_Gratings`.

(b) `Cat_Long`.

(c) `Mouse_All`.

(d) `Mouse_Single`.

Figure 2: Distribution along blank acquisitions of some coefficients of the noise regressions, displayed for each protocol using Tukey box plot.
α_ℓ, β_ℓ: coefficients of the linear regression (1);
r_ℓ, r_q: correlations of the linear (2) and quadratic (4) regressions, respectively;
ρ: fraction of the total high frequency variance attributed to shot noise (5).

strengths and weaknesses of the GLM method presented in § I.3.5. To do so, synthetic VSDOI data are generated according to our model detailed in § II.2, and both methods are applied to decompose them into neuronal activity, periodic artifacts and residual components; since the target signal is known, we can quantify then the quality of the separation. However, it is important to keep in mind that the two methods are hardly comparable. Indeed, the GLM requires precise knowledge of the dynamics of the components, and can retrieve from a VSDOI acquisition only what is known in advance. This allows for only limited variability in the evoked response, and no ongoing activity, as discussed further in this section, § 2.2.3.

2.1 Random Generative Model

For blank and stimulus condition acquisitions, we simulate $T \overset{\text{set}}{=} 256$ frames of size $P \overset{\text{set}}{=} 50 \times 50$ pixels, with a sampling frequency of 500 Hz and spatial resolution of 50 µm per pixels, leading to an acquisition duration of 512 ms and observation field of 2.5×2.5 mm^2. We define a random generative model of synthetic data, so that the resulting separations can be quantified in terms of average and standard deviation. More precisely, we generate ten realizations of $\tilde{Y}^{(\mathrm{b})} = G^{(\mathrm{b})} \cdot \left(Y^{(\mathrm{b,B})} + Y^{(\mathrm{b,P})} \right) + \tilde{R}^{(\mathrm{b})}$ and of $\tilde{Y}^{(\mathrm{s})} = G^{(\mathrm{s})} \cdot \left(Y^{(\mathrm{s,B})} + Y^{(\mathrm{s,P})} + Y^{(\mathrm{s,A})} \right) + \tilde{R}^{(\mathrm{s})}$, where each $\tilde{Y}^{(c)}$ and $\tilde{R}$ are random variables inspired by our real data (see Annex A) and VSDOI literature, mimicking recordings of propagating waves in cat's visual cortex. The random generative model is precisely detailed below, but the resulting components and acquisitions can be directly visualized on Figure 3.

In all this section, the random variables $U \sim \mathcal{U}([0,1])$, $V \sim \mathcal{N}(1, 10^{-2})$ and $W \sim \mathcal{N}(0,1)$ follow respectively a uniform distribution over the set $[0,1]$, a Gaussian distribution with zero mean and unit variance, and a standard distribution with unit mean and hundredth variance. Those distributions are used to introduce variability over some parameters. Single terms in matrices are now written in uppercase notation (*e.g.* $Y_{t,p}^{(c)}$ instead of $y_{t,p}^{(c)}$) when they are random variables.

2.1.1 Gain G

We simulate the gain with a Gaussian spatial profile, reaching its peak in the center of the acquisition. For all pixel p and time frame t,

$$G_p = \overline{g} \exp\left(-\frac{d(p)^2}{2{\sigma_G}^2} \right), \tag{6}$$

where $d(p)$ is the distance between pixel p and the center of the acquisition. The amplitude and the spatial width of the gain are set based on our own data, as

$$\overline{g} \overset{\text{set}}{=} 10^3 \qquad \text{and} \qquad \sigma_G \overset{\text{set}}{=} 1.25\,\text{mm}\,.$$

The gain is deterministic.

2.1.2 Baseline Fluorescence and Bleaching $Y^{(\mathrm{B})}$

The baseline fluorescence is set constant equal to unity (the reference value), and we simulate the bleaching component as a modulation of the baseline fluorescence with a single decreasing exponential. For all time t and pixel p

$$Y^{(\mathrm{B})}_{t,p} = 1 + X^{(\mathrm{B})}_p \left(\exp\left(-t/T_p\right) - \frac{1}{T} \sum_{t'=1}^{T} \exp\left(-t'/T_p\right) \right), \tag{7}$$

where $X^{(\mathrm{B})}_p \sim \overline{x}^{(\mathrm{B})} V$ and $T_p \sim \overline{\tau} V$ are all independent. The order of magnitude of the amplitude and of the bleaching time constant are set based on our own data, as

$$\overline{x}^{(\mathrm{B})} \overset{\text{set}}{=} 10^{-2} \qquad \text{and} \qquad \overline{\tau} \overset{\text{set}}{=} 300\,\text{ms}\,.$$

The bleaching varies from pixel to pixel, but it is kept identical along trials.

2.1.3 Periodic Artifacts $Y^{(\mathrm{P})}$

For each periodic artifact that we consider, we choose a fundamental frequency $\overline{f}_k$, and the corresponding artifact is constructed as

$$Y^{(\mathrm{P})}_{t,p} = \sum_{h=1}^{+\infty} X^{(\mathrm{P})}_{k_h,p} h^{-\alpha_k} \cos\left(2\pi F_{k_h} t + \Phi_{k_h,p}\right), \tag{8}$$

where $F_{k_h} \sim \overline{f}_k h V$ are the (perturbed) harmonics of $\overline{f}_k$, α_k is a damping factor, and $\left(X^{(\mathrm{P})}_{k_h,p}\right)_p$ and $\left(\Phi_{k_h,p}\right)_p$ are spatial maps of amplitude and phases, respectively.

Those maps are generated so as to exhibit some spatial structures, as described below. The spatial map of amplitude is characterized by four parameters: a seed $\left(\overline{X}^{(\mathrm{P})}_{k,p}\right)_p \in \mathbb{R}^P$, a correlation factor $c^{(x)}_k \in \mathbb{R}$, an average amplitude ${}^{\mu}\overline{x}^{(\mathrm{P})}_k \in \mathbb{R}$, and a dispersion of amplitudes ${}^{\sigma}\overline{x}^{(\mathrm{P})}_k \in \mathbb{R}$. It is generated once and for all, that is to say it is identical for all trials.

1. One generates the seed, which is a spatial map. Such seed can already present spatial structure (*e.g.* the locations of the veins for heartbeat artifact, see below), or can be totally random.

2. This spatial map is convolved with a Gaussian kernel of width $c^{(x)}_k$ to introduce local spatial correlations.

3. This map is rescaled and shifted so that its average equals ${}^{\mu}\overline{x}^{(\mathrm{P})}_k$ and its standard deviation equals ${}^{\sigma}\overline{x}^{(\mathrm{P})}_k$.

Similarly, the spatial map of phases is characterized by three parameters: a seed $\left(\overline{\Phi}^{(\mathrm{P})}_{k,p}\right)_p \in \mathbb{R}^P$, a correlation factor $c^{(\phi)}_k$, and an overall phase shift $\overline{\phi}^{(\mathrm{P})}_k \in \mathbb{R}$. It is generated as above, following steps 1 and 2. However in step 3, it is not rescaled but simply shifted by $\overline{\phi}^{(\mathrm{P})}_k$. In contrast to the spatial map of amplitude, a different map of phases is generated for each trials, *i.e.* the periodic artifacts are not synchronized.

The parameters for each periodic artifacts that we consider are listed below.
Heartbeat: (based on our own data)

$$f_k \overset{\text{set}}{=} 3\,\text{Hz}, \quad \alpha_k \overset{\text{set}}{=} 2, \quad c_k^{(x)} \overset{\text{set}}{=} 100\,\mu\text{m}, \quad c_k^{(\phi)} \overset{\text{set}}{=} 1.25\,\text{mm},$$
$$\mu\overline{x}_k^{(\text{P})} \overset{\text{set}}{=} 2\times 10^{-4}, \quad \sigma\overline{x}_k^{(\text{P})} \overset{\text{set}}{=} 1\times 10^{-4}, \quad \overline{\phi}_k^{(\text{P})} \sim 2\pi U,$$
$$\text{for all } p, \quad \overline{X}_{k,p}^{(\text{P})} \sim 10\Omega_p + W\text{i.i.d.}, \quad \overline{\Phi}_{k,p}^{(\text{P})} \sim 16\pi W\text{i.i.d.},$$

where $\left(\Omega_p\right)_p \in \{0,1\}^P$ is a spatial mask indicating the positions of simulated veins over the field of view (they can be distinguished on Figure 3(b)).
Illumination: (based on Reynaud *et al.* (2011))

$$f_k \overset{\text{set}}{=} 10\,\text{Hz}, \quad \alpha_k \overset{\text{set}}{=} 1.5, \quad ; c_k^{(x)} \overset{\text{set}}{=} 50\,\mu\text{m}, \quad c_k^{(\phi)} \overset{\text{set}}{=} 50\,\mu\text{m},$$
$$\mu\overline{x}_k^{(\text{P})} \overset{\text{set}}{=} 3\times 10^{-4}, \quad \sigma\overline{x}_k^{(\text{P})} \overset{\text{set}}{=} 3\times 10^{-5}, \quad \overline{\phi}_k^{(\text{P})} \sim 2\pi U,$$
$$\text{for all } p, \quad \overline{X}_{k,p}^{(\text{P})} \sim W\text{i.i.d.}, \quad \overline{\Phi}_{k,p}^{(\text{P})} \sim 4\pi W\text{i.i.d.}$$

Respiration: (based on our own data)

$$f_k \overset{\text{set}}{=} 1\,\text{Hz}, \quad \alpha_k \overset{\text{set}}{=} 2.5, \quad c_k^{(x)} \overset{\text{set}}{=} 1.25\,\text{mm}, \quad c_k^{(\phi)} \overset{\text{set}}{=} 1.25\,\text{mm},$$
$$\mu\overline{x}_k^{(\text{P})} \overset{\text{set}}{=} 1\times 10^{-4}, \quad \sigma\overline{x}_k^{(\text{P})} \overset{\text{set}}{=} 1\times 10^{-4}, \quad \overline{\phi}_k^{(\text{P})} \sim 2\pi U,$$
$$\text{for all } p, \quad \overline{X}_{k,p}^{(\text{P})} \sim W\text{i.i.d.}, \quad \overline{\Phi}_{k,p}^{(\text{P})} \sim 8\pi W\text{i.i.d.}$$

In practice, the infinite sums in (8) are truncated at $h = 10$.

2.1.4 Neuronal Response $Y^{(\text{A})}$

The neuronal activity component simulates propagating waves of activity. At each pixel, it raises and decreases, with delays and amplitudes that depend on the distance to local spatiotemporal sources. Such a wave is generated as the solution of a *wave equation with linear dissipation*,

$$\left(\frac{\partial}{\partial t} + \frac{1}{\tau_d}\,\text{Id}\right)^2 y - c^2\Delta y = s\,, \tag{9}$$

where y is the spatiotemporal activity component, Δ denotes here the spatial *Laplacian*, and s is an exciting source term. Such linear equation can be derived from neural field models, see for instance Deco *et al.* (2008). It produces waves propagating at speed c, and exponentially dissipated along time with characteristic time τ_d. We set dissipation time and propagation speed to

$$\tau_d \overset{\text{set}}{=} 100\,\text{ms} \qquad \text{and} \qquad c \overset{\text{set}}{=} 7\times 10^{-2}\,\text{m.s}^{-1}\,.$$

In order to emphasize the propagation phenomenon, the latter is voluntarily set slightly slower than values reported for instance in Jancke *et al.* (2004) or Chavane *et al.* (2011), but follows the same order of magnitude.

The source term s is a short bump, simulating a short, localized stimulation, with a short delay between stimulus and neuronal response. For all pixel p and time frame t,

$$s_{t,p} \overset{\text{set}}{=} \begin{cases} \exp\left(-\frac{d(p,p_s)^2}{2{\sigma_s}^2}\right) & \text{if } t_{\text{on}} \le t - t_{\text{delay}} \le t_{\text{off}}\,, \\ 0 & \text{otherwise}\,, \end{cases}$$

where $d(p, p_s)$ is the distance between pixel p and the center of stimulation p_s. We set p_s at one third of the diagonal of the acquisition field, $\sigma_s \overset{\text{set}}{=} 100\,\mu\text{m}$, $t_{\text{on}} \overset{\text{set}}{=} 200\,\text{ms}$, $t_{\text{off}} \overset{\text{set}}{=} 202\,\text{ms}$, and $t_{\text{delay}} \overset{\text{set}}{=} 10\,\text{ms}$. An approximate solution y of (9) is computed on the discretized observation grid with a standard finite difference scheme using the code provided by Nicolas Schmidt from CEREMADE. Finally, $Y^{(\text{A})}$ is obtained from the solution y by linearly rescaling it, so its the maximum value reaches

$$\overline{x}_k^{(\text{A})} \overset{\text{set}}{=} 5 \times 10^{-3} .$$

Note that $Y^{(\text{A})}$ is actually deterministic: there is no trial-to-trial variability.

2.1.5 Random Noise $\tilde{R}$

According to our noise model (see § II.2.1 and § 1), we set, independently for each pixel p of each time frame t, $\tilde{R}_{t,p} \sim \sqrt{\alpha_{\text{noise}} + \beta_{\text{noise}} G_{t,p}}\ W$, where

$$\alpha_{\text{noise}} \overset{\text{set}}{=} \left(1 \times 10^{-8}\right)\overline{g}^2 \qquad \text{and} \qquad \beta_{\text{noise}} \overset{\text{set}}{=} \left(1 \times 10^{-8}\right)\overline{g} .$$

2.2 Separation Results

Before analyzing separation performances, let us first detail the parameters used for each method.

2.2.1 GLM Designs (see § I.3.5)

In the regressor design, we include one constant regressor and a decreasing exponential at time constant $\overline{\tau}$ introduced in (7). This decreasing exponential is shifted to have zero mean, so that the gain can be estimated as the coefficient of the constant regressor. Then, for each periodic artifact in the experimental setting, we include the sine and cosine regressors at frequencies $\left\{\overline{f}_k h \,\middle|\, h^{-\alpha_k} > 5 \times 10^{-2}\right\}$, as introduced in (8). Note however that, as for the SMCS (see below), periodic regressors with frequencies lower than the inverse of the acquisition duration (about 2 Hz) are discarded, because they are likely to capture a significant part of the bleaching, leading to aberrant results.

Now, recall that in our synthetic experimental setting, the neuronal response is the same along all trials. We design the response regressors as the first left singular vectors of the SVD decomposition of the matrix $Y^{(\text{A})}$. This is known to be the best basis of a given size for approximating linearly the response, in term of ℓ_2-norm. Such knowledge in real condition can never be achieved, so that our setting favors largely the GLM method.

Figure 3, *opposite*: Synthetic data and neuronal response recovery by SMCS and GLM 10. The time courses correspond to spatial positions indicated on the frames by a square of the same color. Vertical dashed line indicates stimulus onset. (a) Observations normalized by the gain, single trial. (b) Periodic artifacts, single trial. (c) Neuronal response, identical in all trials. (d) Recovery with SMCS, average across trials, single trials in transparency. (e) Recovery with GLM 10.

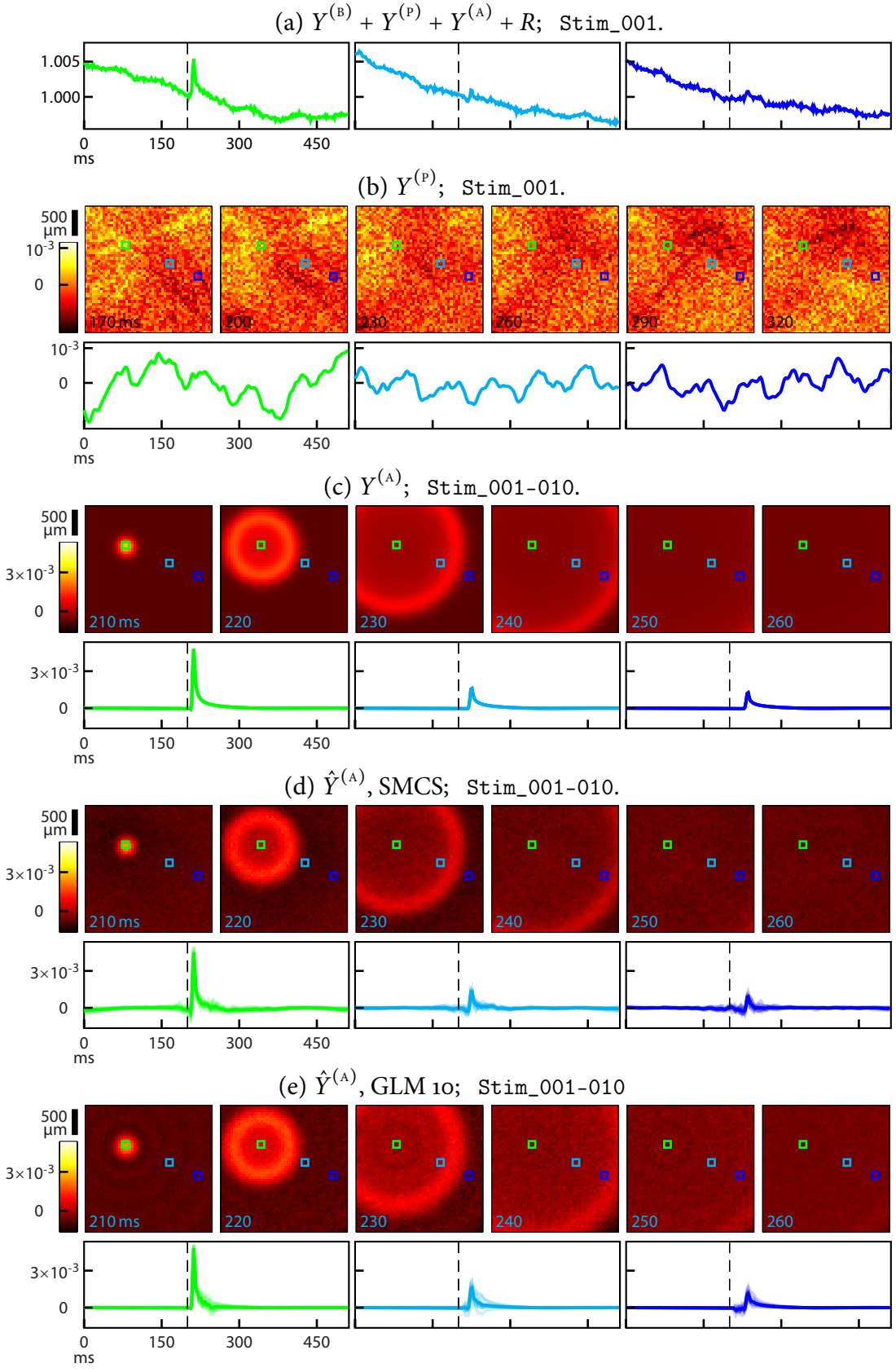

Figure 3: Synthetic data overview. See *opposite*.

We consider two designs: one with ten response regressors (GLM 10), and one with fifteen response regressors (GLM 15).

2.2.2 SMCS Designs (see Table VI.1)

We use the following default parameters:
$K_{\mathrm{B}} \overset{\text{set}}{=} 2$, *i.e.* only one decreasing exponential.
Daubechies wavelets with four vanishing moments (Daubechies, 1992), $j_{\min} \overset{\text{set}}{=} 3$.
$\mathcal{F} \overset{\text{set}}{=} \{0.5f \mid f \in \{4, \dots, 40\}\} \cup \{21, \dots, 60\} \cup \{2f \mid f \in \{31, \dots, 40\}\} \cup \{85, 90, 95\}$, in Hz.
$\mathcal{S}^{(\mathrm{P})} \overset{\text{set}}{=} \{1, 2, 3, 4, 6, 9, 12\}$, in pixels.
$\mathcal{S}_{\ell}^{(\mathrm{A})} \overset{\text{set}}{=} \{2, 3, 4\}$, in pixels.
$\mathcal{S}_{\delta}^{(\mathrm{A})} \overset{\text{set}}{=} \{2\}$, in pixels.
Note that we discard periodic artifacts frequencies $\mathcal{F}$ contains frequencies lower than 2 Hz because the overall duration of the acquisition is only about half a second.

Then, we consider two different box constraints design: the first one (SMCS) uses none, *i.e.* $\underline{Y}^{(\mathrm{A})}$ and $\overline{Y}^{(\mathrm{A})}$ are identically equal to $-\infty$ and $+\infty$, respectively; the second one (SMCS box) uses box constraints enforcing a neuronal activity which is nonnegative everywhere, and null outside frames of interest. More precisely, we set for all pixel p and time frame t,

$$\underline{y}_{t,p}^{(\mathrm{A})} \overset{\text{set}}{=} 0\,; \qquad \text{and} \qquad \overline{y}_{t,p}^{(\mathrm{A})} \overset{\text{set}}{=} \begin{cases} +\infty & \text{if } t_1 \le t \le t_2\,, \\ 0 & \text{otherwise}\,. \end{cases} \tag{10}$$

Following roughly our synthetic response component (see Figure 3(c)), we set $t_1 \overset{\text{set}}{=} 200$ ms and $t_2 \overset{\text{set}}{=} 300$ ms.

2.2.3 Results

Similarity indicators. We quantify the quality of the component separation by comparing each retrieved component with its target component, over the whole spatiotemporal domain. We use both the *signal-to-noise ratio*, expressed in decibels as

$$\mathrm{SNR}\left(\hat{Y}, Y\right) \overset{\text{def}}{=} 20 \log_{10}\left(\frac{\|\hat{Y}\|_2}{\|\hat{Y} - Y\|_2}\right), \tag{11}$$

and the *correlation coefficient*

$$\mathrm{CC}\left(\hat{Y}, Y\right) \overset{\text{def}}{=} \frac{\mathrm{tra}\left({}^{\mathrm{t}}\hat{Y}\, Y\right)}{\|\hat{Y}\|_2 \|Y\|_2}\,. \tag{12}$$

Mean and standard deviation across trials of those similarity indicators, over neuronal response and periodic artifacts components, are shown in Figure 4.

Component separation and denoising with SMCS. We see from Figure 3(d) that our method approximately retrieves the neuronal response component, in spite of a highly perturbed environment and no prior knowledge on the signal activation times.

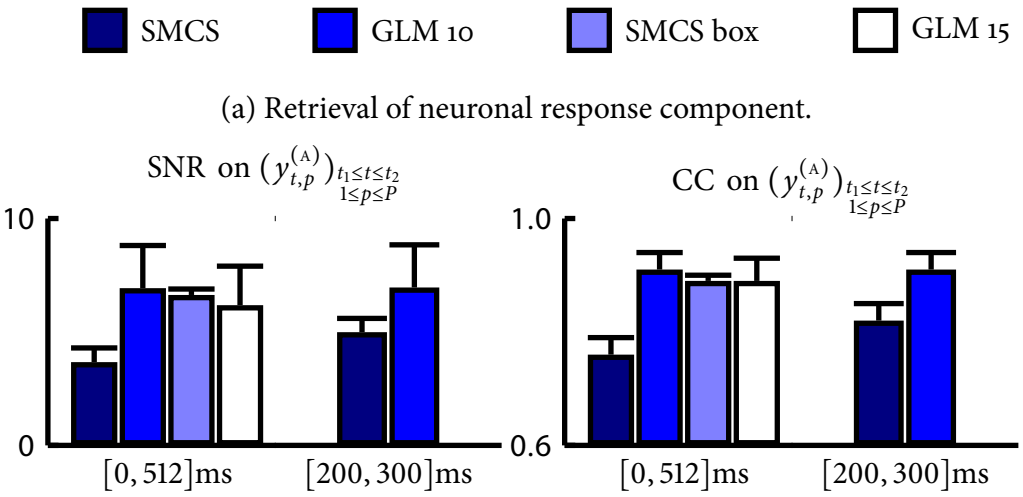

(a) Retrieval of neuronal response component.

(b) Retrieval of periodic artifacts component.

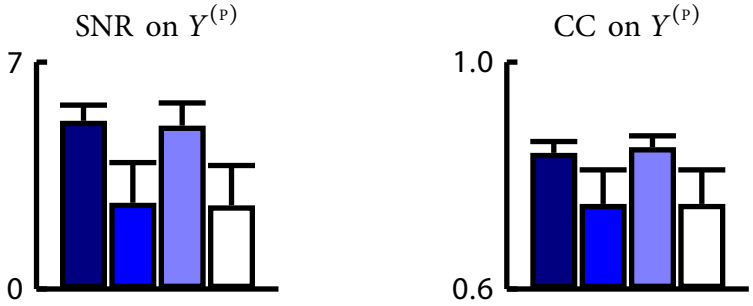

Figure 4: Performance of the component separation for SMCS and GLM methods on synthetic experiments. Results are given as average and standard deviation over ten realizations of the random generative model (see § 2.1). When specified, the signal-to-noise ratios (11) and the correlation coefficients (12) are computed over the frames included in $[t_1, t_2]$.

Comparison with GLM. As can be seen on Figure 4(a) $[0, 512]$ms, GLM (blue) outperforms SMCS (dark blue) for the retrieval of the neuronal response over the whole acquisition time course. This is explained by the fact that the response regressors in GLM are designed to retrieve only phenomena that take place between 200 and 300 ms. On the contrary, our method seeks for neuronal events along the whole acquisition time course, hence is more sensitive to artifacts occurring outside those time frames.

In order to evaluate *sensitivity* of the method to neuronal events, we compute the similarity indicators (11) and (12) restricted to the time frames between 200 and 300 ms. Results Figure 4(a) $[200, 300]$ms shows better similarity indicator for SMCS, but not for GLM. This is further illustrated in Figure 5.

Then, *specificity* of the SMCS method to neuronal events is enhanced by introduction of the box constraints (10). We see on Figure 4(a) that SMCS box (light blue) performs on average as well as GLM 10. Moreover, it is more reliable than GLM since the latter exhibits higher standard deviation. This indicates that the separation performance of GLM on a given trial might depend on the realization of the periodic artifacts.

In fact, it turns out that good performances of GLM are explained by the accurate design of the response regressors (as explained above, § 2.2.1), and not by its component separation ability. To see this, we compute the similarity indicators for the retrieval of the periodic artifacts component. On Figure 4(b), it is obvious that periodic artifacts are better captured by both versions of SMCS (dark and light blue) than by GLM. Moreover, one might think that increasing the dimensionality of the response space in the GLM allows for better reconstruction accuracy. The white bars on Figure 4 show that this actually degrades its performances, because the response component gets mixed with noise and periodic artifacts; this can also be seen on Figure 5.

Finally, let us recall that according to the GLM approach proposed by Reynaud *et al.* (2011), the residual is considered to be part of the signal of interest, and should be added to the neuronal activity component after component separation. This permits the GLM method to capture more complexity and trial-to-trial variability in the neuronal activity, in spite of the restriction imposed over the response space. However, doing so in the current study makes no sense, since the performance indicators measure proximity to a deterministic response, known in advance, and from which the regressors are directly designed. Given the poor periodic artifacts reconstruction with GLM (Figure 4(b)), adding the residual would make the similarity indicators over the neuronal response component drop drastically.

3 Orientation Selectivity in the Cat's Visual Cortex

One of the most striking functional feature of most mammal's primary visual cortex is the *orientation selectivity*, first described by Hubel and Wiesel (1959). Many neurons in this cortical area are sensitive to elongated luminance contrasts that constitute edges in the visual field. Moreover, the intensity of the neuronal response depends on the similarity between the orientation of the edge within the visual field, and an orientation of reference, characteristic of the observed neuron. The closer to this *preferred orientation*, the higher the response.

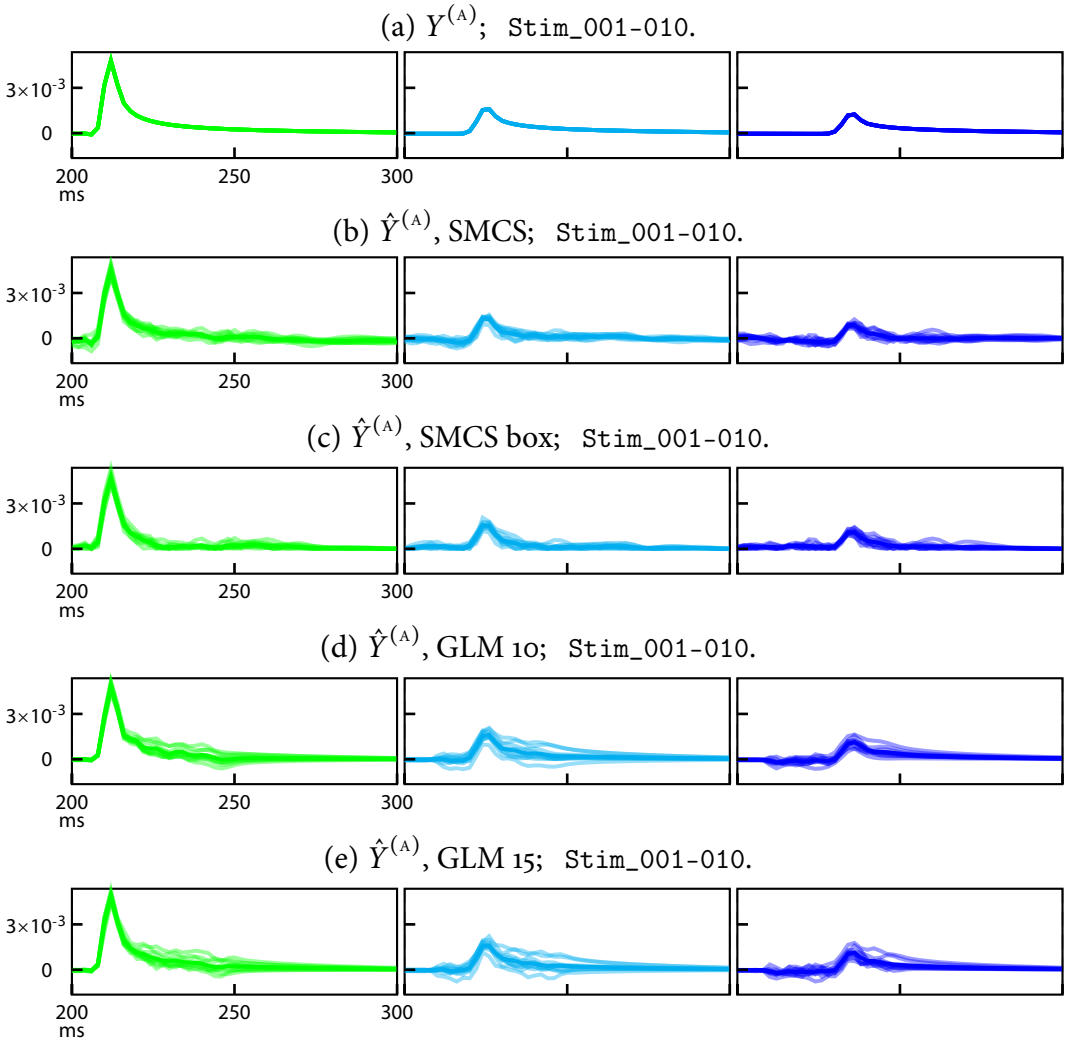

Figure 5: Close-up on the time courses of the targeted and retrieved synthetic neuronal responses. The plotted time courses correspond to spatial positions indicated on the frames of Figure 3 by a square of the same color. Results are shown as average across trials, together with the single trials in transparency.

Following an organization which is common to many cortical functional features, neurons sharing the same preferred orientation are gathered in *columns*, which are functional units extending spatially perpendicularly to the cortical surface (Mountcastle, 1997). In addition, in the cat's visual cortex, the variation of preferred orientation tangentially to the cortical surface is smooth (except at singularity points, where all the orientations are represented, see § 3.2.4). Thus, using optical imaging with sufficient spatial resolution, it is possible to identify the *dominant preferred orientation* underlying each recorded location (see for instance Bonhoeffer and Grinvald (1993)).

When presenting *full field*, *drifting luminance gratings* to the subject, a raise of activity is triggered in the entire primary visual cortex, which can last for the duration of the stimulus. Though most neurons are responding, their responses are modulated by orientation selectivity according to the orientation of the grating. When investigating time-independent orientation selectivity, the quantity of interest is only the *response intensity* so that there is no need for high temporal resolution for recording it. Thus, VSDOI is not the first choice modality for that purpose, and for recordings at the population level, less noisy methods like intrinsic optical imaging should be favored. Since our SMCS method aims at recovering complex temporal dynamics, it is precisely *not* designed for such experiments. However, orientation selectivity is one of the most understood functional properties of the primary visual cortex, and one prerequisite for delving into more complex features is to check that our denoising method does not suppress this information.

For that reason, we study in this section the use of the SMCS method for estimating orientation selectivity at the population level. We compare our method to the classical blank subtraction (§ I.3.1) and to the GLM developed by Yavuz (2012). To our knowledge, the latter is the most efficient approach to date for extracting time-independent orientation selectivity in the cat's visual cortex from VSDOI recordings.

3.1 Data and Denoising Methods

The data set `Cat_Gratings` consists in 1 280 ms long recordings of the primary visual cortex of a single cat, in area 18. The visual stimuli used are full field luminance gratings of four possible orientations, drifting in two possible directions. Each stimulus condition is recorded for ten trials, together with ten corresponding blank conditions. See Annex A.1 for more details.

Before analyzing the orientation selectivity, let us review the different component separation and denoising methods of extraction of the neuronal responses that we compare. Some resulting components on a given stimulus condition are shown for each method in Figure 6.

3.1.1 Blank Subtraction (BkS)

All acquisitions of the protocol are triggered at the same phase of the simultaneously recorded ECG, and respiration of the subject is artificially controlled (see Annex A.1). Thus, the blank subtraction method introduced in § I.3.1 is relatively efficient. We detail here our implementation.

Each trial under stimulus condition $\tilde{Y}^{(\mathrm{s})}$ is associated to its corresponding trial under blank condition $\tilde{Y}^{(\mathrm{b})}$. The gain of each acquisition is evaluated at each pixel p as the average fluorescence value over the frames before stimulus onset,

$$g_p^{(\mathrm{s})} = \frac{1}{t_{\mathrm{on}}} \sum_{1 \leq t \leq t_{\mathrm{on}}} \tilde{Y}_{t,p}^{(\mathrm{s})} \qquad \text{and} \qquad g_p^{(\mathrm{b})} = \frac{1}{t_{\mathrm{on}}} \sum_{1 \leq t \leq t_{\mathrm{on}}} \tilde{Y}_{t,p}^{(\mathrm{b})} \,.$$

Then, each acquisition is normalized by its gain, $Y^{(\mathrm{s})} = \tilde{Y}^{(\mathrm{s})}/G^{(\mathrm{s})}$ and $Y^{(\mathrm{b})} = \tilde{Y}^{(\mathrm{b})}/G^{(\mathrm{b})}$, and we create a smoothed blank acquisition $\Upsilon^{(\mathrm{b})} \overset{\text{def}}{=} \left(v_{t,p}^{(\mathrm{b})}\right)_{t,p}$, getting rid of the high frequency noise by low-pass filtering with a Gaussian kernel. For all pixel p,

$$v_{t,p}^{(\mathrm{b})} = \frac{\sum_{t' \in \{-w_f, \ldots, w_f\}} \exp\left(-\frac{t'^2}{2\sigma_f^2}\right) y_{t+t',p}^{(\mathrm{b})}}{\sum_{t' \in \{-w_f, \ldots, w_f\}} \exp\left(-\frac{t'^2}{2\sigma_f^2}\right)} \,,$$

with symmetric boundary convention, *i.e.* $y_{t+t',p}^{(\mathrm{b})} \overset{\text{def}}{=} y_{1-(t+t'),p}^{(\mathrm{b})}$ if $t + t' < 1$, and $y_{t+t',p}^{(\mathrm{b})} \overset{\text{def}}{=} y_{T-(t+t'),p}^{(\mathrm{b})}$ if $t + t' > T$. In our experiment, we use $w_f \overset{\text{set}}{=} 10\,\mathrm{ms}$ and $\sigma_f \overset{\text{set}}{=} 10\,\mathrm{ms}$. Finally, the neuronal response signal is estimated as $Y^{(\mathrm{s,A})} = Y^{(\mathrm{s})} - \Upsilon^{(\mathrm{b})}$.

3.1.2 GLM Design

We use the method described in Yavuz (2012, §6.2.2), which is a GLM approach (see § I.3.5) inspired by the work of Reynaud *et al.* (2011), adapted to VSDOI recordings of neuronal responses to full field drifting luminance gratings in the cat's visual cortex. In this setting, there is *only one* response regressor, modeling rise and decrease of neuronal activity following respectively stimulus onset and stimulus offset. After source separation between neuronal signal, various artifacts, and residual, the latter is added to the former, as advocated in both above references.

In the work of Yavuz (2012), the choice was made *not* to model the gain. Keep in mind however that in the current study, the only quantity of interest is the polar angle of the vectorial sums (15) described below (§ 3.2.3). Now, even if the gain varies greatly from pixel to pixel, it does not vary much from trial to trial; hence, normalizing by the gain greatly affects the amplitude, but not the polar angle (16) of those vectorial sums.

The subsequent statistical refinement by PCA in the denoising proposed in Yavuz (2012) was not used here.

3.1.3 SMCS Design

We use the same parameters in this setting as in our synthetic data setting, § 2.2.2, except for $K_{\mathrm{B}} \overset{\text{set}}{=} 3$, *i.e.* we model the bleaching with two decreasing exponentials (see § VI.2.1; we find $\mathcal{T} = \{123\,\mathrm{ms}, 584\,\mathrm{ms}\}$), and for periodic artifacts frequencies lower than 2 Hz. Since the acquisition duration is more than one second here, frequencies down to 1 Hz would be considered in our procedure; we discard them because the expected neuronal signal is much more important than respiration artifacts around those frequencies.

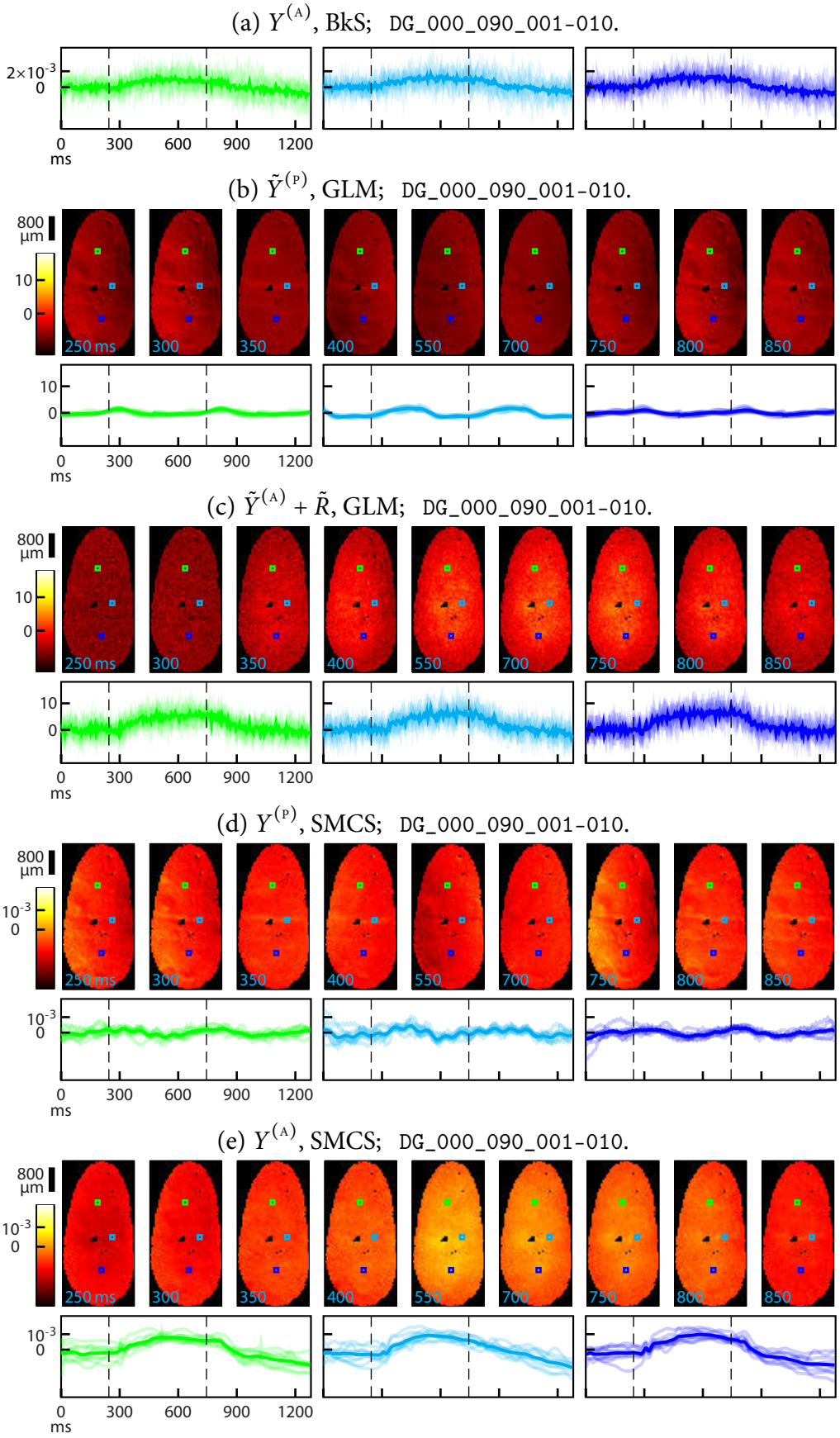

Figure 6: Component separations for the protocol `Cat_Gratings`. See *opposite*.

Figure 6, *opposite*: Component separations for the protocol `Cat_Gratings`, stimulus condition: full field, gratings of orientation 0° (horizontal), drifting direction 90° (upwards). The time courses correspond to spatial positions indicated on the frames by a square of the same color. Vertical dashed line indicates stimulus onset and offset. (a) Neuronal activity retrieved by BkS. (b) Periodic artifacts retrieved by GLM. (c) Neuronal activity retrieved by GLM. (d) Periodic artifacts retrieved by SMCS. (e) Neuronal activity retrieved by SMCS. Results are shown as average across trials, together with single trials time courses plotted in transparency. Note that GLM results are given in arbitrary units of recorded fluorescence level, since they have not been normalized by the gain (see § 3.1.2).

3.1.4 Qualitative Comparisons

As expected, the BkS method (Figure 6(a)), gives a very noisy signal. Still, averages across ten trials are informative about the simple, reproducible response to a drifting grating. In comparison, time courses obtained by GLM are less noisy, even though the residual is added to the response component to obtain the final neuronal activity, as explained above § 3.1.2. On Figure 6(c), the overall response dynamic is more prominent, relatively to the high frequency noise amplitude. Finally, traces obtained by SMCS are almost free of high frequency noise, while still exhibiting significant amplitude of trial-to-trial variability (Figure 6(e)).

Because the heartbeat and respiration are approximately synchronized along trials, their retrieved average contribution presents distinct spatiotemporal patterns. On Figures 6(b) and (d), top rows, one can see fluorescence oscillations on large domains, with phases varying from left to right. Also, higher amplitudes distinguishes veins over the field of view. Note that because the considered GLM implementation does not model the gain (see § 3.1.2), it is not possible to compare directly its results to SMCS. However, periodic artifacts and neuronal activity have been normalized within each methods, in terms of color map and traces amplitude. Hence, we can see that amplitudes of retrieved periodic artifacts are less important in GLM than in SMCS, relatively to the corresponding neuronal activity. Moreover, periodic artifacts retrieved by SMCS exhibit more trial-to-trial variability, and more temporal complexity. We explain those facts by the richer dictionary of sinusoidal regressors modeling periodic artifacts within the SMCS, so that phase and frequency variations, both *inter*- and *intra*-trials, can be better captured. See in particular the significant contribution of the periodic artifacts around 12 Hz, Figures 6(d), middle trace[1]. We believe it to be an harmonic of the heartbeat artifact, since the corresponding pixel (in cyan color) is clearly situated on a vein.

However, higher sensitivity of the periodic artifacts component also presents some drawbacks. According to the SMCS results for the same cyan pixel, the neuronal activity averaged across trials starts to decrease *before* stimulus offset. Given the relative brevity

[1] note that in our data, 12 Hz signal is absent from the periodic artifacts retrieved by GLM because this frequency is actually not included in the regressor basis. However, as stated by Yavuz (2012, § 6.2.3), this artifact is still badly captured by GLM when introducing it. The reason for not including this frequency *at all* is that subsequent statistical refinements proposed by this author give better results that way.

of the stimulus duration, this is not expected; indeed, both BkS and GLM results show a longer sustained neuronal activity at this pixel. We explain the error made by SMCS by the fact that around stimulus offset, the heartbeat artifact at this location is at a rising phase, as indicated by brighter colors along the vein, on the frame 800 ms of both Figures 6(b) and (d).

An other significant difference between GLM and SMCS is the important decrease of the neuronal activity component, occurring around 1 s and until the end of the acquisition. We believe it to be due to intrinsic artifact (described in § I.2.2), because of its slow dynamic and emergence after significant neuronal response. The same trend can be seen on the BkS traces, but much fainter. We believe that this effect is overestimated by the SMCS method because the constant regressor (within the bleaching dictionary, see § II.2.2.1) is not penalized and tends to adjust, at each pixel, to the mean value of the signal along time. This would also explain the slightly negative values before stimulus onset, observed on the mean traces of Figure 6(e).

Finally, let us note the ability of our SMCS method to capture, at the single trial level, a transient phenomenon that takes place between 40 and 80 ms after stimulus onset (*i.e.* around 300 ms after beginning of acquisition). After first increase, evoked activity slightly and rapidly decreases, before increasing again. This phenomenon, coined *deceleration-acceleration notch*, have been documented in the literature, see in particular Sharon and Grinvald (2002).

3.2 Estimation of Preferred Orientation

A VSDOI protocol investigating orientation selectivity over the whole cortical sample should usually contain recordings of neuronal responses to a set of full field drifting luminance gratings of various orientations, taken in a set $\{\theta_1, \dots, \theta_N\}$, sampling uniformly all possible orientations from 0° to 180° (in the case of our data set, $N \overset{\text{set}}{=} 4$). We describe here a procedure for extracting static (*i.e.* we do not study evolution along time) orientation selectivity from such neuronal responses, $\left\{Y^{(\mathrm{s,A})}\right\}_{\mathrm{s}}$ (which can be extracted by any denoising method).

3.2.1 Mean Response Level

In order to estimate the dominant preferred orientation underlying a given spatial location in VSDOI recordings, one must first extract the *mean response level* of that spatial location to each presented orientation of the protocol. We denote it $\tilde{Y}^{(\mathrm{m,A})} \overset{\text{def}}{=} \left(\tilde{y}^{(\mathrm{m,A})}_{n,p}\right)_{\substack{1\le n\le N\\ 1\le p\le P}}$, computed for each pixel p and orientation θ_n as

$$\tilde{y}^{(\mathrm{m,A})}_{n,p} = \frac{1}{|\mathrm{s}(\theta_n)|} \sum_{\mathrm{s}\in \mathrm{s}(\theta_n)} \sum_{t_1\le t\le t_2} y^{(\mathrm{s,A})}_{t,p}\,, \tag{13}$$

where $\mathrm{s}(\theta_n)$ denotes the set of all trials of all grating stimuli with orientation θ_n within the protocol, and $t_1 \le t_2$ delimit the time frames where the most significant response is expected.

In our numerical application, we use $t_1 \overset{\text{set}}{=} t_{\text{on}} + 100\,\text{ms}$ and $t_2 \overset{\text{set}}{=} t_{\text{off}} = t_{\text{on}} + 500\,\text{ms}$.

3.2.2 Normalization Step

On our data set, using the mean response levels directly as defined in (13) for deducing preferred orientation is not satisfying. As can be seen on Figure 7(a), this leads to an overwhelming representation of some preferred orientation angles; such a bias in the distribution is not expected, considering the size of our cortical sample and the distribution of preferred orientations generally accepted (see for instance Mountcastle (1997)). We alleviate this bias by dividing the mean response levels of each orientation by its average across pixels, obtaining $Y^{(\mathrm{m,A})} \stackrel{\text{def}}{=} \left(y_{n,p}^{(\mathrm{m,A})}\right)_{n,p}$ such that for all p and n,

$$y_{n,p}^{(\mathrm{m,A})} = \frac{P}{\sum_{1\le p'\le P} \tilde{y}_{n,p'}^{(\mathrm{m,A})}} \tilde{y}_{n,p}^{(\mathrm{m,A})} \,. \tag{14}$$

This phenomenon might be explained by lateral exciting connections between functional columns enhancing drastically even a small imbalance in the distribution, but we leave this point to future investigations. In the literature, the closest mention to such preprocessing that we could find is Sharon and Grinvald (2002, Note 24.), where the authors perform a spatial high-pass filtering of their data, in order "to remove nonreproducible global differences in the responses to different orientations". However, besides the lack of clarity of this explanation, the *nonreproducible* terminology suggests that these differences are stimulus independent, in contrast to what we observe in our data set. The same need for spatial high-pass filtering is also reported in Chavane *et al.* (2011, Appendix), in order "to remove slow gradients".

3.2.3 Orientation Maps

Finally, we compute the preferred orientation at each spatial location using the *vectorial sum* technique, as briefly described in Blasdel and Salama (1986). It represents the orientation selectivity with a two-dimensional vector, which is the sum of unit vectors of polar angle determined by a given orientation, weighted by the mean response level to that orientation. More precisely, denoting for an angle θ, $\vec{u}(\theta) \stackrel{\text{def}}{=} (\cos(\theta), \sin(\theta))$, the vectorial sum at pixel p is

$$\vec{v}_p = \sum_{1\le n\le N} y_{n,p}^{(\mathrm{m,A})} \vec{u}(2\theta_n) \,. \tag{15}$$

Note the factor 2 applied to each orientation, so that the range of orientations $[0, 180[^\circ$ is mapped to the complete circle $[0, 360[^\circ$ and that the mean response level to two orientations that are orthogonal cancel out in the sum. The preferred orientation angle at pixel p is then half of the polar angle of $\vec{v}_p$; expressed in degrees,

$$\vartheta_p = \begin{cases} \frac{1}{2}\arccos\left(\frac{v_{p,1}}{\|\vec{v}_p\|}\right) & \text{if } v_{p,2} \ge 0 \,, \\ 180 - \frac{1}{2}\arccos\left(\frac{v_{p,1}}{\|\vec{v}_p\|}\right) & \text{if } v_{p,2} < 0 \,, \end{cases} \tag{16}$$

where we denoted the coordinates of the vectorial sum $\vec{v}_p \stackrel{\text{def}}{=} \left(v_{p,1}, v_{p,2}\right)$ and its amplitude $\|\vec{v}_p\| \stackrel{\text{def}}{=} \sqrt{{v_{p,1}}^2 + {v_{p,2}}^2}$. This procedure provides a spatial map of preferred orientations

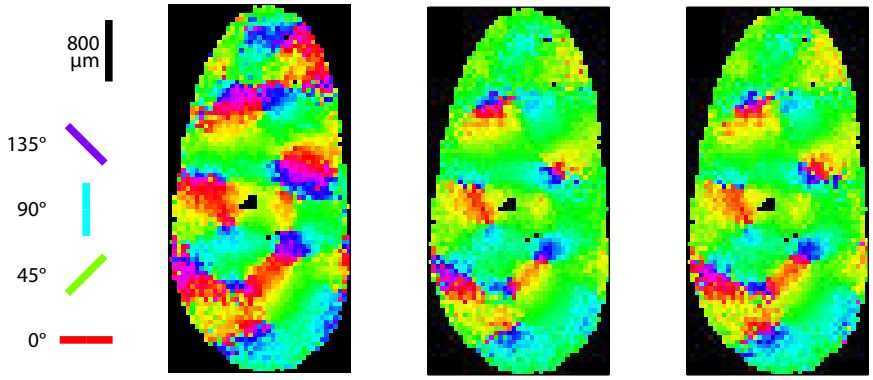

(a) Without the normalization (14).

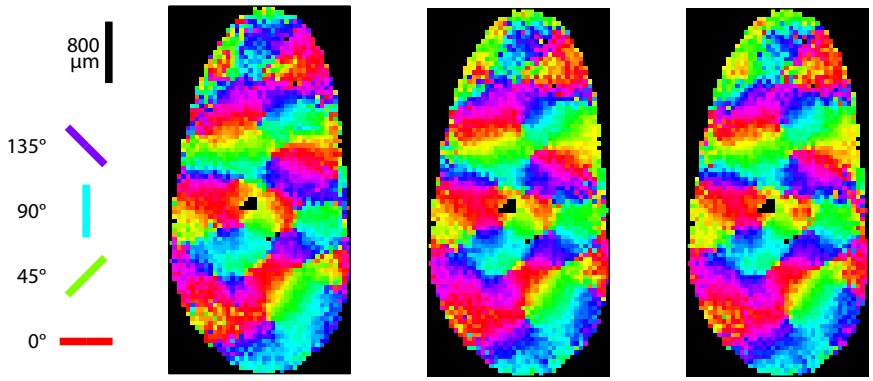

(b) With the normalization (14).

Figure 7: Resulting orientation angle maps Θ, computed with vectorial sum technique according to (15) and (16). The preferred orientation at each pixel is color coded in a circular color map; the colors corresponding to the four orientations of the stimuli used in the protocol `Cat_Gratings` are represented on the left side.

angle $\Theta \overset{\text{def}}{=} \left(\vartheta_p\right)_{1\leq p\leq P}$. The amplitude carries some interesting information about the overall response level and sharpness of orientation selectivity, but we do not use it in the current study.

3.2.4 Results

Resulting orientation angle maps are displayed on figure Figure 7. Observe first the apparent need for the normalization described in (14): on all three panels of Figure 7(a), preferred orientations around 60° are largely dominant; in contrast, the distribution of preferred orientations on Figure 7(b) is well balanced. This phenomenon appears very similar for both GLM and SMCS methods, and seems less pronounced with BkS denoising; we do not know the reason for that.

Now, after applying the normalization, the resulting orientation maps are in accordance with the literature. In particular (see Bonhoeffer and Grinvald (1993)), we observe

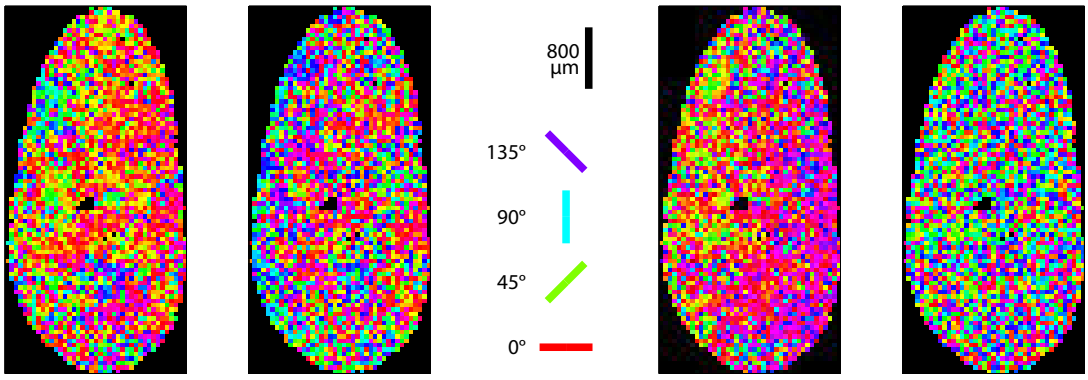

(a) Bias on periodic artifacts. (b) Bias on residuals.

Figure 8: Orientation bias due to the presence of stimulus-related neuronal signal within non neuronal components, for the separations provided by GLM and SMCS methods. Those maps are computed as orientation angle maps but with non neuronal components. Note that normalization (14) makes no sense here, so it is not applied.

a smooth variation of the preferred orientation along the cortical surface, covering the whole orientation space within a characteristic distance of approximately 1 mm, and organized around *pinwheels*, which are locations at the confluence of homogeneous area, around which all orientations are represented.

The three compared denoising methods lead to almost undistinguishable orientation angle maps. This suggests that, in spite of a strong denoising and very few priors over the neuronal signal, SMCS succeeds in capturing orientation selective information. In order to test further this fact, we then check for the presence of stimulus-related signals within other components of the separation. To do so, we apply exactly the same computations of preferred orientations as above, but using the periodic artifacts or the residual instead of the neuronal activity component. In the hypothesis that no stimulus-related signals are present, resulting maps should be meaningless, with random distribution of preferred orientations. On Figure 8(a), areas with dominant preferred orientations are visible, at the same spatial scale as the homogeneous areas in the orientation maps of Figure 7. This proves that stimulus-related neural signal has been captured by the periodic artifacts during the process of component separation. Such bias seems weaker for the SMCS method, probably thanks to the hard constraints on the amplitudes of periodic artifacts (recall § II.3.4.2), which prohibit stronger periodic artifacts in acquisitions with stimulus conditions than in blank acquisitions. Now, the orientation bias on the residuals found by SMCS, Figure 8(b), appears to be completely random. Keep in mind that there still could be neuronal signal left out in the residual, like spontaneous activity or even evoked activity over short periods of time, but this is an encouraging result for our method.

In contrast, the residual found by GLM is strongly biased by the stimulus condition; this was however already expected, and constitutes an additional argument for merging the residual with the neuronal activity component when using a GLM approach.

4 Propagations in the Mouse's Somatosensory Cortex

In a last series of experiments, we explore visually the application of our method to VSDOI recordings of the mouse's somatosensory cortex. Observation of propagating phenomenon have been reported in both awake and anesthetized animals, in response to direct sensory inputs as well as in ongoing neuronal activity, see in particular Ferezou *et al.* (2006).

The data set `Mouse_All` consists in 1 024 ms long recordings of the somatosensory cortex of a single mouse, in the barrel cortex. In the stimulus condition, all the animal's whiskers are briefly and simultaneously deflected, evoking a large raise of neuronal activity, first localized and then spreading rapidly to the entire recorded area (Figure 9(b)). We apply our method to nine recordings with stimulus condition. Moreover, out of twenty blank acquisitions considered, nine presented strong patterns of spontaneous activity, closely resembling the evoked propagations.

The neuronal activity patterns in those data are large, and their overall shape is distinguishable after simple normalization of the raw data by an estimation of the gain (Figure 9(a) or Figure 10(a)). However, the level of high frequency noise is also important, and periodic artifacts are clearly visible. We apply the SMCS methods with the same parameters as in our synthetic data setting, § 2.2.2, except for $K_B \overset{\text{set}}{=} 3$, *i.e.* we model the bleaching with two decreasing exponentials (we find $\mathcal{T} = \{245\,\text{ms}, 5\,576\,\text{ms}\}$).

4.1 Stimulus Condition Acquisitions

We show on Figure 9(b)-(d) the denoising of a single trial, at some spatial positions and time frames of interest. We see that the high frequency noise has been well removed, except perhaps right after stimulus onset ($t_{\text{on}} \overset{\text{set}}{=} 200$ ms, see that the amplitudes of R are smaller on frames 210 ms and 240 ms). Indeed, the activity here is so reproducible that the wavelets capturing the neuronal events occurring over this short time window are not penalized (see second part of § VI.2.8).

Moreover, a substantial part of the periodic artifacts seems to have been removed as well. Consider in particular the green pixel on Figure 9(c), whose time course is affected by consequent heartbeat artifacts, because it is located right over a vein crossing the field of view. However, remaining influence of the veins is still significant on (b), see in particular the first frame, 70 ms: the neuronal activity component has captured periodic artifacts. This is in fact impossible to avoid completely, since we are seeking for *any*

Figure 9, *opposite*, and Figure 10, on page 197: Component separation results for `Mouse_All`, for stimulus condition and spontaneous activity, respectively. The time courses correspond to spatial positions indicated on the frames by a square of the same color. Vertical dashed line indicates stimulus onset, when present. (a) Observations normalized by the estimated gain, single trial. (b) Neuronal activity, single trial. (c) Periodic artifacts, single trial. (d) Residual, single trials. (d) Neuronal activity, average across trials, single trials in transparency.

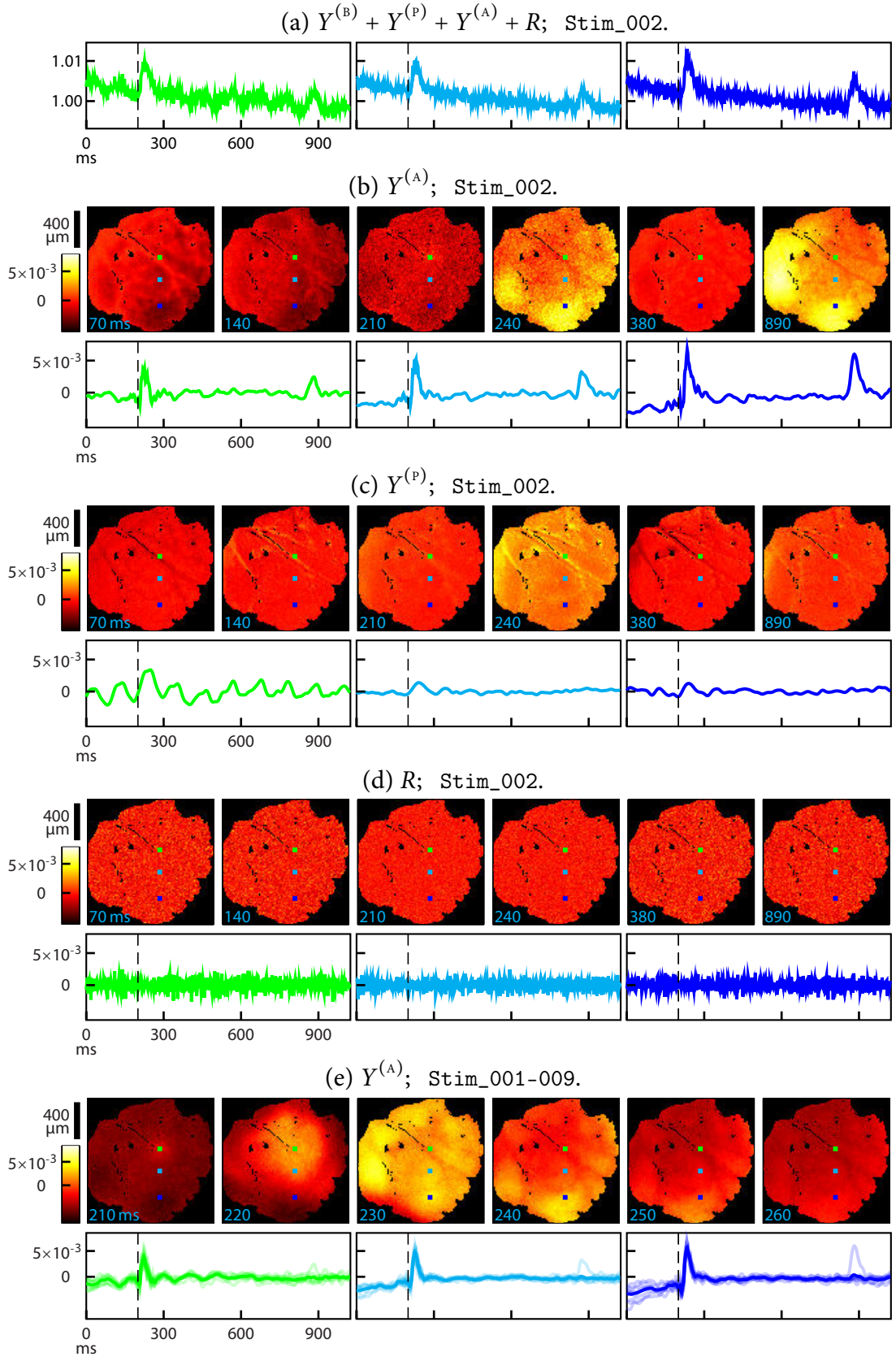

Figure 9: `Mouse_All` data, stimulus conditions. See *opposite*.

possible spatiotemporal neuronal activity, on data that are *not* synchronized with the heartbeat of the animal (see § VI.2.8).

More worrisome, the confusion happens also the other way around. Indeed, each temporal trace of (c) is biased upwards just after stimulus onset; and the overall amplitude is higher on frame 240 ms than on the others. We believe that such loss of signal of interest is not a flaw of the SMCS approach itself, and could be prevented by finer tuning of the parameters. Indeed, on the trial presented on (b) and (c), observe that a second, spontaneous neuronal propagation occurs (peaking around 890 ms), with almost no influence on the periodic artifacts component. This last feature is of particular interest to us, regarding our attempt to capture inter-trial variability. Even though the trial was processed for reproducible, evoked activity, our method was able to extract a significant neuronal event without prior knowledge of it.

4.2 Spontaneous Activity

This last observation motivates the screening of blank acquisitions for spontaneous activity. As described in § VI.2.3, after the first bleaching approximation on blank acquisitions, we put apart those presenting obvious patterns of spontaneous activity, for two reasons. First, they might bias the estimation of the periodic artifacts amplitude, what will impact the processing of the stimulus condition acquisitions. Second, we can actually apply the SMCS method to extract spontaneous activity from noise and artifacts, at the single trial level.

On Figure 9, (e) looks like a cleaner version of (b) (compare frames 210 and 240 ms), for the hundred milliseconds following the stimulus onset: the spread of activity arise from the same spatial location, with the same delay, and similar amplitude.

In contrast, spontaneous activity can only be observed at the single trial level. As shown in Figure 10(b) the SMCS method performs as well for spontaneous activity as for evoked activity (note again, however, that some neuronal signal has been captured by the periodic artifacts component). On that trial, the activity does not originates from the same locations as the above evoked activity, neither does it occurs at the same time. For that reason, after averaging over only nine blank acquisitions, individual neuronal events are almost indistinguishable on (e).

5 Discussion and Perspectives

5.1 Assessment of the Model

As expected by considering Chapter I, the SMCS model appears rather well adapted to VSDOI data. It seems general enough for processing various data sets, obtained with different experimental set-ups, over different subjects, to investigate different phenomenon. Of course, the results presented here should be completed by study from other data sets and by investigating more complex cortical functional properties. In particular, the direct next step is the exploration of the longer acquisitions in `Cat_Long`, and the analysis of functional properties of the propagations in `Mouse_Single`.

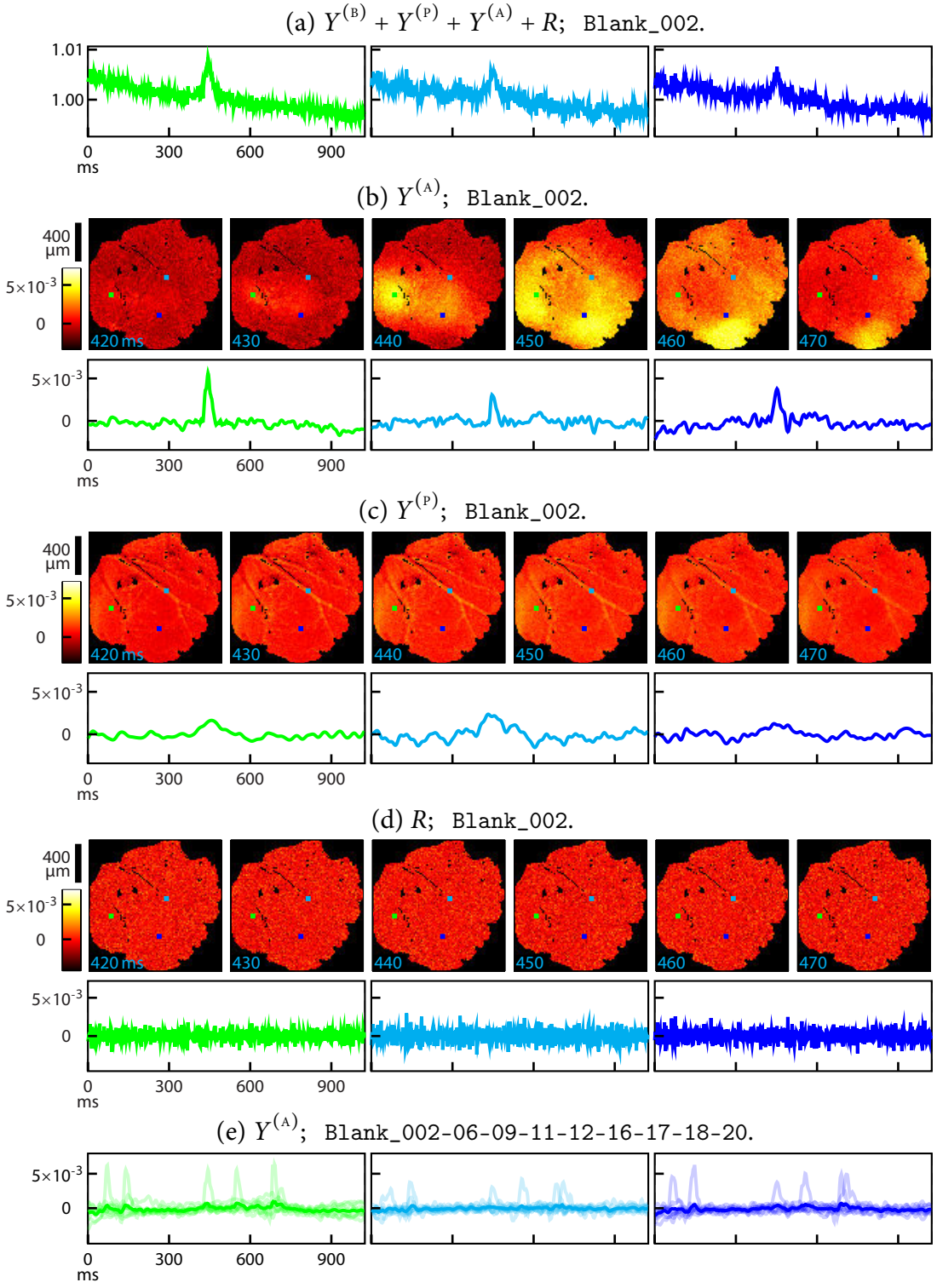

Figure 10: Mouse_All data, spontaneous activity. See bottom of page 194.

The first results presented here are already informative concerning the use of VSDOI *in-vivo*. As we have seen in § 1, it is clear to us that the high frequency fluctuations are dominated by noise, which should be removed prior to fine analysis of VSDOI data. Averaging acquisitions across trials is usually the best way to do it, but this prevents analysis of trial-to-trial variability, as illustrated in § 4.2. Moreover, simple linear smoothing of the data is not an option to us, since many sharp features of the signal would be lost. All those arguments are in favor of a complex, nonlinear model such as the SMCS.

However, the difficulty of the problem at hand makes it necessary to enforce as many priors one can have on the signal; this plays against a method aiming to be general. As far as we can tell from the above results, the wavelet sparsity of the signal is a good prior for VSDOI, allowing in particular adaptive removal of the noise. In addition, it can also separate the neuronal signal from periodic artifacts in many instances but this does not seem very robust. This task is actually what renders the whole method described in Chapter VI so complex, but we believe that it can still be improved.

In particular the very definition of the periodic artifacts component is vague, especially since neuronal activity is known to present oscillatory behaviors at various frequencies. In addition, important information over those artifacts is learnt from the blank acquisitions, which might themselves contains important neuronal signals, which would in turn be considered as artifacts later on. For those reasons, we insist on the need of our method for clean blank acquisitions, and that synchronizing acquisitions with heartbeat and respiration is useful. Note that the real data tested here are recorded on anesthetized animals, and this last inconvenient might reveal worst in acquisitions on awake animals.

Finer study of what actually lies in the periodic artifacts (notably according to the frequency range) should also be considered. This could be done either simply by looking for spatio-temporal patterns (as veins over the field of view) or by testing for functional bias (as we did with orientation selectivity, see Figure 8).

5.2 Practical Use of the Method

Until now, we made few mentions of the practical difficulty of applying the SMCS model to VSDOI data. The most important aspect is the computational load. It is hard to quantify, since it depends on the size of the data, (the number of pixels in the ROI, the number of time frames, the number of blank (b) and stimulus condition (s) acquisitions), on some parameters of the method (the size of the penalization blocks, the level of wavelet decomposition), and, more importantly, on the machine running it.

Our implementation of the minimization problems uses OpenMP specifications, so that it can profits from several clusters running in parallel. Consider that on the *Wave* computing server mentioned in the introduction (sixteen cores of 1.6 GHz), the ten blank and eighty stimulus condition acquisitions of `Cat_Gratings` could be processed in less than 24 h. In contrast, in order to process a full acquisition of `Mouse_All`, a complete hour is necessary, and since it requires more than 4 GB of RAM, many personal computers simply cannot handle it.

For those reasons, it is important to design a final method which is as automatic as

possible, so that it does not necessitate user input during processing. This is a strong limitation; as suggested along this chapter, in most situations, there exists parameters for which the SMCS model would yield excellent results, but they cannot be set by trial-and-error.

Appendix

A Experimental Protocols

A.1 Cat Visual Cortex

These data were acquired by Cyril Monier at the UNIC laboratory; the following description of the experimental set-up can be found in Yavuz (2012).

Set-up. Acquisition, visual stimulation and preliminary online analysis was controlled by the Elphy software, communicating with the acquisition program provided by the imaging system. A CMOS MiCam camera was used, providing 100×100 pixel resolution and up to 10 kHz temporal resolution. The recording was performed at 200 Hz temporal resolution in order to obtain a better sampling of the emitted photons. One pixel in the recording corresponds approximately to 60 × 60 μm^2 of cortical sheet.

Animal preparation. VSDOI was performed on an adult cat. Data were recorded on only one hemisphere, over area 18. The animal was initially anesthetized with intravenous alfaxolone (10 $mg.kg^{-1}$). Following tracheotomy, the animal was kept under artificially respiration and anesthetized with 1-1.5 % (0.6-1 % during recording) isofluorane gas added to the 1:1 N_2O and O_2 mixture. Minimum alveolar concentration was kept above 1 %. The animal was head fixed on the anti-vibration table. The skull was opened above areas 17 and 18 (the size of the craniotomy was approximately 1.5 cm in diameter), and the dura was resected. Paralysis was maintained by pancuronium bromide (0.4 $mg.kg^{-1}.h^{-1}$, intravenous) administered starting less than three hours before imaging in order to abolish eye movements. Accommodation and pupil contraction was blocked by atropine and neosynephrine. Artificial pupils of 3 mm were used and appropriate corrective optical lenses were added when necessary. The position of the area *centralis* of each eye was projected on the screen with light source before and after imaging. Respiration was controlled by an external pump. Electrocardiogram (ECG), expired CO_2, and body temperature were continuously monitored during the experiment. Image acquisition was synchronized with ECG and respiration signals, in order to provide synchronization of the corresponding oscillatory artifacts. For applying the dye on the cortex, a stainless-steel chamber was mounted on the skull over an area which includes areas 17 and 18 of both hemispheres. The cortex was stained for 2.5-3 h with

the oxonol dye RH1691, and unbound dye was washed out after staining. The chamber was then filled with CSF-saline or silicone oil and closed.

Visual stimulation (`Cat_Gratings`). In order to map orientation response on the cortex, full-field drifting grating stimulations were used. The protocol included gratings of four possible orientations, spanning all the orientation domain, and drifting in two possible directions. Stimuli consists in 100 % contrast gratings of 0.2-0.6 cycles per degree, drifting at 2-6Hz temporal frequency. They were pseudo-randomly interleaved with recording epochs during which the screen was blank. Each stimulus was presented for 300-500ms, while the recording duration of each trial was 1 280 ms long. The stimuli were presented full-field on a 22″ CRT monitor placed 57 cm away from the eyes of the animal, at a refresh rate of 150 Hz.

A.2 Mouse Somatosensory Cortex

Those data were acquired by Isabelle Férézou at the ESPCI ParisTech and UNIC laboratories.

Set-up. The voltage-sensitive dye was excited with 630 nm light from a 100 W halogen lamp gated by a Uniblitz shutter (Vincent Associates) under computer control via an ITC-18 (Instrutech) communicating with custom software running within IgorPro (Wavemetrics). The excitation light was reflected using a 650 nm dichroic and focused onto the cortical surface with a 25 mm video lens (Navitar). Fluorescence was collected via the same optical pathway, but without reflection of the dichroic, long-pass filtered at 665 nm, and focused onto the sensor of a high-speed MiCam Ultima (Scimedia) camera via a 135 mm camera lens (Nikon).

Animal preparation. Mice aged one to five months were anesthetized with either urethane (1.5 $mg.g^{-1}$) or isoflurane (1.5 %). Paw withdrawal, whisker movement, and eyeblink reflexes were largely suppressed. A heating blanket maintained the rectally measured body temperature at 37 °C. The head of the mouse was fixed by a nose clamp. The skin overlying the somatosensory cortex was removed and the bone gently cleaned. A 2×2 mm^2 craniotomy was made, centered on the location of the C2 barrel column. Extreme care was taken at all times not to damage the cortex, especially during the removal of the dura. Voltage-sensitive dye RH1691 was dissolved at 1 $mg.mL^{-1}$ in Ringer's solution containing the following (in mM): 135 NaCl, 5 KCl, 5 HEPES, 1.8 $CaCl_2$, and 1 $MgCl_2$. This dye solution was topically applied to the exposed cortex and allowed to diffuse into the cortex over 1 h. The cortex was subsequently washed to remove unbound dye. The cortex was then sealed by gluing on a glass coverslip which was in direct contact with the cortical surface.

Whisker stimulation. 2 ms-long deflections of a C2 whisker were generated with help of a computer-controlled piezoelectric bimorph. Trials were imaged alternatively with and without stimulus delivered to the C2 whisker.

References

G. G. Blasdel and G. Salama. Voltage-sensitive dyes reveal a modular organization in monkey striate cortex. *Nature*, 321(6070):579–585, 1986.

T. Bonhoeffer and A. Grinvald. The layout of iso-orientation domains in area 18 of cat visual cortex: Optical imaging reveals a pinwheel-like organization. *The Journal of Neuroscience*, 13(10):4157–4180, 1993.

F. Chavane, D. Sharon, D. Jancke, O. Marre, Y. Frégnac, and A. Grinvald. Lateral spread of orientation selectivity in v1 is controlled by intracortical cooperativity. *Frontiers in Systems Neuroscience*, 5(4):1–26, 2011.

I. Daubechies. *Ten Lectures on Wavelets*. Society for Industrial and Applied Mathematics, 1992.

G. Deco, V. K. Jirsa, P. A. Robinson, M. Breakspear, and K. Friston. The dynamic brain: from spiking neurons to neural masses and cortical fields. *PLoS Computational Biology*, 4(8):e1000092, 2008.

I. Ferezou, S. Bolea, and C. C. H. Petersen. Visualizing the cortical representation of whisker touch: Voltage-sensitive dye imaging in freely moving mice. *Neuron*, 50(4): 617–629, 2006.

A. Grinvald, D. Shoham, A. Shmuel, D. Glaser, I. Vanzetta, E. Shtoyerman, H. Slovin, C. Wijnbergen, R. Hildesheim, and A. Arieli. In-vivo optical imaging of cortical architecture and dynamics. In *Modern Techniques in Neuroscience Research*, pages 893–969. Springer, 1999.

D. H. Hubel and T. N. Wiesel. Receptive fields of single neurons in the cat's striate cortex. *The Journal of Physiology*, 148(3):574–591, 1959.

D. Jancke, F. Chavane, S. Naaman, and A. Grinvald. Imaging cortical correlates of illusion in early visual cortex. *Nature*, 428(6981):423–426, 2004.

V. B. Mountcastle. The columnar organization of the neocortex. *Brain*, 120(4):701–722, 1997.

A. Reynaud, S. Takerkart, G. S. Masson, and F. Chavane. Linear model decomposition for voltage-sensitive dye imaging signals: application in awake behaving monkey. *NeuroImage*, 54(2):1196–1210, 2011.

D. Sharon and A. Grinvald. Dynamics and constancy in cortical spatiotemporal patterns of orientation processing. *Science*, 295(5554):512–515, 2002.

E. Yavuz. *Source separation analysis of visual cortical dynamics revealed by voltage sensitive dye imaging*. PhD thesis, École doctorale Cerveau, Cognition et Comportement (Paris), 2012.

Conclusion

This thesis is an in-depth exploration of mathematical tools motivated by a specific, practical purpose: improving the extraction of neuronal signal in voltage-sensitive dye optical imaging. This leads us to various developments, theoretical as well as computational, reflecting the challenges of interdisciplinarity, which is the *raison d'être* of applied mathematics.

Our inspection of the literature in biology, described along Chapter I, suggests a components mixture model, which is as simple as the resulting component separation problem is difficult. In an attempt to capture a wide range of possible spatiotemporal dynamics, we recast in Chapter II the inverse problem as an underdetermined linear problem, for which we adapt many popular regularizations in signal processing, in particular sparsity enforcing penalizations.

For solving the resulting variational problem, we have to drift towards more abstract convex analysis considerations in Chapter III, in order to develop a state-of-the-art first-order primal proximal splitting algorithm suitable to our purpose. We show then in Chapter IV the relevance of the tools developed so far for many other tasks, in signal processing and beyond.

Despite the improvement over existing algorithms, the cost for solving the component separation problem still justifies the development of methods allowing to select the parameters tuning the model without many calls to the complete separation algorithm. In that context, we report in Chapter V our work around Stein's unbiased risk estimate for selecting parameters of denoising estimators which are computed by proximal splitting algorithms.

Out of concerns for generality, we endeavor to formulate our results independently from our primary motivation, so that they apply to virtually any signal processing problem. We believe that the contributions in Chapters II to V are useful to the signal processing community, improving in the same time theoretical foundations and practical efficiency of popular approaches.

Last but not least, we describe in Chapter VI a step-by-step method enabling the application of the above work to real voltage-sensitive dye optical imaging data, detailing notably the crucial assumptions on which our final method relies. Its potential is subsequently evaluated from preliminary model validations and results in Chapter VII; at this occasion, it is necessary to perform some functional analysis and confront our observations to the neuroscientific literature of voltage-sensitive dye optical imaging.

The first results are encouraging, but signal processing for voltage-sensitive dye optical imaging, especially *in-vivo*, is still an ongoing research. In our perspective, we are presented with two main directions. First, we believe that simplifications and modifications of our method remain to be done, in order to correct its most obvious flaws and eventually make a public release for direct use by biologists. In parallel, revealing new insights about the functional cortical mechanisms seems mandatory for assessing the method, and this cannot be properly achieved without a more profound understanding of the functional cortical mechanisms.

*

* *

Bibliography

C. D. Acker, P. Yan, and L. M. Loew. Single-voxel recording of voltage transients in dendritic spines. *Biophysical Journal*, 101(2):L11–L13, 2011.

F. Acker and M. A. Prestel. Convergence d'un schéma de minimisation alternée. *Annales de la faculté des sciences de Toulouse*, 5,2(1):1–9, 1980.

M. V. Afonso, J. M. Bioucas-Dias, and M. A. T. Figueiredo. Fast image recovery using variable splitting and constrained optimization. *IEEE Transactions on Image Processing*, 19(9):2345–2356, 2010.

L. Ambrosio, N. Fucso, and D. Pallara. *Functions of Bounded Variation and Free Discontinuity Problems*. Oxford Mathematical Monographs. Oxford University Press, 2000.

A. Arieli, D. Shoham, R. Hildesheim, and A. Grinvald. Coherent spatiotemporal patterns of ongoing activity revealed by real-time optical imaging coupled with single-unit recording in the cat visual cortex. *Journal of Neurophysiology*, 73(5):2072–2093, 1995.

A. Arieli, A. Sterkin, A. Grinvald, and A. Aertsen. Dynamics of ongoing activity: Explanation of the large variability in evoked cortical responses. *Science*, 273(5283): 1868–1871, 1996.

K. J. Arrow, L. Hurwicz, and H. Uzawa. *Studies in linear and nonlinear programming*. Stanford University Press, 1958.

H. Attouch, L. M. Briceño-Arias, and P. L. Combettes. A parallel splitting method for coupled monotone inclusions. *SIAM Journal on Control and Optimization*, 48(5): 3246–3270, 2010.

J.-B. Baillon and G. Haddad. Quelques propriétés des opérateurs angle-bornés et n-cycliquement monotones. *Israel Journal of Mathematics*, 26(2):137–150, 1977.

H. H. Bauschke and P. L. Combettes. *Convex Analysis and Monotone Operator Theory in Hilbert Spaces*. Springer, New York, NY, USA, 2011.

H. H. Bauschke, P. L. Combettes, and S. Reich. The asymptotic behavior of the composition of two resolvents. *Nonlinear Analysis: Theory, Methods and Applications*, 60(2): 283–301, 2005.

A. Beck and M. Teboulle. A fast iterative shrinkage-thresholding algorithm for linear inverse problems. *SIAM Journal on Imaging Sciences*, 2(1):183–202, 2009.

A. Beck and M. Teboulle. A fast dual proximal gradient algorithm for convex minimization and applications. *Operations Research Letters*, 42(1):1–6, 2014.

A. Ben-Tal and A. S. Nemirovski. *Lectures on modern convex optimization: analysis, algorithms, and engineering applications*. Society for Industrial and Applied Mathematics, Philadelphia, PA, USA, 2001.

G. G. Blasdel and G. Salama. Voltage-sensitive dyes reveal a modular organization in monkey striate cortex. *Nature*, 321(6070):579–585, 1986.

T. Blu and F. Luisier. The SURE-let approach to image denoising. *IEEE Transactions on Image Processing*, 16(11):2778–2786, 2007.

J. Bobin, J.-L. Starck, Y. Moudden, and J. M. Fadili. Blind source separation: The sparsity revolution. volume 152 of *Advances in Imaging and Electron Physics*, chapter 5, pages 221–302. Elsevier, 2008.

T. Bonhoeffer and A. Grinvald. The layout of iso-orientation domains in area 18 of cat visual cortex: Optical imaging reveals a pinwheel-like organization. *The Journal of Neuroscience*, 13(10):4157–4180, 1993.

S. Boyd and L. Vandenberghe. *Convex Optimization*. Cambridge University Press, New York, NY, USA, 2004.

K. Bredies and D. A. Lorenz. Linear convergence of iterative soft-thresholding. *Journal of Fourier Analysis and Applications*, 14(5-6):813–837, 2008.

L. M. Briceño-Arias and P. L. Combettes. Convex variational formulation with smooth coupling for multicomponent signal decomposition and recovery. *Numerical Mathematics: Theory, Methods and Applications*, 2(4):485–508, 2009.

L. M. Briceño-Arias and P. L. Combettes. A monotone+skew splitting model for composite monotone inclusions in duality. *SIAM Journal on Optimization*, 21(4):1230–1250, 2011.

L. M. Briceño-Arias, P. L. Combettes, J.-C. Pesquet, and N. Pustelnik. Proximal algorithms for multicomponent image recovery problems. *Journal of Mathematical Imaging and Vision*, 41(1-2):3–22, 2011.

C. Caballero-Gaudes, N. Petridou, S. T. Francis, I. L. Dryden, and P. A. Gowland. Paradigm free mapping with sparse regression automatically detects single-trial functional magnetic resonance imaging blood oxygenation level dependent responses. *Human Brain Mapping*, 34(3):501–518, 2013.

T. T. Cai. Adaptive wavelet estimation: a block thresholding and oracle inequality approach. *The Annals of Statistics*, 27(3):898–924, 1999.

E. J. Candès, M. B. Wakin, and S. P. Boyd. Enhancing sparsity by reweighted ℓ_1 minimization. *Journal of Fourier Analysis and Applications*, 14(5):877–905, 2008.

S. Chakraborty, A. Sandberg, and S. A. Greenfield. Differential dynamics of transient neuronal assemblies in visual compared to auditory cortex. *Experimental Brain Research*, 182(4):491–498, 2007.

A. Chambolle and T. Pock. A first-order primal-dual algorithm for convex problems with applications to imaging. *Journal of Mathematical Imaging and Vision*, 40(1): 120–145, 2011.

A. Chambolle, S. Levine, and B. Lucier. Some variations on total variation–based image smoothing. 2009. URL http://hal.archives-ouvertes.fr/hal-00370195.

A. Chambolle, V. Caselles, D. Cremers, M. Novaga, and T. Pock. An introduction to total variation for image analysis. *Theoretical Foundations and Numerical Methods for Sparse Recovery*, 9:263–340, 2010.

C. Chaux, A. Benazza-Benyahia, and J.-C. Pesquet. A block-thresholding method for multispectral image denoising. In *Proceedings SPIE*, volume 5914, pages 59141H–13, 2005.

C. Chaux, P. L. Combettes, J.-C. Pesquet, and V. R. Wajs. A variational formulation for frame based inverse problems. *Inverse Problems*, 23(4):1495–1518, 2007.

C. Chaux, L. Duval, A. Benazza-Benyahia, and J.-C. Pesquet. A nonlinear Stein-based estimator for multichannel image denoising. *IEEE Transactions on Signal Processing*, 56(8):3855–3870, 2008.

C. Chaux, J.-C. Pesquet, and N. Pustelnik. Nested iterative algorithms for convex constrained image recovery problems. *SIAM Journal on Imaging Sciences*, 2(2):730–762, 2009.

F. Chavane, D. Sharon, D. Jancke, O. Marre, Y. Frégnac, and A. Grinvald. Lateral spread of orientation selectivity in v1 is controlled by intracortical cooperativity. *Frontiers in Systems Neuroscience*, 5(4):1–26, 2011.

S. Chemla and F. Chavane. A biophysical cortical column model to study the multicomponent origin of the VSDI signal. *NeuroImage*, 53(2):420–438, 2010a.

S. Chemla and F. Chavane. Voltage-sensitive dye imaging: Technique review and models. *Journal of Physiology Paris*, 104(1-2):40–50, 2010b.

G. Chen and M. Teboulle. A proximal-based decomposition method for convex minimization problems. *Mathematical Programming*, 64(1-3):81–101, 1994.

G. H.-G. Chen and R. T. Rockafellar. Convergence rates in forward–backward splitting. *SIAM Journal on Optimization*, 7(2):421–444, 1997.

S. S. Chen, D. L. Donoho, and M. A. Saunders. Atomic decomposition by basis pursuit. *SIAM Journal on Scientific Computing*, 20(1):33–61, 1998.

Xi Chen, Qihang Lin, Seyoung Kim, Jaime G. Carbonell, and Eric P. Xing. Smoothing proximal gradient method for general structured sparse regression. *The Annals of Applied Statistics*, 6(2):719–752, 2012.

Y. Chen, W. S. Geisler, and E. Seidemann. Optimal temporal decoding of neural population responses in a reaction-time visual detection task. *Journal of Neurophysiology*, 99(3):1366–1379, 2008.

C. Chesneau, J. M. Fadili, and J.-L. Starck. Stein block thresholding for image denoising. *Applied and Computational Harmonic Analysis*, 28(1):67–88, 2010.

L. B. Cohen, B. M. Salzberg, H. V. Davila, W. N. Ross, D. Landowne, A. S. Waggoner, and C. H. Wang. Changes in axon fluorescence during activity: molecular probes of membrane potential. *Journal of Membrane Biology*, 19(1):1–36, 1974.

P. L. Combettes. Solving monotone inclusions via compositions of nonexpansive averaged operators. *Optimization*, 53(5-6):475–504, 2004.

P. L. Combettes. Iterative construction of the resolvent of a sum of maximal monotone operators. *Journal of Convex Analysis*, 16(4):727–748, 2009.

P. L. Combettes and J.-C. Pesquet. A Douglas-Rachford splitting approach to nonsmooth convex variational signal recovery. *IEEE Journal of Selected Topics in Signal Processing*, 1(4):564–574, 2007.

P. L. Combettes and J.-C. Pesquet. A proximal decomposition method for solving convex variational inverse problems. *Inverse Problems*, 24(6):065014, 2008.

P. L. Combettes and J.-C. Pesquet. *Proximal Splitting Methods in Signal Processing*, volume 49 of *Optimization and Its Applications*, chapter 10, pages 185–212. Springer, New York, NY, USA, 2011.

P. L. Combettes and J.-C. Pesquet. Primal-dual splitting algorithm for solving inclusions with mixtures of composite, Lipschitzian, and parallel-sum monotone operators. *Set-Valued and Variational Analysis*, 20(2):307–330, 2012.

P. L. Combettes and V. R. Wajs. Signal recovery by proximal forward-backward splitting. *SIAM Multiscale Modeling and Simulation*, 4(4):1168, 2005.

P. L. Combettes, D. Dũng, and B. C. Vũ. Dualization of signal recovery problems. *Set-Valued and Variational Analysis*, 18:373–404, 2010.

L. Condat. A primal–dual splitting method for convex optimization involving lipschitzian, proximable and linear composite terms. *Journal of Optimization Theory and Applications*, 158(2):460–479, 2013.

I. Daubechies. *Ten Lectures on Wavelets*. Society for Industrial and Applied Mathematics, 1992.

I. Daubechies, M. Defrise, and C. De Mol. An iterative thresholding algorithm for linear inverse problems with a sparsity constraint. *Communications on Pure and Applied Mathematics*, 57(11):1413–1541, 2004.

H. V. Davila, B. M. Salzberg, L. B. Cohen, and A. S. Waggoner. A large change in axon fluorescence that provides a promising method for measuring membranepotential. *Nature New Biology*, 241(109):159–160, 1973.

G. Deco, V. K. Jirsa, P. A. Robinson, M. Breakspear, and K. Friston. The dynamic brain: from spiking neurons to neural masses and cortical fields. *PLoS Computational Biology*, 4(8):e1000092, 2008.

C.-A. Deledalle, V. Duval, and J. Salmon. Non-local methods with shape-adaptive patches (NLM-SAP). *Journal of Mathematical Imaging and Vision*, 43(2):103–120, 2012a.

C.-A. Deledalle, S. Vaiter, G. Peyré, J. M. Fadili, and C. Dossal. Proximal splitting derivatives for risk estimation. *Journal of Physics: Conference Series*, 386(1):012003, 2012b.

C.-A. Deledalle, S. Vaiter, G. Peyré, and J. M. Fadili. Stein Unbiased GrAdient estimator of the Risk (SUGAR) for multiple parameter selection. 2014. URL http://hal.archives-ouvertes.fr/hal-00987295.

A. Destexhe and M. Rudolph-Lilith. *Neuronal Noise*. Number 8 in Computational Neuroscience. Springer, 2012.

F. Deutsch. *Best Approximation in Inner Product Spaces*. CMS Books in Mathematics. Springer, New York, NY, USA, 2001.

D. L. Donoho and I. M. Johnstone. Ideal spatial adaptation by wavelet shrinkage. *Biometrika*, 81(3):425–455, 1994.

D. L. Donoho and I. M. Johnstone. Adapting to unknown smoothness via wavelet shrinkage. *Journal of the American Statistical Association*, 90(432):1200–1224, 1995.

C. Dossal, M. Kachour, J. M. Fadili, G. Peyré, and C. Chesneau. The degrees of freedom of penalized ℓ_1 minimization. *Statistica Sinica*, 23(2):809–828, 2013.

J. Douglas and H. H. Rachford. On the numerical solution of heat conduction problems in two and three space variables. *Transactions of the American Mathematical Society*, 82(2):421–439, 1956.

F.-X. Dupé, J. M. Fadili, and J.-L. Starck. A proximal iteration for deconvolving Poisson noisy images using sparse representations. *IEEE Transactions on Image Processing*, 18 (2):310–321, 2009.

F.-X. Dupé, J. M. Fadili, and J.-L. Starck. Inverse problems with Poisson noise: Primal and primal-dual splitting. In *International Conference on Image Processing*, pages 1901–1904, 2011.

F.-X. Dupé, J. M. Fadili, and J.-L. Starck. Linear inverse problems with various noise models and mixed regularizations. In *First International Workshop on New Computational Methods for Inverse Problems*, 2011.

F.-X. Dupé, J. M. Fadili, and J.-L. Starck. Deconvolution under Poisson noise using exact data fidelity and synthesis or analysis sparsity priors. *Statistical Methodology*, 9(1-2): 4–18, 2012.

V. Duval, J.-F. Aujol, and Y. Gousseau. A bias-variance approach for the non-local means. *SIAM Journal on Imaging Sciences*, 4(2):760–788, 2011.

J. Eckstein. Parallel alternating direction multiplier decomposition of convex programs. *Journal of Optimization Theory and Applications*, 80(1):39–62, 1994.

J. Eckstein and D. P. Bertsekas. On the Douglas-Rachford splitting method and the proximal point algorithm for maximal monotone operators. *Mathematical Programming*, 55(3):293–318, 1992.

J. Eckstein and B. F. Svaiter. General projective splitting methods for sums of maximal monotone operators. *SIAM Journal on Control and Optimization*, 48(2):787–811, 2009.

B. Efron. The estimation of prediction error. *Journal of the American Statistical Association*, 99(467):619–632, 2004.

Y. C. Eldar. Generalized SURE for exponential families: Applications to regularization. *Signal Processing, IEEE Transactions on*, 57(2):471–481, 2009.

L. C. Evans and R. F. Gariepy. *Measure Theory and Fine Properties of Functions*. Studies in Advanced Mathematics. Taylor & Francis, 1992.

J. M. Fadili and G. Peyré. Total variation projection with first order schemes. *IEEE Transactions on Image Processing*, 20(3):657–669, 2010.

J. M. Fadili, J.-L Starck, and F. Murtagh. Inpainting and zooming using sparse representations. *The Computer Journal*, 52(1):64–79, 2009.

I. Ferezou, S. Bolea, and C. C. H. Petersen. Visualizing the cortical representation of whisker touch: Voltage-sensitive dye imaging in freely moving mice. *Neuron*, 50(4): 617–629, 2006.

M. A. T. Figueiredo and J. M. Bioucas-Dias. Restoration of Poissonian images using alternating direction optimization. *IEEE Transactions on Image Processing*, 19(12): 3133–3145, 2010.

M. A. T. Figueiredo and R. Nowak. An EM algorithm for wavelet-based image restoration. *IEEE Transactions on Image Processing*, 12(8):906–916, 2003.

M. Fortin and R. Glowinski. *Augmented Lagrangian Methods: Applications to the Numerical Solution of Boundary-Value Problems*. Elsevier Science publishers, 1983.

G. J. Foschini, R. D. Gitlin, and J. Salz. Optimum direct detection for digital fiber-optic communication systems. *The Bell System Technical Journal*, 54(8):1389–1430, 1975.

J. Friedman, T. Hastie, H. Höfling, and R. Tibshirani. Pathwise coordinate optimization. *The Annals of Applied Statistics*, 1(2):302–332, 2007.

K. J. Friston, A. P. Holmes, K. J. Worsley, J. B. Poline, C. Frith, and R. S. J. Frackowiak. Statistical parametric maps in functional imaging: A general linear approach. *Human Brain Mapping*, 2(4):189–210, 1995.

R. D. Frostig, editor. *In Vivo Optical Imaging of Brain Function*. Frontiers in Neuroscience. CRC Press, 2nd edition, 2009.

D. Gabay. Applications of the method of multipliers to variational inequalities. In M. Fortin and R. Glowinski, editors, *Augmented Lagrangian Methods: Applications to the Numerical Solution of Boundary-value Problems*, pages 299–331. North-Holland Publishing Company, 1983.

D. Gabay and B. Mercier. A dual algorithm for the solution of nonlinear variational problems via finite element approximation. *Computers & Mathematics with Applications*, 2(1):17–40, 1976.

R. Giryes, M. Elad, and Y. C. Eldar. The projected GSURE for automatic parameter tuning in iterative shrinkage methods. *Applied and Computational Harmonic Analysis*, 30(3):407–422, 2011.

R. Glowinski and P. Le Tallec. *Augmented Lagrangian and Operator-Splitting Methods in Nonlinear Mechanics*. Society for Industrial and Applied Mathematics, 1989.

G. H. Golub, M. Heath, and G. Wahba. Generalized cross-validation as a method for choosing a good ridge parameter. *Technometrics*, 21(2):215–223, 1979.

R. Gribonval, H. Rauhut, K. Schnass, and P. Vandergheynst. Atoms of all channels, unite! average case analysis ofÂămulti-channel sparse recovery using greedy algorithms. *Journal of Fourier Analysis and Applications*, 14(5-6):655–687, 2008.

A. Grinvald and R. Hildesheim. VSDI: a new era in functional imaging of cortical dynamics. *Nature Reviews Neuroscience*, 5(11):874–885, 2004.

A. Grinvald, D. Shoham, A. Shmuel, D. Glaser, I. Vanzetta, E. Shtoyerman, H. Slovin, C. Wijnbergen, R. Hildesheim, and A. Arieli. In-vivo optical imaging of cortical architecture and dynamics. In *Modern Techniques in Neuroscience Research*, pages 893–969. Springer, 1999.

P. Hall, S. Penev, G. Kerkyacharian, and D. Picard. Numerical performance of block thresholded wavelet estimators. *Statistics and Computing*, 7(2):115–124, 1997.

B. He and X. Yuan. Convergence analysis of primal-dual algorithms for a saddle-point problem: From contraction perspective. *SIAM Journal on Imaging Sciences*, 5(1):119–149, 2012.

K. Holthoff, D. Zecevic, and A. Konnerth. Rapid time course of action potentials in spines and remote dendrites of mouse visual cortex neurons. *The Journal of Physiology*, 588(7):1085–1096, 2010.

J. Huang, S. Zhang, H. Li, and D. Metaxas. Composite splitting algorithms for convex optimization. *Computer Vision and Image Understanding*, 115(12):1610–1622, 2011.

D. H. Hubel and T. N. Wiesel. Receptive fields of single neurons in the cat's striate cortex. *The Journal of Physiology*, 148(3):574–591, 1959.

A. Hyvärinen and E. Oja. Independent component analysis: algorithms and applications. *Neural Networks*, 13(4-5):411–430, 2000.

S. Inagaki, T. Katura, H. Kawaguchi, and W. J. Song. Isolation of neural activities from respiratory and heartbeat noises for in vivo optical recording in guinea pigs using independent component analysis. *Neuroscience Letters*, 352(1):9–12, 2003.

D. Jancke, F. Chavane, S. Naaman, and A. Grinvald. Imaging cortical correlates of illusion in early visual cortex. *Nature*, 428(6981):423–426, 2004.

R. Jenatton, J.-Y. Audibert, and F. Bach. Structured variable selection with sparsity-inducing norms. *Journal of Machine Learning Research*, 12(oct):2777–2824, 2011.

R. Jenatton, A. Gramfort, V. Michel, G. Obozinski, E. Eger, F. Bach, and B. Thirion. Multiscale mining of fMRI data with hierarchical structured sparsity. *SIAM Journal on Imaging Sciences*, 5(3):835–856, 2012.

I. T. Jolliffe. *Principal Component Analysis*. Springer, New York, NY, USA, 2002.

F. I. Karahanoğlu, C. G. Caballero, F. Lazeyras, and D. Van De Ville. Total Activation: fMRI deconvolution through spatio-temporal regularization. *NeuroImage*, 73:121–134, 2013.

G. M. Korpelevich. An extragradient method for finding saddle points and for other problems. *Ekonomika i Matematicheskie Metody*, 12(4):747–756, 1976.

I. Lampl, I. Reichova, and D. Ferster. Synchronous membrane potential fluctuations in neurons of the cat visual cortex. *Neuron*, 22(2):361–374, 1999.

K.-C. Li. From Stein's unbiased risk estimates to the method of generalized cross validation. *The Annals of Statistics*, 13(4):1352–1377, 1985.

J. Liang, J. M. Fadili, and G. Peyré. Convergence rates with inexact nonexpansive operators. *preprint arXiv:1404.4837*, 2014.

E. H. Lieb and M. Loss. *Analysis*. CRM Proceedings & Lecture Notes. American Mathematical Society, 2001.

J. Lieutaud. *Approximation d'Opérateurs par des Méthodes de Décomposition*. PhD thesis, Université de Paris, 1969.

P.-L. Lions. Une méthode itérative de résolution d'une inéquation variationnelle. *Israel Journal of Mathematics*, 31(2):204–208, 1978.

P.-L. Lions and B. Mercier. Splitting algorithms for the sum of two nonlinear operators. *SIAM Journal on Numerical Analysis*, 16(6):964–979, 1979.

M. T. Lippert, K. Takagaki, W. Xu, X. Huang, and J. Y. Wu. Methods for voltage-sensitive dye imaging of rat cortical activity with high signal-to-noise ratio. *Journal of Neurophysiology*, 98(1):502–512, 2007.

J. Liu, L. Yuan, and J. Ye. An efficient algorithm for a class of fused lasso problems. In *Proceedings of the 16th ACM SIGKDD International Conference on Knowledge Discovery and Data Mining*, KDD '10, pages 323–332, New York, NY, USA, 2010. ACM.

B. Llanas and C. Moreno. Finding the projection on a polytope: An iterative method. *Computers & Mathematics with Applications*, 32(8):33–39, 1996.

F. Luisier, T. Blu, and M. Unser. SURE-let for orthonormal wavelet-domain video denoising. *IEEE Transactions on Circuits and Systems for Video Technology*, 20(6):913–919, 2010a.

F. Luisier, C. Vonesh, T. Blu, and M. Unser. Fast interscale wavelet denoising of Poisson-corrupted images. *Signal Processing*, 90(2):415–427, 2010b.

H. T. Ma, C. H. Wu, and J. Y. Wu. Initiation of spontaneous epileptiform events in the rat neocortex in vivo. *Journal of Neurophysiology*, 91(2):934–945, 2004.

S. Maeda, S. Inagaki, H. Kawaguchi, and W. J. Song. Separation of signal and noise from in vivo optical recording in Guinea pigs using independent component analysis. *Neuroscience Letters*, 302(2-3):137–140, 2001.

J. Mairal, R. Jenatton, G. Obozinski, and F. Bach. Convex and network flow optimization for structured sparsity. *Journal of Machine Learning Research*, 12(nov):2681–2720, 2011.

S. Mallat. *A Wavelet Tour of Signal Processing, Third Edition: The Sparse Way*. Academic Press, 3rd edition, 2008.

S. Mallat and Z. Zhang. Matching pursuit with time-frequency dictionaries. *IEEE Transactions on Signal Processing*, 41:3397–3415, 1993.

S. Mallat and S. Zhong. Characterization of signals from multiscale edges. *Pattern Analysis and Machine Intelligence, IEEE Transactions on*, 14(7):710–732, 1992.

M. Marcus and V. J. Mizel. Functional composition on Sobolev spaces. *Bulletin of the American Mathematical Society*, 78(1):38–42, 1971.

V. Markounikau, C. Igel, A. Grinvald, and D. Jancke. A dynamic neural field model of mesoscopic cortical activity captured with voltage-sensitive dye imaging. *PLoS Computational Biology*, 6(9):e1000919, 2010.

B. Mercier. Lectures on topics in finite element solution of elliptic problems. *Lectures on Mathematics and Physics*, 63, 1979.

V. Michel, A. Gramfort, G. Varoquaux, E. Eger, and B. Thirion. Total variation regularization for fMRI-based prediction of behavior. *Medical Imaging, IEEE Transactions on*, 30(7):1328–1340, 2011.

O. J. Minty. Montone (nonlinear) operators in Hilbert space. *Duke Mathematical Journal*, 29(3):341–346, 1962.

L. Moisan. How to discretize the total variation of an image? *Proceedings in Applied Mathematics and Mechanics*, 7(1):1041907–1041908, 2007.

R. Monteiro and B. Svaiter. Iteration-complexity of block-decomposition algorithms and the alternating direction method of multipliers. *SIAM Journal on Optimization*, 23(1):475–507, 2013.

J.-J. Moreau. Fonctions convexes duales et points proximaux dans un espace hilbertien. *Comptes Rendus de l'Académie des Sciences de Paris Série A MathÃĺmatiques*, 255:2897–2899, 1962.

J.-J. Moreau. Proximité et dualité dans un espace hilbertien. *Bulletin de la Société Mathématique de France*, 93:273–299, 1965.

V. B. Mountcastle. The columnar organization of the neocortex. *Brain*, 120(4):701–722, 1997.

L. Muller and A. Destexhe. Propagating waves in thalamus, cortex and the thalamocortical system: Experiments and models. *Journal of Physiology Paris*, 106(5-6):222–238, 2012.

J.D.B. Nelson. Fused lasso and rotation invariant autoregressive models for texture classification. *Pattern Recognition Letters*, 34(16):2166–2172, 2013.

Y. Nesterov. Smooth minimization of nonsmooth functions. *Mathematical Programming*, 103(1):127–152, 2005.

Y. Nesterov. Gradient methods for minimizing composite functions. *Mathematical Programming*, 140(1):125–161, 2013.

G. Nowak, T. Hastie, J. R. Pollack, and R. Tibshirani. A fused lasso latent feature model for analyzing multi-sample acgh data. *Biostatistics*, 12(4):776–791, 2011.

G. Obozinski, B. Taskar, and M. Jordan. Joint covariate selection and joint subspace selection for multiple classification problems. *Statistics and Computing*, 20(2):231–252, 2010.

N. Ogura and I. Yamada. Nonstrictly convex minimization over the fixed point set of an asymptotically shrinking nonexpansive mapping. *Numerical Functional Analisys and Optimization*, 23(1-2):113–137, 2002.

S. Onat, P. Konig, and D. Jancke. Natural scene evoked population dynamics across cat primary visual cortex captured with voltage-sensitive dye imaging. *Cerebral Cortex*, 21(11):2542–2554, 2011a.

S. Onat, N. Nortmann, S. Rekauzke, P. Konig, and D. Jancke. Independent encoding of grating motion across stationary feature maps in primary visual cortex visualized with voltage-sensitive dye imaging. *NeuroImage*, 55(4):1763–1770, 2011b.

G. B. Passty. Ergodic convergence to a zero of the sum of monotone operators in Hilbert space. *Journal of Mathematical Analysis and Applications*, 72(2):383–390, 1979.

J.-C. Pesquet and N. Pustelnik. A parallel inertial proximal optimization method. *Pacific Journal of Optimization*, 8(2):273–306, 2012.

J.-C. Pesquet, A. Benazza-Benyahia, and C. Chaux. A SURE approach for digital signal/image deconvolution problems. *IEEE Transactions on Signal Processing*, 57(12): 4616–4632, 2009.

D. S. Peterka, H. Takahashi, and R. Yuste. Imaging voltage in neurons. *Neuron*, 69(1): 9–21, 2011.

C. C. H. Petersen, T. T. G. Hahn, M. Mehta, A. Grinvald, and B. Sakmann. Interaction of sensory responses with spontaneous depolarization in layer 2/3 barrel cortex. *Proceedings of the National Academy of Sciences*, 100(23):13638–13643, 2003.

R. R. Phelps. *Convex Functions, Monotone Operators and Differentiability*, volume 1364 of *Lecture Notes in Mathematics*. Springer Berlin Heidelberg, second edition, 1993.

T. Pock and A. Chambolle. Diagonal preconditioning for first order primal-dual algorithms in convex optimization. pages 1762–1769, 2011.

L. D. Popov. A modification of the Arrow-Hurwitz method of search for saddle points. *Matematicheskie Zametki*, 28(5):777–784, 1980.

N. Pustelnik, C. Chaux, and J.-C. Pesquet. Parallel ProXimal algorithm for image restoration using hybrid regularization. *IEEE Transactions on Image Processing*, 20 (9):2450–2462, 2011.

H. Raguet, J. M. Fadili, and G. Peyré. A generalized forward-backward splitting. *SIAM Journal on Imaging Sciences*, 6(3):1199–1226, 2013.

S. Ramani, T. Blu, and M. Unser. Monte-Carlo SURE: A black-box optimization of regularization parameters for general denoising algorithms. *IEEE Transactions on Image Processing*, 17(9):1540–1554, 2008.

S. Ramani, Z. Liu, J. Rosen, J.-F. Nielsen, and J. A. Fessler. Regularization parameter selection for nonlinear iterative image restoration and MRI reconstruction using GCV and SURE-based methods. *IEEE Transactions on Image Processing*, 21(8):3659–3672, 2012a.

S. Ramani, J. Rosen, Z. Liu, and J. A. Fessler. Iterative weighted risk estimation for nonlinear image restoration with analysis priors. *Proceedings SPIE*, 8296:82960NâĂŞ12, 2012b.

S. C. Rao, L. J. Toth, and M. Sur. Optically imaged maps of orientation preference in primary visual cortex of cats and ferrets. *Journal of Comparative Neurology*, 287(3): 358–370, 1997.

M. Raphan and E. P. Simoncelli. Optimal denoising in redundant representations. *IEEE Transactions on Image Processing*, 17(8):1342–1352, 2008.

J. Reidl, J. Starke, D. B. Omer, A. Grinvald, and H. Spors. Independent component analysis of high-resolution imaging data identifies distinct functional domains. *NeuroImage*, 34(1):94–108, 2007.

A. Reynaud, S. Takerkart, G. S. Masson, and F. Chavane. Linear model decomposition for voltage-sensitive dye imaging signals: application in awake behaving monkey. *NeuroImage*, 54(2):1196–1210, 2011.

R. T. Rockafellar. *Convex Analysis*. Princeton University Press, 1970.

R. T. Rockafellar. Monotone operators and the proximal point algorithm. *SIAM Journal on Control and Optimization*, 14(3):877–898, 1976.

F. Roosta-Khorasani and U. M. Ascher. Improved bounds on sample size for implicit matrix trace estimators. *CoRR*, abs/1308.2475, 2013.

L. I. Rudin, S. Osher, and E. Fatemi. Nonlinear total variation based noise removal algorithms. *Physica D: Nonlinar Phenomena*, 60(1-4):259–268, 1992.

B. M. Salzberg, H. V. Davila, and L. B. Cohen. Optical recording of impulses in individual neurones of an invertebrate central nervous system. *Nature*, 246(5434):508–509, 1973.

D. Sharon and A. Grinvald. Dynamics and constancy in cortical spatiotemporal patterns of orientation processing. *Science*, 295(5554):512–515, 2002.

D. Shoham, D. E. Glaser, A. Arieli, T. Kenet, C. Wijnbergen, Y. Toledo, R. Hildesheim, and A. Grinvald. Imaging cortical dynamics at high spatial and temporal resolution with novel blue voltage-sensitive dyes. *Neuron*, 24(4):791–802, 1999.

V. Solo and M. Ulfarsson. Threshold selection for group sparsity. In *2010 IEEE International Conference on Acoustics Speech and Signal Processing (ICASSP)*, pages 3754–3757, 2010.

M. V. Solodov. A class of decomposition methods for convex optimization and monotone variational inclusions via the hybrid inexact proximal point framework. *Optimization Methods and Software*, 19(5):557–575, 2004.

L. Song, E. J. Hennink, I. T. Young, and H. J. Tanke. Photobleaching kinetics of fluorescein in quantitative fluorescence microscopy. *Biophysical Journal*, 68(6):2588–2600, 1995.

J. E. Spingarn. Partial inverse of a monotone operator. *Applied Mathematics and Optimization*, 10(1):247–265, 1983.

J.-L. Starck, M. Elad, and D. L. Donoho. Redundant multiscale transforms and their application for morphological component separation. In *Advances in Imaging and Electron Physics*, volume 132 of *Advances in Imaging and Electron Physics*, pages 287–348. Elsevier, 2004.

J.-L. Starck, F. Murtagh, and J. M. Fadili. *Sparse Signal and Image Processing: Wavelets, Curvelets and Morphological Diversity*. Cambridge University Press, 2010.

C. M. Stein. Estimation of the mean of a multivariate normal distribution. *The Annals of Statistics*, 9(6):1135–1151, 1981.

K. Takagaki, M. T. Lippert, B. Dann, T. Wanger, and F. W. Ohl. Normalization of voltage-sensitive dye signal with functional activity measures. *PLoS ONE*, 3(12):e4041, 2008.

H. J. Tanke, P. van Oostveldt, and P. van Duijn. A parameter for the distribution of fluorophores in cells derived from measurements of inner filter effect and reabsorption phenomenon. *Cytometry*, 2(6):359–369, 1982.

R. Tibshirani. Regression shrinkage and selection via the LASSO. *Journal of the Royal Statistical Society*, 58(1):267–288, 1994.

R. Tibshirani, M. Saunders, S. Rosset, J. Zhu, and K. Knight. Sparsity and smoothness via the fused lasso. *Journal of the Royal Statistical Society B*, 67:91–108, 2005.

T. Tominaga and Y. Tominaga. A new nonscanning confocal microscopy module for functional voltage-sensitive dye and calcium imaging of neuronal circuit activity. *Journal of Neurophysiology*, 110(2):553–561, 2013.

P. Tseng. Applications of splitting algorithm to decomposition in convex programming and variational inequalities. *SIAM Journal on Control and Optimization*, 29(1):119–138, 1991.

P. Tseng. Alternating projection-proximal methods for convex programming and variational inequalities. *SIAM Journal on Optimization*, 7(4):951–965, 1997.

P. Tseng. A modified forward-backward splitting method for maximal monotone mapping. *SIAM Journal on Control and Optimization*, 38(2):431–446, 2000.

S. Vaiter, C.-A. Deledalle, G. Peyré, J. M. Fadili, and C. Dossal. The degrees of freedom of partly smooth regularizers. 2014. URL http://hal.archives-ouvertes.fr/hal-00981634.

D. Van De Ville and M. Kocher. SURE-based nonlocal means. *IEEE Signal Processing Letters*, 16(11):973–976, 2009.

D. Van De Ville and M. Kocher. Nonlocal means with dimensionality reduction and sure-based parameter selection. *IEEE Transactions on Image Processing*, 20(9):2683–2690, 2011.

R. Von Mises and H. Pollaczek-Geiringer. Praktische verfahren der gleichungsauflösung. *Zeitschrift für Angewandte Mathematik und Mechanik*, 9(2):152–164, 1929.

C. Vonesh, S. Ramani, and M. Unser. Recursive risk estimation for nonlinear image deconvolution with a wavelet-domain sparsity constraint. *IEEE International Conference on Image Processing*, pages 665–668, 2008.

B. C. Vũ. A splitting algorithm for dual monotone inclusions involving cocoercive operators. *Advances in Computational Mathematics*, 38(3):667–681, 2013.

M. H. Wright. The interior-point revolution in optimization: history, recent developments, and lasting consequences. *Bulletin of the American Mathematical Society*, 42 (1):39–56, 2004.

J. Y. Wu, X. Huang, and C. Zhang. Propagating waves of activity in the neocortex: What they are, what they do. *The Neuroscientist*, 14(5):487–502, 2008.

E. Yavuz. *Source separation analysis of visual cortical dynamics revealed by voltage sensitive dye imaging*. PhD thesis, École doctorale Cerveau, Cognition et Comportement (Paris), 2012.

G. Yu, S. Mallat, and E. Bacry. Audio denoising by time-frequency block thresholding. *IEEE Transactions on Signal Processing*, 56(5):1830–1839, 2008.

E. H. Zarantonello. Projections on convex sets, contributions to nonlinear functional analysis. In *Projections on convex sets in Hilbert space and spectral theory*, pages 237–341. Academic Press, 1971.

A. Zepeda, C. Arias, and F. Sengpiel. Optical imaging of intrinsic signals: recent developments in the methodology and its applications. *Journal of Neuroscience Methods*, 136(1):1–21, 2004.

P. Zhao, G. Rocha, and B. Yu. The composite absolute penalties family for grouped and hierarchical variable selection. *The Annals of Statistics*, 37(6A):3468–3497, 2009.

M. Zibulevsky and B. A. Pearlmutter. Blind source separation by sparse decomposition in a signal dictionary. *Neural Computation*, 13(4):863–882, 2001.

H. Zou, T. Hastie, and R. Tibshirani. On the "degrees of freedom" of the LASSO. *The Annals of Statistics*, 35(5):2173–2192, 2007.